

Abstract

Progress Toward Observing Quantum Effects in an Optomechanical System in Cryogenics

Cheng Yang

2011

Quantum optomechanical systems use radiation pressure of light to couple the optical field and the center-of-mass motion of micromechanical devices. Such systems provide powerful tools for generating and manipulating quantum mechanical states. In this thesis, a 8.3 mm long high finesse optical cavity coupled to a $1.5 \text{ mm} \times 1.5 \text{ mm} \times 50 \text{ nm}$ stoichiometric silicon nitride membrane is used as the optomechanical system, placed at 400 mK inside a ^3He fridge. The major goals of this research are: laser cooling the 261 kHz membrane vibrational mode to its quantum ground state; detecting the quantum fluctuation of radiation pressure, known as radiation pressure shot noise; and generating squeezed light.

The low mechanical frequency in this optomechanical system makes it susceptible to substantial laser phase noise. This large phase noise limits the lowest phonon number we can reach with laser cooling, and complicates the detection of mechanical motional state. In this thesis, based on Børkje's calculations[1], a clear understanding of laser cooling and heterodyne detection spectra when the laser classical noise is non-negligible is presented and compared to measured results. Preliminary laser cooling results down to about 60 phonons are shown, and method to observe radiation pressure shot noise is discussed. To reduce the laser phase noise, a filter cavity is built and is verified to have lowered the classical noise by a factor of over 560, paving the way for achieving ground state cooling and observation of radiation pressure shot noise.

The thesis begins with an overview of optomechanical systems and major efforts to achieve ground state cooling and observation of radiation pressure shot noise. The necessary theory is then presented, with a focus on the effects of laser classical noise. Experimental design and measurement methods are then discussed, highlighting our technical accomplishments by successfully implementing various feedback and feedforward schemes. A chapter is devoted to discussing the measured

laser classical noise. Then measurements of optomechanical effects and laser cooling down to about 60 phonons are presented. Finally future directions using filtered lasers are discussed.

Progress Toward Observing Quantum Effects in an Optomechanical System in Cryogenics

A Dissertation
Presented to the Faculty of the Graduate School
of
Yale University
in Candidacy for the Degree of
Doctor of Philosophy

by
Cheng Yang

Dissertation Director: Jack Harris

07/31/2011

Copyright © 2011 by Cheng Yang
All rights reserved.

Contents

Contents	iii
List of Symbols	vii
List of Figures	x
List of Tables	1
1 Introduction	2
1.1 Overview of quantum optomechanics	2
1.2 Basic optomechanical effects and laser cooling	3
1.3 Quantum limited measurement and radiation pressure shot noise	8
1.4 Membrane-in-the-middle setup	9
2 Basic Theory of Laser Cooling and Measurement of Mechanical Motion	12
2.1 Introduction	12
2.2 Basic theory of laser cooling	13
2.2.1 Equations of motion for the optomechanical system	13
2.2.2 Optical resonant frequency shift and optical damping	17
2.2.3 Laser cooling of effective phonon number	19
2.3 Heterodyne detection scheme	24
2.3.1 Basic theoretical framework	25
2.3.2 Power spectra of mechanical sidebands	31

2.3.3	Cross-correlation spectrum of mechanical sidebands	37
2.4	Spectrum of squeezing	43
2.5	Laser noise reduction by a filter cavity	48
3	Experimental Design	51
3.1	Membrane in the middle setup	51
3.1.1	Mechanical properties of Si ₃ N ₄ membrane	51
3.1.2	Optical properties of the cavity	51
3.1.3	Optomechanical coupling of the membrane-in-the-middle cavity	53
3.2	Overview of the optical setup	55
3.3	Heterodyne detection and PDH lock setup	56
3.4	Cooling beam locking	59
3.5	Cooling beam filter cavity	62
3.6	Measurement electronics	67
3.7	Heterodyne data analysis	71
3.7.1	Heterodyne carrier data analysis	71
3.7.2	Heterodyne power spectrum analysis	75
3.7.3	Heterodyne cross-correlation spectrum analysis	77
4	Laser Noise Characterization	83
4.1	Laser amplitude noise measurement	83
4.2	Laser phase noise measurement	85
4.2.1	Measurement method	85
4.2.2	Data analysis	89
4.2.2.1	Signal laser phase noise characterization	89
4.2.2.2	Cooling laser phase noise characterization	93
4.3	Filtered cooling laser phase noise characterization	96
4.3.1	Theoretical predictions of filter cavity performance	97
4.3.2	Measurements of filter cavity performance	97

4.4	Summary	99
5	Preliminary laser cooling results and discussions	100
5.1	Optomechanics as a function of cooling beam detuning	100
5.2	Laser cooling limited by classical laser noise	101
5.3	Laser cooling as a function of cooling beam power	105
5.3.1	Classical noise measurement	105
5.3.2	Thermometry based on heterodyne PSDs	107
5.3.2.1	Extracting signal beam detuning from PSD background ratio	107
5.3.2.2	Extracting effective phonon number from PSD Lorentzian peak ratio	109
5.4	Laser cooling as a function of signal beam detuning	116
6	Future directions and conclusions	119
6.1	Future directions	119
6.1.1	Laser cooling with filtered lasers	120
6.1.2	Spectrum of squeezing	122
6.2	Conclusion	123
A	Membrane Mechanical Properties	126
A.1	Derivation of membrane vibrational mode frequency	126
A.2	Derivation of membrane Duffing coefficient	127
B	Laser Technical Notes	130
B.1	Basics of Nd:YAG laser	130
B.1.1	Nd:YAG laser	130
B.1.2	Inside the Prometheus laser	133
B.2	Instructions for replacing laser diode	135
B.2.1	Replacing the laser diode	135
B.2.2	Laser output optimization	136
B.2.3	Noise eater adjustment	138

B.3 Changing the laser controller potentiometer 138

Bibliography **139**

List of Symbols

\hat{a}	annihilation operator of the optical field inside a cavity
\bar{a}	mean field amplitude of the intracavity optical field
$\hat{a}_{\{\text{in,ref}\}}$	annihilation operator of the cavity input and reflected optical field
\hat{a}_{out}	annihilation operator of the effective output optical field for the heterodyne spectra
$a_{\{\text{bb,rr,rb}\}}[\omega]$	anti-symmetric term in the upper, lower mechanical sideband of the heterodyne power spectrum and the cross correlation of the heterodyne mechanical sidebands
$a_{\{2,3,23\}}[\omega]$	anti-symmetric term in the lower, upper mechanical sideband of the heterodyne PSDs and the CSD calculated from the HF2 lock-in amplifier demodulated time traces
A	coefficient of linear coupling in the optomechanical system
$b_{\{\text{bb,rr,rb}\}}[\omega]$	background term in the upper, lower mechanical sideband of the heterodyne power spectrum and the cross correlation of the heterodyne mechanical sidebands
$b_{\{2,3,23\}}[\omega]$	background term in the lower, upper mechanical sideband of the heterodyne PSDs and the CSD calculated from the HF2 lock-in amplifier demodulated time traces
$B_{\pm}[\omega]$	coefficient of the optomechanical system's susceptibility to classical amplitude noise and phase noise
$B_{\text{mod}}[\omega]$	classical noise term in the heterodyne power spectra
\hat{c}	annihilation operator of the mechanical oscillator

$C_{\{xx,yy,xy\}}$	classical amplitude noise, phase noise and their correlation of an optical field. $C_{xx} = 0.25$ corresponds to an amplitude noise at the shot noise level
\hat{d}	intracavity optical field fluctuation
$\hat{d}_{\{\text{in,ref}\}}$	cavity input and reflected optical field fluctuations
\hat{d}_{out}	fluctuation in the effective output optical field for the heterodyne spectra
$D_{\text{mod}}[\omega]$	classical noise term in the heterodyne cross correlation spectrum
$f_{\{c,h\}}$	center frequency and halfwidth of the heterodyne mechanical sideband power spectral density Fano peak fit
F	cavity finesse
m	effective mass of the mechanical oscillator
n_{eff}	effective phonon number of the mechanical oscillator including optomechanical effects
n_{opt}	effective phonon number due to optomechanical effects
n_{th}	thermal phonon number
P_{in}	optical power incident on a cavity
Q	mechanical quality factor of a mechanical oscillator
r_{d}	membrane amplitude reflection coefficient
$s_{\{\text{bb,rr,rb}\}}[\omega]$	symmetric term in the upper, lower mechanical sideband of the heterodyne power spectrum and the cross correlation of the heterodyne mechanical sidebands
$s_{\{2,3,23\}}[\omega]$	symmetric term in the lower, upper mechanical sideband of the heterodyne PSDs and the CSD calculated from the HF2 lock-in amplifier demodulated time traces
$S_{\{\text{bb,rr,rb}\}}[\omega]$	heterodyne mechanical sideband power spectra and the cross correlation spectrum

$S_{\{2,3,23\}}[\omega]$	heterodyne mechanical sideband PSDs and CSD calculated from the HF2 lock-in amplifier demodulated time traces
$S_{\varphi}^{out}[\omega]$	squeezing spectrum of the cavity output field
\hat{z}	mechanical oscillator position operator, normalized from position x by the zero point motion
$Z_{\{L,U,reference\}}$	lock-in demodulated time traces by the reflected photodiode heterodyne signal at upper and lower mechanical sideband frequencies and by the reference photodiode heterodyne signal
α	effective optomechanical coupling $A\bar{a}$
ϕ	intracavity optical field phase relative to the input optical field
$\gamma_m, \tilde{\gamma}_m$	intrinsic and effective energy decay rate (damping rate) of a mechanical harmonic oscillator
γ_{opt}	optomechanical damping
$\chi_c[\omega]$	cavity susceptibility
$\chi_m[\omega]$	mechanical susceptibility
κ	full cavity linewidth. Same as the total energy decay rate of the intracavity field. $\kappa_{\{L,R,M\}}$ are the decay rates from the left mirror, the right mirror and the other internal loss mechanisms
λ	wavelength of light
θ	LO beam input field phase relative to the signal beam input field
θ_{cal}	phase difference between the heterodyne reflected carrier and the reference carrier
$\omega_m, \tilde{\omega}_m$	intrinsic and effective mechanical resonant frequencies
$\Delta_{\{s,p\}}$	cavity detuning of the signal and cooling beams

List of Figures

- 1.1 (a) Schematic of a typical optomechanical system consisting of an optical cavity with a movable end-mirror. (b) Sideband picture of laser cooling. The optomechanical coupling creates two sidebands at the mechanical frequency $\pm\omega_m$ away on the carrier laser field with frequency ω_L . The net cooling is optimized when the cooling sideband at $\omega_L + \omega_m$ is enhanced by the cavity resonance. When ω_m is larger than the cavity linewidth κ , in the resolved sideband limit, the cooling sideband is much stronger than the heating sideband, enabling cooling to the quantum ground state. 4
- 2.1 Schematic of a laser interacting with a cavity with a membrane in the middle. $\hat{a}_{in,L}$ includes an input beam and quantum noise. Cavity coupling to the vacuum noise bath through other loss mechanisms is described by the quantum noise input $\hat{a}_{in,M}$. The intracavity field \hat{a} is coupled to the membrane motion \hat{z} through radiation pressure. 14
- 2.2 Theoretical plot of $|B_{\pm}[\omega_m]|$ as a function of cavity detuning $\Delta/2\pi$. The blue curve is $|B_{+}[\omega_m]|$, a measure of the classical amplitude noise's contributes to optomechanical effects. The green curve is $|B_{-}[\omega_m]|$, a measure of the contribution from classical phase noise. The parameters used are $\kappa/2\pi = 119$ kHz, $\kappa_L = 0.165\kappa$, $\omega_m = 261$ kHz. Both functions reach maximum near $\Delta = -\omega_m = -261$ kHz. 21

2.3	Schematic of heterodyne detection setup. The cavity with membrane in the middle has three inputs: a cooling beam $\hat{a}_{\text{in,p}}$ for laser cooling the membrane motion, a signal beam $\hat{a}_{\text{in,s}}$ for locking to the cavity and detection, and an LO beam $\hat{a}_{\text{in,LO}}$ as the local oscillator for the heterodyne detection. The reflected beams from the cavity are directed to a reflected photodiode (PD).	24
3.1	Membrane mechanical ringdown measured with a lock-in amplifier. Blue dots are data, the red curve is a theoretical fit. The membrane is driven on resonance. Once the drive is turned off, the amplitude of the vibration at the mechanical resonance decays exponentially. The 6.351 s ringdown time corresponds to a mechanical linewidth $\gamma_{\text{m}}/2\pi = 0.050$ Hz, and a mechanical Q factor of 5.21×10^6	52
3.2	Cavity optical ringdown recorded by a DAQ card. Blue dots are real data, the red curve is theoretical fit. Reflected power decays exponentially when the beam is blocked. The exponential ringdown time constant is $\tau = 1.404 \mu\text{s}$, corresponding to a cavity linewidth $\kappa/2\pi = 113$ kHz. For a cavity length $L = 3.39$ cm, this corresponds to a finesse $F = (c/2L)/\kappa = 39100$	53
3.3	Overview of the measurement setup. Cooling filter cavity: reduces phase noise from the cooling laser. Heterodyne and PDH lock setup: generates a signal beam and an LO beam for heterodyne detection. The signal beam is locked to the experiment cavity using PDH locking. Cooling laser lock: locks the cooling laser to the signal laser. Reference PD: measures the phase of LO beam. Reflected PD: collect heterodyne signal and PDH signal. FP: fiberport. Half waveplate (HWP), quarter waveplate (QWP), and calcite polarizer (CP): used for matching polarization to fiber.	56
3.4	Frequency components of signal, LO and cooling beams	57

3.5	Schematic of the heterodyne and PDH lock setup. The signal beam goes through an EOM to generate the 15 MHz phase sidebands for PDH locking. It then goes through an AOM (Gooch&Housego R46080-1-1.06). The +1 order output of the AOM is 80 MHz shifted from the LO beam. Two Thorlabs PAF-X-7C fiberports (FP) transfer the beams to and from this setup. A half waveplate (HWP1) is put before a polarizing beamsplitter (PBS) to adjust the power ratio of the signal and LO beams. Another half waveplate (HWP2) matches the polarization of the calcite polarizer (CP), which is oriented for vertical polarization to minimize amplitude modulation at the EOM. A pair of $f = 200$ mm lenses (LS) focus the beam for EOM aperture. Another two pairs of half waveplates and quarter waveplates (QWP) match the preferred polarization of the fiber. A beamsplitter recombines the signal and LO beams before they go to the output fiberport.	58
3.6	Cooling beam lock electronics. A signal generator provides a ~ 9 GHz local oscillator to mixes down the photodiode (PD) beat signal to MHz range. This signal, after amplification, is split into two paths. One of the paths has a 1.9 MHz low pass filter to create a frequency dependent phase shift. The two signals are then combined at a mixer and creates a frequency dependent error signal. The error signal goes through a 160 kHz low pass filter, a PI controller, an op-amp and finally a 69 Hz low pass filter formed by a 1 MHz resistor and the 2.3 nF laser piezo capacitance.	60
3.7	PSD of mixed down beat signal between free-running signal and cooling lasers. The two lasers are locked 8.85 GHz apart using the cooling laser lock setup. The linewidth is less than 10 Hz.	61
3.8	Schematic of the slope difference between the cooling and signal beam cavity resonance dispersion curves. The cooling beam is addressing the n th longitudinal mode, the signal beam is addressing the $(n + 2)$ th longitudinal mode. For comparison, the resonant frequency of the cooling beam is shifted up by 2 free spectral ranges. The two curves have the same slope at the “sweet spot” in membrane position. This also corresponds to the position of maximal difference in the two resonant frequencies. .	62

3.9	Cooling filter cavity setup. An EOM produces 15 MHz PM sidebands. A photodiode (PD1) monitors the reflected beam to generate the error signal, another one (PD2) monitors a small portion of the transmitted beam, after the beam sampler (BSP). A CCD camera is used to verify the mode coupled. Two lenses (LS1, 2) are used to mode-match the cavity. LS1: $f = -100$ mm. LS2: $f = 200$ mm. A conflat can keeps the filter cavity in high vacuum environment, pumped by an ion pump. Both fiberports used are Thorlabs PAF-X-7C with a 1.4 mm diameter collimated output.	63
3.10	Mag-phase plot of the FPGA transfer function measured by lock-in amplifier. The blue curve shows a flat FPGA response when no transfer function is implemented. The green curve shows the response when we implement the phase lead on FPGA. When implemented, the phase edge around 10 kHz is increased by up to 75°	66
3.11	Filter cavity feedforward scheme. The PI controller output in the cooling laser feedback is sent to the filter cavity piezo for feedforward. The feedforward gain is adjusted by a $0 - 5$ k Ω potentiometer and fine tuned by a $0 - 5$ k Ω potentiometer in series with a 100 k Ω resistor. The feedforward phase is adjusted by a $2 - 7$ k Ω resistor before the 491 nF piezo capacitance.	67
3.12	Feedforward cancellation of low frequency noise. The blue curve shows the PDH error signal of the signal laser feedback when it is locked to the experimental cavity. The green curve shows the filter cavity PDH error signal when the filter cavity is simultaneously locked to the cooling laser, which is locked to the experiment cavity and the signal laser. The noise peaks below 1 kHz in the two plots match each other. The relative flatness of the green curve below 1 kHz compared to the blue curve is due to feedforward cancellation of low frequency noise from the cooling laser.	68

3.13 Schematic of the measurement electronics. The reflected photodiode (PD) signal is separated into its DC and AC parts at a bias T. Its 15 MHz component is further separated out by a low pass filter (LPF) and mixing with a 15 MHz local oscillator created by a Rigol signal generator. The mixed down signal is used as the PDH error signal for the signal laser feedback, and is also sent to input 2 on the HF2 lock-in amplifier. The reflected signal around 79.5 MHz is separated out by going through a bandpass filter (BPF) and mixed down to 21.3985 MHz by a 100.8985 MHz local oscillator created by an HP RF signal generator. The mixed down signal then goes into the HF2 input 1. The 80 MHz component of the reference photodiode signal is also mixed down to 20 MHz using the same local oscillator and goes to HF2 input 2.	69
3.14 Schematic of reflected signal beam phasor ρ .	73
3.15 Heterodyne carrier phase when the signal beam is swept through cavity resonance. (a) The blue curve is the reflected heterodyne carrier phase, the green curve is the reference carrier phase, the red curve is their difference, the calibrated phase. (b) a zoom-in of the calibrated phase around the cavity resonance.	74
3.16 Measured reflected signal beam phasor ρ .	75
3.17 A typical pair of heterodyne sideband PSDs fit to Fano lineshapes simultaneously. (a) is the lower sideband S_2 , and (b) is the upper sideband S_3 . The fit parameters as defined in (3.29) and (3.30) are: $f_c = 261.07$ Hz, $f_h = 8.81$ Hz, $b_2 = 3.249 \times 10^{-14}$, $b_3 = 3.431 \times 10^{-14}$, $s_2 = 3.41 \times 10^{-13}$, $s_3 = 3.59 \times 10^{-13}$, $a_2 = -8.24 \times 10^{-14}$, $a_3 = -8.49 \times 10^{-14}$.	78
3.18 Fit of measured PM sideband heterodyne phase $\theta_{\text{Calib}}/2$ as a function of frequency f around $f_{\text{Demod2}} = 261.1$ kHz.	81
3.19 Fano fits of S_{23} (a) real and (b) imaginary parts, generated from the same dataset as Figure 3.17. The fit parameters: $f_c = 261.07$ Hz, $f_h = 9.30$ Hz, $b_{23,r} = -1.355 \times 10^{-14}$, $b_{23,i} = -2.535 \times 10^{-14}$, $s_{23,r} = -1.87 \times 10^{-13}$, $s_{23,i} = -2.75 \times 10^{-13}$, $a_2 = 4.77 \times 10^{-14}$, $a_3 = 5.06 \times 10^{-14}$.	82

4.1	PSD of the signal laser amplitude noise. $142 \mu\text{W}$ from the signal beam is incident on a PDA10CF photodiode. The signal is amplified by an SRS 560 amplifier with 10^3 gain, and measured by a DAQ card. The blue curve is the dark noise of the detector. The green curve is the measured amplitude noise PSD. The noise level is $2.9 \times 10^{-8} \text{V}^2/\text{Hz}$ at 261 kHz. The black dashed line is the expected shot noise level at $142 \mu\text{W}$	84
4.2	PSD of the cooling laser amplitude noise. $158 \mu\text{W}$ from the signal beam is incident on a PDA10CF photodiode, the signal is amplified by an SRS 560 amplifier with gain= 10^3 , and measured by a DAQ card. The blue curve is the dark noise of the detector. The green curve is the measured amplitude noise PSD. The noise level is $2.0 \times 10^{-8} \text{V}^2/\text{Hz}$ at 261 kHz. The black dashed line is the expected shot noise level at $158 \mu\text{W}$	85
4.3	S_{tr} noise floor coefficients using experiment parameters $\kappa = 119 \text{kHz}$, $\kappa_{\text{L}} = 0.165\kappa$, $\Delta = 0$. At $\omega/2\pi = 261 \text{kHz}$, the coefficients for “Common C_{yy} ”, “Signal C_{xx} or C_{yy} ”, “Common C_{xx} ”, and “Common C_{xy} ” are 0.10, 0.97, 2.74, and -0.096	88
4.4	(a) FFT of reference photodiode oscilloscope time trace demodulated at 79.91 MHz. The Fourier transformed data is normalized, notice the center peak at 0 is 1. Big peaks show up at multiples of 15MHz . (b) Zoom in of the $\pm 260 \text{kHz}$ peaks. The averaged height is 0.0023, the average phase is -90.7° . This confirms the injected noise is almost pure phase modulation, with magnitude 2.3 mrad.	90
4.5	Signal laser off resonance heterodyne upper and lower sideband PSDs. The upper sideband PSD (green line) is reversed in frequency to compare with the lower sideband PSD (blue line). The noise floor is $1.8 \times 10^{-15} \text{V}^2/\text{Hz}$. PM tone peak shows up at 2 kHz. The black dashed line is the inferred detection shot noise level.	91

4.6	Signal laser on resonance heterodyne upper and lower sideband PSDs. The blue curve is the lower sideband PSD, and the green curve is the upper sideband PSD. The upper sideband PSD is reversed in frequency to compare with the lower sideband PSD. For the lower sideband, the noise floor is at $1.4 \times 10^{-14} \text{ V}^2/\text{Hz}$. The PM tone peak integrated area is $8.7 \times 10^{-9} \text{ V}^2$. For the upper sideband, the noise floor is at $1.6 \times 10^{-14} \text{ V}^2/\text{Hz}$. The PM tone peak integrated area is $8.5 \times 10^{-9} \text{ V}^2$. The peak around 0 Hz is the motional sideband, the peak around 1 kHz is due to signal laser phase noise. The black dashed line is the inferred detection shot noise level.	92
4.7	FFT of reference photodiode oscilloscope time trace demodulated at 79.91 MHz, zoomed in at the $\pm 260 \text{ kHz}$ peaks. The averaged height is 0.0022, the averaged phase is -87.9° . This confirms the injected noise is almost pure phase modulation, with magnitude 2.2 mrad.	94
4.8	Cooling laser off resonance heterodyne upper and lower sideband PSDs. The blue curve is the lower sideband PSD, and the green curve is the upper sideband PSD. The upper sideband PSD is reversed in frequency to compare with the lower sideband PSD. The noise floor around 0 Hz is $2.3 \times 10^{-15} \text{ V}^2/\text{Hz}$. The noise floor roll-off is due to the 7 kHz low pass filters in the HF2. The black dashed line is the inferred detection shot noise level.	95
4.9	Cooling laser on resonance heterodyne upper and lower sideband PSDs. The blue curve is the lower sideband PSD, and the green curve is the upper sideband PSD. The upper sideband PSD is reversed in frequency to compare with the lower sideband PSD. For the lower sideband, the noise floor around 0 Hz is $1.3 \times 10^{-14} \text{ V}^2/\text{Hz}$. The PM tone peak integrated area is $1.1 \times 10^{-8} \text{ V}^2$. For the upper sideband, the noise floor is at $1.2 \times 10^{-14} \text{ V}^2/\text{Hz}$. The PM tone peak integrated area is $1.07 \times 10^{-9} \text{ V}^2$. The peak around 0 kHz is the motional sideband. The overall roll-off at higher frequencies is due to the 7 kHz low pass filters in the HF2. The black dashed line is the inferred detection shot noise level.	96

4.10	Heterodyne lower sideband PSD of filtered cooling laser. The green curve is the off resonance power spectrum. The blue curve is the on resonance power spectrum. The PM tone peak integrated area is $2.6 \times 10^{-9} \text{ V}^2$. Around 0 Hz , the noise floor change from off resonance to on resonance is about $1 \times 10^{-16} \text{ V}^2/\text{Hz}$. The broad peak around 0 kHz is the mechanical sideband. The other noise peaks are likely due to frequency fluctuations caused by an imperfect lock. The overall roll-off is due to the HF2 7 kHz low pass filters. The black dashed line is the inferred detection shot noise level. . . .	98
5.1	Fit of sideband heterodyne PSDs. (a) upper sideband, (b) lower sideband. The blue diamonds are data points, the red curves are the Fano peak fits using Equations (3.29) and (3.30). From the fits, we extract the center frequency $f_c = 261123.8 \text{ Hz}$, peak halfwidth $f_h = 24.497 \text{ Hz}$	101
5.2	Fit of (a) Fano peak frequency shift and (b) Fano peak linewidth in the heterodyne sideband PSDs as a function of cooling beam detuning. The blue dots are data extracted from sideband heterodyne PSD fits. The red curves are the theory fits. Parameters used in the red curves are: cavity decay rate $\kappa/2\pi = 119 \text{ kHz}$; cooling power $P_{\text{in,p}} = 2.35 \mu\text{W}$ before 15% power loss; cavity coupling $A = 19.0 \text{ rad}/(\text{m} \times \text{s})$. The fit variables are: intrinsic mechanical resonant frequency $\omega_m/2\pi = 261.153 \text{ kHz}$; cavity coupling $\kappa_L/\kappa = 0.193$; and an offset in the cooling beam detuning from an arbitrary setpoint $\Delta_0/2\pi = 52331.8 \text{ kHz}$	102
5.3	Theoretical plot of effective phonon number as a function of cooling beam input power, including all laser classical noise. The signal beam is $2 \mu\text{W}$ at -10 kHz detuning. The cooling beam is at -260 kHz detuning. The classical noise of the two lasers at $1 \mu\text{W}$ are: for the signal beam, $C_{\text{xx,s}} = 0.016$, $C_{\text{yy,s}} = 105$; for the cooling beam, $C_{\text{xx,p}} = 0.0089$, $C_{\text{yy,p}} = 61$. The lowest achievable phonon number is 30. . . .	103

5.4	Theoretical plot of equivalent phonon numbers $n_{s,rr}$, $n_{s,bb}$, $n_{a,rr}$, and $n_{a,bb}$ created by signal laser classical noise in the (a) lower and (b) upper sideband heterodyne power spectra. The blue curves are for the symmetric terms, and the green curves are for the anti-symmetric terms. The parameters used in the plots are: signal beam input power is $2\mu\text{W}$, $C_{xx,s} = 0.016$, $C_{yy,s} = 105$ at $1\mu\text{W}$	104
5.5	Off resonance upper and lower sideband heterodyne PSDs. The blue curve is for the lower sideband, the green curve is for the upper sideband. The upper sideband PSD is reversed in frequency to compare with the lower sideband PSD. The average noise floor is $2.7 \times 10^{-14} \text{V}^2/\text{Hz}$	106
5.6	On resonance upper and lower sideband heterodyne PSDs. The blue curve is for the lower sideband, the green curve is for the upper sideband. The upper sideband PSD is reversed in frequency to compare with the lower sideband PSD. The average noise floor is $4.1 \times 10^{-14} \text{V}^2/\text{Hz}$	106
5.7	Theoretical plot of $\frac{b_{bb}}{b_{rr}}$ as a function of $\Delta_s/2\pi$. The signal beam classical noise terms used in this plot are $C_{xx} = 0.031$, $C_{xx}^{(1)} = 49$, $C_{yy} = 280$, and $C_{xy} = 0$ at $1.95\mu\text{W}$. . .	108
5.8	Inferred signal beam detuning $\Delta_s/2\pi$ as a function of cooling power $P_{in,p}$. At each $P_{in,p}$, $\Delta_s/2\pi$ value is inferred from the $\frac{b_{bb}}{b_{rr}}$ value extracted from the fitted heterodyne PSDs.	109
5.9	Measured background ratio $\frac{b_{bb}}{b_{rr}}$ vs measured calibrated heterodyne carrier phase θ_{cal} . The fit is $\frac{b_{bb}}{b_{rr}} = 1.98 + 0.0072\theta_{cal}(\circ)$	110
5.10	Plot of effective phonon number inferred from heterodyne PSDs as a function of cooling power. The black diamonds are n_{eff} inferred from measured $\frac{s_{bb}}{s_{rr}}$. The error bars only contain propagated uncertainties of s_{bb} and s_{rr} in the PSD Fano fits. The blue curve is the theory including all measured classical noise. The green curve is the the theory without any classical noise. Parameters used for the plots are listed in Table 5.1.	112

5.11	Plot of measured Fano peak halfwidth f_h as a function of cooling beam power. The blue dots are f_h extracted from heterodyne PSDs. The error bars only include uncertainties of f_h in the PSD Fano fits. The green curve is the theory including optical damping from both the signal beam and the cooling beam. Parameters used for the plot are the same as in Figure 5.10.	113
5.12	(a) Cavity temperature change when the signal beam is locked to the cavity and the LO beams is turned on. (b) Mechanical frequency shift as a function of cavity temperature. The cavity temperature is monitored by a sensor attached to the cavity. The mechanical frequency is extracted from sideband heterodyne PSDs. Both curves are measured with signal beam input $P_{in,s} = 1.95 \mu\text{W}$, LO beam input $P_{in,LO} = 298 \mu\text{W}$ and no cooling beam.	114
5.13	Measured mechanical frequency shift as a function of fridge temperature for a low stress $1 \text{ mm} \times 1 \text{ mm} \times 50 \text{ nm}$ Si_3N_4 membrane. The fundamental vibrational mode's resonant frequency is around 118.98 kHz. The mechanical frequency is measured by a lock-in amplifier for mechanical ringdown measurements, the fridge temperature is measured by a thermometer near the membrane.	115
5.14	Plot of $\frac{df_c}{dP_{in,p}}$ as a function of signal beam detuning $\Delta_s/2\pi$. The signal beam detunings are inferred from $\frac{b_{bb}}{b_{rr}}$ and θ_{cal} using measured parameters.	117
5.15	Plot of effective phonon number inferred from heterodyne PSDs as a function of signal beam detuning. The cooling power is fixed at $P_{in,p} = 2.30 \mu\text{W}$. The black dots are produced using measured parameters and $\Delta_p - \Delta_s = -233 \text{ kHz} \times 2\pi$. The error bars only contain propagated uncertainties of s_{rr} and s_{bb} in the PSD Fano fits. The blue curve is the theory including all measured classical noise. The green curve is the the theory without any classical noise.	118

6.1	Theoretical plot of effective phonon number as a function of cooling beam input power. The blue curve includes all laser classical noise. The green curve has the cooling laser filtered by the filter cavity once. The red curve has the cooling laser filtered twice. In all three curves, the signal beam input power is $2 \mu\text{W}$, with -10 kHz detuning. The cooling beam detuning is $\Delta_p/2\pi = -260 \text{ kHz}$. The classical noise of the signal beam at $1 \mu\text{W}$ is $C_{xx,s} = 0.016$, $C_{yy,s} = 105$ for all three curves. The cooling beam classical noise terms at $1 \mu\text{W}$ are: for the blue curve, $C_{xx,p} = 0.0089$, $C_{yy,p} = 61$; for the green curve, $C_{xx,p} = 0.0089/563$, $C_{yy,p} = 61/563$; for the red curve, $C_{xx,p} = 0.0089/(563)^2$, $C_{yy,p} = 61/(563)^2$	121
6.2	Theoretical plot of equivalent phonon numbers $n_{s,rr}$, $n_{a,rr}$, $n_{s,bb}$, and $n_{a,bb}$ created by signal laser classical noise in the (a) lower and (b) upper sideband heterodyne power spectra around $\Delta_p/2\pi = -260 \text{ kHz}$. The blue curves are for the symmetric terms, and the green curves are for the anti-symmetric terms. The parameters used in the plots are: cooling beam power $P_{in,p} = 100 \mu\text{W}$; the filtered classical noise terms are $C_{xx,p} = 0.0089/(563)^2$, $C_{yy,p} = 61/(563)^2$ at $1 \mu\text{W}$	122
6.3	Theoretical plot of maximal output field squeezing $\min(S_\varphi^{out}[\omega])$ as a function of frequency ω and cooling beam detuning Δ_p . The cooling beam power is $P_{in,p} = 1 \text{ mW}$, with double-pass filtered classical noise $C_{xx,p} = 0.0089/(563)^2$, $C_{yy,p} = 61/(563)^2$ at $1 \mu\text{W}$. The signal beam power $P_{in,s} = 1 \mu\text{W}$ with $C_{xx,s} = 0.016$, $C_{yy,s} = 105$. Its detuning is $\Delta_s/2\pi = -10 \text{ kHz}$. The detection efficiency $\sigma = 0.71$	124
B.1	Energy levels of Nd^{3+} used to form the 1064 nm four-level system	131

B.2 Schematic of the Prometheus laser optical setup. The pump diode output at 808 nm goes through two lenses (LS1 and LS2) and a dichroic mirror (DM), into the MISER. The 1064 nm output of the MISER then goes to a beam sampler (BS) where a small part of it goes to a lens (LS3) and onto a photodiode (PD), which is used for the noise eater to feedback to the pump diode current. The rest of the beam goes through doubling crystal optics, where a small portion of the 1064 nm beam is used to generate 532 nm output. The pump diode is connected to a heat sink (HS). The MISER has two magnets on its sides, and a piezoelectric transducer (PZT) on its top. 133

List of Tables

3.1	HF2 lock-in amplifier inputs and settings.	71
4.1	Summary of classical phase and amplitude noise at 261 kHz of the signal laser, unfiltered cooling laser, and filtered cooling laser.	99
5.1	Summary of parameters used in Figures 5.10 and 5.11 and measurement methods to independently verify them.	111

Chapter 1

Introduction

1.1 Overview of quantum optomechanics

The mechanical effects of light, known as radiation pressure, were theoretically derived when Maxwell proposed his famous equations. Radiation pressure was then first experimentally observed over 100 years ago[2, 3]. However, there were few application of this minute force for a long time. This changed after the invention of the laser, which enabled high intensity, coherent light sources. Radiation pressure of a highly focused beam became a tool to trap small particles in the 1970s[4, 5]. It was then used to laser cool the translational motion of individual atoms[6–9], and later led to the creation of Bose-Einstein condensate (BEC)[10], which is a purely quantum state.

In recent years, developments in micro-fabrication technologies enabled radiation pressure to be applied to manipulate the motional mode of more macroscopic mechanical devices[11–18]. This created a new frontier in physics, known as quantum optomechanics. So far, devices have spanned from hundreds of nanometer to tens of centimeters, but they all intend to use radiation pressure to generate, detect, and utilize mechanical quantum states. Reaching the mechanical quantum ground state using laser cooling is an important goal of such efforts. The radiation pressure fluctuation caused by the quantum fluctuation of light, known as the radiation pressure shot noise (RPSN), is another important subject, as it sets a limit of the precision in optical interferometric position measurements. Observing RPSN remains a key first step in further efforts to improve precision

position measurement. The nonlinear optomechanical interaction between the light field and the mechanical motion also has the potential to produce nonclassical states of light and mechanical motion, such as squeezing of light[19, 20], mechanical squeezed state[21], and entanglement between the light field and the mechanical device[22].

In the following sections, I will first review some basic concepts in optomechanics, and present an overview of the basic idea and various experimental approaches to laser cooling the mechanical state. Then I will discuss RPSN with a focus on its relation to quantum limited measurements, and review different efforts to observe RPSN. Finally I will briefly introduce the optomechanical setup used in this thesis, and present an outline of the thesis chapters.

1.2 Basic optomechanical effects and laser cooling

As outlined in the pioneering theory works[23, 24], the most basic optomechanical system consists of an optical cavity where one end-mirror is suspended on a spring, as shown in Figure 1.1(a). When light circulates inside the cavity, the radiation pressure of light moves the suspended end mirror, thus coupling the optical and mechanical degrees of freedom parametrically. In essence, the photon number of the intracavity optical field is coupled to the position of the mechanical device—the movable end mirror. The suspended end mirror motional mode is a harmonic oscillator. When its motion is coupled to the radiation pressure, the mechanical susceptibility of the mirror is modified. This gives rise to two optomechanical effects: a shift in the effective mechanical resonant frequency, known as the *optical spring*; and a change in the effective damping of the mechanical oscillator, known as the *optical damping*. Both the frequency shift and the optical damping scale linearly with the laser power, and depend on the relative detuning of the laser frequency from the cavity resonance, or equivalently, the mirror position.

For such a non-equilibrium system, according to the fluctuation-dissipation theorem, the mechanical mode’s coupling to a thermal bath at temperature T is solely described by its damping rate. The optomechanical interaction modifies the damping rate, but it does not change the thermal Brownian drive. This implies a change in the effective temperature of the mechanical mode[25].

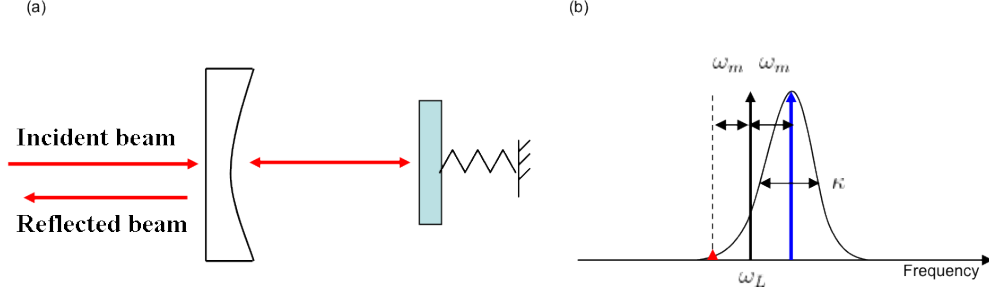


Figure 1.1: (a) Schematic of a typical optomechanical system consisting of an optical cavity with a movable end-mirror. (b) Sideband picture of laser cooling. The optomechanical coupling creates two sidebands at the mechanical frequency $\pm\omega_m$ away on the carrier laser field with frequency ω_L . The net cooling is optimized when the cooling sideband at $\omega_L + \omega_m$ is enhanced by the cavity resonance. When ω_m is larger than the cavity linewidth κ , in the resolved sideband limit, the cooling sideband is much stronger than the heating sideband, enabling cooling to the quantum ground state.

To be more quantitative, consider a mechanical mode with mean energy E_m , subject to Brownian noise from the thermal bath at temperature T . Without optomechanics, the mean energy of the mechanical mode follows

$$d \langle E_m \rangle / dt = -\gamma_m \langle E_m \rangle + \gamma_m k_B T \quad (1.1)$$

where γ_m is the intrinsic mechanical damping rate. The steady state solution of equation (1.1) is

$$\langle E_m \rangle = k_B T \quad (1.2)$$

given by the temperature T . However, when the laser is introduced, it changes the mechanical damping rate. If the laser is negatively detuned relative to the cavity, the effective damping rate γ_{tot} is larger than the intrinsic mechanical damping rate γ_m . Now Equation (1.1) modifies to

$$d \langle E_m \rangle / dt = -\gamma_{\text{tot}} \langle E_m \rangle + \gamma_m k_B T \quad (1.3)$$

The new steady state is

$$\langle E_m \rangle = k_B T \frac{\gamma_m}{\gamma_{\text{tot}}} \quad (1.4)$$

The effective temperature of the mechanical mode is therefore reduced to

$$T_{\text{eff}} = T \frac{\gamma_m}{\gamma_{\text{tot}}} \quad (1.5)$$

This classical picture implies that laser cooling can be made arbitrarily large, which is not true once we consider the complete quantum picture, i.e. the laser’s finite “temperature”.

Since both the optical field and the mechanical motion are described by harmonic oscillators, we can use the photon-phonon interaction picture to gain greater intuition. As shown in Figure 1.1(b), in frequency space, consider a laser with frequency ω_L coupled to the motion of the moving end mirror with a resonant frequency ω_m . Similar to the Raman scatterings, the optomechanical coupling creates an Anti-Stokes sideband at $\omega_L + \omega_m$ and a Stokes sideband at $\omega_L - \omega_m$ for the optical field. The Stokes sideband corresponds to the physical process of creating one extra phonon by extracting energy from the optical mode, hence heating the mechanical oscillator; while the latter process corresponds to cooling of the mechanical motion. We can use the cavity resonance to selectively enhance the cooling process, by putting the anti-Stokes sideband at the cavity resonance ω_c . The Stokes process is also suppressed due to the cavity response roll-off. It is also easy to see that in order to cool the mechanical motion to ground state, a big asymmetry between the anti-Stokes and the Stokes sidebands needs to be achieved, this requires the mechanical frequency ω_m to be larger than the cavity linewidth κ . This is known as the “resolved sideband limit”. Calculations[26] show the lowest achievable effective phonon number when $\omega_m \ll \kappa$ is

$$n_{\text{min}} = \left(\frac{\kappa}{4\omega_m}\right)^2 \quad (1.6)$$

This nonzero minimum phonon number is limited by RPSN, which always produces a small amount of mechanical motion.

The cooling also needs to be strong enough to cancel out any thermal excitation caused by the mechanical device’s coupling with the environment. This requires both high light intensity, and small mechanical coupling to the surroundings, denoted by a high mechanical quality factor $Q = \frac{\omega_m}{\gamma_m}$, where γ_m is the mechanical damping rate. To satisfy the resolved sideband limit and the

low dissipation requirements, we need a combination of high optical finesse F and high mechanical Q .

In the past few years, various groups have come up with diverse approaches to fulfill these requirements and achieve laser cooling, here I summarize some of the recent experiments that have reached or are close to reaching quantum ground state.

1. Optical cavity with a movable end-mirror.

Groups pursuing such setups focus on fabricating end mirrors with both good optical quality and low mechanical dissipation. The Aspelmeyer group[27] employed a Si_3N_4 micromechanical resonator with a multilayer dielectric Bragg mirror deposited on it which works as the movable end mirror of a Fabry Perot cavity. The effective mass of the movable mirror is $m = 43$ ng, its fundamental mechanical frequency is $\omega_m/2\pi = 945$ kHz, with mechanical $Q = 30,000$. The cavity linewidth is $\kappa/2\pi = 770$ kHz, making their setup slightly into the resolved sideband limit. Starting at $T = 5.3$ K, they were able to cool the mechanical motion down to 30 phonons, using 7 mW of cooling power. This minimum phonon number is limited by the thermal dissipation between the mechanical oscillator and the thermal environment, as is shown by the relatively low mechanical Q .

2. Whispering gallery mode (WGM) in microtoroids and microspheres.

In these experiments, light is coupled into a silica toroid or sphere through an evanescent field[28], and bounces inside the device many times through internal reflection. This creates a high Finesse optical cavity[29, 30]. The light couples to the radial breathing modes of the toroid, and changes the optical path length. Because of the small size (usually ~ 10 μm) of these devices, their vibrational modes usually start at 10s of MHz or higher. In recent works by the Kippenberg group[31], they used a silica microtoroid with cavity linewidth $\kappa/2\pi = 19$ MHz, and mechanical frequency $\omega_m/2\pi = 62$ MHz, deep inside the resolved sideband limit. Starting from $T = 1.65$ K or thermal phonon number $n_{\text{th}} \simeq 560$, using a ^4He fridge, the effective phonon number was cooled down to 63 with 200 μW laser power. Heating caused by optical absorption etc. starts to limit the cooling process. Later, using a higher optical finesse toroid starting at 600 mK in a ^4He fridge, they cooled a 70 MHz mechanical mode down to 9 phonons[32]. Most recently, they used a modified microtoroid supported by spikes to reduce the mechanical damping and the effective mass. Starting at 600 mK in a ^3He

fridge, they cooled a 78 MHz mechanical mode down to 1.7 phonons[33], limited by the onset of strong coupling between the optical mode and the mechanical mode.

Similarly, Park et al. [34] used the WGM in an asymmetric microsphere. In their case, the cavity $\kappa/2\pi = 26$ MHz, the mechanical mode $\omega_m/2\pi = 118.6$ MHz. Starting from $T = 1.4$ K, the effective phonon number went down to 37. The minimum phonon number is limited by its low mechanical quality factor $Q = 1540$, due to ultrasonic attenuation in silica.

3. Other nanomechanical devices.

Recently, the Painter group [35] has used techniques borrowed from the field of photonic crystals to engineer a Si nanobeam with periodic patterning added with perturbation at the center. This creates a co-localized optical and mechanical resonances near the beam center, coupled through radiation pressure. The mechanical mode frequency is $\omega_m/2\pi = 3.68$ GHz. They also created a phononic bandgap shield on the periphery of the nanobeam to increase the mechanical Q factor. The optical linewidth is $\kappa/2\pi = 500$ MHz. Starting from $T = 20$ K, they were able to laser cool the mechanical mode to a phonon number of 0.85.

4. Parametric coupling to superconducting microwave resonator.

The optomechanical coupling of a light field with a mechanical device can be easily extended to include electromagnetic field at microwave frequencies. The Schwab group[36] used a mechanical resonator formed by stoichiometric SiN and Al, with resonant frequency $\omega_m/2\pi = 6.3$ MHz. This mechanical device is capacitively coupled to a superconducting microwave resonator with resonant frequency $\omega_{sr}/2\pi = 7.5$ GHz. At $T = 145$ mK, the initial thermal occupation number is $n_{th} = 480$. The lowest effective phonon number achieved was $n_{eff} = 3.8$. This minimum was limited by the microwave resonator thermal occupation. In the measured noise spectra, the anti-correlation of the mechanical resonator motion and the microwave field creates squashing like inverted peaks. Similar effects in our system will be discussed later. In another recent experiment by Teufel et al.[37], a flexural mode of a 48 pg aluminum membrane is parametrically coupled to a superconducting microwave resonant circuit. With mechanical $\omega_m/2\pi = 10.56$ MHz, $Q = 3.3 \times 10^5$, and cavity $\kappa/2\pi = 200$ kHz, they achieved a phonon number of 0.34 at 15 mK.

1.3 Quantum limited measurement and radiation pressure shot noise

RPSN not only sets the limit for laser cooling, as discussed in the previous section, it also limits the precision of optical interferometric displacement measurements. This is of particular interest to sensitive measurements such as the Laser Interferometer Gravitational Wave Observatory (LIGO) project. In this project, a large laser interferometer is built to detect length-changing effects due to gravitational waves. The signal shows up as a phase difference between the optical lengths of the two arms in a Michelson interferometer. There are two fundamental quantum noise sources in this displacement measurement[38]: one is the photon counting noise, due to quantum fluctuations in the number of photons detected in the output ports; this term is inversely proportional to the light intensity. The other is the mirror position fluctuation due to RPSN, which is proportional to the light intensity. The sum of these two quantum noise sources sets the sensitivity, which is minimized when the contributions are equal. This minimum detection uncertainty is known as the standard quantum limit (SQL).

Notice the SQL is based on the assumption that the two noise sources are independent. It is therefore possible to beat the SQL in measurement precision by correlating the two fluctuations using squeezed light[39]. The classical analogy of such quantum noise reduction has been demonstrated[40]. However, RPSN has not yet been observed experimentally. The observation of RPSN in an optomechanical system is also closely linked to the quantum nondemolition measurement (QND) of the intracavity photon number[41, 42]. If such a QND measurement is achieved, then RPSN can be observed from the fluctuations of the intracavity photon number.

RPSN is usually much smaller than the thermal fluctuations of the mechanical oscillator, this makes it very difficult to observe. This can in principle be overcome by clever correlation schemes. Verlot et al. demonstrated the classical noise version of such a correlation scheme[43] in a standard optomechanical cavity. The basic idea is when the cavity is on resonance, the reflected light intensity contains only information of the intracavity light intensity and not the cavity, whereas the phase of the output contains information of the cavity displacement, caused by both radiation pressure

and thermal noise. The correlation of these two terms is therefore averaged to only include the intracavity photon number, making it a QND measurement of the photon state, and a measurement of RPSN. Børkje et al.[44] then modified this scheme to look for signatures of RPSN by correlating outputs of the membrane-in-the-middle cavity, a proof-of-principle experiment was carried out by Zwickl et al.[45].

1.4 Membrane-in-the-middle setup

The optomechanical system used in our research group consists of a high finesse Fabry Perot cavity and a silicon nitride (Si_3N_4) membrane in the middle of the optical cavity. Because the optical cavity is separated from the mechanical device, high optical quality and low mechanical dissipation can be achieved independently. The mechanical modes in this optomechanical setup are the vibrational modes of the silicon nitride membrane, with a typical fundamental mode frequency of a few hundred kHz. These modes have shown high mechanical $Q \sim 10^6$ even at room temperature[46]. The membrane also has little optical loss[47, 48], so integrating the membrane with an optical cavity does not degrade the optical quality.

A unique feature of this setup is its ability to change the optomechanical coupling from linear to quadratic or even quartic in the membrane position[47]. If the membrane is at a node (anti-node) of the intracavity field, the cavity resonance is changed minimally (maximally). This means the cavity resonant frequency has a quadratic dependence on the small membrane displacement at a node or anti-node. At other positions, the cavity resonance is linear with membrane displacement, equivalent to the standard setup in Figure 1.1(a). Furthermore, if we consider the different transverse modes of the cavity, some of them cross each other in the cavity dispersion curve. The membrane again acts as a perturbation to make these crossings avoided. Sankey et al. showed[48] such avoided crossing can be systematically tuned to create large quadratic or quartic optomechanical couplings, by adjusting the membrane position and tilt. This makes the membrane-in-the-middle system ideal for many quantum experiments, such as observation of quantum jump and phonon shot noise, and creation of a mechanical Schrödinger cat state. But in this thesis, I will focus on the case of linear

optomechanical coupling. Earlier, laser cooling by a factor of 40,000 times from room temperature was demonstrated[18]. In this thesis, I will describe our efforts toward ground state cooling and observation of RPSN in a cryogenic environment.

The optomechanical system discussed in this thesis has a mechanical frequency $\omega_m/2\pi = 261$ kHz, and an optical linewidth $\kappa/2\pi = 115$ kHz, slightly inside the resolved sideband limit. At 400 mK, the thermal phonon number is $n_{\text{th}} = 32,000$. The mechanical $Q = 5 \times 10^6$, corresponding to a mechanical damping rate $\gamma_m/2\pi = \omega_m/(2\pi Q) = 0.052$ Hz.

The mechanical frequency in our setup is much lower than all the devices in other laser cooling experiments mentioned in Section 1.2. This makes our system more susceptible to classical phase noise on the laser. We model the laser frequency noise spectral density at different frequencies by[49, 50]

$$S_{\dot{\phi}\dot{\phi}}[\omega] = \Gamma_1 \frac{2\gamma_c^2}{\gamma_c^2 + \omega^2} \quad (1.7)$$

in unit of (s^{-2}/Hz), where Γ_1 is the laser linewidth in (rad/s), and γ_c^{-1} is a finite correlation time. The frequency noise spectrum can be regarded as white at frequencies below γ_c ,

$$S_{\dot{\phi}\dot{\phi}}[\omega] = 2\Gamma_1 \quad (1.8)$$

set by the linewidth Γ_1 . This is the common assumptions used when discussing laser frequency noise[51]. But at high frequencies ($\omega \gg \gamma_c$) it rolls off as

$$S_{\dot{\phi}\dot{\phi}}[\omega] \simeq \frac{2\Gamma_1\gamma_c^2}{\omega^2} \propto 1/\omega^2 \quad (1.9)$$

At a certain frequency ω , the phase fluctuation $\delta\phi[\omega]$ is related to the frequency fluctuation $\delta\dot{\phi}[\omega]$ by

$$\delta\dot{\phi}[\omega] = \omega\delta\phi[\omega] \quad (1.10)$$

So the phase noise spectral density is expressed by

$$S_{\phi\phi}[\omega] = \frac{1}{\omega^2} S_{\dot{\phi}\dot{\phi}}[\omega] = \Gamma_1 \frac{2\gamma_c^2}{(\gamma_c^2 + \omega^2)\omega^2} \quad (1.11)$$

in unit of (rad^2/Hz). At high frequencies, the phase noise rolls off as $1/\omega^4$. Therefore, the phase noise at our mechanical frequency 261 kHz is considerably larger than the phase noise for other setups at MHz and GHz frequencies. At 261 kHz, the measured laser phase noise is about 400 times above the shot noise level for a $1\ \mu\text{W}$ beam.

As worked out in detail by Børkje[1], this high phase noise brings two complications to our experiment: (1) The large noise limits the lowest phonon number we can reach by laser cooling. As we increase the cooling power, the classical noise also increases, and produces additional mechanical motion. (2) The phase noise also distorts the measured output optical spectra, and makes it difficult to resolve RPSN. Because the light phase noise can have constructive or destructive correlation with the radiation induced mechanical motion, the area under the mechanical peak in the output spectra is not solely proportional to the mechanical motion. Therefore we cannot reliably estimate our phonon number from the mechanical peak linewidth and area, as all the other experiments discussed in Section 1.2 did. The RPSN measurement is also complicated because we need to carefully distinguish the anti-correlation signature of RPSN from the similar effects caused by phase noise. A full understanding of the effects of the large laser phase noise and efforts to reduce it will be the center topic of this thesis.

The rest of this thesis is organized as follows. Chapter 2 describes the theory of laser cooling and the heterodyne detection scheme used to measure the effective phonon number, RPSN, and squeezed light, with an emphasis on the modifications of ideal results by the classical laser noise. I will also discuss how a filter cavity can reduce the laser noise. Chapter 3 describes the designs of the experiment, and the heterodyne measurement and data analysis methods. Chapter 4 presents the methods and results of the laser noise measurement. It also demonstrates our ability to reduce the laser phase noise with a filter cavity, as predicted by theory. Chapter 5 discusses measurements of optomechanical effects and preliminary laser cooling results using unfiltered lasers. Chapter 6 discusses the future directions of the laser cooling and RPSN experiments with an improved experimental setup, and the potential to observe squeezed light using this new setup.

Chapter 2

Basic Theory of Laser Cooling and Measurement of Mechanical Motion

2.1 Introduction

In this chapter, I will discuss the theoretical framework for understanding laser cooling and heterodyne detection of the mechanical motional state. Before providing a mathematical description, I will begin with a qualitative discussion.

The membrane motion starts at a very high phonon number, due to the random excitations of its thermal bath. If we create another thermal link between it and a very “cold” bath (in this case a laser), at equilibrium the “temperature” of the membrane would be lower. This is the basic idea behind laser cooling. The better the thermal link between the membrane and the laser, and the worse the thermal link between the membrane and the environment, the closer the final temperature is to the laser "temperature". The thermal link to the laser is proportional to the number of photons interacting with the membrane per unit time. The thermal link with the bath is characterized by the membrane’s mechanical quality factor Q . A high Q is therefore desirable for the mechanical device we choose.

The limit of the laser cooling process is set by how "cold" the laser is. Fundamentally, the laser “temperature” is limited by quantum noise. This, in the resolved sideband limit, is enough to bring

the membrane to its quantum ground state. However, if there is additional classical noise on the laser, the effective temperature of the laser is raised, making laser cooling more challenging.

Once the membrane motional state is close to the ground state, various quantum effects can be explored. One thing we are interested in observing is the radiation pressure shot noise (RPSN). It is the back-action of the laser on the membrane caused by the quantum noise on the laser. This signal is usually buried beneath the effects of the larger thermal Langevin force, but at low effective temperature, we should be able to see it. However, the back-action caused by quantum noise on the laser is not easily separated from the noise caused by classical laser noise.

The observation of RPSN would pave the way for testing schemes to beat the standard quantum limit (SQL). Because RPSN also couples the mechanical state of the membrane with the optical state, it creates relatively broadband squeezed light.

2.2 Basic theory of laser cooling

2.2.1 Equations of motion for the optomechanical system

We first consider the simple case of having one laser interacting with the membrane in the middle of an optical cavity as depicted in Figure 2.1. The Hamiltonian of this system is

$$\hat{H} = \hbar\omega_m\hat{c}^\dagger\hat{c} + \hbar(\omega_c - A\hat{z})(\hat{a}^\dagger\hat{a} - \langle \hat{a}^\dagger\hat{a} \rangle) + \hat{H}_\kappa + \hat{H}_\gamma \quad (2.1)$$

\hat{a} and \hat{c} are the annihilation operators of the intracavity optical field and the mechanical oscillator respectively, and $\hat{z} = (\hat{c}^\dagger + \hat{c})$ is the normalized position operator for the mechanical oscillator. The first term describes the isolated mechanical oscillator. The second term describes the intracavity optical field. The angular frequency of the cavity resonance and the mechanical oscillator are denoted as ω_c and ω_m . The optical field is coupled to the mechanical motion through the linear coupling coefficient defined by $A \equiv \frac{\partial\omega_{cav}}{\partial\hat{z}}$, the slope of the cavity resonance $\omega_{cav}(\hat{z})$. The third term \hat{H}_κ denotes the intracavity field coupling to the optical input and the external vacuum noise bath. The interaction with vacuum noise bath, using Markov approximations, can be treated heuristically

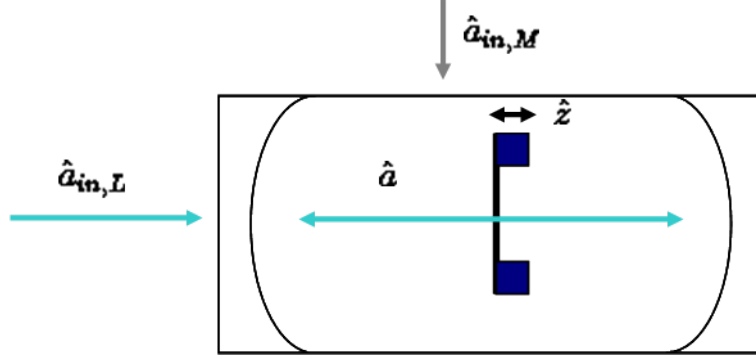


Figure 2.1: Schematic of a laser interacting with a cavity with a membrane in the middle. $\hat{a}_{in,L}$ includes an input beam and quantum noise. Cavity coupling to the vacuum noise bath through other loss mechanisms is described by the quantum noise input $\hat{a}_{in,M}$. The intracavity field \hat{a} is coupled to the membrane motion \hat{z} through radiation pressure.

as vacuum inputs similar to the optical input[52]. The final term \hat{H}_γ is the mechanical damping.

Based on the Hamiltonian, we write down the equations of motion[53]

$$\dot{\hat{a}} = -\left(\frac{\kappa}{2} + i\omega_c\right)\hat{a} - iA\hat{a}\hat{z} + \sqrt{\kappa_L}\hat{a}_{in,L} + \sqrt{\kappa_M}\hat{a}_{in,M} + \sqrt{\kappa_R}\hat{a}_{in,R} \quad (2.2)$$

$$\dot{\hat{c}} = -\left(\frac{\gamma_m}{2} + i\omega_m\right)\hat{c} - iA(\hat{a}^\dagger\hat{a} - \langle \hat{a}^\dagger\hat{a} \rangle) + \sqrt{\gamma_m}\hat{\eta} \quad (2.3)$$

where $\hat{a}_{in,\{L,R,M\}}$ are the annihilation operators for the optical input and vacuum noise inputs on the left, right end mirrors and the other loss mechanisms inside the cavity. The various loss mechanisms inside the cavity include coupling to other optical modes and absorption at the membrane or mirrors. Correspondingly, κ_L , κ_R , and κ_M denote the energy decay rate of the intracavity field through the left mirror, the right mirror and the other internal loss mechanisms. They satisfy $\kappa = \kappa_L + \kappa_M + \kappa_R$. For the single-sided cavity we use in this experiment, κ_R is negligible.

Assume the input optical field, with angular frequency ω_p , is from the left side of the cavity. In rotating frame, $\hat{a}_{in,L}(t) = e^{-i\omega_p t}(\bar{a}_{in}(t) + \delta x(t) + i\delta y(t) + \hat{\zeta}_L(t))$. $\bar{a}_{in}(t)$ is the mean field amplitude, $\delta x, \delta y$ are the classical amplitude and phase noise on the laser, $\hat{\zeta}_L$ is the vacuum noise entering from the left side. Similarly, the other vacuum noise inputs are included as $\hat{a}_{in,M}(t) = e^{-i\omega_p t}\hat{\zeta}_M(t)$.

Around the mechanical resonance frequency, we can assume the classical noise terms to be white,

and define their amplitudes by

$$\begin{aligned}
\langle \delta x(t)\delta x(t') \rangle &= C_{xx}\delta(t-t') \\
\langle \delta y(t)\delta y(t') \rangle &= C_{yy}\delta(t-t') \\
\langle \delta x(t)\delta y(t') \rangle &= C_{xy}\delta(t-t')
\end{aligned} \tag{2.4}$$

C_{xy} reflects the fact that, as will be mentioned in Appendix B, there are mechanisms that might correlate the laser amplitude and phase noise. The classical nature of this correlation makes it satisfy Cauchy's Inequality $C_{xy}^2 \leq C_{xx}C_{yy}$. Physically, an optical field with $C_{xx} = 0.25$ means the classical amplitude noise is at the shot noise level, similarly for C_{yy} and C_{xy} .

The quantum noise inputs satisfy

$$\begin{aligned}
\langle \hat{\zeta}(t)\hat{\zeta}^\dagger(t') \rangle &= (n_c + 1)\delta(t-t') \\
\langle \hat{\zeta}^\dagger(t)\hat{\zeta}(t') \rangle &= n_c\delta(t-t')
\end{aligned} \tag{2.5}$$

n_c is the thermal occupation number at cavity resonant frequency ω_c . Since $\hbar\omega_c \gg k_B T$, $n_c = \frac{1}{e^{\frac{\hbar\omega_c}{k_B T}} - 1} \simeq \frac{k_B T}{\hbar\omega_c} \simeq 0$. A quantum noise limited laser is therefore ‘‘cold’’.

For the mechanical oscillator, γ_m is the decay rate of the oscillation amplitude. It also denotes the oscillator's coupling to the thermal bath. γ_m is linked to the mechanical Q factor as $Q = \omega_m/\gamma_m$. The mechanical mode is excited by the thermal Langevin force $\hat{\eta}$. This stochastic Brownian noise is in general non-Markovian[54]. But at high Q , only a narrow frequency range around ω_m will contribute to the Brownian motion, we can treat the interaction as a Markovian process, and the thermal bath satisfies[52, 55]

$$\begin{aligned}
\langle \hat{\eta}(t)\hat{\eta}^\dagger(t') \rangle &= (n_{\text{th}} + 1)\delta(t-t') \\
\langle \hat{\eta}^\dagger(t)\hat{\eta}(t') \rangle &= n_{\text{th}}\delta(t-t')
\end{aligned} \tag{2.6}$$

where $n_{\text{th}} = \frac{1}{e^{\frac{\hbar\omega_m}{k_B T}} - 1} \simeq \frac{k_B T}{\hbar\omega_m}$ is the average phonon number of the motional state determined by the

thermal bath.

The above definitions can also be expressed in Fourier space as

$$\begin{aligned}
\langle \hat{\eta}[\omega]\hat{\eta}^\dagger[-\omega] \rangle &= n_{\text{th}} + 1 \\
\langle \hat{\eta}^\dagger[\omega]\hat{\eta}[-\omega] \rangle &= n_{\text{th}} \\
\langle \hat{\zeta}[\omega]\hat{\zeta}^\dagger[-\omega] \rangle &= 1 \\
\langle \hat{\zeta}^\dagger[\omega]\hat{\zeta}[-\omega] \rangle &= 0 \\
\langle \delta x[\omega]\delta x[-\omega] \rangle &= C_{\text{xx}} \\
\langle \delta y[\omega]\delta y[-\omega] \rangle &= C_{\text{yy}} \\
\langle \delta x[\omega]\delta y[-\omega] \rangle &= \langle \delta y[\omega]\delta x[-\omega] \rangle = C_{\text{xy}}
\end{aligned} \tag{2.7}$$

For the optical powers we are dealing in this thesis, the amplitude of the laser beam is always large compared to the fluctuations or modulations on it. We can therefore use the linearized quantum noise description. In the rotating frame, we can write the intracavity field as $\hat{a}(t) = e^{-i\omega_p t}(\bar{a} + \hat{d}(t))$, where \bar{a} is the mean field amplitude and $\hat{d}(t)$ the fluctuations. To the first order in the fluctuations, the intracavity field and motional state fluctuations satisfy:

$$\dot{\hat{d}} = -\left(\frac{\kappa}{2} - i\Delta\right)\hat{d} - i\alpha\hat{z} + \sqrt{\kappa_L}(\delta x + i\delta y + \hat{\zeta}_L) + \sqrt{\kappa_M}\hat{\zeta}_M \tag{2.8}$$

$$\dot{\hat{c}} = -\left(\frac{\gamma_m}{2} + i\omega_m\right)\hat{c} - i(\alpha^*\hat{d} + \alpha\hat{d}^\dagger) + \sqrt{\gamma_m}\hat{\eta} \tag{2.9}$$

Here we define detuning $\Delta = \omega_p - \omega_c$, and effective coupling $\alpha = A\bar{a}$. It is also straightforward to get $\bar{a} = \frac{\sqrt{\kappa_L}}{\kappa/2 - i\Delta}\bar{a}_{\text{in}}$. This means the phase of the intracavity field is shifted from that of the input field by $\phi = \arctan(\frac{2\Delta}{\kappa})$. In all our following discussions, we will be referencing phases against the input field, i.e. assuming \bar{a}_{in} to be real. We could therefore write the intracavity field as $\bar{a} = e^{i\phi}|\bar{a}|$.

2.2.2 Optical resonant frequency shift and optical damping

In Fourier space, the solutions to the linearized equations and their conjugates are

$$\hat{d}[\omega] = \int dt e^{i\omega t} \hat{d}(t) = \chi_c[\omega](\hat{\xi}[\omega] - i\alpha\hat{z}[\omega]) \quad (2.10)$$

$$\hat{d}^\dagger[\omega] = \int dt e^{i\omega t} \hat{d}^\dagger(t) = \chi_c^*[-\omega](\hat{\xi}^\dagger[\omega] + i\alpha^*\hat{z}[\omega]) \quad (2.11)$$

$$\begin{aligned} \hat{c}[\omega] &= \int dt e^{i\omega t} \hat{c}(t) \\ &= \chi_m[\omega][\sqrt{\gamma_m}\hat{\eta}[\omega] - i(\alpha^*\chi_c[\omega]\hat{\xi}[\omega] + \alpha\chi_c^*[-\omega]\hat{\xi}^\dagger[\omega])] - |\alpha|^2(\chi_c[\omega] - \chi_c^*[-\omega])\hat{z}[\omega] \end{aligned} \quad (2.12)$$

$$\begin{aligned} \hat{c}^\dagger[\omega] &= \int dt e^{i\omega t} \hat{c}^\dagger(t) \\ &= \chi_m^*[-\omega][\sqrt{\gamma_m}\hat{\eta}^\dagger[\omega] + i(\alpha^*\chi_c[\omega]\hat{\xi}[\omega] + \alpha\chi_c^*[-\omega]\hat{\xi}^\dagger[\omega])] + |\alpha|^2(\chi_c[\omega] - \chi_c^*[-\omega])\hat{z}[\omega] \end{aligned} \quad (2.13)$$

where we define $\hat{\xi} = \sqrt{\kappa_L}(\delta x + i\delta y + \hat{\zeta}_L) + \sqrt{\kappa_M}\hat{\zeta}_M$ as the effective noise source, $\chi_c[\omega] = [\kappa/2 - i(\omega + \Delta)]^{-1}$ the cavity susceptibility. And $\chi_m[\omega] = [\gamma_m/2 - i(\omega - \omega_m)]^{-1}$ is the mechanical susceptibility. Also notice $\hat{c}^\dagger[\omega] \neq (\hat{c}[\omega])^\dagger$.

It is easier to solve for $\hat{z}[\omega] = \hat{c}[\omega] + \hat{c}^\dagger[\omega]$. Note

$$\chi_m^{*-1}[-\omega] - \chi_m^{-1}[\omega] = -2i\omega_m \quad (2.14)$$

We get

$$\hat{z}[\omega] = \frac{1}{N[\omega]}[\sqrt{\gamma_m}(\chi_m^{*-1}[-\omega]\hat{\eta}[\omega] + \chi_m^{-1}[\omega]\hat{\eta}^\dagger[\omega]) - 2\omega_m(\alpha^*\chi_c[\omega]\hat{\xi}[\omega] + \alpha\chi_c^*[-\omega]\hat{\xi}^\dagger[\omega])] \quad (2.15)$$

The first term inside the square bracket of \hat{z} expression comes from the thermal drive. The second term denotes the additional drive created by optomechanical effects. The optical field not only provides new drive force terms, it also alters the effective mechanical susceptibility. The denominator

in Equation (2.15) is:

$$N[\omega] = \chi_m^{-1}[\omega]\chi_m^{*-1}[-\omega] + 2\omega_m\Sigma[\omega] \quad (2.16)$$

$$\Sigma[\omega] = -i|\alpha|^2(\chi_c[\omega] - \chi_c^*[-\omega]) \quad (2.17)$$

We can compare Equation (2.15) to a driven simple harmonic oscillator:

$$\hat{z}_o[\omega] = \frac{1}{\chi_m^{-1}[\omega]\chi_m^{*-1}[-\omega]} \sqrt{\gamma_m}(\chi_m^{*-1}[-\omega]\hat{\eta}[\omega] + \chi_m^{-1}[\omega]\hat{\eta}^\dagger[\omega]) \quad (2.18)$$

In the limit of weak coupling, i.e. the total damping $\tilde{\gamma}_m \ll \kappa$, the mechanical oscillator only responds to frequencies around its resonance. So we compare the $\hat{\eta}[\omega]$ drive terms in Equations (2.15) and (2.18) explicitly around $\omega = \omega_m$. The denominator in the simple harmonic oscillator case is

$$\chi_m^{-1}[\omega] = \gamma_m/2 - i(\omega - \omega_m)$$

In the optomechanical case, the denominator around $\omega = \omega_m$ is

$$\chi_m^*[-\omega]N[\omega] \approx \gamma_m/2 - i(\omega - \omega_m) + i\Sigma[\omega_m] = \tilde{\gamma}_m/2 - i(\omega - \tilde{\omega}_m) \equiv \chi_{\text{eff}}^{-1}[\omega] \quad (2.19)$$

We realize that $\Sigma[\omega]$ can be seen as the optomechanical "self-energy", and the effective mechanical resonant frequency and damping rate are

$$\tilde{\omega}_m = \omega_m + \delta\omega_m \quad (2.20)$$

$$\tilde{\gamma}_m = \gamma_m + \gamma_{\text{opt}} \quad (2.21)$$

$$\delta\omega_m = \text{Re}(\Sigma[\omega]) = 2\Delta|\chi_m(\omega)|^2|\chi_m(-\omega)|^2|\alpha|^2[(\kappa/2)^2 - \omega_m^2 + \Delta^2] \quad (2.22)$$

$$\gamma_{\text{opt}} = -2\text{Im}(\Sigma[\omega_m]) = -4\Delta|\chi_m[\omega]|^2|\chi_m[-\omega]|^2|\alpha|^2\kappa\omega_m \quad (2.23)$$

Once again, these equations are valid in the weak-coupling limit $\gamma_m + \gamma_{\text{opt}} \ll \kappa$, which is the case for our experiment.

2.2.3 Laser cooling of effective phonon number

To understand the "thermal" effects of the laser better, we can write down the expression for $S_{\hat{c}^\dagger\hat{c}}[\omega] \equiv \langle \hat{c}^\dagger[\omega]\hat{c}[-\omega] \rangle = \int_{-\infty}^{+\infty} dt e^{i\omega\tau} \langle \hat{c}^\dagger(t)\hat{c}(t+\tau) \rangle$, which provides us the effective phonon number when integrating over the whole frequency space[26]. The second step in this equation is given by the Wiener-Khinchin theorem[52]. Notice since \hat{c} is a quantum operator, we do not expect $S_{\hat{c}^\dagger\hat{c}}[\omega] = S_{\hat{c}^\dagger\hat{c}}[-\omega]$ as in the case of a classical signal.

Putting Equation (2.15) back into Equations (2.12) and (2.13), we can solve for $\hat{c}^\dagger[\omega]$ and $\hat{c}[\omega]$:

$$\begin{aligned} \hat{c}^\dagger[\omega] = \frac{\chi_m^*[-\omega]}{N[\omega]} \{ & -\Lambda[\omega]N[\omega] + 2\omega_m\Sigma[\omega]\Lambda[\omega] \\ & + \sqrt{\gamma_m}[(\hat{\eta}^\dagger[\omega]N[\omega] + i\Sigma[\omega](\chi_m^{*-1}[-\omega]\hat{\eta}[\omega] + \chi_m^{-1}[\omega]\hat{\eta}^\dagger[\omega]))] \} \end{aligned} \quad (2.24)$$

$$\begin{aligned} \hat{c}[\omega] = \frac{\chi_m[\omega]}{N[\omega]} \{ & \Lambda[\omega]N[\omega] - 2\omega_m\Sigma[\omega]\Lambda[\omega] \\ & + \sqrt{\gamma_m}[\hat{\eta}[\omega]N[\omega] - i\Sigma[\omega](\chi_m^{*-1}[-\omega]\hat{\eta}[\omega] + \chi_m^{-1}[\omega]\hat{\eta}^\dagger[\omega])] \} \end{aligned} \quad (2.25)$$

where we have defined

$$\Lambda[\omega] = -i(\alpha^*\chi_c[\omega]\hat{\xi}[\omega] + \alpha\chi_c^*[-\omega]\hat{\xi}^\dagger[\omega]) \quad (2.26)$$

which includes all the optical drive terms.

The expressions could then be simplified by using the relations

$$N[\omega] - 2\omega_m\Sigma[\omega] = \chi_m^{-1}[\omega]\chi_m^{*-1}[-\omega] \quad (2.27)$$

$$N[-\omega] = N^*[\omega] \quad (2.28)$$

$$\Sigma[-\omega] = \Sigma^*[\omega] \quad (2.29)$$

We get

$$\begin{aligned}
S_{\hat{c}^\dagger \hat{c}}[\omega] = & \langle \hat{c}^\dagger[\omega] \hat{c}[-\omega] \rangle = \frac{|\chi_m[-\omega]|^2}{|N[\omega]|^2} (-|\chi_m^{-1}[\omega]|^2 |\chi_m^{-1}[-\omega]|^2 \langle \Lambda[\omega] \Lambda[-\omega] \rangle \\
& + \gamma_m |\chi_m^{-1}[-\omega]|^2 |\Sigma[\omega]|^2 \langle \hat{\eta}[\omega] \hat{\eta}^\dagger[-\omega] \rangle + \gamma_m |N[\omega] + i\chi_m^{-1}[\omega] \Sigma[\omega]|^2 \langle \hat{\eta}^\dagger([\omega] \hat{\eta}[-\omega] \rangle) \quad (2.30)
\end{aligned}$$

The optical drive terms give us

$$\begin{aligned}
\langle \Lambda[\omega] \Lambda[-\omega] \rangle = & -|\alpha|^2 \langle [e^{-i\varphi} \chi_c[\omega] (\sqrt{\kappa_L}(\delta x[\omega] + i\delta y[\omega] + \hat{\zeta}_L[\omega]) + \sqrt{\kappa_M} \hat{\zeta}_M[\omega]) \\
& + e^{i\varphi} \chi_c^*[-\omega] (\sqrt{\kappa_L}(\delta x[\omega] - i\delta y[\omega] + \hat{\zeta}_L^\dagger[\omega]) + \sqrt{\kappa_M} \hat{\zeta}_M^\dagger[\omega])] \\
& [e^{-i\varphi} \chi_c[-\omega] (\sqrt{\kappa_L}(\delta x[-\omega] + i\delta y[-\omega] + \hat{\zeta}_L[-\omega]) + \sqrt{\kappa_M} \hat{\zeta}_M[-\omega]) \\
& + e^{i\varphi} \chi_c^*[\omega] (\sqrt{\kappa_L}(\delta x[-\omega] - i\delta y[-\omega] + \hat{\zeta}_L^\dagger[-\omega]) + \sqrt{\kappa_M} \hat{\zeta}_M^\dagger[-\omega])] \rangle \quad (2.31)
\end{aligned}$$

We then define

$$B_{\pm}[\omega] = e^{-i\phi} \chi_c[\omega] \pm e^{i\phi} \chi_c^*[-\omega] \quad (2.32)$$

Physically they are measures of how much classical amplitude and phase noise contribute to various optomechanical effects. B_{\pm} depend on the cavity detuning Δ . When the laser is right on resonance with the cavity, $B_-[\omega] = 0$, meaning the optomechanics is not susceptible to laser phase noise at all. We are interested in the optomechanical effects at $\omega = \pm\omega_m$. So in Figure 2.2, we plot $|B_+[\omega_m]|$ and $|B_-[\omega_m]|$ as a function of cavity detuning Δ , using experimental parameters. As shown by the curves, both amplitude noise and phase noise have maximal effects around $\Delta = -\omega_m$.

Notice $B_+[-\omega] = B_+^*[\omega]$, $B_-[-\omega] = -B_-^*[\omega]$, we can rewrite the optomechanical part as:

$$\begin{aligned}
S_{\hat{c}^\dagger \hat{c}}[\omega]_{\text{opt}} = & \frac{|\chi_m^{-1}[\omega]|^2}{|N[\omega]|^2} |\alpha|^2 [\kappa_L (|B_+[\omega]|^2 C_{xx} + |B_-[\omega]|^2 C_{yy} + 2\text{Im}(B_+[\omega] B_-^*[\omega]) C_{xy}) \\
& + \kappa (|\chi_c([\omega])|^2 \langle \hat{\zeta}[\omega] \hat{\zeta}^\dagger[-\omega] \rangle + |\chi_c[-\omega]|^2 \langle \hat{\zeta}^\dagger[\omega] \hat{\zeta}[-\omega] \rangle)] \quad (2.33)
\end{aligned}$$

The thermal drive terms can also be simplified using the following relation derived from Equa-

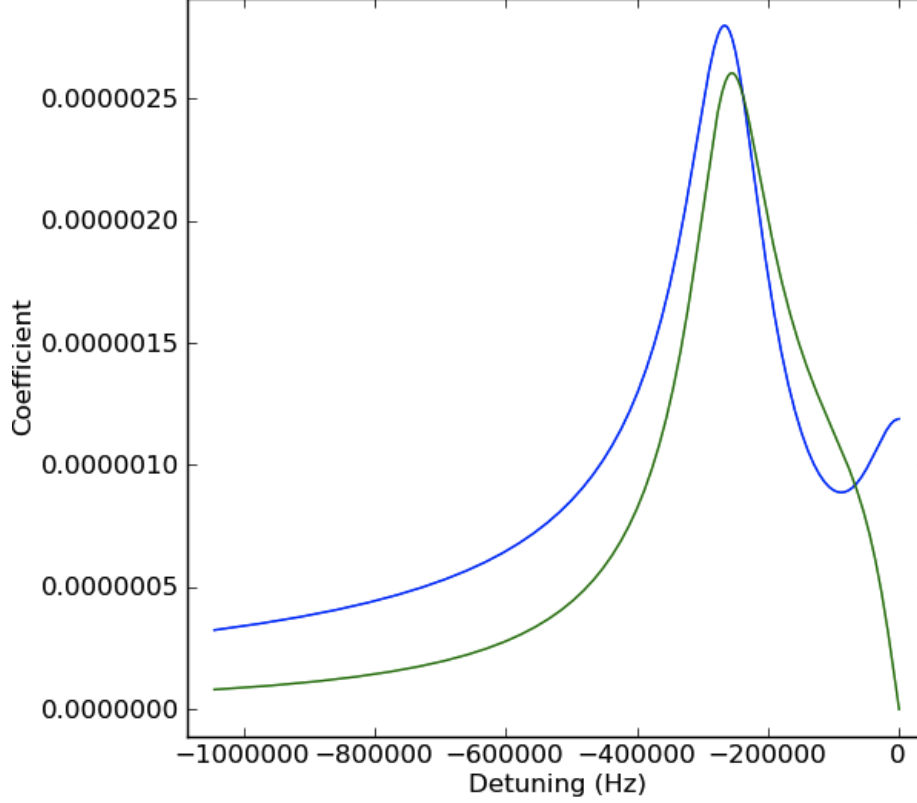


Figure 2.2: Theoretical plot of $|B_{\pm}[\omega_m]|$ as a function of cavity detuning $\Delta/2\pi$. The blue curve is $|B_+[\omega_m]|$, a measure of the classical amplitude noise's contributes to optomechanical effects. The green curve is $|B_-[\omega_m]|$, a measure of the contribution from classical phase noise. The parameters used are $\kappa/2\pi = 119$ kHz, $\kappa_L = 0.165\kappa$, $\omega_m = 261$ kHz. Both functions reach maximum near $\Delta = -\omega_m = -261$ kHz.

tions (2.14), (2.19) and (2.27):

$$\begin{aligned}
N[\omega] + i\chi_m^{-1}[\omega]\Sigma[\omega] &= \chi_m^{-1}[\omega]\chi_m^{*-1}[-\omega] + 2\omega_m\Sigma[\omega] + i\chi_m^{-1}[\omega]\Sigma[\omega] \\
&= \chi_m^{-1}[\omega]\chi_m^{*-1}[-\omega] + i(\chi_m^{*-1}[-\omega] - \chi_m^{-1}[\omega])\Sigma[\omega] + i\chi_m^{-1}[\omega]\Sigma[\omega] \\
&= \chi_m^{*-1}[-\omega]\chi_{\text{eff}}^{-1}[\omega] \quad (2.34)
\end{aligned}$$

Therefore

$$\begin{aligned}
S_{\hat{c}\dagger\hat{c}}[\omega] &= \frac{1}{|N[\omega]|^2} \{ \gamma_m |\Sigma[\omega]|^2 \langle \hat{\eta}[\omega] \hat{\eta}^\dagger[-\omega] \rangle + \gamma_m |\chi_{\text{eff}}^{-1}[\omega]|^2 \langle \hat{\eta}^\dagger[\omega] \hat{\eta}[-\omega] \rangle \\
&\quad + |\chi_m^{-1}[\omega]|^2 |\alpha|^2 [\kappa_L (|B_+[\omega]|^2 C_{xx} + |B_-[\omega]|^2 C_{yy} + 2\text{Im}(B_+[\omega] B_-^*[\omega]) C_{xy}) \\
&\quad + \kappa (|\chi_c([\omega]|^2 \langle \hat{\zeta}[\omega] \hat{\zeta}^\dagger[-\omega] \rangle + |\chi_c[-\omega]|^2 \langle \hat{\zeta}^\dagger[\omega] \hat{\zeta}[-\omega] \rangle)] \} \\
&\simeq |\chi_{\text{eff}}[-\omega]|^2 \{ \gamma_m n_{th} + |\alpha|^2 [\kappa_L (|B_+[\omega]|^2 C_{xx} + |B_-[\omega]|^2 C_{yy} + 2\text{Im}(B_+[\omega] B_-^*[\omega]) C_{xy}) \\
&\quad + \kappa |\chi_c([\omega]|^2 \langle \hat{\zeta}[\omega] \hat{\zeta}^\dagger[-\omega] \rangle)] \} \quad (2.35)
\end{aligned}$$

The first term is the thermal drive, the second is the classical noise contribution, and the third term is the quantum noise contribution.

The effective phonon number is then calculated by integrating $S_{\hat{c}\dagger\hat{c}}[\omega]$ over all frequencies. From Equation (2.19) and its conjugate, the mechanical oscillator only responds to frequencies close to $\omega = \pm\tilde{\omega}_m$. Therefore the integration has two significant terms, corresponding to the two mechanisms in which optical field contributes to the phonon number: one is at $\omega = \omega_m$ in the optical field spectrum $\langle \hat{d}^\dagger[\omega] \hat{d}[-\omega] \rangle$, and contributes to $S_{\hat{c}\dagger\hat{c}}[\omega = \tilde{\omega}_m]$. This corresponds to taking a photon from the cavity resonance, extracting energy $\hbar\omega_m$ from the mechanical oscillator, and creating a photon $\hbar\omega_m$ above cavity resonance, thus cooling the mechanical motion. The other is at $\omega = -\omega_m$ in optical field spectrum $\langle \hat{d}^\dagger[\omega] \hat{d}[-\omega] \rangle$, and contributes to $S_{\hat{c}\dagger\hat{c}}[\omega = -\tilde{\omega}_m]$, corresponding to the heating process. In the final expression, we see the only significant term is $S_{\hat{c}\dagger\hat{c}}[\omega = -\tilde{\omega}_m]$ for a high Q oscillator. Physically, this means the lowest achievable phonon number is limited by the optomechanical heating terms.

Integrating (2.35), we get

$$\begin{aligned}
n_{\text{eff}} &= \frac{1}{2\pi} \int_{-\infty}^{+\infty} S_{\hat{c}\dagger\hat{c}}[\omega] d\omega \\
&= \frac{1}{2\pi} (2\pi \tilde{\gamma}_m) \{ \gamma_m n_{th} + |\alpha|^2 [\kappa_L (|B_+[-\tilde{\omega}_m]|^2 C_{xx} + |B_-[-\tilde{\omega}_m]|^2 C_{yy} \\
&\quad + 2\text{Im}(B_+[-\tilde{\omega}_m] B_-^*[-\tilde{\omega}_m]) C_{xy}) + \kappa |\chi_c([-\tilde{\omega}_m]|^2)] \} \quad (2.36)
\end{aligned}$$

Equation (2.36) leads to the main expression in laser cooling:

$$n_{\text{eff}} = \frac{\gamma_{\text{m}} n_{\text{th}} + \gamma_{\text{opt}} n_{\text{opt}}}{\tilde{\gamma}_{\text{m}}} \quad (2.37)$$

where

$$\gamma_{\text{opt}} n_{\text{opt}} = |\alpha|^2 [\kappa_{\text{L}} (|B_+[\tilde{\omega}_{\text{m}}]|^2 C_{xx} + |B_-[\tilde{\omega}_{\text{m}}]|^2 C_{yy} + 2\text{Im}(B_+[\tilde{\omega}_{\text{m}}] B_-^*[\tilde{\omega}_{\text{m}}]) C_{xy}) + \kappa |\chi_{\text{c}}[-\tilde{\omega}_{\text{m}}]|^2] \quad (2.38)$$

In the resolved sideband limit, by detuning the laser to $\Delta = -\omega_{\text{m}}$ from the cavity resonance, the cooling process is maximally amplified by the cavity resonance, and the heating process is heavily suppressed as it is far detuned from the cavity resonance. Under this optimal cooling condition, in the limiting case where there is negligible classical noise, the lowest phonon number achievable is $(\frac{\kappa}{4\omega_{\text{m}}})^2$. This is less than 1 in the resolved sideband limit. The above formulae is the most important basis for efforts to reach the quantum ground state of a mechanical oscillator by resolved sideband laser cooling.

In reality, the laser always has some classical noise, particularly classical phase noise. Naively, we would expect the criteria for getting to the ground state be that the classical noise be lower than the quantum noise. However, the classical noise terms contribute differently from the quantum noise term:

Consider the optimal cooling case $\Delta = -\omega_{\text{m}}$, we see the coefficient for classical phase noise contribution has a leading term $\frac{1}{(\kappa/2)^2}$ whereas the quantum noise contribution only has a term that goes as $\frac{1}{(\kappa/2)^2 + (2\omega_{\text{m}})^2} \simeq \frac{1}{(2\omega_{\text{m}})^2}$. If the classical phase noise has the same magnitude as the quantum phase noise, the effective phonon number gets a boost by a factor of $(2\omega_{\text{m}}/\kappa)^2$ more from the classical noise. This makes the condition for achieving ground state cooling more stringent than merely having the classical noise below shot noise level.

As can be seen in (2.35), this difference comes from the fact that $\langle \hat{\zeta}^\dagger[\omega] \hat{\zeta}[-\omega] \rangle = 0$. Physically, if we want to create a phonon, with classical noise we could have two processes: either first creating one photon then destroy another photon, or first destroying one then creating another, at $\pm\omega_{\text{m}}$ away. However, for quantum noise, we can only have the first-create-then-destroy process, corresponding

to $\langle \hat{\zeta}[\omega]\hat{\zeta}^\dagger[-\omega] \rangle$, because there is no photon to be annihilated in the first place.

As a side note, the limit of laser cooling when there is large classical phase noise, as calculated from Equation (2.38), is in agreement with the results of Ref[50].

2.3 Heterodyne detection scheme

Once the mechanical motion is cooled to a low phonon number state, the detection can be done by using the heterodyne scheme as shown in Figure 2.3. Besides the cooling beam described in the previous section, we now have one signal beam at frequency ω_s that is locked to the cavity, and has information about the membrane motion encoded in the quadratures of the beam. A much stronger beam at frequency $\omega_{LO} = \omega_s - \omega_{IF}$, ω_{IF} below the signal beam, serves as the local oscillator (LO) of the heterodyne scheme. These two beams are combined before entering the cavity. When the signal beam is locked to the cavity and interacts with the membrane, the LO beam is far off resonance, so it bounces off the cavity directly. The two beams then land on a photodiode in the reflected beam path together. A beating signal at ω_{IF} is generated, with motional sidebands at mechanical frequency $\pm\omega_m$.

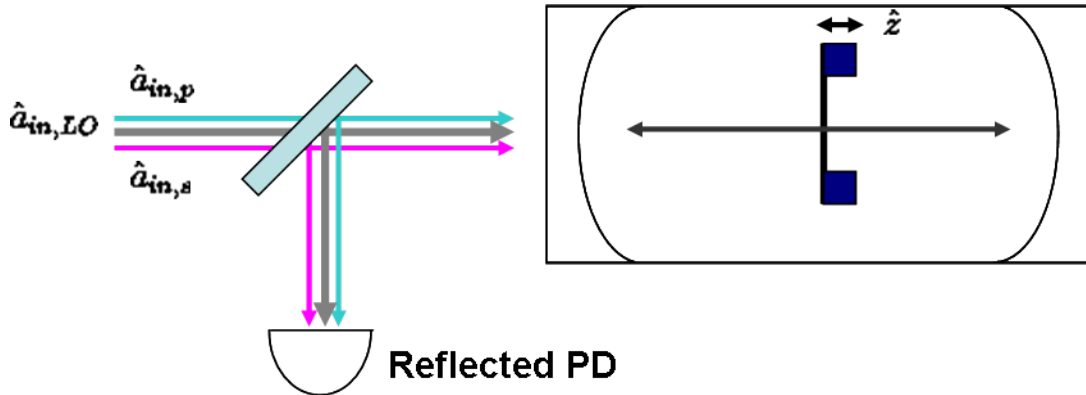


Figure 2.3: Schematic of heterodyne detection setup. The cavity with membrane in the middle has three inputs: a cooling beam $\hat{a}_{in,p}$ for laser cooling the membrane motion, a signal beam $\hat{a}_{in,s}$ for locking to the cavity and detection, and an LO beam $\hat{a}_{in,LO}$ as the local oscillator for the heterodyne detection. The reflected beams from the cavity are directed to a reflected photodiode (PD).

2.3.1 Basic theoretical framework

To understand the heterodyne spectrum quantitatively, similar to the last section, we write down the cooling input beam as $\hat{a}_{\text{in,p}}(t) = e^{-i\omega_p t}(\bar{a}_p(t) + \delta x_p(t) + i\delta y_p(t) + \hat{\zeta}_{\text{L,p}}(t))$, signal input as $\hat{a}_{\text{in,s}}(t) = e^{-i\omega_s t}(\bar{a}_{\text{in,s}}(t) + \delta x_s(t) + i\delta y_s(t) + \hat{\zeta}_{\text{L,s}}(t))$, and LO input as $a_{\text{in,LO}}(t) = e^{-i\omega_{\text{LO}} t}(\bar{a}_{\text{in,LO}}(t) + \delta x_{\text{LO}}(t) + i\delta y_{\text{LO}}(t) + \hat{\zeta}_{\text{L,LO}}(t))$. Again, we define the cooling and signal beam detunings as $\Delta_p = \omega_p - \omega_c$ and $\Delta_s = \omega_s - \omega_c$, and similarly $\chi_{c,\{p,s\}}$, $\alpha_{p,s}$, $\hat{d}_{p,s}$, and $\hat{\xi}_{p,s}$ etc.

Notice here we assigned vacuum noise terms at the different input ports for each beam. As mentioned in Section 2.2.1, the vacuum noise is the sum of the intracavity field's coupling to all vacuum modes in the environment, and has a white spectrum over all frequencies. In reality, the intracavity field only interacts with vacuum modes in a small bandwidth (set by cavity decay rate κ) around the cavity resonance. In our case, the three inputs are well separated in frequency, we can therefore assign vacuum noise terms to the three inputs separately.

The expressions are now modified as:

$$\hat{d}_p[\omega] = \chi_{c,p}[\omega](\hat{\xi}_p[\omega] - i\alpha_p \hat{z}[\omega]) \quad (2.39)$$

$$\hat{d}_s[\omega] = \chi_{c,s}[\omega](\hat{\xi}_s[\omega] - i\alpha_s \hat{z}[\omega]) \quad (2.40)$$

$$\begin{aligned} \hat{z}[\omega] = & \frac{1}{N[\omega]} [\sqrt{\gamma_m}(\chi_m^{-1*}[-\omega]\hat{\eta}[\omega] + \chi_m^{-1}[\omega]\hat{\eta}^\dagger[\omega]) \\ & - 2\omega_m(\alpha_s^* \chi_{c,s}[\omega]\hat{\xi}_s[\omega] + \alpha \chi_{c,s}^*[-\omega]\hat{\xi}_s^\dagger[\omega] + \alpha_p^* \chi_{c,p}[\omega]\hat{\xi}_p[\omega] + \alpha \chi_{c,p}^*[-\omega]\hat{\xi}_p^\dagger[\omega])] \end{aligned} \quad (2.41)$$

The signal beam also contributes to change in the effective mechanical linewidth, the resonant frequency, and the net effective phonon number

$$n_{\text{eff}} = \frac{\gamma_m n_{\text{th}} + \gamma_{\text{opt,p}} n_{\text{opt,p}} + \gamma_{\text{opt,s}} n_{\text{opt,s}}}{\tilde{\gamma}_m}$$

again with

$$\begin{aligned} \gamma_{\text{opt},\{s,p\}} n_{\text{opt},\{s,p\}} &= |\alpha_{\{s,p\}}|^2 [\kappa_L (|B_{+,\{s,p\}}[\omega_m]|^2 C_{xx,\{s,p\}} + |B_{-,\{s,p\}}[\omega_m]|^2 C_{yy,\{s,p\}} \\ &\quad + 2\text{Im}(B_{+,\{s,p\}}[\omega] B_{-,\{s,p\}}^*[\omega_m]) C_{xy,\{s,p\}}) + \kappa |\chi_{c,\{s,p\}}[-\omega_m]|^2] \end{aligned} \quad (2.42)$$

As discussed in Chapter 3, the cooling beam and the signal beam come from two different lasers 9 GHz away from each other in frequency, so it is safe to assume that their classical noises are uncorrelated. In that case, the effect of the cooling laser noise only shows up in determining n_{eff} . Therefore for the discussion of how correlations of laser classical noises modify the heterodyne spectrum, we only need to consider classical noises from the signal and LO beams.

Consider the heterodyne detection process of Figure 2.3. In our setup, the signal beam and the LO beam are generated by the same laser source, shifted in frequency by an AOM $\omega_{\text{LO}} = \omega_s - \omega_{\text{IF}}$. We could therefore write down the LO beam as $\hat{a}_{\text{in,LO}}(t) = \sqrt{p} \hat{a}_{\text{in,s}}(t) e^{i\omega_{\text{IF}}t + \theta(t)}$, where p is the ratio of LO beam power to signal beam power, we maintain $p \gg 1$ in our measurements. $\theta(t)$ is the phase difference between the LO beam and the signal beam accumulated before entering the cavity.

From input-output theory[53], the reflected signal beam is expressed as

$$\hat{a}_{\text{refl},s}(t) = \sqrt{\kappa_L} \hat{a}_s(t) - \hat{a}_{\text{in},s}(t) = e^{-i\omega_s t} (\bar{a}_{\text{refl},s} + \hat{d}_{\text{refl},s}(t)) \quad (2.43)$$

In Fourier space we have

$$\begin{aligned} \hat{d}_{\text{refl},s}[\omega] &= \sqrt{\kappa_L} \hat{d}_s[\omega] - \delta x_s[\omega] - i\delta y_s[\omega] - \hat{\zeta}_{L,s}[\omega] \\ &= [(\kappa_L \chi_{c,s}[\omega] - 1)(\delta x_s[\omega] + i\delta y_s[\omega]) - i\sqrt{\kappa_L} \alpha \chi_{c,s}[\omega] \hat{z}[\omega] + (\kappa_L \chi_{c,s}[\omega] - 1) \hat{\xi}_{L,s}[\omega] + \sqrt{\kappa_L \kappa_M} \chi_{c,s}[\omega] \hat{\xi}_{M,s}[\omega]] \end{aligned} \quad (2.44)$$

The mechanical motion information is thus contained in both $\hat{d}_s[\omega]$ and $\hat{d}_{\text{refl},s}[\omega]$. For the directly reflected LO field, the output is the same as the input:

$$\hat{a}_{\text{refl,LO}}(t) = -\hat{a}_{\text{in,LO}}(t) \quad (2.45)$$

$$\hat{d}_{\text{refl,LO}}(t) = -\hat{d}_{\text{in,LO}}(t) = -\sqrt{p}(\delta x_s(t) + i\delta y_s(t)) \quad (2.46)$$

From Equations (2.43)-(2.46), we get

$$\hat{a}_{\text{refl}}(t) = e^{-i\omega_s t}(\bar{a}_{\text{refl}}(t) + \hat{d}_{\text{refl}}(t)) \quad (2.47)$$

where the carrier is

$$\bar{a}_{\text{refl}}(t) = -\bar{a}_{\text{in,s}}(\rho + \sqrt{p}e^{i\omega_{\text{IF}}t + \theta(t)}) \quad (2.48)$$

and the fluctuating part is

$$\hat{d}_{\text{refl}}(t) = \hat{d}_{\text{refl,s}}(t) + \sqrt{p}\hat{d}_{\text{refl,LO}}(t)e^{i\omega_{\text{IF}}t + \theta(t)} \quad (2.49)$$

In the above expressions, for future convenience, we changed the definition of $\hat{d}_{\text{refl,LO}}(t)$ by scaling it down by a factor of \sqrt{p} . So now we have $\hat{d}_{\text{refl,LO}}(t) = -(\delta x_s(t) + i\delta y_s(t))$. The cavity filtering of the signal beam amplitude is

$$\rho = 1 - \frac{\kappa_{\text{L}}}{\kappa/2 - i\Delta} \quad (2.50)$$

The reflected signal beam and the directly reflected LO beam combine to produce $\hat{a}_{\text{refl}}(t) = \hat{a}_{\text{refl,s}}(t) + \hat{a}_{\text{refl,LO}}(t)$. This combined beam creates a photocurrent $i(t) = \sigma G e N(t)$ on the detector, where $N(t) = \hat{a}_{\text{refl}}^\dagger(t)\hat{a}_{\text{refl}}(t)$ is the photon number landing on the photodiode, σ the photodiode quantum efficiency, and G is the gain. The Fourier transform of the photocurrent, within a measurement window T is $i[\omega] = \frac{1}{\sqrt{T}} \int_{-T/2}^{T/2} dt e^{i\omega t} i(t)$. The power spectrum of the photodiode current is

$$\begin{aligned} S[\omega] = |i[\omega]|^2 &= \frac{1}{\sqrt{T}} \int_{-T/2}^{T/2} dt e^{-i\omega t} i(t) \frac{1}{\sqrt{T}} \int_{-T/2}^{T/2} dt' e^{i\omega t'} i(t') \\ &= \frac{1}{T} \int_{-T/2}^{T/2} dt \int_{-T/2}^{T/2} dt' e^{i\omega(t'-t)} i(t) i(t') \\ &= \frac{1}{T} \int_{-T/2}^{T/2} dt \int_{-\infty}^{+\infty} d\tau e^{i\omega\tau} \overline{i(t) i(t+\tau)} \quad (2.51) \end{aligned}$$

As discussed in Ref[56], the correlation could be separated into two parts. The first term is the time-ordered correlation of two photon counting, which is of interest to us. The second term comes from the self correlation of photon counting. This can be understood by visualizing the photo-detection events as creating photoelectric pulses of nonzero duration τ_d . The photodetector bandwidth is proportional to τ_d^{-1} . In the correlation expression of Equation (2.51), for $\tau < \tau_d$, a single photo-detection happened during t to $t + \tau$ will contribute to both $i(t)$ and $i(t + \tau)$. This self correlation of a single photon counting event will add a nonzero contribution to $S[\omega]$. This is the shot noise of the heterodyne detection. Note this shot noise has nothing to do with the quantum noise going into the cavity. For simplicity, we approximate the photodiode as having infinite bandwidth, $\tau_d = 0$, and the self correlation happens only for $\tau = 0$:

$$\overline{i(t)i(t + \tau)} = G^2 e^2 [\sigma^2 \langle : N(t)N(t + \tau) : \rangle + \sigma \langle : N(t) : \rangle \delta(\tau)] \quad (2.52)$$

Putting in (2.47)-(2.49), we could expand $N(t)$ up to first order as

$$\begin{aligned} N(t) &= a_{\text{refl}}^\dagger(t) a_{\text{refl}}(t) \\ &= [-\bar{a}_{\text{in},s}(\rho^* + \sqrt{p}e^{-i\omega_{\text{IF}}t - \theta(t)}) + \hat{d}_{\text{refl},s}^\dagger(t) + \sqrt{p}\hat{d}_{\text{refl},\text{LO}}^\dagger(t)e^{-i\omega_{\text{IF}}t - \theta(t)}] \\ &\quad \times [-\bar{a}_{\text{in},s}(\rho + \sqrt{p}e^{i\omega_{\text{IF}}t + \theta(t)}) + \hat{d}_{\text{refl},s}(t) + \sqrt{p}\hat{d}_{\text{refl},\text{LO}}(t)e^{i\omega_{\text{IF}}t + \theta(t)}] \\ &= \bar{a}_{\text{in},s}^2(|\rho|^2 + p + 2\text{Re}(\rho\sqrt{p}e^{-i\omega_{\text{IF}}t - \theta(t)})) - \sqrt{p}\bar{a}_{\text{in},s}(\rho\hat{d}_{\text{refl},\text{LO}}^\dagger(t) + \hat{d}_{\text{refl},s}(t))e^{-i\omega_{\text{IF}}t - \theta(t)} \\ &\quad - \sqrt{p}\bar{a}_{\text{in},s}(\hat{d}_{\text{refl},s}^\dagger(t) + \rho^*\hat{d}_{\text{refl},\text{LO}}(t))e^{i\omega_{\text{IF}}t + \theta(t)} \\ &\simeq p\bar{a}_{\text{in},s}^2 - \sqrt{p}\bar{a}_{\text{in},s}(\rho\hat{d}_{\text{refl},\text{LO}}^\dagger(t) + \hat{d}_{\text{refl},s}(t))e^{-i\omega_{\text{IF}}t - \theta(t)} - \sqrt{p}\bar{a}_{\text{in},s}(\hat{d}_{\text{refl},s}^\dagger(t) + \rho^*\hat{d}_{\text{refl},\text{LO}}(t))e^{i\omega_{\text{IF}}t + \theta(t)} \end{aligned} \quad (2.53)$$

This is the same result if we instead have a noiseless LO beam $\hat{a}_{\text{LO}}(t) = -\sqrt{p}\bar{a}_{\text{in},s}e^{i\omega_{\text{IF}}t + \theta(t)}$ beating with an effective reflected field $\hat{a}_{\text{out}}(t) = \bar{a}_{\text{out}}(t) + \hat{d}_{\text{out}}(t)$. The mean amplitude of this effective field is

$$\bar{a}_{\text{out}}(t) = -\bar{a}_{\text{in},s}(t) \quad (2.54)$$

and the fluctuation part is given by

$$\hat{d}_{\text{out}}(t) = \hat{d}_{\text{refl},s}(t) + \rho \hat{d}_{\text{refl},\text{LO}}^\dagger(t) \quad (2.55)$$

We perform the time-ordered, normal-ordered calculation. For simplicity, here we treat the LO beam phase θ as a constant over the time scale we care about.

$$\begin{aligned} \langle : N(t)N(t+\tau) : \rangle &= p^2 \bar{a}_{\text{in},s}^4 \\ &+ p \bar{a}_{\text{in},s}^2 e^{-i\omega_{\text{IF}}t - \theta + i\omega_{\text{IF}}(t+\tau) + \theta} \langle : \hat{d}_{\text{out}}(t) \hat{d}_{\text{out}}^\dagger(t+\tau) : \rangle \\ &+ p \bar{a}_{\text{in},s}^2 e^{i\omega_{\text{IF}}t + \theta - i\omega_{\text{IF}}(t+\tau) - \theta} \langle : \hat{d}_{\text{out}}^\dagger(t) \hat{d}_{\text{out}}(t+\tau) : \rangle \\ &+ p \bar{a}_{\text{in},s}^2 e^{-i\omega_{\text{IF}}t - \theta - i\omega_{\text{IF}}(t+\tau) - \theta} \langle : \hat{d}_{\text{out}}(t) \hat{d}_{\text{out}}(t+\tau) : \rangle \\ &+ p \bar{a}_{\text{in},s}^2 e^{i\omega_{\text{IF}}t + \theta + i\omega_{\text{IF}}(t+\tau) + \theta} \langle : \hat{d}_{\text{out}}^\dagger(t) \hat{d}_{\text{out}}^\dagger(t+\tau) : \rangle \quad (2.56) \end{aligned}$$

Expanding (2.56) using (2.55), we get

$$\begin{aligned} \langle : N(t)N(t+\tau) : \rangle &= p^2 \bar{a}_{\text{in},s}^4 \\ &+ p \bar{a}_{\text{in},s}^2 e^{-i\omega_{\text{IF}}t - \theta + i\omega_{\text{IF}}(t+\tau) + \theta} (|\rho|^2 \langle : \hat{d}_{\text{refl},\text{LO}}^\dagger(t) \hat{d}_{\text{refl},\text{LO}}(t+\tau) : \rangle + \langle : \hat{d}_{\text{refl},s}(t) \hat{d}_{\text{refl},s}^\dagger(t+\tau) : \rangle \\ &\quad + \rho \langle : \hat{d}_{\text{refl},\text{LO}}^\dagger(t) \hat{d}_{\text{refl},s}^\dagger(t+\tau) : \rangle + \rho^* \langle : \hat{d}_{\text{refl},s}(t) \hat{d}_{\text{refl},\text{LO}}(t+\tau) : \rangle) \\ &+ p \bar{a}_{\text{in},s}^2 e^{i\omega_{\text{IF}}t + \theta - i\omega_{\text{IF}}(t+\tau) - \theta} (|\rho|^2 \langle : \hat{d}_{\text{refl},\text{LO}}(t) \hat{d}_{\text{refl},\text{LO}}^\dagger(t+\tau) : \rangle + \langle : \hat{d}_{\text{refl},s}^\dagger(t) \hat{d}_{\text{refl},s}(t+\tau) : \rangle \\ &\quad + \rho \langle : \hat{d}_{\text{refl},s}^\dagger(t) \hat{d}_{\text{refl},\text{LO}}^\dagger(t+\tau) : \rangle + \rho^* \langle : \hat{d}_{\text{refl},\text{LO}}(t) \hat{d}_{\text{refl},s}(t+\tau) : \rangle) \\ &+ p \bar{a}_{\text{in},s}^2 e^{-i\omega_{\text{IF}}t - \theta - i\omega_{\text{IF}}(t+\tau) - \theta} (\rho^2 \langle : \hat{d}_{\text{refl},\text{LO}}^\dagger(t) \hat{d}_{\text{refl},\text{LO}}^\dagger(t+\tau) : \rangle + \langle : \hat{d}_{\text{refl},s}(t) \hat{d}_{\text{refl},s}(t+\tau) : \rangle \\ &\quad + \rho \langle : \hat{d}_{\text{refl},\text{LO}}^\dagger(t) \hat{d}_{\text{refl},s}(t+\tau) : \rangle + \rho \langle : \hat{d}_{\text{refl},s}(t) \hat{d}_{\text{refl},\text{LO}}^\dagger(t+\tau) : \rangle) \\ &+ p \bar{a}_{\text{in},s}^2 e^{i\omega_{\text{IF}}t + \theta + i\omega_{\text{IF}}(t+\tau) + \theta} (\rho^{*2} \langle : \hat{d}_{\text{refl},\text{LO}}(t) \hat{d}_{\text{refl},\text{LO}}(t+\tau) : \rangle + \langle : \hat{d}_{\text{refl},s}^\dagger(t) \hat{d}_{\text{refl},s}^\dagger(t+\tau) : \rangle \\ &\quad + \rho^* \langle : \hat{d}_{\text{refl},s}^\dagger(t) \hat{d}_{\text{refl},\text{LO}}(t+\tau) : \rangle + \rho^* \langle : \hat{d}_{\text{refl},\text{LO}}(t) \hat{d}_{\text{refl},s}^\dagger(t+\tau) : \rangle) \quad (2.57) \end{aligned}$$

For a quantum operator \hat{d} , the time ordering and normal ordering will rearrange the operators as

$\langle d^\dagger(t)d^\dagger(t+\tau)d(t+\tau)d(t) \rangle$. Following this rule, the different terms in (2.56) become

$$\begin{aligned}
& \langle : \hat{d}_{\text{refl,LO}}^\dagger(t)\hat{d}_{\text{refl,LO}}(t+\tau) : \rangle = \langle \hat{d}_{\text{refl,LO}}^\dagger(t)\hat{d}_{\text{refl,LO}}(t+\tau) \rangle \\
& \langle : \hat{d}_{\text{refl,s}}^\dagger(t)\hat{d}_{\text{refl,s}}^\dagger(t+\tau) : \rangle = \langle \hat{d}_{\text{refl,s}}^\dagger(t+\tau)\hat{d}_{\text{refl,s}}(t) \rangle \\
& \langle : \hat{d}_{\text{refl,LO}}^\dagger(t)\hat{d}_{\text{refl,s}}^\dagger(t+\tau) : \rangle = \langle \hat{d}_{\text{refl,LO}}^\dagger(t)\hat{d}_{\text{refl,s}}^\dagger(t+\tau) \rangle \\
& \langle : \hat{d}_{\text{refl,s}}^\dagger(t)\hat{d}_{\text{refl,LO}}(t+\tau) : \rangle = \langle \hat{d}_{\text{refl,LO}}(t+\tau)\hat{d}_{\text{refl,s}}(t) \rangle \text{ etc.} \tag{2.58}
\end{aligned}$$

Therefore

$$\begin{aligned}
\langle : N(t)N(t+\tau) : \rangle &= p^2 \bar{a}_{\text{in,s}}^4 \\
&+ e^{i\omega_{\text{IF}}\tau} p \bar{a}_{\text{in,s}}^2 (|\rho|^2 \langle \hat{d}_{\text{refl,LO}}^\dagger(t)\hat{d}_{\text{refl,LO}}(t+\tau) \rangle + \langle \hat{d}_{\text{refl,s}}^\dagger(t+\tau)\hat{d}_{\text{refl,s}}(t) \rangle \\
&\quad + \rho \langle \hat{d}_{\text{refl,LO}}^\dagger(t)\hat{d}_{\text{refl,s}}^\dagger(t+\tau) \rangle + \rho^* \langle \hat{d}_{\text{refl,LO}}(t+\tau)\hat{d}_{\text{refl,s}}(t) \rangle) \\
&+ e^{-i\omega_{\text{IF}}\tau} p \bar{a}_{\text{in,s}}^2 (|\rho|^2 \langle \hat{d}_{\text{refl,LO}}^\dagger(t+\tau)\hat{d}_{\text{refl,LO}}(t) \rangle + \langle \hat{d}_{\text{refl,s}}^\dagger(t)\hat{d}_{\text{refl,s}}(t+\tau) \rangle \\
&\quad + \rho \langle \hat{d}_{\text{refl,s}}^\dagger(t)\hat{d}_{\text{refl,LO}}(t+\tau) \rangle + \rho^* \langle \hat{d}_{\text{refl,s}}(t+\tau)\hat{d}_{\text{refl,LO}}(t) \rangle) \\
&+ e^{-2i\omega_{\text{IF}}t-i\omega_{\text{IF}}\tau-2i\theta} p \bar{a}_{\text{in,s}}^2 (\rho^2 \langle \hat{d}_{\text{refl,LO}}^\dagger(t)\hat{d}_{\text{refl,LO}}^\dagger(t+\tau) \rangle + \langle \hat{d}_{\text{refl,s}}(t+\tau)\hat{d}_{\text{refl,s}}(t) \rangle \\
&\quad + \rho \langle \hat{d}_{\text{refl,LO}}^\dagger(t)\hat{d}_{\text{refl,s}}(t+\tau) \rangle + \rho \langle \hat{d}_{\text{refl,LO}}^\dagger(t+\tau)\hat{d}_{\text{refl,s}}^\dagger(t) \rangle) \\
&+ e^{2i\omega_{\text{IF}}t+i\omega_{\text{IF}}\tau+2i\theta} p \bar{a}_{\text{in,s}}^2 (\rho^{*2} \langle \hat{d}_{\text{refl,LO}}(t+\tau)\hat{d}_{\text{refl,LO}}(t) \rangle + \langle \hat{d}_{\text{refl,s}}^\dagger(t)\hat{d}_{\text{refl,s}}^\dagger(t+\tau) \rangle \\
&\quad + \rho^* \langle \hat{d}_{\text{refl,s}}^\dagger(t)\hat{d}_{\text{refl,LO}}(t+\tau) \rangle + \rho^* \langle \hat{d}_{\text{refl,s}}^\dagger(t+\tau)\hat{d}_{\text{refl,LO}}(t) \rangle) \tag{2.59}
\end{aligned}$$

The shot noise term is

$$\langle : N(t) : \rangle = \bar{a}_{\text{in,s}}^2 (|\rho|^2 + p + 2\text{Re}(\rho\sqrt{p}e^{-i\omega_{\text{IF}}t-\theta(t)})) \simeq p \bar{a}_{\text{in,s}}^2 \tag{2.60}$$

2.3.2 Power spectra of mechanical sidebands

Inserting Equations (2.59) and (2.60) into (2.51) and (2.52), and dropping the $e^{\pm 2i\omega_{\text{IF}}t}$ terms, we obtain the heterodyne power spectrum

$$S[\omega] = G^2 e^2 \sigma p |\bar{a}_{\text{in},s}|^2 (1 + \sigma S_{\hat{d}_{\text{out}}\hat{d}_{\text{out}}}^{\dagger}[\omega + \omega_{\text{IF}}] + S_{\hat{d}_{\text{out}}\hat{d}_{\text{out}}}^{\dagger}[\omega - \omega_{\text{IF}}]) \quad (2.61)$$

where

$$\begin{aligned} S_{\hat{d}_{\text{out}}\hat{d}_{\text{out}}}^{\dagger}[\omega] &= \int d\tau e^{i\omega\tau} \langle: \hat{d}_{\text{out}}(t) \hat{d}_{\text{out}}^{\dagger}(t + \tau) : \rangle \\ &= \int d\tau e^{i\omega\tau} (|\rho|^2 \langle \hat{d}_{\text{refl,LO}}^{\dagger}(0) \hat{d}_{\text{refl,LO}}(\tau) \rangle + \langle \hat{d}_{\text{refl,s}}^{\dagger}(\tau) \hat{d}_{\text{refl,s}}(0) \rangle \\ &\quad + \rho \langle \hat{d}_{\text{refl,LO}}^{\dagger}(0) \hat{d}_{\text{refl,s}}^{\dagger}(\tau) \rangle + \rho^* \langle \hat{d}_{\text{refl,LO}}(\tau) \hat{d}_{\text{refl,s}}(0) \rangle) \\ &= |\rho|^2 \langle \hat{d}_{\text{refl,LO}}^{\dagger}[-\omega] \hat{d}_{\text{refl,LO}}[\omega] \rangle + \langle \hat{d}_{\text{refl,s}}^{\dagger}[\omega] \hat{d}_{\text{refl,s}}[-\omega] \rangle \\ &\quad + \rho \langle \hat{d}_{\text{refl,LO}}^{\dagger}[-\omega] \hat{d}_{\text{refl,s}}^{\dagger}[\omega] \rangle + \rho^* \langle \hat{d}_{\text{refl,LO}}[\omega] \hat{d}_{\text{refl,s}}[-\omega] \rangle \end{aligned} \quad (2.62)$$

and

$$\begin{aligned} S_{\hat{d}_{\text{out}}\hat{d}_{\text{out}}}^{\dagger}[\omega] &= \int d\tau e^{i\omega\tau} \langle: \hat{d}_{\text{out}}^{\dagger}(t) \hat{d}_{\text{out}}(t + \tau) : \rangle \\ &= |\rho|^2 \langle \hat{d}_{\text{refl,LO}}^{\dagger}[\omega] \hat{d}_{\text{refl,LO}}[-\omega] \rangle + \langle \hat{d}_{\text{refl,s}}^{\dagger}[-\omega] \hat{d}_{\text{refl,s}}[\omega] \rangle \\ &\quad + \rho \langle \hat{d}_{\text{refl,s}}^{\dagger}[-\omega] \hat{d}_{\text{refl,LO}}[\omega] \rangle + \rho^* \langle \hat{d}_{\text{refl,s}}[\omega] \hat{d}_{\text{refl,LO}}[-\omega] \rangle \end{aligned} \quad (2.63)$$

In our setup, we are looking at photocurrent components around $\omega = \omega_{\text{IF}}$, so only $S_{\hat{d}_{\text{out}}\hat{d}_{\text{out}}}^{\dagger}[\omega - \omega_{\text{IF}}]$ is of interest. The upper and lower mechanical sidebands arise at frequencies around $\omega_{\text{IF}} \pm \tilde{\omega}_m$. As can be seen in the $N(t)$ expression (2.53), two interfering terms contribute to $S[\omega]$: the reflected signal beam carrier beating with fluctuations of the LO beam, and the LO beam carrier beating with fluctuations of the signal beam. Both terms contribute to the background in $S[\omega]$, but since the LO beam does not have any motional information, only the second term and its interference with the first term lead to the mechanical sidebands.

As mentioned in Section 2.2.3, the upper (lower) sideband in the output optical field spectrum $S_{\hat{a}_{\text{out}}^\dagger \hat{a}_{\text{out}}}[\omega]$ corresponds to the processes of cooling (heating) the mechanical motion by shifting the photon frequency up (down) $\hbar\omega_m$. When there is no classical noise on the laser, from Fermi's Golden Rule, the probability of the cooling (heating) process is proportional to $n_{\text{eff}} (n_{\text{eff}} + 1)$ [26]. The heterodyne sideband power spectra should then have Lorentzian peaks with center frequency and linewidth determined by Equations (2.20)-(2.23). The height of the upper (lower) sideband should be proportional to $n_{\text{eff}} (n_{\text{eff}} + 1)$.

When there is classical noise, as seen in Equation (2.15), it modifies the oscillator position \hat{z} . So we get additional terms in $S_{\hat{a}_{\text{out}}^\dagger \hat{a}_{\text{out}}}[\omega]$ from correlations of classical noise terms (in the background) and the classical noise contained in \hat{z} (modifying the peaks). The in-phase correlation contributes to the motional Lorentzian peak, the out-of-phase correlation creates an anti-Lorentzian shape. The power spectra of the mechanical sidebands therefore have Fano shapes.

Another conclusion: there is no information about RPSN in the heterodyne power spectra. The reason for this is that the normal ordering of the operators eliminates all nonzero quantum noise terms in the form of $\langle \hat{\zeta}[\omega] \hat{\zeta}^\dagger[-\omega] \rangle$. As will be explained in the next subsection, to study RPSN, we must look at the cross-correlation.

Now we look at the heterodyne power spectra quantitatively. We define $\omega = \delta\omega + \omega_{\text{IF}}$. From Equation (2.59), we can calculate $S[\delta\omega]$ around the lower (red) sideband $\omega \simeq -\omega_m + \omega_{\text{IF}}$

$$S_{\text{rr}}[\delta\omega] = G^2 e^2 \sigma p |\bar{a}_{\text{in},s}|^2 [b_{\text{rr}} + \frac{s_{\text{rr}}}{(\tilde{\gamma}_m/2)^2 + (\delta\omega + \tilde{\omega}_m)^2} + \frac{a_{\text{rr}}(\delta\omega + \tilde{\omega}_m)}{(\tilde{\gamma}_m/2)^2 + (\delta\omega + \tilde{\omega}_m)^2}] \quad (2.64)$$

The spectrum consists of the background, a Lorentzian peak centered at the sideband frequency, with a width determined by effective mechanical linewidth. It also contains an anti-Lorentzian part with the same center frequency and halfwidth. To calculate these terms explicitly, we rewrite the Equations (2.44) and (2.46) here for convenience:

$$\hat{d}_{\text{ref},\text{LO}}[\delta\omega] = -(\delta x_s[\delta\omega] + i\delta y_s[\delta\omega])$$

$$\begin{aligned}\hat{d}_{\text{refl},s}[\delta\omega] &= [(\kappa_L\chi_{c,s}[\delta\omega] - 1)(\delta x_s[\delta\omega] + i\delta y_s[\delta\omega]) \\ &\quad - i\sqrt{\kappa_L}\alpha\chi_{c,s}[\delta\omega]\hat{z}[\delta\omega] + (\kappa_L\chi_{c,s}[\delta\omega] - 1)\hat{\xi}_L[\delta\omega] + \sqrt{\kappa_L\kappa_M}\chi_{c,s}[\delta\omega]\hat{\xi}_M[\delta\omega]]\end{aligned}$$

$$\begin{aligned}\hat{d}_{\text{refl},s}^\dagger[\delta\omega] &= [(\kappa_L\chi_{c,s}^*[-\delta\omega] - 1)(\delta x_s[\delta\omega] - i\delta y_s[\delta\omega]) \\ &\quad + i\sqrt{\kappa_L}\alpha^*\chi_{c,s}^*[-\delta\omega]\hat{z}[\delta\omega] + (\kappa_L\chi_{c,s}^*[-\delta\omega] - 1)\hat{\xi}_L^\dagger[\delta\omega] + \sqrt{\kappa_L\kappa_M}\chi_{c,s}^*[-\delta\omega]\hat{\xi}_M^\dagger[\delta\omega]]\end{aligned}\quad (2.65)$$

The background includes the detection shot noise, the classical noise part of the two beating terms mentioned earlier, and the interference between those two beating signals. Since $\delta\omega \simeq -\omega_m$, we could treat $\chi_{c,s}[\delta\omega] \simeq \chi_{c,s}[-\omega_m]$.

$$|\rho|^2 < \hat{d}_{\text{refl},\text{LO}}^\dagger[\delta\omega]\hat{d}_{\text{refl},\text{LO}}[-\delta\omega] > = |\rho|^2(C_{\text{xx}} + C_{\text{yy}}) \quad (2.66)$$

$$< \hat{d}_{\text{refl},s}^\dagger[-\delta\omega]\hat{d}_{\text{refl},s}[\delta\omega] > |_{\text{classical-classical}} = |\kappa_L\chi_{c,s}[-\omega_m] - 1|^2(C_{\text{xx}} + C_{\text{yy}}) \quad (2.67)$$

$$\begin{aligned}\rho < \hat{d}_{\text{refl},\text{LO}}^\dagger[-\delta\omega]\hat{d}_{\text{refl},s}^\dagger[\delta\omega] > |_{\text{classical-classical}} \\ &= \rho < -(\delta x_s[\delta\omega] - i\delta y_s[\delta\omega])(\kappa_L\chi_{c,s}^*[\delta\omega] - 1)(\delta x_s[-\delta\omega] - i\delta y_s[-\delta\omega]) > \\ &= -\rho(\kappa_L\chi_{c,s}^*[-\omega_m] - 1)(C_{\text{xx}} + 2iC_{\text{xy}} - C_{\text{yy}})\end{aligned}\quad (2.68)$$

$$\begin{aligned}\rho^* < \hat{d}_{\text{refl},\text{LO}}[\delta\omega]\hat{d}_{\text{refl},s}[-\delta\omega] > |_{\text{classical-classical}} \\ &= \rho^* < -(\delta x_s[-\delta\omega] + i\delta y_s[-\delta\omega])(\kappa_L\chi_{c,s}[\delta\omega] - 1)(\delta x_s[\delta\omega] + i\delta y_s[\delta\omega]) > \\ &= -\rho^*(\kappa_L\chi_{c,s}[-\omega_m] - 1)(C_{\text{xx}} + 2iC_{\text{xy}} - C_{\text{yy}})\end{aligned}\quad (2.69)$$

Therefore the background term is

$$b_{\text{rr}} = 1 + \sigma[(|\rho|^2 + |\kappa_L\chi_{c,s}[-\omega_m] - 1|^2)(C_{\text{xx}} + C_{\text{yy}}) - 2\text{Re}[\rho^*(\kappa_L\chi_{c,s}[-\omega_m] - 1)](C_{\text{xx}} + 2iC_{\text{xy}} - C_{\text{yy}})] \quad (2.70)$$

For the Fano terms, as mentioned above, we look at three contributions:

1. Correlation between the position \hat{z} and itself: $z - z$ correlation

$$\begin{aligned}
\langle \hat{d}_{\text{refl},s}^\dagger[-\delta\omega] \hat{d}_{\text{refl},s}[\delta\omega] \rangle |_{z-z} &= \kappa_L |\alpha|^2 |\chi_{c,s}[\delta\omega]|^2 \langle \hat{z}[-\delta\omega] \hat{z}[\delta\omega] \rangle \\
&= \kappa_L |\alpha|^2 |\chi_{c,s}[\delta\omega]|^2 \tilde{\gamma}_m [|\chi_{\text{eff},s}[-\delta\omega]|^2 (n_{\text{eff}} + 1) + |\chi_{c,s}[\delta\omega]|^2 |\chi_{\text{eff},s}[\delta\omega]|^2 n_{\text{eff}}] \\
&\simeq \kappa_L |\alpha|^2 |\chi_{c,s}[\delta\omega]|^2 |\chi_{\text{eff},s}[-\delta\omega]|^2 \tilde{\gamma}_m (n_{\text{eff}} + 1) \\
&= \frac{\kappa_L |\alpha|^2 |\chi_{c,s}[-\omega_m]|^2 \tilde{\gamma}_m (n_{\text{eff}} + 1)}{(\tilde{\gamma}_m/2)^2 + (\delta\omega + \tilde{\omega}_m)^2} \quad (2.71)
\end{aligned}$$

2. Correlation between the position \hat{z} and classical noise in the reflected signal beam: z -classical correlation

$$\begin{aligned}
\langle \hat{d}_{\text{refl},s}^\dagger[-\delta\omega] \hat{d}_{\text{refl},s}[\delta\omega] \rangle |_{z\text{-classical}} &= \langle (\kappa_L \chi_{c,s}^*[\delta\omega] - 1)(\delta x_s[-\delta\omega] - i\delta y_s[-\delta\omega])(-i\sqrt{\kappa_L} \alpha \chi_{c,s}[\delta\omega] \hat{z}[\delta\omega]) \rangle \\
&\quad + \langle (i\sqrt{\kappa_L} \alpha^* \chi_{c,s}^*[\delta\omega] \hat{z}[-\delta\omega] \kappa_L \chi_{c,s}[\delta\omega] - 1)(\delta x_s[\delta\omega] + i\delta y_s[\delta\omega]) \rangle \\
&= (\kappa_L |\chi_{c,s}[\delta\omega]|^2 - \chi_{c,s}[\delta\omega]) |\alpha|^2 \kappa_L (B_+[\delta\omega] C_{xx} - iB_+[\delta\omega] C_{xy} - iB_-[\delta\omega] C_{xy} - B_-[\delta\omega] C_{yy}) e^{i\phi} \frac{2i\omega_m}{N[\delta\omega]} \\
&+ (\kappa_L |\chi_{c,s}[\delta\omega]|^2 - \chi_{c,s}^*[\delta\omega]) |\alpha|^2 \kappa_L (B_+[-\delta\omega] C_{xx} + iB_+[-\delta\omega] C_{xy} + iB_-[-\delta\omega] C_{xy} - B_-[-\delta\omega] C_{yy}) e^{-i\phi} \frac{-2i\omega_m}{N[-\delta\omega]} \\
&\quad (2.72)
\end{aligned}$$

From Equation (2.19), we know when $\delta\omega \simeq -\omega_m$

$$N[-\delta\omega] = \chi_m^{*-1}[\delta\omega] \chi_{\text{eff}}^{-1}[-\delta\omega] \simeq -2i\omega_m [\tilde{\gamma}_m/2 + i(\delta\omega + \tilde{\omega}_m)] \quad (2.73)$$

$$N[\delta\omega] = N[-\delta\omega]^* = 2i\omega_m [\tilde{\gamma}_m/2 - i(\delta\omega + \tilde{\omega}_m)] \quad (2.74)$$

The Lorentzian peak from this correlation is

$$\begin{aligned}
2\text{Re}[(\kappa_L |\chi_{c,s}[\delta\omega]|^2 - \chi_{c,s}^*[\delta\omega]) |\alpha|^2 \kappa_L (B_+[-\delta\omega] C_{xx} + iB_+[-\delta\omega] C_{xy} + iB_-[-\delta\omega] C_{xy} - B_-[-\delta\omega] C_{yy}) e^{-i\phi}] \\
\times \frac{\tilde{\gamma}_m/2}{(\tilde{\gamma}_m/2)^2 + (\delta\omega + \tilde{\omega}_m)^2} \quad (2.75)
\end{aligned}$$

The anti-Lorentzian peak is

$$2\text{Im}[(\kappa_L|\chi_{c,s}[\delta\omega]|^2 - \chi_{c,s}^*[\delta\omega])|\alpha|^2\kappa_L(B_+[-\delta\omega]C_{xx} + iB_+[-\delta\omega]C_{xy} + iB_-[-\delta\omega]C_{xy} - B_-[-\delta\omega]C_{yy})e^{-i\phi}] \\ \times \frac{\delta\omega + \tilde{\omega}_m}{(\tilde{\gamma}_m/2)^2 + (\delta\omega + \tilde{\omega}_m)^2} \quad (2.76)$$

3. Correlation between the position \hat{z} and classical noise in the reflected LO beam: z – classical correlation

$$\rho < \hat{d}_{\text{refl,LO}}^\dagger[\delta\omega]\hat{d}_{\text{refl,s}}^\dagger[-\delta\omega] > |_{z\text{-classical}} \\ = \rho < -(\delta x_s[\delta\omega] - i\delta y_s[\delta\omega])(i\sqrt{\kappa_L}\alpha^*\chi_{c,s}^*[\delta\omega]\hat{z}[-\delta\omega]) > \\ = -\rho|\alpha|^2\kappa_L e^{-i\phi}\chi_{c,s}^*[\delta\omega](B_+[-\delta\omega]C_{xx} - iB_+[-\delta\omega]C_{xy} + iB_-[-\delta\omega]C_{xy} + B_-[-\delta\omega]C_{yy})e^{-i\phi} \frac{-2i\omega_m}{N[-\delta\omega]} \quad (2.77)$$

$$\rho^* < \hat{d}_{\text{refl,LO}}[-\delta\omega]\hat{d}_{\text{refl,s}}[\delta\omega] > |_{z\text{-classical}} \\ = \rho^* < -(\delta x_s[-\delta\omega] + i\delta y_s[-\delta\omega])(-i\sqrt{\kappa_L}\alpha\chi_{c,s}[\delta\omega]\hat{z}[\delta\omega]) > \\ = -\rho^*|\alpha|^2\kappa_L e^{i\phi}\chi_{c,s}[\delta\omega](B_+[\delta\omega]C_{xx} + iB_+[\delta\omega]C_{xy} + iB_-[\delta\omega]C_{xy} - B_-[\delta\omega]C_{yy})e^{-i\phi} \frac{2i\omega_m}{N[\delta\omega]} \quad (2.78)$$

The Lorentzian peak from this correlation is

$$2\text{Re}[-\rho|\alpha|^2\kappa_L e^{-i\phi}\chi_{c,s}^*[\delta\omega](B_+[-\delta\omega]C_{xx} - iB_+[-\delta\omega]C_{xy} + iB_-[-\delta\omega]C_{xy} + B_-[-\delta\omega]C_{yy})e^{-i\phi}] \\ \times \frac{\tilde{\gamma}_m/2}{(\tilde{\gamma}_m/2)^2 + (\delta\omega + \tilde{\omega}_m)^2} \quad (2.79)$$

The anti-Lorentzian peak is

$$2\text{Im}[-\rho|\alpha|^2\kappa_L e^{-i\phi}\chi_{c,s}^*[\delta\omega](B_+[-\delta\omega]C_{xx} - iB_+[-\delta\omega]C_{xy} + iB_-[-\delta\omega]C_{xy} + B_-[-\delta\omega]C_{yy})e^{-i\phi}] \\ \times \frac{\tilde{\gamma}_m/2}{(\tilde{\gamma}_m/2)^2 + (\delta\omega + \tilde{\omega}_m)^2} \quad (2.80)$$

Combining all three terms, and treating $B_{\pm}[\omega]$ and $\chi_{c,s}[\omega]$ as constants replaced by $\delta\omega = -\omega_m$.

We get the final expression for the Lorentzian coefficient:

$$s_{\text{rr}} = \sigma\kappa_{\text{L}}|\alpha_{\text{s}}|^2\tilde{\gamma}_{\text{m}}[|\chi_{c,s}[-\omega_m]|^2(n_{\text{eff}} + 1) + \text{Re}(B_{\text{mod}}[\omega_m])] \quad (2.81)$$

The anti-Lorentzian coefficient is

$$a_{\text{rr}} = 2\sigma\kappa_{\text{L}}|\alpha_{\text{s}}|^2\text{Im}(B_{\text{mod}}[\omega_m]) \quad (2.82)$$

where $B_{\text{mod}}[\omega]$ is defined as:

$$\begin{aligned} B_{\text{mod}}[\omega] = & \kappa_{\text{L}}|\chi_{\text{C}}[-\omega]|^2e^{-i\phi}[(C_{\text{xx}} + iC_{\text{xy}})B_{+}[\omega] + (iC_{\text{xy}} - C_{\text{yy}})B_{-}[\omega]] \\ & - \chi_{c,s}^*[-\omega]e^{-i\phi}[(C_{\text{xx}}B_{+}[\omega] + iC_{\text{xy}}B_{-}[\omega])(1 + \rho) + (iC_{\text{xy}}B_{+}[\omega] - C_{\text{yy}}B_{-}[\omega])(1 - \rho)] \end{aligned} \quad (2.83)$$

Similarly, the upper (blue) sideband around $\omega \simeq \omega_m + \omega_{\text{IF}}$ can be written as

$$S_{\text{bb}}[\delta\omega] = G^2e^2\sigma p|\bar{a}_{\text{in,s}}|^2[b_{\text{bb}} + \frac{s_{\text{bb}}}{(\tilde{\gamma}_{\text{m}}/2)^2 + (\delta\omega - \tilde{\omega}_{\text{m}})^2} + \frac{a_{\text{bb}}(\delta\omega - \tilde{\omega}_{\text{m}})}{(\tilde{\gamma}_{\text{m}}/2)^2 + (\delta\omega - \tilde{\omega}_{\text{m}})^2}] \quad (2.84)$$

with

$$b_{\text{bb}} = 1 + \sigma[(|\rho|^2 + |\kappa_{\text{L}}\chi_{c,s}[\omega_m] - 1|^2)(C_{\text{xx}} + C_{\text{yy}}) - 2\text{Re}[\rho^*(\kappa_{\text{L}}\chi_{c,s}[\omega_m] - 1)](C_{\text{xx}} + 2iC_{\text{xy}} - C_{\text{yy}})] \quad (2.85)$$

$$s_{\text{bb}} = \sigma\kappa_{\text{L}}|\alpha_{\text{s}}|^2\tilde{\gamma}_{\text{m}}[|\chi_{c,s}[\omega_m]|^2n_{\text{eff}} - \text{Re}(B_{\text{mod}}[-\omega_m])] \quad (2.86)$$

$$a_{\text{bb}} = -2\sigma\kappa_{\text{L}}|\alpha_{\text{s}}|^2\text{Im}(B_{\text{mod}}[-\omega_m]) \quad (2.87)$$

When there is no classical noise on the laser, $B_{\text{mod}} = 0$. The upper and lower sidebands are then purely Lorentzians with heights proportional to n_{eff} and $n_{\text{eff}} + 1$, in agreement with predictions from Fermi's Golden Rule. The classical noise terms change the heights of the Lorentzian peaks, and add anti-Lorentzian components to the sidebands.

2.3.3 Cross-correlation spectrum of mechanical sidebands

Besides the auto-correlation of the photocurrent at the upper and lower mechanical sidebands, we can also look at the cross-correlation of the two sidebands, this amounts to calculating

$$\begin{aligned} S_{\text{rb}}[\omega] &= i^*[\omega]i[\omega - 2\omega_{\text{IF}}] = \frac{1}{2T} \int dt e^{-2i\omega_{\text{IF}}t} \int d\tau e^{-i\omega\tau} (\overline{i(t)i(t+\tau)} + \overline{i(t+\tau)i(t)}) \\ &= \frac{1}{2T} \int dt e^{-2i\omega_{\text{IF}}t} \int d\tau (e^{-i\omega\tau} + e^{i\omega\tau - 2i\omega_{\text{IF}}\tau}) \overline{i(t)i(t+\tau)} \end{aligned} \quad (2.88)$$

From Equation (2.59), we get from the $e^{2i\omega_{\text{IF}}t}$ term

$$S_{\text{rb}}[\omega] = \frac{1}{2} G^2 e^2 \sigma p \bar{a}_{\text{in},s}^2 e^{2i\theta} (S_{\hat{d}_{\text{out}}^\dagger \hat{d}_{\text{out}}}[\omega - \omega_{\text{IF}}] + S_{\hat{d}_{\text{out}}^\dagger \hat{d}_{\text{out}}}[-(\omega - \omega_{\text{IF}})]) \quad (2.89)$$

where

$$\begin{aligned} S_{\hat{d}_{\text{out}}^\dagger \hat{d}_{\text{out}}}[\omega] &= \rho^{*2} \langle \hat{d}_{\text{refl,LO}}[-\omega] \hat{d}_{\text{refl,LO}}[\omega] \rangle + \langle \hat{d}_{\text{refl,s}}^\dagger[\omega] \hat{d}_{\text{refl,s}}^\dagger[-\omega] \rangle \\ &\quad + \rho^* \langle \hat{d}_{\text{refl,s}}^\dagger[\omega] \hat{d}_{\text{refl,LO}}[-\omega] \rangle + \rho^* \langle \hat{d}_{\text{refl,s}}^\dagger[-\omega] \hat{d}_{\text{refl,LO}}[\omega] \rangle \end{aligned} \quad (2.90)$$

The factor of $\frac{1}{2}$ in Equation (2.89) is a normalization factor to make it consistent with the definitions of S_{rr} and S_{bb} .

For $\omega = \delta\omega + \omega_{\text{IF}} \approx \omega_m + \omega_{\text{IF}}$, again the cross-correlation spectrum consists of a background term, a Lorentzian peak and an anti-Lorentzian part. The background in $S_{\hat{d}_{\text{out}}^\dagger \hat{d}_{\text{out}}}[\delta\omega]$ comes from

$$\rho^{*2} \langle \hat{d}_{\text{refl,LO}}[-\delta\omega] \hat{d}_{\text{refl,LO}}[\delta\omega] \rangle = \rho^{*2} (C_{\text{xx}} + 2iC_{\text{xy}} - C_{\text{yy}}) \quad (2.91)$$

$$\begin{aligned} &\langle \hat{d}_{\text{refl,s}}^\dagger[\delta\omega] \hat{d}_{\text{refl,s}}^\dagger[-\delta\omega] \rangle |_{\text{classical-classical}} \\ &= (\kappa_{\text{L}} \chi_{\text{c,s}}^*[-\delta\omega] - 1) \langle (\delta x_{\text{s}}[\delta\omega] - i\delta y_{\text{s}}[\delta\omega]) (\kappa_{\text{L}} \chi_{\text{c,s}}^*[\delta\omega] - 1) (\delta x_{\text{s}}[-\delta\omega] - i\delta y_{\text{s}}[-\delta\omega]) \rangle \\ &= (\kappa_{\text{L}} \chi_{\text{c,s}}^*[-\omega_m] - 1) (\kappa_{\text{L}} \chi_{\text{c,s}}^*[-\omega] - 1) (C_{\text{xx}} - 2iC_{\text{xy}} - C_{\text{yy}}) \end{aligned} \quad (2.92)$$

$$\begin{aligned}
\rho^* &< \hat{d}_{\text{refl},s}^\dagger[\delta\omega] \hat{d}_{\text{refl,LO}}[-\delta\omega] >|_{\text{classical-classical}} \\
&= -\rho^* < (\kappa_L \chi_{c,s}^*[-\delta\omega] - 1)(\delta x_s[\delta\omega] - i\delta y_s[\delta\omega])(\delta x_s[-\delta\omega] + i\delta y_s[-\delta\omega]) > \\
&= -\rho^* (\kappa_L \chi_{c,s}^*[-\omega_m] - 1)(C_{xx} + C_{yy}) \quad (2.93)
\end{aligned}$$

$$\begin{aligned}
\rho^* &< \hat{d}_{\text{refl},s}^\dagger[-\delta\omega] \hat{d}_{\text{refl,LO}}[\delta\omega] >|_{\text{classical-classical}} \\
&= -\rho^* < (\kappa_L \chi_{c,s}^*[\delta\omega] - 1)(\delta x_s[-\delta\omega] - i\delta y_s[-\delta\omega])(\delta x_s[\delta\omega] + i\delta y_s[\delta\omega]) > \\
&= -\rho^* (\kappa_L \chi_{c,s}^*[\omega_m] - 1)(C_{xx} + C_{yy}) \quad (2.94)
\end{aligned}$$

Similarly, we get the same results for $S_{\hat{a}_{\text{out}}^\dagger \hat{a}_{\text{out}}^\dagger}[-\delta\omega]$.

The Fano terms can also be calculated in a similar fashion:

1. $z - z$ correlation. From $S_{\hat{a}_{\text{out}}^\dagger \hat{a}_{\text{out}}^\dagger}[\delta\omega]$:

$$\begin{aligned}
< \hat{d}_{\text{refl},s}^\dagger[\delta\omega] \hat{d}_{\text{refl},s}^\dagger[-\delta\omega] >|_{z-z} &= -\chi_{c,s}^*[\omega_m] \chi_{c,s}^*[-\omega_m] < \hat{z}[-\delta\omega] \hat{z}[\delta\omega] > \\
&= -\kappa_L \alpha_s^{*2} \chi_{c,s}^*[\omega_m] \chi_{c,s}^*[-\omega_m] \tilde{\gamma}_m [|\chi_{\text{eff},s}[-\delta\omega]|^2 (n_{\text{eff}} + 1) + |\chi_{\text{eff},s}[\delta\omega]|^2 n_{\text{eff}}] \\
&\simeq -\kappa_L \alpha_s^{*2} \chi_{c,s}^*[\omega_m] \chi_{c,s}^*[-\omega_m] \tilde{\gamma}_m |\chi_{\text{eff},s}[\omega_m]|^2 n_{\text{eff}} \quad (2.95)
\end{aligned}$$

From $S_{\hat{a}_{\text{out}}^\dagger \hat{a}_{\text{out}}^\dagger}[-\delta\omega]$:

$$\begin{aligned}
< \hat{d}_{\text{refl},s}^\dagger[-\delta\omega] \hat{d}_{\text{refl},s}^\dagger[\delta\omega] >|_{z-z} &= -\chi_{c,s}^*[\omega_m] \chi_{c,s}^*[-\omega_m] < \hat{z}[\delta\omega] \hat{z}[-\delta\omega] > \\
&= -\kappa_L \alpha_s^{*2} \chi_{c,s}^*[\omega_m] \chi_{c,s}^*[-\omega_m] \tilde{\gamma}_m [|\chi_{\text{eff},s}[\delta\omega]|^2 (n_{\text{eff}} + 1) + |\chi_{\text{eff},s}[-\delta\omega]|^2 n_{\text{eff}}] \\
&\simeq -\kappa_L \alpha_s^{*2} \chi_{c,s}^*[\omega_m] \chi_{c,s}^*[-\omega_m] \tilde{\gamma}_m |\chi_{\text{eff},s}[\omega_m]|^2 (n_{\text{eff}} + 1) \quad (2.96)
\end{aligned}$$

Adding together and taking in the $\frac{1}{2}$ factor from Equation (2.89), we get

$$-\kappa_L \alpha_s^{*2} \chi_{c,s}^*[-\omega_m] \chi_{c,s}^*[\omega_m] \frac{\tilde{\gamma}_m (n_{\text{eff}} + 1/2)}{(\tilde{\gamma}_m/2)^2 + (\delta\omega - \tilde{\omega}_m)^2} \quad (2.97)$$

2. z - classical correlation. From $S_{\hat{d}_{\text{out}}^\dagger \hat{d}_{\text{out}}}[\delta\omega]$:

$$\begin{aligned}
& \langle \hat{d}_{\text{refl},s}^\dagger[\delta\omega] \hat{d}_{\text{refl},s}^\dagger[-\delta\omega] \rangle |_{z\text{-classical}} \\
&= \langle (\kappa_L \chi_{c,s}^*[-\delta\omega] - 1)(\delta x_s[\delta\omega] - i\delta y_s[\delta\omega])(i\sqrt{\kappa_L} \alpha^* \chi_{c,s}^*[\delta\omega] \hat{z}[-\delta\omega]) \rangle \\
&+ \langle (i\sqrt{\kappa_L} \alpha^* \chi_{c,s}^*[-\delta\omega] \hat{z}[\delta\omega])(\kappa_L \chi_{c,s}^*[\delta\omega] - 1)(\delta x_s[-\delta\omega] - i\delta y_s[-\delta\omega]) \rangle \\
&= -(\kappa_L \chi_{c,s}^*[-\omega_m] \chi_{c,s}^*[\omega_m] - \chi_{c,s}^*[\omega_m]) \alpha_s^{*2} \kappa_L \\
&\times (B_+[-\omega_m] C_{xx} - iB_+[-\omega_m] C_{xy} + iB_-[-\omega_m] C_{xy} + B_-[-\omega_m] C_{yy}) e^{i\phi} \frac{2i\omega_m}{N[-\delta\omega]} \\
&+ (\kappa_L \chi_{c,s}^*[-\omega_m] \chi_{c,s}^*[\omega_m] - \chi_{c,s}^*[\omega_m]) \alpha_s^{*2} \kappa_L \\
&\times (B_+[\omega_m] C_{xx} - iB_+[\omega_m] C_{xy} + iB_-[\omega_m] C_{xy} + B_-[\omega_m] C_{yy}) e^{i\phi} \frac{-2i\omega_m}{N[\delta\omega]} \quad (2.98)
\end{aligned}$$

$$\begin{aligned}
& \rho^* \langle \hat{d}_{\text{refl},s}^\dagger[\delta\omega] \hat{d}_{\text{refl,LO}}[-\delta\omega] \rangle |_{z\text{-classical}} \\
&= \rho^* \langle (i\sqrt{\kappa_L} \alpha^* \chi_{c,s}^*[-\delta\omega] \hat{z}[\delta\omega])(-\delta x_s[-\delta\omega] - i\delta y_s[-\delta\omega]) \rangle \\
&= -\rho^* \alpha_s^{*2} \kappa_L e^{i\phi} \chi_{c,s}^*[-\omega_m] \\
&\times (B_+[\omega_m] C_{xx} + iB_+[\omega_m] C_{xy} + iB_-[\omega_m] C_{xy} - B_-[\omega_m] C_{yy}) e^{i\phi} \frac{-2i\omega_m}{N[\delta\omega]} \quad (2.99)
\end{aligned}$$

$$\begin{aligned}
& \rho^* \langle \hat{d}_{\text{refl},s}^\dagger[-\delta\omega] \hat{d}_{\text{refl,LO}}[\delta\omega] \rangle |_{z\text{-classical}} \\
&= \rho^* \langle (i\sqrt{\kappa_L} \alpha^* \chi_{c,s}^*[\delta\omega] \hat{z}[-\delta\omega])(-\delta x_s[\delta\omega] - i\delta y_s[\delta\omega]) \rangle \\
&= \rho^* \alpha_s^{*2} \kappa_L e^{i\phi} \chi_{c,s}^*[\omega_m] \\
&\times (B_+[-\omega_m] C_{xx} + iB_+[-\omega_m] C_{xy} + iB_-[-\omega_m] C_{xy} - B_-[-\omega_m] C_{yy}) e^{i\phi} \frac{2i\omega_m}{N[-\delta\omega]} \quad (2.100)
\end{aligned}$$

Similarly, from $S_{\hat{d}_{\text{out}}^\dagger \hat{d}_{\text{out}}^\dagger}[-\delta\omega]$:

$$\begin{aligned}
\langle \hat{d}_{\text{refl},s}^\dagger[-\delta\omega] \hat{d}_{\text{refl},s}^\dagger[\delta\omega] \rangle_{|z\text{-classical}} &= (\kappa_L \chi_{c,s}^*[-\omega_m] \chi_{c,s}^*[\omega_m] - \chi_{c,s}^*[-\omega_m]) |\alpha|^2 \kappa_L \\
&\times (B_+[\omega_m] C_{xx} - iB_+[\omega_m] C_{xy} + iB_-[\omega_m] C_{xy} + B_-[\omega_m] C_{yy}) e^{-i\phi} \frac{-2i\omega_m}{N[\delta\omega]} \\
&- (\kappa_L \chi_{c,s}^*[-\omega_m] \chi_{c,s}^*[\omega_m] - \chi_{c,s}^*[\omega_m]) |\alpha|^2 \kappa_L \\
&\times (B_+[-\omega_m] C_{xx} - iB_+[-\omega_m] C_{xy} + iB_-[-\omega_m] C_{xy} + B_-[-\omega_m] C_{yy}) e^{-i\phi} \frac{2i\omega_m}{N[-\delta\omega]} \quad (2.101)
\end{aligned}$$

the two other terms repeat Equations (2.97) and (2.98).

We combine (2.96)-(2.99), and take in the $\frac{1}{2}$ factor in $S_{rb}[\omega]$. Notice when $\delta\omega \simeq \omega_m$

$$N[\delta\omega] = \chi_m^{*-1}[-\delta\omega] \chi_{\text{eff}}^{-1}[\delta\omega] \simeq -2i\omega_m[\tilde{\gamma}_m/2 - i(\delta\omega - \tilde{\omega}_m)] \quad (2.102)$$

$$N[-\delta\omega] = N[\delta\omega]^* = 2i\omega_m[\tilde{\gamma}_m/2 + i(\delta\omega - \tilde{\omega}_m)] \quad (2.103)$$

Their contribution to the Lorentzian peak is

$$\frac{\kappa_L \tilde{\gamma}_m}{2} \frac{D_{\text{mod}}[\omega_m] - D_{\text{mod}}[-\omega_m]}{(\tilde{\gamma}_m/2)^2 + (\delta\omega - \tilde{\omega}_m)^2} \quad (2.104)$$

and the contribution to the anti-Lorentzian part is

$$i\kappa_L(\delta\omega - \tilde{\omega}_m) \frac{D_{\text{mod}}[\omega_m] + D_{\text{mod}}[-\omega_m]}{(\tilde{\gamma}_m/2)^2 + (\delta\omega - \tilde{\omega}_m)^2} \quad (2.105)$$

where we define

$$\begin{aligned}
D_{\text{mod}}[\omega] &= \kappa_L \chi_{c,s}^*[\omega_m] \chi_{c,s}^*[-\omega_m] e^{i\phi} [(C_{xx} - iC_{xy})B_+[\omega] + (iC_{xy} + C_{yy})B_-[\omega]] \\
&- \chi_{c,s}^*[-\omega_m] e^{i\phi} [(C_{xx} B_+[\omega] + iC_{xy} B_-[\omega])(1 + \rho^*) - (iC_{xy} B_+[\omega] - C_{yy} B_-[\omega])(1 - \rho^*)] \quad (2.106)
\end{aligned}$$

3. Beside the correlation of position \hat{z} with the classical noise, there is also a nonzero correlation

between the position \hat{z} and the quantum noise. This z – *quantum* correlation is the effect of RPSN.

From $S_{\hat{d}_{out}^\dagger \hat{d}_{out}^\dagger}[\delta\omega]$:

$$\begin{aligned}
& \langle \hat{d}_{refl,s}^\dagger[\delta\omega] \hat{d}_{refl,s}^\dagger[-\delta\omega] \rangle_{|z\text{-quantum}} \\
& = \langle (i\sqrt{\kappa_L}\alpha^* \chi_{c,s}^*[-\delta\omega] \hat{z}[\delta\omega]) [(\kappa_L \chi_{c,s}^*[\delta\omega] - 1) \hat{\xi}_L^\dagger[-\delta\omega] + \sqrt{\kappa_L \kappa_M} \chi_{c,s}^*[\delta\omega] \hat{\xi}_M^\dagger[-\delta\omega]] \rangle \\
& = \sqrt{\kappa_L} \alpha^* \chi_{c,s}^*[-\delta\omega] \langle \frac{-i2\omega_m}{N[\delta\omega]} \alpha^* \chi_{c,s}[\delta\omega] (\sqrt{\kappa_L} \hat{\xi}_L[\delta\omega] + \sqrt{\kappa_M} \hat{\xi}_M[\delta\omega]) \\
& \quad \times [(\kappa_L \chi_{c,s}^*[\delta\omega] - 1) \hat{\xi}_L^\dagger[-\delta\omega] + \sqrt{\kappa_L \kappa_M} \chi_{c,s}^*[\delta\omega] \hat{\xi}_M^\dagger[-\delta\omega]] \rangle \\
& = \kappa_L \alpha^{*2} \chi_{c,s}^*[-\delta\omega] \chi_{c,s}[\delta\omega] \frac{-i2\omega_m}{N[\delta\omega]} [(\kappa_L \chi_{c,s}^*[\delta\omega] - 1) \langle \hat{\xi}_L[\delta\omega] \hat{\xi}_L^\dagger[\delta\omega] \rangle + \kappa_M \chi_{c,s}^*[\delta\omega] \langle \hat{\xi}_M[\delta\omega] \hat{\xi}_M^\dagger[\delta\omega] \rangle] \\
& = \kappa_L \alpha^{*2} \chi_{c,s}^*[-\delta\omega] \chi_{c,s}[\delta\omega] \frac{-i2\omega_m}{N[\delta\omega]} (\kappa \chi_{c,s}^*[\delta\omega] - 1) \quad (2.107)
\end{aligned}$$

From $S_{\hat{d}_{out}^\dagger \hat{d}_{out}^\dagger}[-\delta\omega]$:

$$\begin{aligned}
& \langle \hat{d}_{refl,s}^\dagger[-\delta\omega] \hat{d}_{refl,s}^\dagger[\delta\omega] \rangle_{|z\text{-quantum}} \\
& = \langle (i\sqrt{\kappa_L}\alpha^* \chi_{c,s}^*[\delta\omega] \hat{z}[-\delta\omega]) [(\kappa_L \chi_{c,s}^*[\delta\omega] - 1) \hat{\xi}_L^\dagger[-\delta\omega] + \sqrt{\kappa_L \kappa_M} \chi_{c,s}^*[\delta\omega] \hat{\xi}_M^\dagger[-\delta\omega]] \rangle \\
& = -\sqrt{\kappa_L} \alpha^* \chi_{c,s}^*[\delta\omega] \langle \frac{i2\omega_m}{N[-\delta\omega]} \alpha^* \chi_{c,s}[-\delta\omega] (\sqrt{\kappa_L} \hat{\xi}_L[-\delta\omega] + \sqrt{\kappa_M} \hat{\xi}_M[-\delta\omega]) \\
& \quad \times [(\kappa_L \chi_{c,s}^*[-\delta\omega] - 1) \hat{\xi}_L^\dagger[\delta\omega] + \sqrt{\kappa_L \kappa_M} \chi_{c,s}^*[\delta\omega] \hat{\xi}_M^\dagger[\delta\omega]] \rangle \\
& = -\kappa_L \alpha^{*2} \chi_{c,s}^*[\delta\omega] \chi_{c,s}[-\delta\omega] \frac{i2\omega_m}{N[-\delta\omega]} [(\kappa_L \chi_{c,s}^*[-\delta\omega] - 1) \langle \hat{\xi}_L[-\delta\omega] \hat{\xi}_L^\dagger[\delta\omega] \rangle + \kappa_M \chi_{c,s}^*[-\delta\omega] \langle \hat{\xi}_M[\delta\omega] \hat{\xi}_M^\dagger[\delta\omega] \rangle] \\
& = -\kappa_L \alpha^{*2} \chi_{c,s}^*[\delta\omega] \chi_{c,s}[-\delta\omega] \frac{i2\omega_m}{N[-\delta\omega]} (\kappa \chi_{c,s}^*[-\delta\omega] - 1) \quad (2.108)
\end{aligned}$$

To simplify (2.103) and (2.104), we use the relation

$$\kappa \chi_{c,s}^*[\omega] - 1 = \frac{\kappa}{\kappa/2 + i(\omega + \Delta)} - 1 = \frac{\kappa/2 - i(\omega + \Delta)}{\kappa/2 + i(\omega + \Delta)} = \chi_{c,s}^{-1}[\omega] \chi_{c,s}^*[\omega] \quad (2.109)$$

The sum of the two z – *quantum* correlation terms becomes

$$\begin{aligned} \kappa_L \alpha^{*2} \chi_{c,s}^*[-\delta\omega] \chi_{c,s}[\delta\omega] \frac{-i2\omega_m}{N[\delta\omega]} \chi_{c,s}^{-1}[\delta\omega] \chi_{c,s}^*[\delta\omega] - \kappa_L \alpha^{*2} \chi_{c,s}^*[-\delta\omega] \chi_{c,s}[\delta\omega] \frac{-i2\omega_m}{N[\delta\omega]} \chi_{c,s}^{-1}[\delta\omega] \chi_{c,s}^*[\delta\omega] \\ = i\kappa_L \alpha^{*2} \chi_{c,s}^*[-\delta\omega] \chi_{c,s}^*[\delta\omega] \frac{2(\delta\omega - \tilde{\omega}_m)}{(\tilde{\gamma}_m/2)^2 + (\delta\omega - \tilde{\omega}_m)^2} \end{aligned}$$

Gathering all the terms together, the cross-correlation spectrum is

$$S_{\text{rb}}[\delta\omega] = (Ge)^2 \sigma p |\bar{a}_{\text{in},s}|^2 e^{2i\theta} \left[b_{\text{rb}} + \frac{s_{\text{rb}}}{(\tilde{\gamma}_m/2)^2 + (\delta\omega - \tilde{\omega}_m)^2} + \frac{a_{\text{rb}}(\delta\omega - \tilde{\omega}_m)}{(\tilde{\gamma}_m/2)^2 + (\delta\omega - \tilde{\omega}_m)^2} \right] \quad (2.110)$$

with

$$\begin{aligned} b_{\text{rb}} = \sigma [\rho^{*2} (C_{\text{xx}} + 2iC_{\text{xy}} - C_{\text{yy}}) + (\kappa_L \chi_{c,s}^*[\omega_m] - 1)(\kappa_L \chi_{c,s}^*[-\omega_m] - 1)(C_{\text{xx}} - 2iC_{\text{xy}} - C_{\text{yy}}) \\ - \rho^* (\kappa_L \chi_{c,s}^*[\omega_m] + \kappa_L \chi_{c,s}^*[-\omega_m] - 2)(C_{\text{xx}} + C_{\text{yy}})] \quad (2.111) \end{aligned}$$

$$s_{\text{rb}} = \sigma \kappa_L \alpha_s^{*2} \tilde{\gamma}_m \{ -\chi_{c,s}^*[\omega_m] \chi_{c,s}^*[-\omega_m] (n_{\text{eff}} + 1/2) + 1/2 D_{\text{mod},-}[\omega_m] \} \quad (2.112)$$

$$a_{\text{rb}} = i\sigma \kappa_L \alpha_s^{*2} (\chi_{c,s}^*[\omega_m] \chi_{c,s}^*[-\omega_m] + D_{\text{mod},+}[\omega_m]) \quad (2.113)$$

The classical noise coefficients are defined by

$$D_{\text{mod},\pm}[\omega] = D_{\text{mod}}[\omega] \pm D_{\text{mod}}[-\omega] \quad (2.114)$$

$$\begin{aligned} D_{\text{mod}}[\omega] = \kappa_L \chi_{c,s}^*[\omega_m] \chi_{c,s}^*[-\omega_m] e^{i\phi} [(C_{\text{xx}} - iC_{\text{xy}})B_+[\omega] + (iC_{\text{xy}} + C_{\text{yy}})B_-[\omega]] \\ - \chi_{c,s}^*[-\omega_m] e^{i\phi} [(C_{\text{xx}}B_+[\omega] + iC_{\text{xy}}B_-[\omega])(1 + \rho^*) - (iC_{\text{xy}}B_+[\omega] - C_{\text{yy}}B_-[\omega])(1 - \rho^*)] \end{aligned}$$

When the classical noise terms are small compared to the shot noise level, the anti-symmetric part is non-zero and is completely produced by RPSN. This is similar to the cross-correlation scheme

proposed in Ref[44] to observe RPSN. In that paper, Børkje et al. pointed out that the signature of RPSN is the anti-symmetry of the correlation around mechanical resonance, as is seen here. It was also pointed out that at finite detuning, it is difficult to separate the effects of classical noise from that of RPSN, as can be seen in a_{rb} expression. Having the signal beam classical noise close to the shot noise level is necessary for clear observation of RPSN.

Notice the coefficients of the thermal term and the RPSN term are proportional to $-\chi_{\text{c,s}}^*[\omega_{\text{m}}]\chi_{\text{c,s}}^*[-\omega_{\text{m}}]$ and $i\chi_{\text{c,s}}^*[\omega_{\text{m}}]\chi_{\text{c,s}}^*[-\omega_{\text{m}}]$ respectively. When the signal beam classical noise is small, we can apply a phase θ to rotate $S_{\text{rb}}[\delta\omega]$. By choosing $\theta = -\arg(\chi_{\text{c,s}}^*[\omega_{\text{m}}]\chi_{\text{c,s}}^*[-\omega_{\text{m}}])$, the symmetric part of $e^{i\theta}S_{\text{rb}}$ is completely real, whereas the anti-symmetric part is completely imaginary. At this point, a non-zero, purely-imaginary anti-symmetric term is the evidence that we have observed RPSN.

Even when classical noise is not completely negligible, we can differentiate the effects of classical noise from that of RPSN by measuring S_{rb} and varying the signal beam power. Looking at a_{rb} , the RPSN term $\chi_{\text{c,s}}^*[\omega_{\text{m}}]\chi_{\text{c,s}}^*[-\omega_{\text{m}}]$ does not depend on signal beam power whereas $D_{\text{mod,+}}[\omega_{\text{m}}]$ is linear with signal beam power.

2.4 Spectrum of squeezing

At low phonon number, the nonlinear radiation pressure back-action creates squeezed light. The squeezing is characterized by the time-ordered, normal-ordered quantity of the output field quadrature[19, 57]

$$S_{\varphi}^{\text{out}}[\omega] = 1 + 4 \int_{-\infty}^{+\infty} dt e^{i\omega t} \langle : \Delta \hat{X}_{\text{out},\varphi}(0) \Delta \hat{X}_{\text{out},\varphi}(t) : \rangle \quad (2.115)$$

where the output field quadrature is defined as

$$\begin{aligned} \Delta \hat{X}_{\text{out},\varphi}(t) &= \frac{1}{2} [\hat{d}_{\text{out}}(t) e^{-i\varphi} + \hat{d}_{\text{out}}^{\dagger}(t) e^{i\varphi}] \\ &= \frac{1}{2} [e^{-i\varphi} (\hat{d}_{\text{refl,s}}(t) + \rho \hat{d}_{\text{refl,LO}}^{\dagger}(t)) + e^{i\varphi} (\hat{d}_{\text{refl,s}}^{\dagger}(t) + \rho \hat{d}_{\text{refl,LO}}(t))] \end{aligned} \quad (2.116)$$

If the classical noise is negligible, the output field expressed by Equations (2.54) and (2.55) simplifies to $\hat{a}_{\text{out}}(t) = \hat{a}_{\text{refl,s}}(t)$, and $\Delta \hat{X}_{\text{out},\varphi}(t) = \frac{1}{2} [e^{-i\varphi} \hat{d}_{\text{refl,s}}(t) + e^{i\varphi} \hat{d}_{\text{refl,s}}^{\dagger}(t)]$.

If at a frequency ω , a certain phase angle φ would provide a minimum of $S_\varphi^{out}[\omega] < 1$, this would be the signature of observing a squeezed state. We could use the heterodyne spectra to calculate the squeezing spectrum of the reflected light. From the previous section, we see

$$\begin{aligned} S_{rr}[-\omega + \omega_{IF}] + S_{bb}[\omega + \omega_{IF}] + 2\text{Re}(e^{2i(\varphi+\theta)} S_{rb}[\omega + \omega_{IF}]) \\ = 2(Ge)^2 \sigma p |\bar{a}_{in}|^2 (1 + 4\sigma \int_{-\infty}^{+\infty} dt e^{i\omega t} \langle: \Delta \hat{X}_{out,\varphi}(0) \Delta \hat{X}_{out,\varphi}(t) : \rangle) \end{aligned} \quad (2.117)$$

Squeezing is inevitably compromised by the detection efficiency, as shown by the extra σ in (2.117).

Inserting heterodyne spectra results from the previous section, we get when $\omega \simeq \omega_m$:

$$\begin{aligned} S_\varphi^{out}[\omega] = \frac{1}{2} [b_{rr} + b_{bb} + 2\text{Re}(e^{2i(\varphi+\theta)} b_{rb}) \\ + \frac{s_{rr} + s_{bb} + 2\text{Re}(e^{2i(\varphi+\theta)} s_{rb})}{(\tilde{\gamma}_m/2)^2 + (\omega - \tilde{\omega}_m)^2} + \frac{-a_{rr} + a_{bb} + 2\text{Re}(e^{2i(\varphi+\theta)} a_{rb})}{(\tilde{\gamma}_m/2)^2 + (\omega - \tilde{\omega}_m)^2} (\omega - \tilde{\omega}_m)] \end{aligned} \quad (2.118)$$

at each detuning Δ_s and frequency ω , we can vary the quadrature angle φ and find the optimal squeezing $\min(S_\varphi^{out}[\omega])$.

To understand how the squeezing happens, we look at the analytical expression of $S_\varphi^{out}[\omega]$ when laser classical noise is small and the effective phonon number is small. We take the approximation $C_{xx,s} = C_{xy,s} = C_{yy,s} = 0$ and get the simplified forms of Equations (2.70, 2.81-2.82, 2.85-2.87, 2.111-2.113):

$$\begin{aligned} b_{rr} \\ = 1 + \sigma [(|\rho|^2 + |\kappa_L \chi_{c,s}[-\omega_m] - 1|^2) (C_{xx} + C_{yy}) - 2\text{Re}[\rho^* (\kappa_L \chi_{c,s}[-\omega_m] - 1)] (C_{xx} + 2iC_{xy} - C_{yy})] \\ \simeq 1 \end{aligned} \quad (2.119)$$

b_{bb}

$$= 1 + \sigma[(|\rho|^2 + |\kappa_{\text{L}}\chi_{\text{c,s}}[\omega_{\text{m}}] - 1|^2)(C_{\text{xx}} + C_{\text{yy}}) - 2\text{Re}[\rho^*(\kappa_{\text{L}}\chi_{\text{c,s}}[\omega_{\text{m}}] - 1)](C_{\text{xx}} + 2iC_{\text{xy}} - C_{\text{yy}})] \simeq 1 \quad (2.120)$$

$$s_{\text{rr}} = \sigma\kappa_{\text{L}}|\alpha_{\text{s}}|^2\tilde{\gamma}_{\text{m}}[|\chi_{\text{c,s}}[-\omega_{\text{m}}]|^2(n_{\text{eff}} + 1) + \text{Re}(B_{\text{mod}}[\omega_{\text{m}}])] \simeq \sigma\kappa_{\text{L}}|\alpha_{\text{s}}|^2\tilde{\gamma}_{\text{m}}[|\chi_{\text{c,s}}[-\omega_{\text{m}}]|^2(n_{\text{eff}} + 1)] \quad (2.121)$$

$$s_{\text{bb}} = \sigma\kappa_{\text{L}}|\alpha_{\text{s}}|^2\tilde{\gamma}_{\text{m}}[|\chi_{\text{c,s}}[\omega_{\text{m}}]|^2n_{\text{eff}} - \text{Re}(B_{\text{mod}}[-\omega_{\text{m}}])] \simeq \sigma\kappa_{\text{L}}|\alpha_{\text{s}}|^2\tilde{\gamma}_{\text{m}}[|\chi_{\text{c,s}}[\omega_{\text{m}}]|^2n_{\text{eff}}] \quad (2.122)$$

$$a_{\text{rr}} = 2\sigma\kappa_{\text{L}}|\alpha_{\text{s}}|^2\text{Im}(B_{\text{mod}}[\omega_{\text{m}}]) \simeq 0 \quad (2.123)$$

$$a_{\text{bb}} = -2\sigma\kappa_{\text{L}}|\alpha_{\text{s}}|^2\text{Im}(B_{\text{mod}}[-\omega_{\text{m}}]) \simeq 0 \quad (2.124)$$

$$b_{\text{rb}} = \sigma[\rho^{*2}(C_{\text{xx}} + 2iC_{\text{xy}} - C_{\text{yy}}) + (\kappa_{\text{L}}\chi_{\text{c,s}}^*[\omega_{\text{m}}] - 1)(\kappa_{\text{L}}\chi_{\text{c,s}}^*[-\omega_{\text{m}}] - 1)(C_{\text{xx}} - 2iC_{\text{xy}} - C_{\text{yy}}) - \rho^*(\kappa_{\text{L}}\chi_{\text{c,s}}^*[\omega_{\text{m}}] + \kappa_{\text{L}}\chi_{\text{c,s}}^*[-\omega_{\text{m}}] - 2)(C_{\text{xx}} + C_{\text{yy}})] \simeq 0 \quad (2.125)$$

$$s_{\text{rb}} = \sigma\kappa_{\text{L}}\alpha_{\text{s}}^{*2}\tilde{\gamma}_{\text{m}}\{-\chi_{\text{c,s}}^*[\omega_{\text{m}}]\chi_{\text{c,s}}^*[-\omega_{\text{m}}](n_{\text{eff}} + 1/2) + 1/2D_{\text{mod},-}[\omega_{\text{m}}]\} \simeq -\sigma\kappa_{\text{L}}|\alpha_{\text{s}}|^2e^{-2i\phi}\tilde{\gamma}_{\text{m}}\chi_{\text{c,s}}^*[\omega_{\text{m}}]\chi_{\text{c,s}}^*[-\omega_{\text{m}}](n_{\text{eff}} + 1/2) \quad (2.126)$$

$$a_{\text{rb}} = i\sigma\kappa_{\text{L}}\alpha_{\text{s}}^{*2}(\chi_{\text{c,s}}^*[\omega_{\text{m}}]\chi_{\text{c,s}}^*[-\omega_{\text{m}}] + D_{\text{mod},+}[\omega_{\text{m}}]) \simeq i\sigma\kappa_{\text{L}}|\alpha_{\text{s}}|^2e^{-2i\phi}\tilde{\gamma}_{\text{m}}\chi_{\text{c,s}}^*[\omega_{\text{m}}]\chi_{\text{c,s}}^*[-\omega_{\text{m}}] \quad (2.127)$$

We can then rewrite Equation (2.118) as

$$\begin{aligned}
S_\varphi^{out}[\omega] = & 1 + \sigma\kappa_L|\alpha_s|^2\{\tilde{\gamma}_m[|\chi_{c,s}[-\omega_m]|^2(n_{\text{eff}} + 1) + |\chi_{c,s}[\omega_m]|^2n_{\text{eff}} \\
& - 2\text{Re}[e^{2i(\varphi+\theta-\phi)}\chi_{c,s}^*[\omega_m]\chi_{c,s}^*[-\omega_m](n_{\text{eff}} + 1/2)] \\
& + 2\text{Re}[e^{2i(\varphi-\theta)}\chi_{c,s}^*[\omega_m]\chi_{c,s}^*[-\omega_m]i(\omega - \tilde{\omega}_m)]\}\frac{1}{(\tilde{\gamma}_m/2)^2 + (\omega - \tilde{\omega}_m)^2} \quad (2.128)
\end{aligned}$$

In the limiting case of $n_{\text{eff}} \simeq 0$, Equation (2.128) can be further simplified to

$$\begin{aligned}
S_\varphi^{out}[\omega] = & 1 + \sigma\kappa_L|\alpha_s|^2\{\tilde{\gamma}_m[|\chi_{c,s}[-\omega_m]|^2 - \text{Re}(e^{2i(\varphi+\theta-\phi)}\chi_{c,s}^*[\omega_m]\chi_{c,s}^*[-\omega_m])] \\
& + 2\text{Re}[e^{2i(\varphi+\theta-\phi)}i\chi_{c,s}^*[\omega_m]\chi_{c,s}^*[-\omega_m]](\omega - \tilde{\omega}_m)\}\frac{1}{(\tilde{\gamma}_m/2)^2 + (\omega - \tilde{\omega}_m)^2} \quad (2.129)
\end{aligned}$$

Here we discuss the analytical expression of Equation (2.129) in two cases.

(1) Small detuning, $\Delta_s \simeq 0$

Because $\omega \simeq \omega_m$, we get in the resolved sideband limit

$$\chi_{c,s}[\pm\omega_m] = [\kappa/2 - i(\pm\omega_m + \Delta)]^{-1} \simeq [\kappa/2 \mp i\omega_m]^{-1} \simeq (\mp i\omega_m)^{-1}$$

We can then rewrite Equation (2.129) as

$$\begin{aligned}
S_\varphi^{out}[\omega] \simeq & 1 + \sigma\kappa_L|\alpha_s|^2\{\tilde{\gamma}_m[\frac{1}{\omega_m^2} - \text{Re}(e^{2i\varphi'})\frac{1}{\omega_m^2}] \\
& + 2\text{Re}(ie^{i\varphi'})\frac{1}{\omega_m^2}(\omega - \tilde{\omega}_m)\}\frac{1}{(\tilde{\gamma}_m/2)^2 + (\omega - \tilde{\omega}_m)^2} \quad (2.130)
\end{aligned}$$

where $\varphi' = \varphi + \theta - \phi + \frac{1}{2} \arg(\chi_{c,s}^*[\omega_m]\chi_{c,s}^*[-\omega_m])$. For the RPSN term, which is the second term in the curly bracket, its anti-symmetric function $\frac{(\omega - \tilde{\omega}_m)}{(\tilde{\gamma}_m/2)^2 + (\omega - \tilde{\omega}_m)^2}$ gets extrema when $\omega - \tilde{\omega}_m = \pm\tilde{\gamma}_m/2$.

Equation (2.129) can therefore be further simplified to

$$S_\varphi^{out}[\omega] \simeq 1 + \sigma\kappa_L|\alpha_s|^2 \frac{1}{\omega_m^2} \tilde{\gamma}_m [1 - \cos(2\varphi') \pm \sin(2\varphi')] \frac{1}{(\tilde{\gamma}_m/2)^2 + (\tilde{\gamma}_m/2)^2} \quad (2.131)$$

The optimal squeezing is then

$$\min(S_\varphi^{out}[\omega]) = 1 - \frac{2(\sqrt{2}-1)\sigma\kappa_L|\alpha_s|^2}{\omega_m^2 \tilde{\gamma}_m} < 1 \quad (2.132)$$

(2) Optimal detuning for cooling, $\Delta_s \simeq -\omega_m$

In this case, because $\omega \simeq \omega_m$,

$$\chi_{c,s}[-\omega_m] = [\kappa/2 - i(\omega + \Delta)]^{-1} \simeq [\kappa/2 - i(\omega - \omega_m)]^{-1} \simeq (-2i\omega_m)^{-1}$$

and

$$\chi_{c,s}[\omega_m] \simeq (\kappa/2)^{-1}$$

Equation (2.129) becomes

$$S_\varphi^{out}[\omega] \simeq 1 + \sigma\kappa_L|\alpha_s|^2 \left\{ \tilde{\gamma}_m \left[\frac{1}{4\omega_m^2} - \cos(2\varphi') \frac{1}{\kappa\omega_m} \right] + 2 \sin(2\varphi') \frac{1}{\kappa\omega_m} (\omega - \tilde{\omega}_m) \right\} \frac{1}{(\tilde{\gamma}_m/2)^2 + (\omega - \tilde{\omega}_m)^2} \quad (2.133)$$

Again when $\omega - \tilde{\omega}_m = \pm \tilde{\gamma}_m/2$, we get

$$S_\varphi^{out}[\omega] \simeq 1 + \sigma\kappa_L|\alpha_s|^2 \tilde{\gamma}_m \left[\frac{1}{4\omega_m^2} - \cos(2\varphi') \frac{1}{\kappa\omega_m} \pm \sin(2\varphi') \frac{1}{\kappa\omega_m} \right] \frac{1}{(\tilde{\gamma}_m/2)^2 + (\tilde{\gamma}_m/2)^2}$$

The optimal squeezing then becomes

$$\min(S_\varphi^{out}[\omega]) = 1 + \frac{\sigma\kappa_L|\alpha_s|^2}{2\omega_m^2 \tilde{\gamma}_m} - \frac{2(\sqrt{2}-1)\sigma\kappa_L|\alpha_s|^2}{\kappa\omega_m \tilde{\gamma}_m} \quad (2.134)$$

In the resolved sideband limit, $\omega_m > \kappa$, so $\min(S_\varphi^{out}[\omega]) < 1$.

2.5 Laser noise reduction by a filter cavity

As shown by Equation (2.36), excessive laser classical noise around the mechanical resonant frequency $\omega = \pm\omega_m$ will limit the minimum phonon number we can achieve. In order to reduce the classical noise, we can pass the laser through a filter cavity, with a linewidth κ_f substantially lower than the frequency we are interested in, ω_m . The classical amplitude and phase noises at $\omega = \pm\omega_m$ are then passively filtered by a factor of $(\frac{2\omega_m}{\kappa_f})^2$ if the cavity is locked on resonance with the laser. The details of this passive filtering can be worked out using the cavity equation of motion.

Consider an input $a_{\text{in}}(t) = e^{-i\omega_0 t}(\bar{a}_{\text{in}} + \delta x_{\text{in}}(t) + i\delta y_{\text{in}}(t))$. This creates an intracavity field $a(t) = e^{-i\omega_0 t}[\bar{a} + \delta a(t)]$. Here we neglected the quantum noise. Similar to Equation (2.10), in the rotating wave frame and in Fourier space, we solve for the intra-cavity noise annihilation operator $\delta a[\omega]$ and get

$$\delta a[\omega] = \chi_{\text{c,f}}[\omega]\delta a_{\text{in}}[\omega] = \frac{\sqrt{\kappa_L}(\delta x_{\text{in}}[\omega] + i\delta y_{\text{in}}[\omega])}{\kappa_f/2 - i(\Delta + \omega)} \quad (2.135)$$

Assuming the cavity is symmetric on the two sides, $\kappa_L = \kappa_R = \kappa_1$, The DC amplitude of transmitted beam is $\bar{a}_{\text{trans}} = \frac{\kappa_1 \bar{a}_{\text{in}}}{\kappa_f/2 - i\Delta}$. The transmitted field operator is

$$\delta a_{\text{tran}}[\omega] = \kappa_R a[\omega] = \frac{\kappa_1(\delta x_{\text{in}}[\omega] + i\delta y_{\text{in}}[\omega])}{\kappa_f/2 - i(\Delta + \omega)} \quad (2.136)$$

The transmitted classical amplitude noise is

$$\begin{aligned} \delta x_{\text{tran}}[\omega] &= \frac{\delta a_{\text{tran}}[\omega] + \delta a_{\text{tran}}^\dagger[\omega]}{2} \\ &= \frac{\kappa_1}{2} [\delta x_{\text{in}}[\omega] \left(\frac{1}{\kappa_f/2 - i(\Delta + \omega)} + \frac{1}{\kappa_f/2 + i(\Delta - \omega)} \right) + i\delta y_{\text{in}}[\omega] \left(\frac{1}{\kappa_f/2 - i(\Delta + \omega)} - \frac{1}{\kappa_f/2 + i(\Delta - \omega)} \right)] \end{aligned} \quad (2.137)$$

The transmitted classical phase noise is

$$\begin{aligned} \delta y_{\text{tran}}[\omega] &= \frac{i(\delta a_{\text{tran}}^\dagger[\omega] - \delta a_{\text{tran}}[\omega])}{2} \\ &= \frac{\kappa_1}{2} [\delta y_{\text{in}}[\omega] \left(\frac{1}{\kappa_f/2 - i(\Delta + \omega)} + \frac{1}{\kappa_f/2 + i(\Delta - \omega)} \right) - i\delta x_{\text{in}}[\omega] \left(\frac{1}{\kappa_f/2 - i(\Delta + \omega)} - \frac{1}{\kappa_f/2 + i(\Delta - \omega)} \right)] \end{aligned} \quad (2.138)$$

Assuming input classical amplitude noise and phase noise are uncorrelated, the transmitted amplitude noise is

$$\begin{aligned} C_{\text{xx,tran}}[\omega] &= \langle \delta x_{\text{tran}}[\omega] \delta x_{\text{tran}}[-\omega] \rangle \\ &= \frac{1}{4} \kappa_1^2 C_{\text{xx,in}} \left(\frac{1}{(\kappa_f/2)^2 + (\Delta + \omega)^2} + \frac{1}{(\kappa_f/2)^2 + (\Delta - \omega)^2} + \frac{2[(\kappa_f/2)^2 - (\Delta^2 - \omega^2)]}{[(\kappa_f/2)^2 - (\Delta^2 - \omega^2)]^2 + \kappa_f^2 \Delta^2} \right) \\ &+ \frac{1}{4} \kappa_1^2 C_{\text{yy,in}} \left(\frac{1}{(\kappa_f/2)^2 + (\Delta + \omega)^2} + \frac{1}{(\kappa_f/2)^2 + (\Delta - \omega)^2} - \frac{2[(\kappa_f/2)^2 - (\Delta^2 - \omega^2)]}{[(\kappa_f/2)^2 - (\Delta^2 - \omega^2)]^2 + \kappa_f^2 \Delta^2} \right) \end{aligned} \quad (2.139)$$

The transmitted phase noise is

$$\begin{aligned} C_{\text{yy,tran}}[\omega] &= \langle \delta y_{\text{tran}}[\omega] \delta y_{\text{tran}}[-\omega] \rangle \\ &= \frac{1}{4} \kappa_1^2 C_{\text{yy,in}} \left(\frac{1}{(\kappa_f/2)^2 + (\Delta + \omega)^2} + \frac{1}{(\kappa_f/2)^2 + (\Delta - \omega)^2} + \frac{2[(\kappa_f/2)^2 - (\Delta^2 - \omega^2)]}{[(\kappa_f/2)^2 - (\Delta^2 - \omega^2)]^2 + \kappa_f^2 \Delta^2} \right) \\ &+ \frac{1}{4} \kappa_1^2 C_{\text{xx,in}} \left(\frac{1}{(\kappa_f/2)^2 + (\Delta + \omega)^2} + \frac{1}{(\kappa_f/2)^2 + (\Delta - \omega)^2} - \frac{2[(\kappa_f/2)^2 - (\Delta^2 - \omega^2)]}{[(\kappa_f/2)^2 - (\Delta^2 - \omega^2)]^2 + \kappa_f^2 \Delta^2} \right) \end{aligned} \quad (2.140)$$

For the simple case of on resonance $\Delta = 0$, $P_{\text{trans}} = P_{\text{in}} \frac{\kappa_1^2}{(\kappa_f/2)^2}$, $C_{\text{xx,tran}}[\omega] = \frac{\kappa_1^2}{(\kappa_f/2)^2 + \omega^2} C_{\text{xx,in}}[\omega]$, $C_{\text{yy,tran}}[\omega] = \frac{\kappa_1^2}{(\kappa_f/2)^2 + \omega^2} C_{\text{yy,in}}[\omega]$. Therefore at $\omega = \pm\omega_m$, the classical noise is filtered by a factor of $\frac{(\kappa_f/2)^2 + \omega_m^2}{(\kappa_f/2)^2}$. When $\omega_m \gg \kappa_f/2$, the classical noise terms are filtered by $(\frac{2\omega_m}{\kappa_f})^2$.

It is hard to maintain zero detuning in reality. At finite detuning, a part of the input amplitude noise contribute to the output phase noise and input phase noise contributes to the output amplitude

noise. At small finite detuning Δ , from Equation (2.139) we get

$$C_{\text{xx,tran}}[\omega] \simeq \frac{\kappa_1^2}{(\kappa_f/2)^2 + \omega^2} C_{\text{xx,in}}[\omega] + \frac{\kappa_1^2 \Delta^2}{[(\kappa_f/2)^2 + \omega^2]^2} C_{\text{yy,in}}[\omega] \quad (2.141)$$

and similarly for $C_{\text{yy,tran}}$. We can view this as adding $\frac{\Delta^2}{(\kappa_f/2)^2 + \omega^2} C_{\text{yy,in}}$ and $\frac{\Delta^2}{(\kappa_f/2)^2 + \omega^2} C_{\text{xx,in}}$ to the input amplitude noise $C_{\text{xx,in}}$ and phase noise $C_{\text{yy,in}}$.

Chapter 3

Experimental Design

3.1 Membrane in the middle setup

3.1.1 Mechanical properties of Si_3N_4 membrane

The mechanical device of our optomechanical system is a commercially available stoichiometric Si_3N_4 membrane from Norcada Inc. The SiN membrane is $1.5 \text{ mm} \times 1.5 \text{ mm} \times 50 \text{ nm}$ in size, with an effective mass $m = 96.8 \text{ ng}$. Its fundamental vibrational mode frequency is $\omega_m/2\pi = 261 \text{ kHz}$. The mechanical Q factor at 400 mK is around 5×10^6 , this gives it an intrinsic mechanical linewidth $\gamma_m/2\pi = 0.052 \text{ Hz}$. A typical mechanical ringdown of this mechanical mode is shown in Figure 3.1. More details about models to understand the membrane's vibrational eigenmodes and its nonlinear behaviors are given in Appendix A.

3.1.2 Optical properties of the cavity

The experimental cavity we use is a length $L = 3.39 \text{ cm}$ single-sided cavity with one end-mirror spec'd to be 10 times more transmissive than the other one at 1064 nm . Due to the optical loss at the membrane, the cavity finesse varies depending on where the membrane is relative to the intracavity electric field[47, 48]. At the spot we use for measurements, the cavity finesse is around $F = 37,000$, as shown in the optical ringdown measurement of Figure 3.2.

The coupling efficiency of the cavity is measured by the reflection dip, as detailed in Section

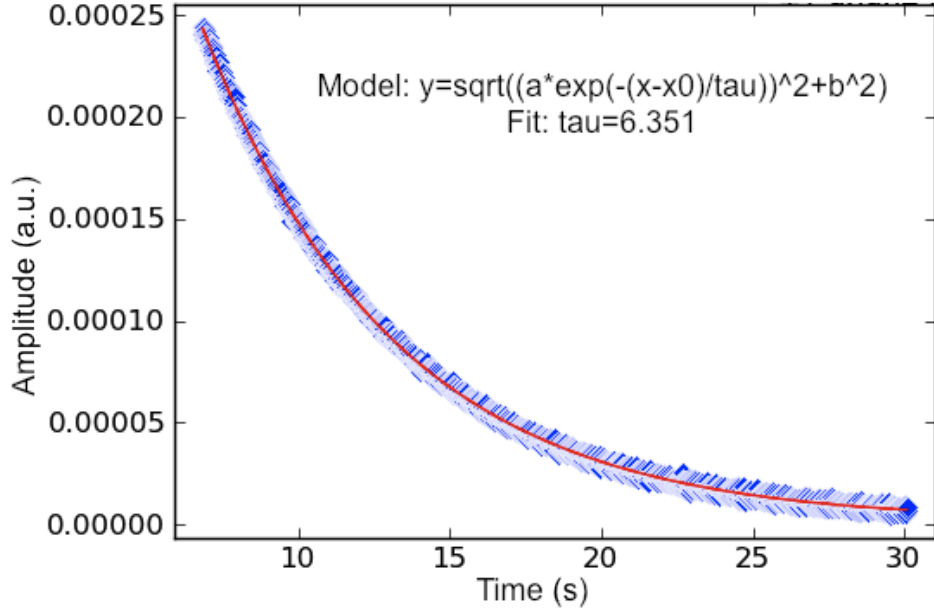


Figure 3.1: Membrane mechanical ringdown measured with a lock-in amplifier. Blue dots are data, the red curve is a theoretical fit. The membrane is driven on resonance. Once the drive is turned off, the amplitude of the vibration at the mechanical resonance decays exponentially. The 6.351 s ringdown time corresponds to a mechanical linewidth $\gamma_m/2\pi = 0.050$ Hz, and a mechanical Q factor of 5.21×10^6 .

3.6. Derived from Equation (2.50), the reflected dip as a percentage of the far off-resonance power R provides a measure of the front cavity mirror κ_L

$$\kappa_L = \frac{(1 - \sqrt{R})}{2} \kappa \quad (3.1)$$

The measured reflection dip is 55%. This implies $\kappa_L = 0.165\kappa$.

The cavity also exhibits birefringence, which means each cavity spatial mode is split into two polarization eigenmodes. The frequency split between the two polarizations is close to the mechanical resonant frequency. To make sure we are always cooling the membrane motion, the laser should only excite the lower polarization mode, so that even if there is a small upper polarization component in the cavity input, its frequency is far negatively detuned from the cavity resonant.

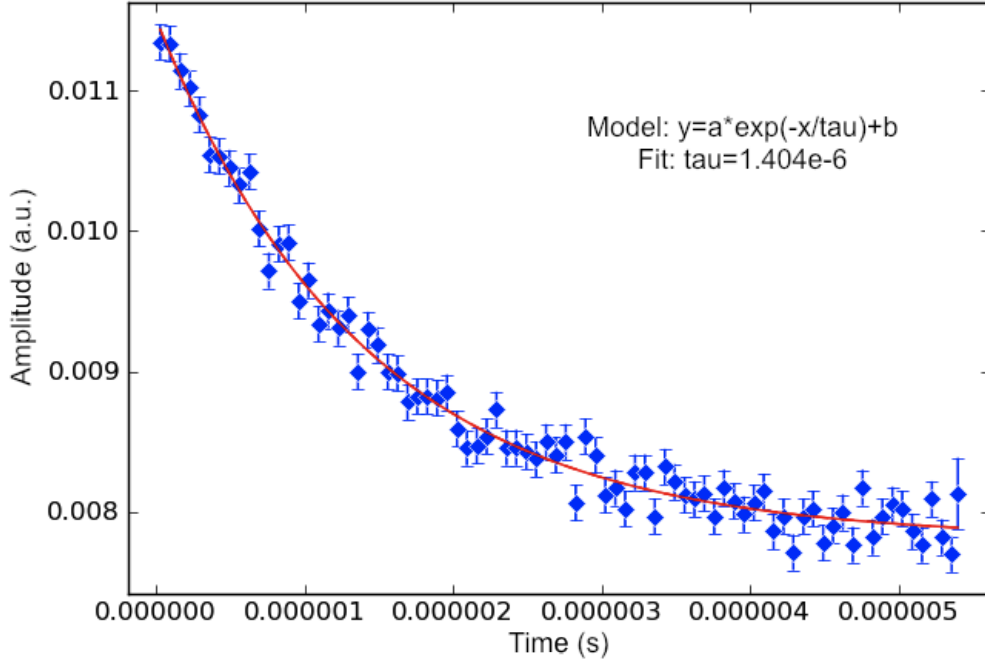


Figure 3.2: Cavity optical ringdown recorded by a DAQ card. Blue dots are real data, the red curve is theoretical fit. Reflected power decays exponentially when the beam is blocked. The exponential ringdown time constant is $\tau = 1.404 \mu\text{s}$, corresponding to a cavity linewidth $\kappa/2\pi = 113 \text{ kHz}$. For a cavity length $L = 3.39 \text{ cm}$, this corresponds to a finesse $F = (c/2L)/\kappa = 39100$.

3.1.3 Optomechanical coupling of the membrane-in-the-middle cavity

The coupling between the membrane and the cavity is determined by the membrane reflectivity r_d at 1064 nm and the membrane position in the cavity. The resonant frequency ω_{cav} of the combined cavity as a function of membrane distance from the center x is described by[47]

$$\omega_{\text{cav}} = 2 \frac{c}{2L} \arccos[r_d \cos(\frac{4\pi x}{\lambda})] \quad (3.2)$$

where $L = 0.034 \text{ m}$ is the cavity length, $\lambda = 1064 \text{ nm}$ is the optical wavelength.

When the membrane is 100% reflective, $r_d = 1$, Equation (3.1) becomes

$$\omega_{\text{cav}} = \frac{2\pi \frac{c}{2L}}{\lambda/4} x = \frac{FSR}{\lambda/4} x \quad (3.3)$$

where $FSR = 2\pi \frac{c}{2L}$ is the free spectral range of the optical cavity. This is consistent with the cavity resonance of a $L/2$ long single-sided cavity with a movable end-mirror.

Taking a derivative of Equation (3.2), we get the coupling coefficient to be

$$\frac{\partial\omega_{\text{cav}}}{\partial x} = 2r_{\text{d}}\frac{\omega_{\text{opt}}}{L}\frac{1}{\sqrt{1 - [r_{\text{d}}\cos(\frac{4\pi x}{\lambda})]^2}}\sin(\frac{4\pi x}{\lambda}) \quad (3.4)$$

where $\omega_{\text{opt}} = \frac{2\pi c}{\lambda}$ is the optical circular frequency. When the membrane is at a node or anti-node of the intracavity electrical field, the slope is 0, and we get pure quadratic optomechanical coupling.

The maximum linear slope is

$$\left(\frac{\partial\omega_{\text{cav}}}{\partial x}\right)_{\text{max}} = 2r_{\text{d}}\frac{\omega_{\text{opt}}}{L} \quad (3.5)$$

when $|\sin(\frac{4\pi x}{\lambda})| = 1$ and $\cos(\frac{4\pi x}{\lambda}) = 0$. This is a factor of $2r_{\text{d}}$ attenuated compared to a single-sided cavity with a movable end-mirror. When the membrane reflectivity is low, Equation (3.4) can also be approximated by

$$\frac{\partial\omega_{\text{cav}}}{\partial x} = 2r_{\text{d}}\frac{\omega_{\text{opt}}}{L}\sin(\frac{4\pi x}{\lambda}) \quad (3.6)$$

For the experimental cavity, we measured $\frac{\partial\omega_{\text{cav}}}{\partial x}$ using the signal beam. When the signal beam is locked on resonance with the cavity, we move the membrane position by the attocube (a piezo translation stage) it rests on, and record the change in the signal laser frequency feedback, denoted by the output of the laser piezo feedback PI controller described in Section 3.3. The attocube voltage V_{atto} (before a $\times 2$ amplifier) in terms of actual membrane displacement is converted by 13.3 nm/V. This is calculated from the fact that the membrane moves from a node to an anti-node (corresponding to $\frac{\lambda}{4} = 266$ nm) when attocube voltage is changed by 20 V. The laser piezo PI output voltage V_{aux} (before a $\times 10$ amplifier) is converted to laser frequency by 14.2 MHz/V. To measure this, we put phase modulation sidebands at ± 15 MHz on the signal beam. We then sweep V_{aux} and measure the change in V_{aux} between successive resonances of the signal beam carrier and its 15 MHz sideband.

The measured maximal slope in $V_{\text{atto}}/V_{\text{aux}}$ is $(V_{\text{atto}}/V_{\text{aux}})_{\text{max}} = 4.89$, corresponding to an actual coupling

$$\left(\frac{\partial\omega_{\text{cav}}}{\partial x}\right)_{\text{max}} = (V_{\text{atto}}/V_{\text{aux}})_{\text{max}} \times \frac{2\pi \times 14.2 \text{ MHz/V}}{13.3 \text{ nm/V}} = 3.28 \times 10^{16} \text{ rad/m} = 0.630 \frac{\omega_{\text{opt}}}{L}$$

This corresponds to $r_d = 0.315$, similar to what we measured previously in room temperature setup[47]. We can further convert $(\frac{\partial\omega_{\text{cav}}}{\partial x})_{\text{max}}$ into the linear coupling coefficient A defined in Section 2.2.1:

$$A \equiv (\frac{\partial\omega_{\text{cav}}}{\partial \hat{z}})_{\text{max}} = (\frac{\partial\omega_{\text{cav}}}{\partial x})_{\text{max}} \sqrt{\frac{\hbar}{2m\omega_m}} = 19.0 \text{ rad}/(\text{m} \times \text{s})$$

3.2 Overview of the optical setup

A common practice in optomechanical experiments is to split one laser output for both the cooling beam and the detection beam[27, 33, 35]. However, once we consider the classical noise on the lasers, because the noises on the two beams are correlated, complicated behavior similar to electromagnetically induced transparency (EIT) can happen[58–60]. It is therefore advantageous to use two separate lasers, as their classical noises should be largely uncorrelated.

The basic optical setup is laid out as in Figure 3.3. Two lasers are used. The signal laser is separated in the heterodyne and PDH lock setup to generate a signal beam and an LO beam for heterodyne detection of the mechanical motional state. This is done by using an acousto-optic modulator (AOM) to shift the signal beam 80 MHz up from the LO beam. Phase modulated sidebands at ± 15 MHz are also added onto the signal beam by an electro-optic modulator (EOM). This is used to generate the Pound-Drever-Hall (PDH) error signal[61] to lock the signal laser to the experiment cavity.

The cooling laser is used to laser cool the vibrational mode of the membrane. In Figure 3.3, I also included a filter cavity that can be used to reduce the classical phase noise from the cooling laser. I will discuss its design in Section 3.5, and demonstrate the filtering effects in Chapter 4. As will be discussed in Chapter 6, the filter cavity is an important improvement for future experiments. But it is not used in the laser cooling measurements presented in this thesis.

The two lasers are locked at 9 GHz apart by the cooling laser lock. Another AOM is used to control the power and detuning of the cooling beam. The different frequency components being sent to the experimental cavity is shown in Figure 3.4.

The experimental cavity with the Si_3N_4 membrane in the middle is kept in a ^3He fridge, and is

at 400 mK during measurement, monitored by a thermometer attached to the setup. Signals are collected at the reference photodiode and the reflected photodiode. The reference photodiode is used to track the change in the LO phase due to beam path changes. The reflected photodiode collects the 15 MHz beat signal for PDH locking, and 80 MHz beat signal for the heterodyne measurement.

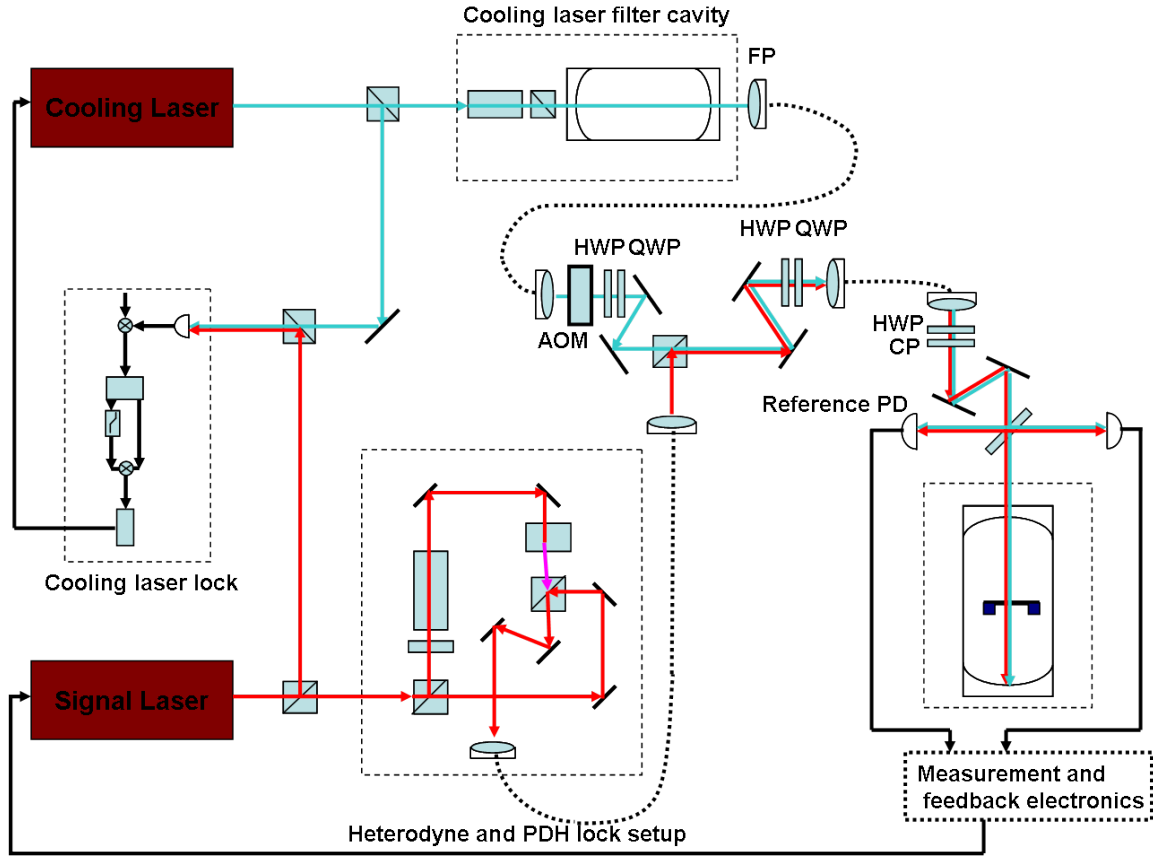


Figure 3.3: Overview of the measurement setup. Cooling filter cavity: reduces phase noise from the cooling laser. Heterodyne and PDH lock setup: generates a signal beam and an LO beam for heterodyne detection. The signal beam is locked to the experiment cavity using PDH locking. Cooling laser lock: locks the cooling laser to the signal laser. Reference PD: measures the phase of LO beam. Reflected PD: collect heterodyne signal and PDH signal. FP: fiberport. Half waveplate (HWP), quarter waveplate (QWP), and calcite polarizer (CP): used for matching polarization to fiber.

3.3 Heterodyne detection and PDH lock setup

A detailed schematic of the signal and LO beams for locking and heterodyne detection are set up as shown in Fig 3.5. A New Focus 4001 EOM adds phase modulation (PM) at 15 MHz to the signal beam. These PM sidebands are used to generate PDH error signal at the experimental cavity. The

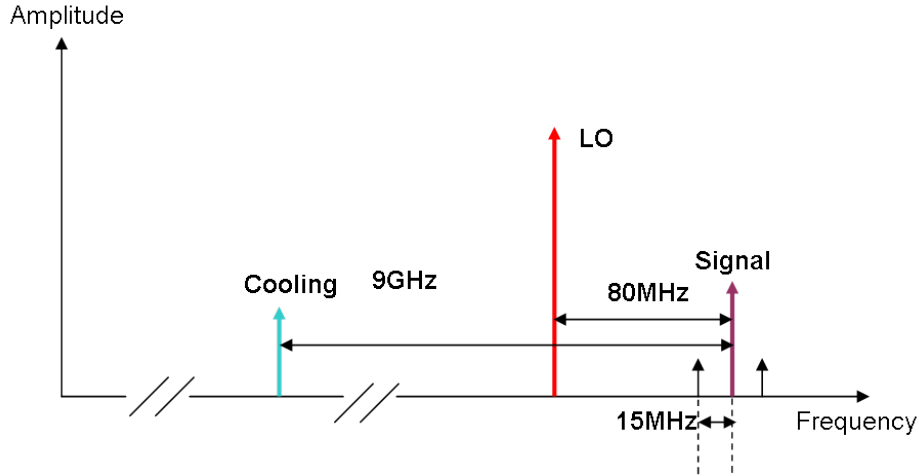


Figure 3.4: Frequency components of signal, LO and cooling beams

EOM uses a lithium niobate crystal, which provides far IR cutoff. It comes with a resonant tank circuit that amplifies the drive at 15 MHz. With the tank circuit, the voltage required to produce a π phase shift is $V_{1/2} = 16$ V at 1064 nm. To minimize the parasitic amplitude modulation (AM) created by EOM, we use a calcite polarizer to match the EOM input polarization to the crystal e-axis polarization. We also use the New Focus EOM mount to make sure the beam path matches with the crystal propagation axis. To observe the unwanted AM, we put a polarizer after the EOM, and rotate its polarization to find maximized AM peak in the FFT mode of oscilloscope. To minimize the AM, we iteratively adjust the input polarization, EOM orientation, and rotate the output polarizer for maximized AM peak, until it diminishes.

The signal beam with its PM sidebands goes to the experimental cavity. When the signal beam is close to cavity resonance, the reflected signal beam is added with a detuning-dependent phase shift. The two PM sidebands, being far off cavity resonance, are directly reflected without additional phase shift. On the reflected photodiode, the beating between the signal beam and its sidebands create a 15 MHz sinusoid, with the detuning-dependent phase shift imprinted on its amplitude. The demodulated 15 MHz beat thus produces the PDH error signal.

Three different locking schemes are used together to stably lock the signal beam near cavity resonance. The whole error signal is fed back to the piezo on the signal laser. The error signal first go through a proportional-integral (PI) controller. The ± 10 V output is then amplified by a low noise op-amp. Its output then goes through a 32 k Ω resistor to the laser piezo. This 32 k Ω resistor

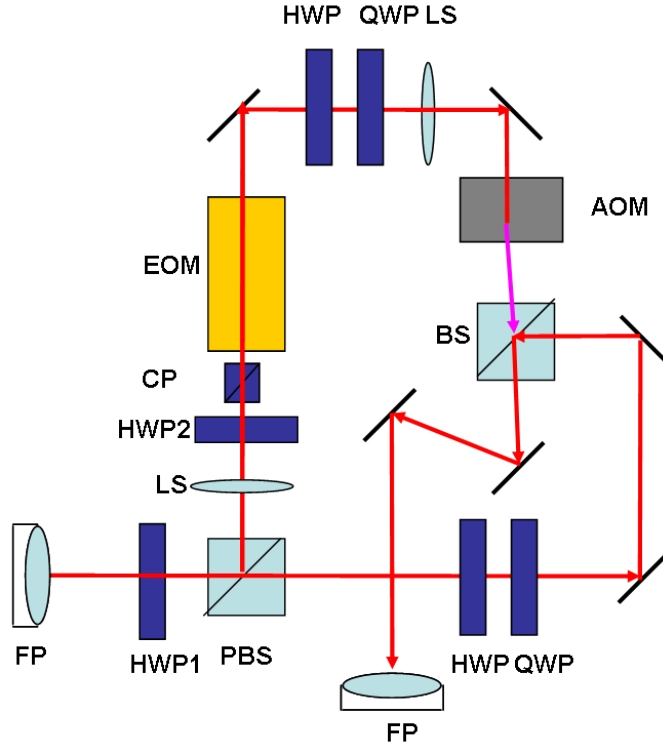


Figure 3.5: Schematic of the heterodyne and PDH lock setup. The signal beam goes through an EOM to generate the 15 MHz phase sidebands for PDH locking. It then goes through an AOM (Gooch&Housego R46080-1-1.06). The +1 order output of the AOM is 80 MHz shifted from the LO beam. Two Thorlabs PAF-X-7C fiberports (FP) transfer the beams to and from this setup. A half waveplate (HWP1) is put before a polarizing beamsplitter (PBS) to adjust the power ratio of the signal and LO beams. Another half waveplate (HWP2) matches the polarization of the calcite polarizer (CP), which is oriented for vertical polarization to minimize amplitude modulation at the EOM. A pair of $f = 200$ mm lenses (LS) focus the beam for EOM aperture. Another two pairs of half waveplates and quarter waveplates (QWP) match the preferred polarization of the fiber. A beamsplitter recombines the signal and LO beams before they go to the output fiberport.

combined with the 2.2 nF piezo capacitance to create a 2.2 kHz low pass filter. Besides the laser piezo feedback, the very low frequency (< 200 Hz) component of the PDH error signal is fed back to the Attocube piezo stack which the cavity rests on. To cancel out the long term slow temperature drift, we also send the feedback output to the signal laser temperature control, which only responds at sub-Hz frequencies.

3.4 Cooling beam locking

In order to avoid the correlation between laser noises around ω_m , we lock the cooling laser 2 free spectral ranges (~ 9 GHz) away from the signal laser, so they address two different longitudinal modes of the experimental cavity. We choose the frequency difference to be 2 free spectral ranges so the cavity dispersion curves of the two longitudinal modes have roughly the same shape as a function of membrane position. The details of the cooling beam lock setup are shown in Fig 3.6. A small part of the outputs of the two lasers are combined at a fast photodiode with 12 GHz bandwidth. The beat signal is then mixed down from around 9 GHz to tens of MHz using a Rohde-Schwarz (RS) SMB100A signal generator. Here we used a Minicircuits ZX05-153MH mixer. The mixed down signal is then amplified by a Minicircuits ZHL-3A amplifier.

In order to create an error signal, we split the beam into two using a Minicircuits ZCS-2 splitter. We then create an interference scheme. In one path, the signal goes through directly. Half of the signal is split to be used for monitoring the beat frequency. In the other path, the signal goes through a component to create a frequency dependent phase shift. This frequency dependent phase shift could be created by using a very long BNC cable[62]. Here, we use a first order Butterworth low pass filter (Minicircuits BLP-1.9) to create this phase shift. At frequencies below the 3 dB point (1.9 MHz), the magnitude is maximally flat and is still very close to the input magnitude. But the phase already starts to roll off. The two paths are recombined at a Minicircuits ZP-3 mixer to create a frequency dependent error signal. This error signal then goes through a 160 kHz low pass filter to filter out high frequency noise. It then goes through a PI controller with 10 kHz PI corner. The PI output goes through a 1 M Ω resistor, into the cooling laser piezo. This 1 M Ω resistor and the 2.3 nF piezo capacitance create a 69 Hz low pass filter.

The PI corner and the resistor are chosen to maximize feedback gain at low frequencies. Most of the noise we are trying to cancel is below 1 kHz. Part of this noise is from low frequency vibrations in the free-running laser. But a larger part of the low frequency noise comes from the vibrations of the experimental cavity. Such vibrations are caused by the membrane mount, and has a large number of resonances from 20 Hz to several hundred Hz. When the signal laser is locked to the

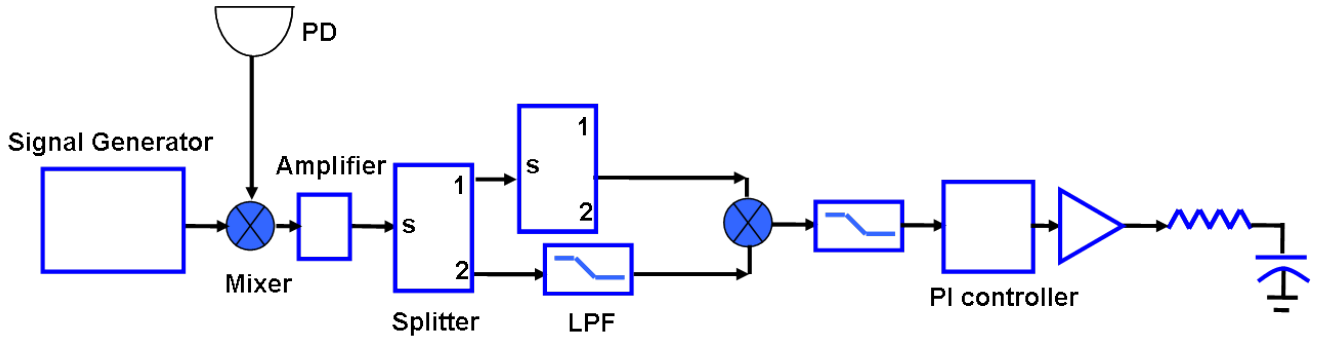


Figure 3.6: Cooling beam lock electronics. A signal generator provides a ~ 9 GHz local oscillator to mixes down the photodiode (PD) beat signal to MHz range. This signal, after amplification, is split into two paths. One of the paths has a 1.9 MHz low pass filter to create a frequency dependent phase shift. The two signals are then combined at a mixer and creates a frequency dependent error signal. The error signal goes through a 160 kHz low pass filter, a PI controller, an op-amp and finally a 69 Hz low pass filter formed by a 1 MHz resistor and the 2.3 nF laser piezo capacitance.

experimental cavity, it follows the jitters in the experimental cavity's frequency. The cooling laser piezo, on the other hand, has a relatively flat response up to its first mechanical resonance at 200 kHz. To maximize the feedback at low frequency, we use a 2 pole gain roll-off from a very low frequency (here we chose 70 Hz). The phase is kept above -180° to avoid positive feedback. Since each pole creates a -90° phase drop, this is the optimal setting for maximizing low frequency gain.

With this feedback, the two free-running lasers are locked 9 GHz apart with a beat linewidth less than 10 Hz. A PSD of the beat signal is shown in Figure 3.7.

During measurement, we first lock the signal beam to the experimental cavity using PDH locking. Then we turn on the cooling laser feedback to lock the cooling laser to the signal laser. The RS signal generator frequency is chosen to be close to two free spectral ranges of the cavity. However, we cannot use RS to fine tune the beat frequency. This is because spikes are generated every time we change its setting. These spikes destroy the cooling beam lock instantly. So instead, we use an AOM in the cooling beam path to bring it close to resonance with the cavity from the cooling side. Since the AOM only has a few MHz bandwidth around 80 MHz, we need to choose the RS output to be close to the desired frequency. To do this, we use the frequency modulation (FM) mode of the RS. When the RS frequency is close, we should see reflected power dips when the cooling beam frequency sweeps through resonance. We then adjust the AOM frequency to make the reflected dips distribute evenly. Finally, we compensate for this shift in AOM frequency from 80 MHz by

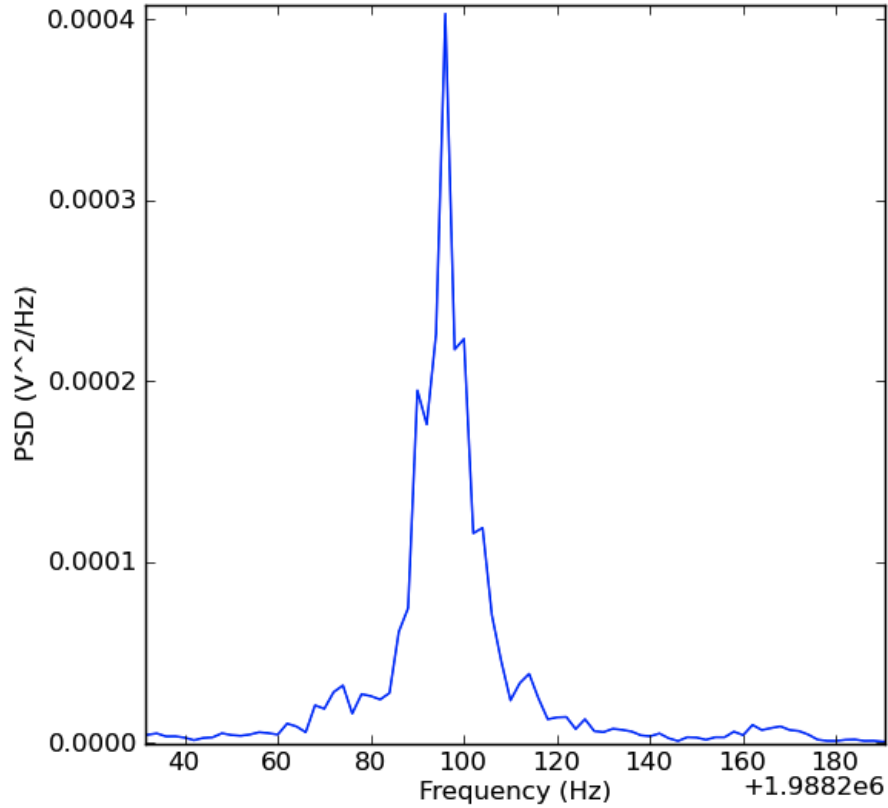


Figure 3.7: PSD of mixed down beat signal between free-running signal and cooling lasers. The two lasers are locked 8.85 GHz apart using the cooling laser lock setup. The linewidth is less than 10 Hz.

subtracting the same amount in the RS frequency, and turn off the FM.

Now with the RS set at the right frequency, we slowly increase the AOM RF drive frequency from 79 MHz. The cooling beam frequency approaches cavity resonance from the cooling side. We see a gradual decrease in the reflected DC power. However, we could still see a lot of fluctuation in the reflected DC power. Again, these fluctuations are caused by the jitters of the membrane position. Because the cooling beam and the signal beam are addressing two different longitudinal modes, the slope of the two dispersion curves are slightly different, as shown in Figure 3.8. When the membrane moves, this slope difference creates a resonant frequency difference. To create a clean cooling beam with stable detuning, we need to park the membrane at the “sweet spot”, where the slope in the two longitudinal mode dispersion curves are the same. This position also corresponds to the maximal frequency difference in the two dispersion curves. When we move the membrane position and change the AOM frequency to keep the reflected dip constant, the position where the

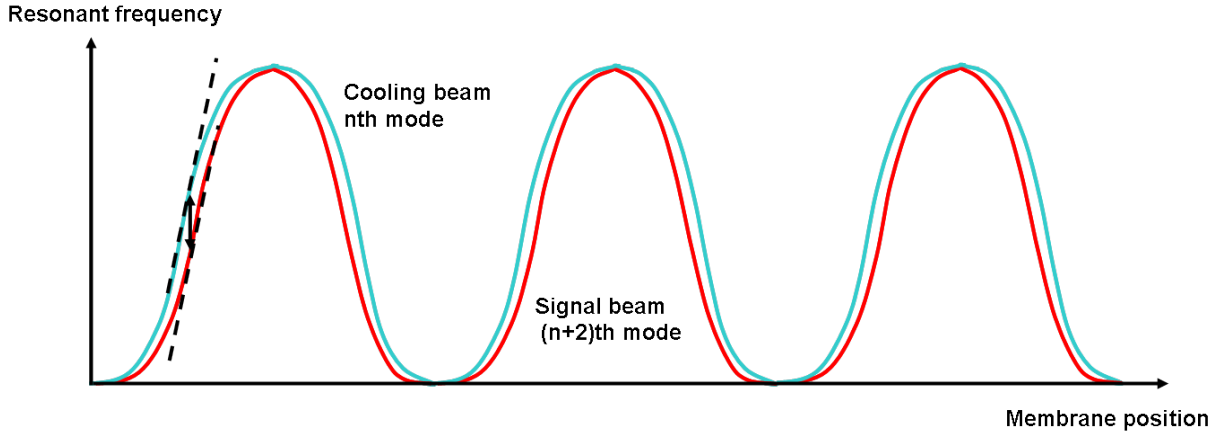


Figure 3.8: Schematic of the slope difference between the cooling and signal beam cavity resonance dispersion curves. The cooling beam is addressing the n th longitudinal mode, the signal beam is addressing the $(n + 2)$ th longitudinal mode. For comparison, the resonant frequency of the cooling beam is shifted up by 2 free spectral ranges. The two curves have the same slope at the “sweet spot” in membrane position. This also corresponds to the position of maximal difference in the two resonant frequencies.

AOM frequency change switches sign is the “sweet spot”. When the membrane is close to the “sweet spot”, reflection power fluctuations become sporadic spikes. All these spikes point towards higher reflected power, or more negative detuning. This is because membrane position fluctuation in either direction will change the frequency difference between the two dispersion curves in the same way. The fact that the noise spikes all point towards more negative detuning confirms the cooling beam is addressing a lower longitudinal mode than the signal beam.

3.5 Cooling beam filter cavity

As described in Section 2.5, a filter cavity can reduce the high frequency classical noise in the transmitted beam compared to its input. Figure 3.9 shows a detailed schematic of the filter cavity setup. The filter cavity has a measured optical linewidth $\kappa/2\pi = 22$ kHz. To eliminate the optical Kerr effect when using high power (input power $P_{\text{in}} = 150$ mW) in air, the filter cavity is put in a conflat vacuum can and kept at below 10^{-6} Torr with an ion pump. The filter cavity is locked on resonance to the cooling laser by a PDH lock. A Conoptics 360-40 EOM is used to create the phase modulation sidebands. This EOM uses lithium tantalate as the crystal, and has a $V_{1/2} = 400$ V at 1064 nm.

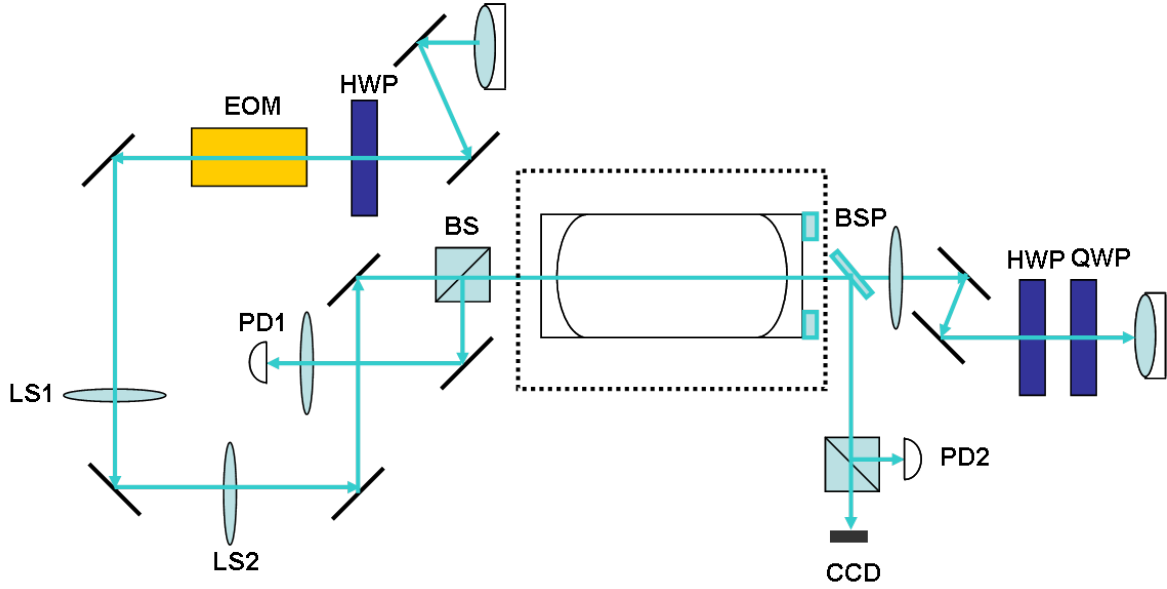


Figure 3.9: Cooling filter cavity setup. An EOM produces 15 MHz PM sidebands. A photodiode (PD1) monitors the reflected beam to generate the error signal, another one (PD2) monitors a small portion of the transmitted beam, after the beam sampler (BSP). A CCD camera is used to verify the mode coupled. Two lenses (LS1, 2) are used to mode-match the cavity. LS1: $f = -100$ mm. LS2: $f = 200$ mm. A conflat can keeps the filter cavity in high vacuum environment, pumped by an ion pump. Both fiberports used are Thorlabs PAF-X-7C with a 1.4 mm diameter collimated output.

A ring piezo from Noliac is attached to one of the filter cavity end mirrors. The piezo response is 14 nm/V. It is straight forward to send the PDH error signal to this piezo and lock the filter cavity on resonance with the free-running cooling laser. However, when locked to the signal laser, the cooling laser is tracking the frequency changes in the experimental cavity, and it becomes much more difficult for the filter cavity to stay locked to the cooling laser. In order to follow the big frequency excursions at low frequencies, we improved the feedback performance by Labview FPGA. We also implement a feedforward scheme. Both of these are described below.

The feedback bandwidth is limited by the first mechanical resonance of the filter cavity, which is around 8 – 10 kHz. For the first pass, we use a PI controller with 3 kHz PI corner. Its output goes through a summing amplifier made of OPA445AP op-amp, then a 2 – 7 k Ω potentiometer, onto the piezo. The piezo capacitance is 491 nF. With the resistor, they create a low pass filter below 160 Hz. When we increase the proportional gain of the PI controller, we see it starts to ring at 8 kHz, which is the frequency the open-loop transfer function of cavity + feedback crosses -1 in

the Bode plot.

To extend the feedback bandwidth, we use a Labview FPGA to increase the phase margin[63].

We create a second order transfer function by combining a resonance with an anti-resonance

$$F(s) = \frac{s^2 + d\omega_1 s + \omega_1^2}{s^2 + d\omega_2 s + \omega_2^2} \quad (3.7)$$

The physical meaning of the parameters ω_1 , ω_2 , $d\omega_1$, and $d\omega_2$ can be seen more clearly if we take the transform $s = i\omega$. Equation (3.7) becomes

$$F(\omega) = \frac{(\omega_1^2 - \omega^2) + id\omega_1\omega}{(\omega_2^2 - \omega^2) + id\omega_2\omega} \quad (3.8)$$

ω_1 and ω_2 are the center frequencies of the resonance and anti-resonance, $d\omega_1$ and $d\omega_2$ are their widths respectively. If $\omega_1 < \omega_2$, we get a phase increase at frequencies between $\omega_1/2\pi$ and $\omega_2/2\pi$. Alternatively, if $\omega_1 > \omega_2$, we get a phase ‘‘bump’’ at frequencies between $\omega_1/2\pi$ and $\omega_2/2\pi$. The transfer function we implement has $\omega_1/2\pi = 10$ kHz, $d\omega_1/2\pi = 5$ kHz, $\omega_2/2\pi = 20$ kHz, and $d\omega_2/2\pi = 15$ kHz.

The analytical transfer function $F(\omega)$ is then converted into a discrete transfer function $F(z)$ using bilinear transform: $s \rightarrow \frac{2}{T} \frac{z-1}{z+1}$, where T is the sample time. In this implementation, we choose $T = 2.5 \mu\text{s}$, close to the maximal processing speed the FPGA allows. The generated discrete transfer function has the form $F(z) = \frac{a_0 + a_1 z^{-1} + a_2 z^{-2}}{b_0 + b_1 z^{-1} + b_2 z^{-2}}$, with

$$a_0 = 1 + \frac{d\omega_1}{2} T + \left(\frac{\omega_1}{2} T\right)^2$$

$$a_1 = 2\left[\left(\frac{\omega_1}{2} T\right)^2 - 1\right]$$

$$a_2 = 1 - \frac{d\omega_1}{2} T + \left(\frac{\omega_1}{2} T\right)^2$$

$$b_0 = 1 + \frac{d\omega_2}{2} T + \left(\frac{\omega_2}{2} T\right)^2$$

$$b_1 = 2\left[\left(\frac{\omega_2}{2} T\right)^2 - 1\right]$$

$$b_2 = 1 - \frac{d\omega_2}{2}T + \left(\frac{\omega_2}{2}T\right)^2 \quad (3.9)$$

These numerator and denominator coefficients are then sent to an already compiled FPGA VI modified from the FPGA VI example for creating notch filter. This updates the filter in real time. As long as the resulting discrete transfer function can be written in second-order infinite impulse response (IIR) form, this method can also be used for creating other filters that can update in real time.

The measured mag-phase response of the FPGA is shown in Figure 3.10. The phase around 10 kHz is lifted up. Putting this FPGA after the PI controller, the feedback ringing point is extended to 20 kHz, and the maximum proportional gain is increased by a factor of 10.

A feedforward scheme is also used because we have precise information about the upcoming fluctuation. Most of these fluctuations the filter cavity needs to follow are from the low frequency membrane motion. The signal laser follows such fluctuations by its PDH lock. The cooling laser then follows the signal laser using its piezo. Since we know the cooling laser lock signal, we can anticipate the frequency fluctuations coming into the filter cavity, and cancel them by creating the same frequency fluctuations using the filter cavity piezo. This requires a perfect match between the transfer functions of the cooling laser feedback and the filter cavity feedforward in the bandwidth of interest. This is done as shown in Figure 3.11.

In the cooling laser feedback, as mentioned in the last section, the PI controller output goes through an op-amp and a 69 Hz low pass filter. For the filter cavity feedforward, we send the same PI output through a Stanford Research SR540 amplifier to invert the signal. The inverted output then goes to the summing amplifier shared by feedback and a DC offset. Luckily, the amplifiers used in both circuits have flat response in the frequency range we are interested in (20 – 200 Hz). The feedforward gain is adjusted by voltage dividers made of potentiometers. A 0 – 5 k Ω potentiometer is used for large range adjustment, and another 0 – 5 k Ω potentiometer in series with a 100 k Ω resistor is used for fine adjustment. The feedforward phase is adjusted by a 2 – 7 k Ω resistor in front of the 491 nF piezo capacitance. To match the transfer functions, we lock the filter cavity to a free-running cooling laser. We then use a lock-in amplifier to inject sinusoidal signal to the

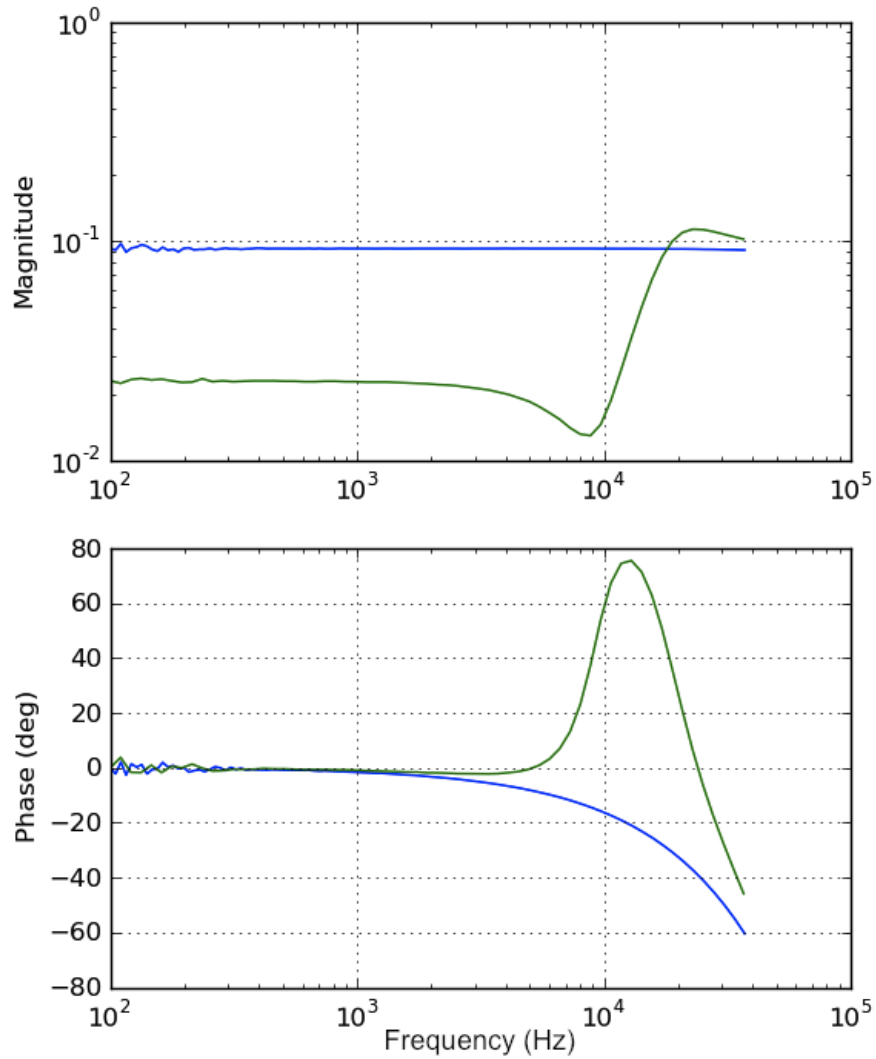


Figure 3.10: Mag-phase plot of the FPGA transfer function measured by lock-in amplifier. The blue curve shows a flat FPGA response when no transfer function is implemented. The green curve shows the response when we implement the phase lead on FPGA. When implemented, the phase edge around 10 kHz is increased by up to 75°.

cooling feedback PI controller input at 100 Hz, and monitor the 100 Hz component of filter cavity feedback error signal with the lock-in amplifier. We then adjust the feedforward gain and phase potentiometers to minimize the lock-in reading. We do this iteratively until we get the optimal feedforward settings. These settings are good over 20 – 200 Hz.

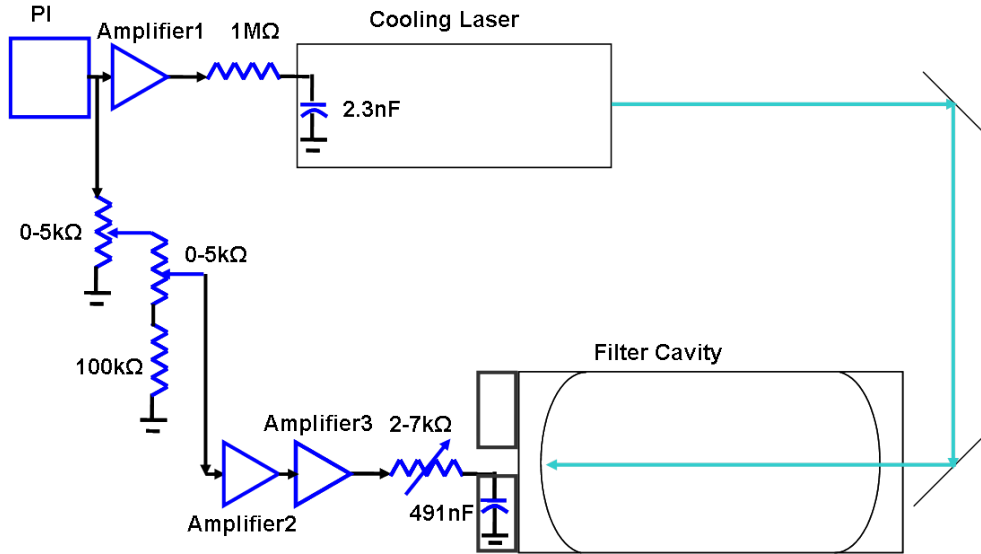


Figure 3.11: Filter cavity feedforward scheme. The PI controller output in the cooling laser feedback is sent to the filter cavity piezo for feedforward. The feedforward gain is adjusted by a 0 – 5 k Ω potentiometer and fine tuned by a 0 – 5 k Ω potentiometer in series with a 100 k Ω resistor. The feedforward phase is adjusted by a 2 – 7 k Ω resistor before the 491 nF piezo capacitance.

Using feedforward and an improved feedback, we are able to lock the filter cavity stably when the lasers are locked to the experimental cavity. As an illustration of the usefulness of the feedforward scheme, in Figure 3.12 we plot the PDH error signal of the signal laser feedback and the filter cavity error signal together. They are on different scales, but we can match many noise peaks below 1 kHz. The feedforward effectively reduced the noise below 500 Hz by at least 2 orders of magnitude.

3.6 Measurement electronics

Signals collected at the reflected and the reference photodiodes are processed by the electronics shown in Figure 3.13. For the reflected photodiode, we are interested in signals at DC, 15 MHz, and 80 MHz. The DC power monitors the cavity coupling and quality of signal beam locking. The 15 MHz beat signal creates the PDH error signal for signal beam locking. It also has mechanical

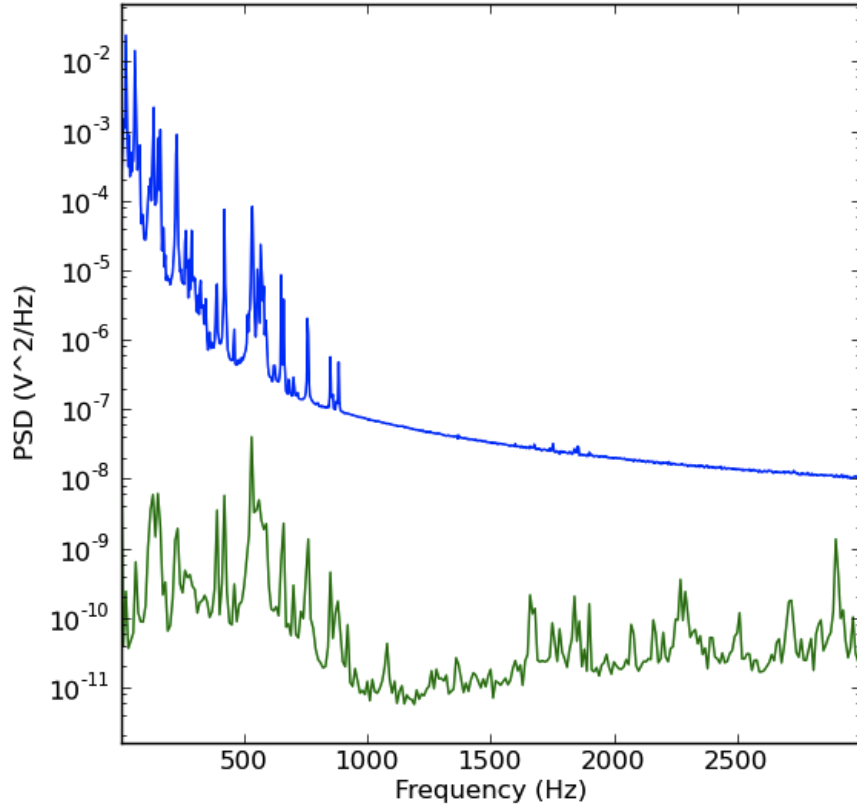


Figure 3.12: Feedforward cancellation of low frequency noise. The blue curve shows the PDH error signal of the signal laser feedback when it is locked to the experimental cavity. The green curve shows the filter cavity PDH error signal when the filter cavity is simultaneously locked to the cooling laser, which is locked to the experiment cavity and the signal laser. The noise peaks below 1 kHz in the two plots match each other. The relative flatness of the green curve below 1 kHz compared to the blue curve is due to feedforward cancellation of low frequency noise from the cooling laser.

motion information imprinted on it at 261 kHz. The 80 MHz signal contains beating of the reflected signal beam and the LO beam, and has motional sidebands on it. It is used to derive the heterodyne spectra described in Chapter 2. For the reference photodiode, we are interested in the signal at 80 MHz, which contains phase and amplitude fluctuations of the LO beam, and is used for correcting the heterodyne spectra.

The reflected DC power is monitored by an oscilloscope. To measure the cavity coupling, we sweep the signal laser piezo and measure the reflected DC power on a DAQ card. A Labview VI synchronizes the frequency sweep with the DAQ card signal. This enables us to optimize the cavity coupling and make sure the cavity input is in the desired polarization.

The 15 MHz signal for the signal beam EOM drive and the mixer local oscillator is generated

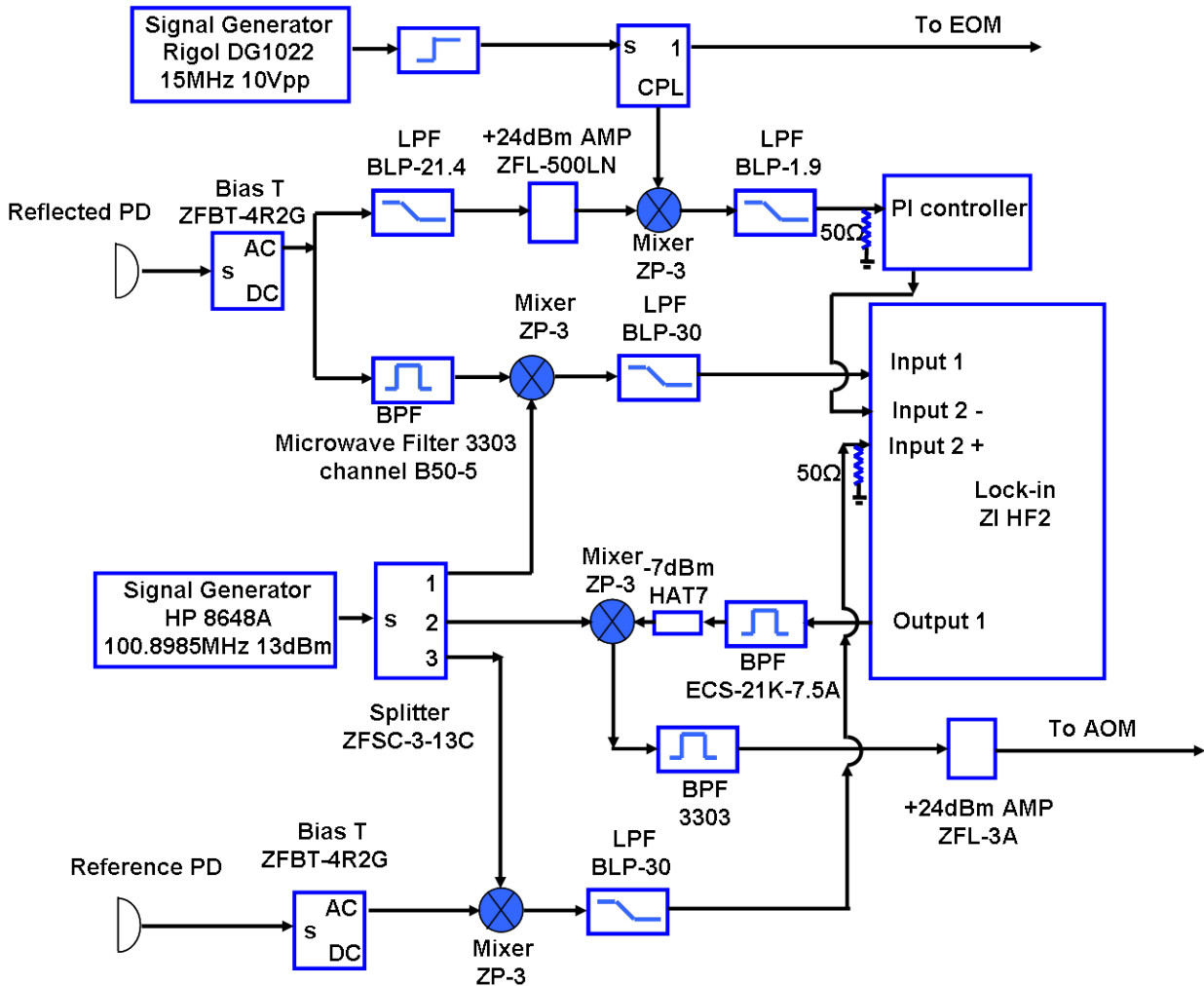


Figure 3.13: Schematic of the measurement electronics. The reflected photodiode (PD) signal is separated into its DC and AC parts at a bias T. Its 15 MHz component is further separated out by a low pass filter (LPF) and mixing with a 15 MHz local oscillator created by a Rigol signal generator. The mixed down signal is used as the PDH error signal for the signal laser feedback, and is also sent to input 2 on the HF2 lock-in amplifier. The reflected signal around 79.5 MHz is separated out by going through a bandpass filter (BPF) and mixed down to 21.3985 MHz by a 100.8985 MHz local oscillator created by an HP RF signal generator. The mixed down signal then goes into the HF2 input 1. The 80 MHz component of the reference photodiode signal is also mixed down to 20 MHz using the same local oscillator and goes to HF2 input 2.

by a Rigol DG1022 signal generator. The heterodyne signals are generated and demodulated using an Zurich Instruments HF2 lock-in amplifier. Because 80 MHz is outside the available range of HF2 outputs, we create a 20 MHz output from HF2 and mix it with a 100 MHz RF signal from an HP 8648A signal generator. The mixed output is sent through an 80 MHz notch filter to filter out unwanted frequency components. It is then amplified and sent to the signal beam AOM. The 80 MHz signals detected by the reflected photodiode and the reference photodiode are also mixed down to 20 MHz and sent back to HF2 inputs.

As shown in Figure 3.13, the reflected signal is first separated at a bias-T into DC and AC components. The 15 MHz signal is picked off by a 22 MHz low pass filter, then amplified by +24 dBm, and mixed down with the 15 MHz local oscillator. The demodulated error signal is filtered at 1.9 MHz and sent to a PI controller for feedback. The 80 MHz signal is singled out by a bandpass filter, then mixed down with the 100 MHz source to 20 MHz, and goes into the HF2 input.

To create a symmetric PDH error signal, we need to adjust the phase of the EOM RF drive. Instead of using a phase shifter, which adds attenuation and noise, we adjust the Rigol frequency slightly around 15 MHz, and use the BNC cable it runs through to create the phase shift we need. For the heterodyne setup, the HF2 output is chosen at 21.3985 MHz to match the center frequency of the ECS-21K-7.5A crystal notch filter. The local oscillator for mixing this signal down to 80 MHz is chosen to be 100.8985 MHz. This is to make the mixed down frequency at 79.5 MHz, the center of the 3303 notch filter passband. We checked the symmetry of the transfer function of the 3303 notch filter with a network analyzer, this eliminated one potential cause for unwanted asymmetry in the mechanical sidebands.

The HF2 lock-in amplifier is used for recording laser cooling measurements. The three inputs and their demodulators are listed in Table 3.1. Demodulators 1 and 2 are in the amplitude modulation (AM) mode, which means they demodulate inputs at frequencies f_{Demod1} , $f_{\text{Demod1}} + f_{\text{Demod2}}$, and $f_{\text{Demod1}} - f_{\text{Demod2}}$. The $f_{\text{Demod1}} + f_{\text{Demod2}}$, and $f_{\text{Demod1}} - f_{\text{Demod2}}$ demodulators have the same phase relation as AM sidebands. Notice because the 20 MHz signal for input 1 is produced by mixing the 80 MHz heterodyne signal and the 100 MHz local oscillator, the upper and lower motional sidebands are flipped in order. Finally, input 1 is in AC and 50Ω mode. Input 2 is in differential mode.

HF2 input	Demodulator	Demodulator frequency	Signal
Channel 1+	1	$f_{\text{Demod1}} = 21.3985 \text{ MHz}$	Reflected heterodyne carrier
Channel 1+	2	$f_{\text{Demod1}} + 261.1 \text{ kHz}$	Heterodyne lower motional sideband
Channel 1+	2	$f_{\text{Demod1}} - 261.1 \text{ kHz}$	Heterodyne upper motional sideband
Channel 2+	1	21.3985 MHz	Reference heterodyne carrier
Channel 2-	3	261.1 kHz	Motional signal of PDH error signal

Table 3.1: HF2 lock-in amplifier inputs and settings.

3.7 Heterodyne data analysis

3.7.1 Heterodyne carrier data analysis

The reference heterodyne carrier is created by the beating of two inputs: the signal beam carrier $\bar{a}_{\text{in,s}}$ and the LO beam carrier $\bar{a}_{\text{in,LO}}e^{i\omega_{\text{IF}}t+\theta(t)}$:

$$|\bar{a}_{\text{in,s}} + \bar{a}_{\text{in,LO}}e^{i\omega_{\text{IF}}t+\theta(t)}|^2 = D.C.terms + 2\bar{a}_{\text{in,s}}\bar{a}_{\text{in,LO}} \cos[\omega_{\text{IF}}t + \theta(t)] \quad (3.10)$$

After mixing with the 100 MHz local oscillator and going through all the electronics to filter out unwanted frequencies, we write the 20 MHz signal to the lock-in input as

$$I_{\text{reference}} = C\bar{a}_{\text{in,s}}\bar{a}_{\text{in,LO}}e^{i(2\pi f_{\text{Demod1}}t-\theta(t)+\theta_{\text{elec}})} \quad (3.11)$$

where $f_{\text{Demod1}} = 21.3985 \text{ MHz}$ is the mixed down frequency of the reference heterodyne signal. θ_{elec} is the additional phase caused by electronic components, and C is the real part of the gain of the electronics.

The demodulator 1 at f_{Demod1} mixes the time trace with $Ae^{i(2\pi f_{\text{Demod1}}t+\theta_1)}$, where θ_1 is the initial phase of the demodulator, and A a constant amplitude. The demodulated reference heterodyne carrier as a complex time trace $Z_{\text{reference}} = X_{\text{reference}}(t) + iY_{\text{reference}}(t)$ is given by

$$Z_{\text{reference}} = AC\bar{a}_{\text{in,s}}\bar{a}_{\text{in,LO}}e^{i(-\theta(t)+\theta_{\text{elec}}-\theta_1)} \quad (3.12)$$

The phase of the demodulated reference heterodyne carrier is therefore

$$\theta_{\text{reference}} = -\theta(t) + \theta_{\text{elec}} - \theta_1 \quad (3.13)$$

Similarly, we can calculate the phase of the reflected heterodyne carrier. Compared to the input signal beam, the reflected signal beam is filtered by $\rho = 1 - \frac{\kappa_L}{\kappa/2 - i\Delta}$. We therefore write the demodulated reflected heterodyne carrier as

$$Z_{\text{reflected}} = AC\bar{a}_{\text{in,s}}\bar{a}_{\text{in,LO}}\rho^* e^{i(-\theta(t)+\theta_{\text{elec1}}-\theta_1)} \quad (3.14)$$

The phase of the reflected heterodyne carrier is

$$\theta_{\text{reflected}} = -\arg(\rho) - \theta(t) + \theta_{\text{elec1}} - \theta_1 \quad (3.15)$$

Here we denote the electronics phase as θ_{elec1} because the signal goes through a different circuit from the reference heterodyne signal.

Subtracting Equation (3.15) from (3.13), we get a detuning dependent calibrated phase

$$\theta_{\text{cal}} = \theta_{\text{reflected}} - \theta_{\text{reference}} = -\arg\left(1 - \frac{\kappa_L}{\kappa/2 - i\Delta}\right) + (\theta_{\text{elec1}} - \theta_{\text{elec}}) \quad (3.16)$$

The electronic phase is a constant offset.

If we plot ρ in phase space, we get a circle as shown in Figure 3.14. It is centered at $1 - \frac{\kappa_L}{\kappa}$, with a radius $\frac{\kappa_L}{\kappa}$. Therefore, when we sweep the signal beam frequency through the cavity resonance, the maximum phase deviation of calibrated phase in (3.16) from the offset $(\theta_{\text{elec1}} - \theta_{\text{elec}})$ is

$$\arg(\rho)_{\text{max}} = \arctan\left(\frac{\kappa_L}{\sqrt{\kappa^2 - \kappa_L^2}}\right) \quad (3.17)$$

When the detuning Δ is small compared to $\kappa/2$, the calibrated phase's deviation from the offset is

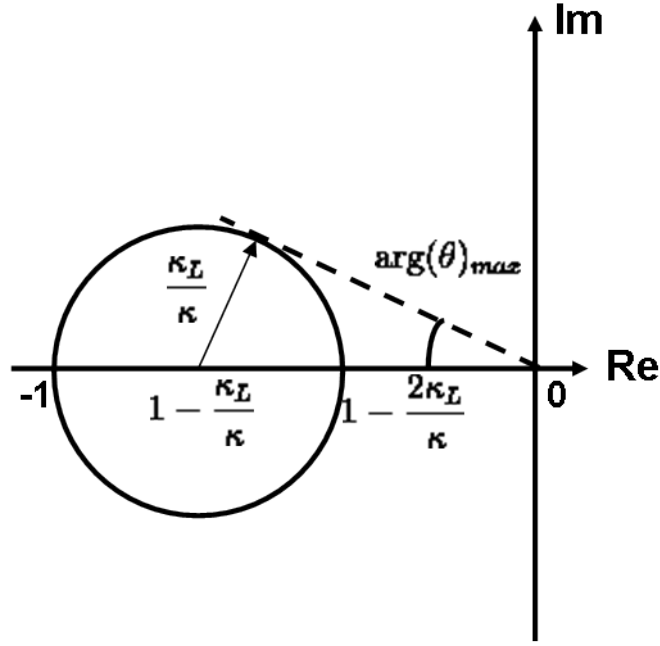


Figure 3.14: Schematic of reflected signal beam phasor ρ .

linear in detuning:

$$\arg(\rho) \simeq \frac{2\kappa_L}{\kappa - 2\kappa_L} \frac{2\Delta}{\kappa} \quad (3.18)$$

Equations (3.16)-(3.18) are used to measure the cavity coupling and to figure out the signal beam detuning.

An example of the sweep measurement is shown in Figure 3.15(a) and (b). We sweep the signal beam frequency through the cavity resonance. The membrane is sitting at a node in the intracavity electrical field, this minimizes the cavity resonant frequency fluctuations caused by membrane position fluctuations. Figure 3.15(a) shows the reflected heterodyne carrier phase $\theta_{\text{reflected}}$, the reference carrier phase $\theta_{\text{reference}}$, and their difference θ_{cal} . Figure 3.15(b) shows a zoom-in of θ_{cal} around the cavity resonance, the phase goes over 26° . From these sweeps, we can also generate the ρ phasor plot in Figure 3.16. Compared to Figure 3.14, we get $\frac{\kappa_L}{\kappa/2} = 0.34$, or $\kappa_L = 0.17\kappa$. The ellipticity is most likely caused by the filter on the HF2 lock-in amplifier.

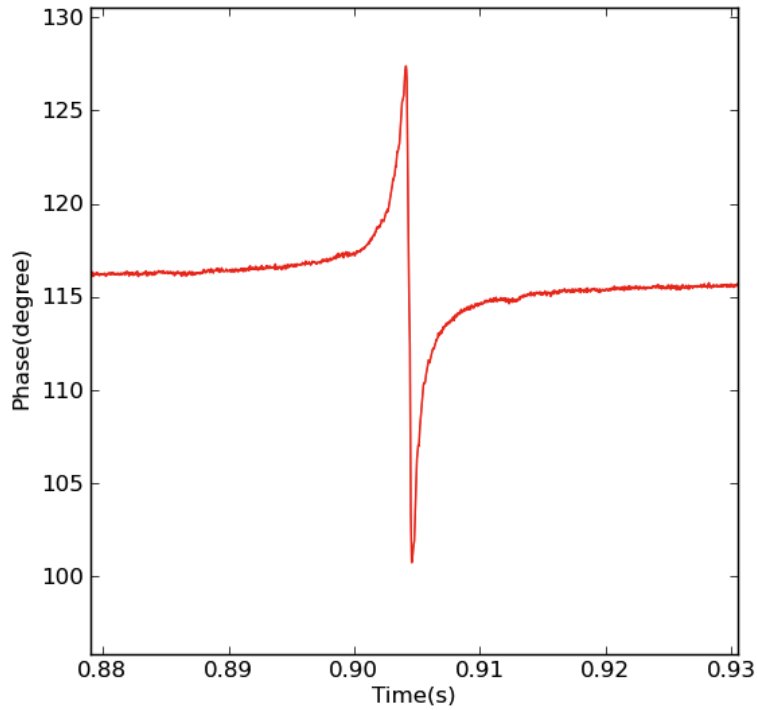
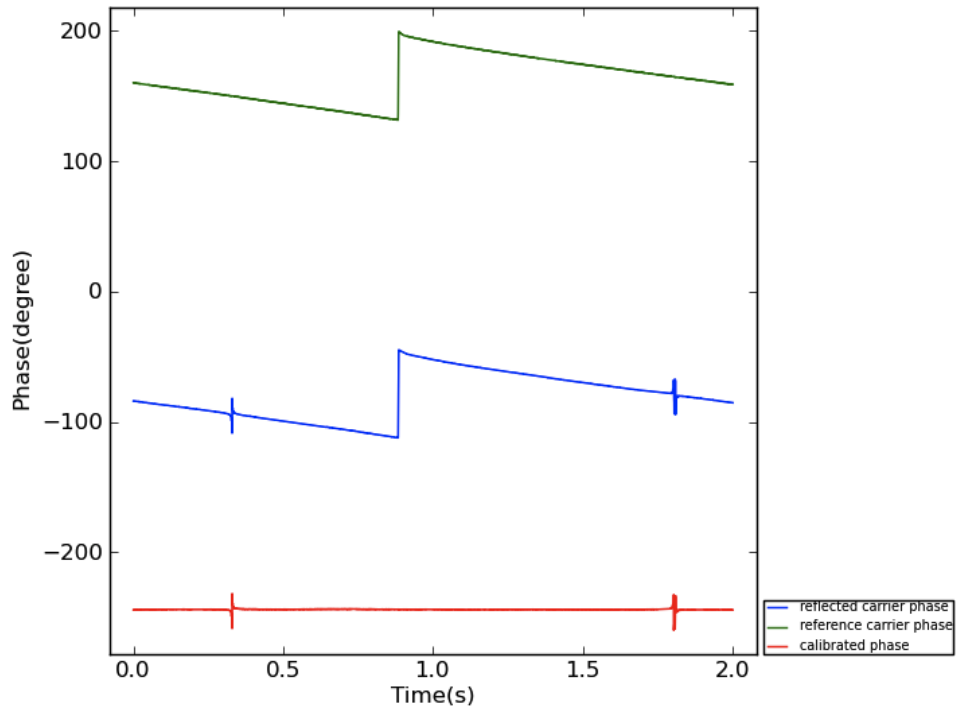


Figure 3.15: Heterodyne carrier phase when the signal beam is swept through cavity resonance. (a) The blue curve is the reflected heterodyne carrier phase, the green curve is the reference carrier phase, the red curve is their difference, the calibrated phase. (b) a zoom-in of the calibrated phase around the cavity resonance.

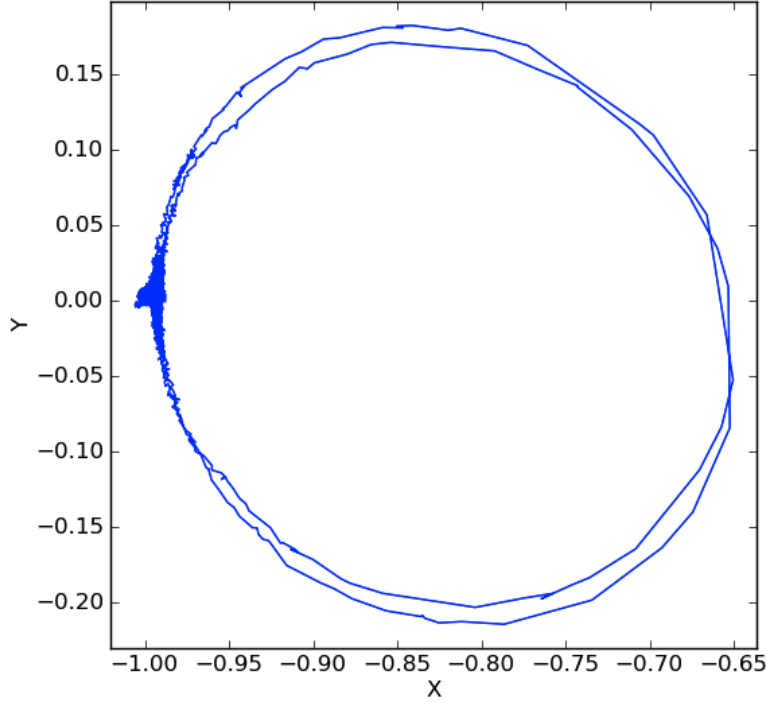


Figure 3.16: Measured reflected signal beam phasor ρ .

3.7.2 Heterodyne power spectrum analysis

Similar to the reflected carrier, the upper and lower sidebands at frequencies $\pm f$ (in the vicinity of $f = \tilde{\omega}_m/2\pi$) in the reflected signal can be written as $a_U[f]e^{-i(2\pi ft + \theta_U)}$ and $a_L[f]e^{-i(-2\pi ft + \theta_L)}$ respectively. Their beat notes with the LO beam are:

$$|a_U e^{-i(2\pi ft + \theta_U)} + \bar{a}_{\text{in,LO}} e^{i\omega_{\text{IF}} t + \theta(t)}|^2 = D.C.terms + 2a_U \bar{a}_{\text{in,LO}} \cos[(\omega_{\text{IF}} + 2\pi f)t + \theta(t) + \theta_U] \quad (3.19)$$

$$|a_L e^{-i(-2\pi ft + \theta_L)} + \bar{a}_{\text{in,LO}} e^{i\omega_{\text{IF}} t + \theta(t)}|^2 = D.C.terms + 2a_L \bar{a}_{\text{in,LO}} \cos[(\omega_{\text{IF}} - 2\pi f)t + \theta(t) + \theta_L] \quad (3.20)$$

Mixing with the 100 MHz local oscillator, the resulting 20 MHz $\pm f$ signals at the lock-in inputs are

$$I_U = C_U a_U \bar{a}_{\text{in,LO}} e^{i[(2\pi f_{\text{Demod1}} - 2\pi f)t - \theta(t) - \theta_U + \theta_{\text{elec,U}}]} \quad (3.21)$$

$$I_L = C_L a_L \bar{a}_{\text{in,LO}} e^{i[(2\pi f_{\text{Demod1}} + 2\pi f)t - \theta(t) - \theta_L + \theta_{\text{elec,L}}]} \quad (3.22)$$

where $C_{U(L)}$ and $\theta_{\text{elec,U(L)}}$ are the gain and phase acquired at the electronics.

Inputs 2 and 3 are demodulated at $(f_{\text{Demod1}} \pm f_{\text{Demod2}})/2\pi$ by mixing $I_{\text{U(L)}}$ with $Ae^{i[2\pi(f_{\text{Demod1}} \pm f_{\text{Demod2}})t + \theta_{2(3)}]}$, where $\theta_{2(3)}$ are the initial phases of the demodulators, and $A_{2(3)}$ the gain of the demodulators. The demodulated complex time traces are

$$Z_2 = A_2 C_L a_L \bar{a}_{\text{in,LO}} e^{i[2\pi(f - f_{\text{Demod2}})t - \theta(t) - \theta_L + \theta_{\text{elec,L}} - \theta_2]} \quad (3.23)$$

$$Z_3 = A_3 C_U a_U \bar{a}_{\text{in,LO}} e^{i[2\pi(f_{\text{Demod2}} - f)t - \theta(t) - \theta_U + \theta_{\text{elec,U}} - \theta_3]} \quad (3.24)$$

The demodulated time traces contain fluctuations in LO beam power and phase. To eliminate these unwanted fluctuations, we can divide (3.23) and (3.24) by (3.12), the resulting normalized sideband time traces are

$$Z'_2 = \frac{A_2 C_L}{AC} \frac{a_L}{\bar{a}_{\text{in,s}}} e^{i[2\pi(f - f_{\text{Demod2}})t - \theta_L + \theta_{\text{elec,L}} - \theta_2 + \theta_1]} \quad (3.25)$$

$$Z'_3 = \frac{A_3 C_U}{AC} \frac{a_U}{\bar{a}_{\text{in,s}}} e^{i[2\pi(f_{\text{Demod2}} - f)t - \theta_U + \theta_{\text{elec,U}} - \theta_3 + \theta_1]} \quad (3.26)$$

To calculate the heterodyne power spectra defined in Equation (2.51), we take Fourier transforms of Z'_2 and Z'_3 and get the sideband PSDs

$$S_2[f] = \frac{1}{\Delta f} |\mathcal{F}\{Z'_2\}|^2 \quad (3.27)$$

$$S_3[f] = \frac{1}{\Delta f} |\mathcal{F}\{Z'_3\}|^2 \quad (3.28)$$

where $\Delta f = \frac{2}{T}$ is the frequency step in PSDs, given by the inverse of half the time trace duration T . For ease of plotting, we flip the upper sideband $S_3[f]$ in frequency. The two PSDs are then fit together using the functional forms

$$S_2[f] = b_2 + \frac{s_2 + a_2(f - f_c + f_{\text{Demod2}})/f_h}{1 + [(f - f_c + f_{\text{Demod2}})/f_h]^2} \quad (3.29)$$

$$S_3[f] = b_3 + \frac{s_3 + a_3(f - f_c + f_{\text{Demod2}})/f_h}{1 + [(f - f_c + f_{\text{Demod2}})/f_h]^2} \quad (3.30)$$

$f_c = \tilde{\omega}_m/2\pi$ is the center frequency of the sideband Fano peaks, f_h is the halfwidth of the Fano

peaks. b_2 and b_3 are proportional to the background b_{rr} and b_{bb} in the lower and upper sideband PSDs. s_2 and s_3 are proportional to the symmetric coefficients s_{rr} and s_{bb} defined by Equations (2.81) and (2.86). a_2 and a_3 are proportional to the anti-symmetric coefficients a_{rr} and $-a_{bb}$ defined by Equations (2.82) and (2.87). Notice because the upper sideband is flipped in frequency, a_3 gets an opposite sign from a_{bb} .

A typical pair of sideband PSDs is shown in Figure 3.17.

3.7.3 Heterodyne cross-correlation spectrum analysis

The heterodyne cross-correlation spectrum is defined in Equation (2.88). To relate it to the demodulated signals, we define $\omega = \delta\omega + \omega_{IF}$, for the upper sideband $\delta\omega \simeq \omega_m$. Equation (2.86) can be rewritten as

$$S_{rb}[\omega] = i^*[\omega]i[\omega - 2\omega_{IF}] = i^*[\delta\omega + \omega_{IF}]i[\delta\omega - \omega_{IF}] = i^*[\delta\omega + \omega_{IF}]i^*[\delta\omega - \omega_{IF}] \quad (3.31)$$

It is the conjugate of the product of the two Fourier transformed sidebands. The last step is valid because $i(t)$ is a real signal, so its Fourier transform satisfies $i[-\omega] = i^*[\omega]$.

Because S_{rb} is a complex quantity, we need to be careful with the phase. There are two factors we need to account for: (1) the time varying LO beam phase $\theta(t)$, and (2) phases from electronics and demodulators. The LO beam phase $\theta(t)$ can be eliminated by normalizing the demodulated signals using the reference signal, as expressed by Equations (3.25) and (3.26). This amounts to setting $\theta = 0$. S_{rb} is related to Z'_2 and Z'_3 by

$$S_{rb}[f] \propto (a_U[f]e^{i\theta_U}a_L[f]e^{i\theta_L})^* = A_{rb}(|\mathcal{F}\{Z'_3\}| \times |\mathcal{F}\{Z'_2\}|)e^{i\theta_{rb}} \quad (3.32)$$

The constant gain A_{rb} only changes the scale of the spectrum, so we can ignore it. But we need to correctly calculate the phase

$$\theta_{rb} = \theta_{elec,L} + \theta_{elec,U} - 2\theta_{elec} - \theta_2 - \theta_3 + 2\theta_1 \quad (3.33)$$

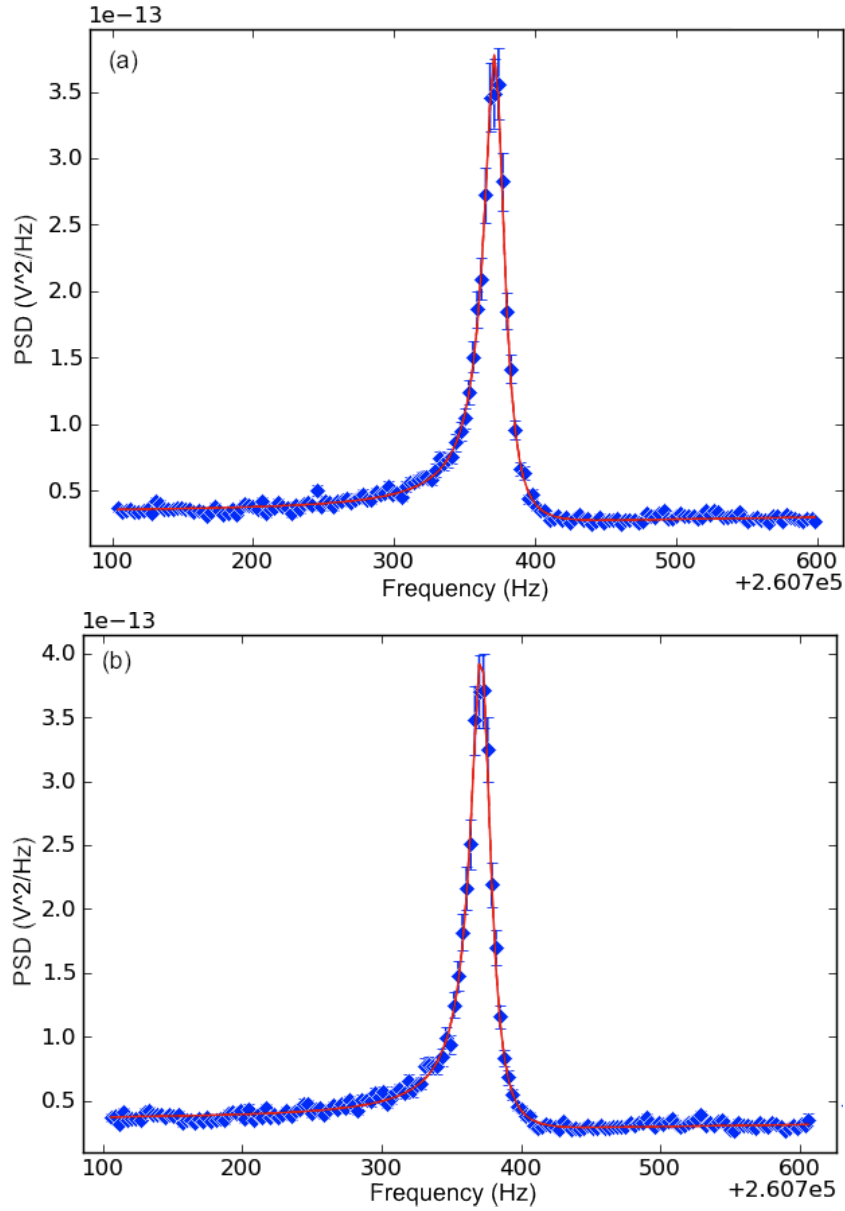


Figure 3.17: A typical pair of heterodyne sideband PSDs fit to Fano lineshapes simultaneously. (a) is the lower sideband S_2 , and (b) is the upper sideband S_3 . The fit parameters as defined in (3.29) and (3.30) are: $f_c = 261.07 \text{ Hz}$, $f_h = 8.81 \text{ Hz}$, $b_2 = 3.249 \times 10^{-14}$, $b_3 = 3.431 \times 10^{-14}$, $s_2 = 3.41 \times 10^{-13}$, $s_3 = 3.59 \times 10^{-13}$, $a_2 = -8.24 \times 10^{-14}$, $a_3 = -8.49 \times 10^{-14}$.

The initial phases of the demodulators are determined by an unknown start time τ by $\theta_1 = 2\pi f_{\text{Demod1}}(t_0 - \tau)$ etc., where t_0 is the start time of a time trace. Therefore

$$\begin{aligned}
& 2\theta_1 - \theta_2 - \theta_3 \\
&= 2 \times 2\pi f_{\text{Demod1}}(t_0 - \tau) - 2\pi(f_{\text{Demod1}} + f_{\text{Demod2}})(t_0 - \tau) - 2\pi(f_{\text{Demod1}} - f_{\text{Demod2}})(t_0 - \tau) \\
&= 0 \quad (3.34)
\end{aligned}$$

This simplifies Equation (3.33) to

$$\theta_{\text{rb}} = \theta_{\text{elec,L}} + \theta_{\text{elec,U}} - 2\theta_{\text{elec}} \quad (3.35)$$

This phase can be calculated by performing a circuit calibration measurement: We use the signal beam EOM to generate PM sidebands at frequencies $\pm f$, with depth of modulation $\beta \ll 1$.

$$\begin{aligned}
a_s &= \bar{a}_s e^{-i[\omega_s t - \beta \sin(2\pi f t + \varphi_{\text{PM}})]} \simeq e^{-i\omega_s t} \bar{a}_s [1 + i \sin(2\pi f t + \varphi_{\text{PM}})] \\
&= e^{i\omega_s t} \bar{a}_s \left[1 + \frac{\beta}{2} e^{i(2\pi f t + \varphi_{\text{PM}})} - \frac{\beta}{2} e^{-i(2\pi f t + \varphi_{\text{PM}})} \right] \quad (3.36)
\end{aligned}$$

with φ_{PM} as the initial phase of the PM tones. A method to verify if the generated modulation is purely PM is described in Section 4.2.2.1. When the signal beam is far off the cavity resonance, it reflects directly off the cavity $a_{\text{refl,s}} = -a_s$. This reflected signal beam beats with the LO beam $a_{\text{LO}} e^{i([\omega_{\text{IF}} t + \theta(t)])}$, on the photodiode we get the signal

$$\begin{aligned}
& | -a_s + a_{\text{LO}} e^{i([\omega_{\text{IF}} t + \theta(t)])} |^2 = \\
&= D.C.term - a_{\text{LO}} e^{i\omega_{\text{IF}} t} \bar{a}_s \left[1 + \frac{\beta}{2} e^{i(2\pi f t + \varphi_{\text{PM}})} - \frac{\beta}{2} e^{-i(2\pi f t + \varphi_{\text{PM}})} \right] + c.c \\
&= D.C.term - a_{\text{LO}} e^{i\omega_{\text{IF}} t} \bar{a}_s \left[1 + \frac{\beta}{2} e^{i(2\pi f t + \varphi_{\text{PM}})} + \frac{\beta}{2} e^{-i(2\pi f t - \varphi_{\text{PM}} - \pi)} \right] + c.c \quad (3.37)
\end{aligned}$$

This photodiode beat signal is mixed down to $20\text{MHz} \mp f$ and demodulated in the same way as described in Section 3.7.2. From Equations (3.25) and (3.26), we get the phases of the two

demodulated PM peaks are

$$\arg(Z'_2) = 2\pi(f - f_{\text{Demod2}})t - \varphi_{\text{PM}} + \theta_{\text{elec,L}} - \theta_{\text{elec}} - \theta_2 + \theta_1 \quad (3.38)$$

$$\arg(Z'_3) = 2\pi(f - f_{\text{Demod2}})t + \varphi_{\text{PM}} + \pi + \theta_{\text{elec,U}} - \theta_{\text{elec}} - \theta_2 + \theta_1 \quad (3.39)$$

Using Equation (3.34), the sum of the two phases is

$$\theta_{\text{Calib}} = \arg(Z'_2) + \arg(Z'_3) = \pi + \theta_{\text{elec,L}} + \theta_{\text{elec,U}} - 2\theta_{\text{elec}} \quad (3.40)$$

We get

$$\theta_{\text{rb}} = \theta_{\text{Calib}} - \pi \quad (3.41)$$

From Equations (3.25) and (3.26), the ratio of the two demodulated PM sideband magnitudes can also be used to calibrate the gain difference between the two demodulators, if the input sideband magnitudes are identical.

$$G_{\text{calib}} = \frac{|Z'_2|}{|Z'_3|} = \frac{A_2 C_L}{A_3 C_U} \quad (3.42)$$

An example of the circuit phase calibration is shown in Figure 3.18. We inject the PM sidebands at the signal beam EOM using an Agilent signal generator. The signal generator frequency is manually swept around $f_{\text{Demod2}} = 261.1$ kHz. The measured average phase of the two PM sidebands gives $\theta_{\text{Calib}}/2$. In Figure 3.18, the phase at frequency f around f_{Demod2} follows a linear relationship:

$$\theta_{\text{Calib}}/2 (^{\circ}) = -51.9 - 0.00013f \text{ (Hz)} \quad (3.43)$$

If the injected sidebands are purely phase modulations, we get

$$\theta_{\text{rb}} (^{\circ}) = -283.8 - 0.00026f \text{ (Hz)} \quad (3.44)$$

The heterodyne cross-correlation spectrum defined in (2.110) can be calculated from FFTs of

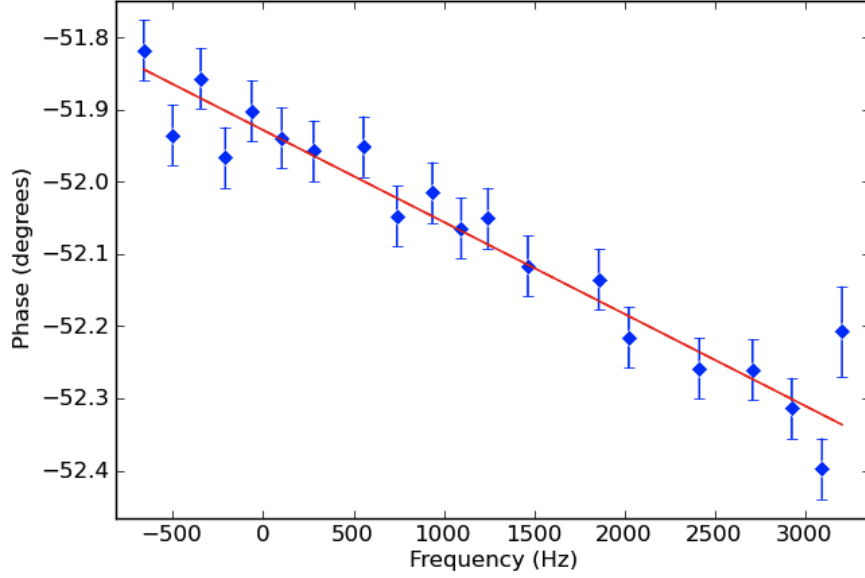


Figure 3.18: Fit of measured PM sideband heterodyne phase $\theta_{\text{Calib}}/2$ as a function of frequency f around $f_{\text{Demod2}} = 261.1$ kHz.

the normalized demodulated time traces:

$$S_{23}[f] = \frac{1}{\Delta f} (\mathcal{F}\{Z'_3\} \times |\mathcal{F}\{Z'_3\}|^*) e^{i\theta_{\text{Calib}} - \pi} \quad (3.45)$$

The real and imaginary parts of $S_{23}[f]$ can be treated as independent variables, they are fit together using the functional forms

$$S_{23,r}[f] = b_{23,r} + \frac{s_{23,r} + a_{23,r}(f - f_c)/f_h}{1 + [(f - f_c)/f_h]^2} \quad (3.46)$$

$$S_{23,i}[f] = b_{23,i} + \frac{s_{23,i} + a_{23,i}(f - f_c)/f_h}{1 + [(f - f_c)/f_h]^2} \quad (3.47)$$

and compared to the terms in Equations (2.110)-(2.113), with the LO beam phase $\theta = 0$ in those formulae.

For the same dataset used to generate Figure 3.17, after correcting the phase using Equation (3.44), we fit the real and imaginary parts of S_{23} with Fano lineshapes. The plots are given in Figure 3.19.

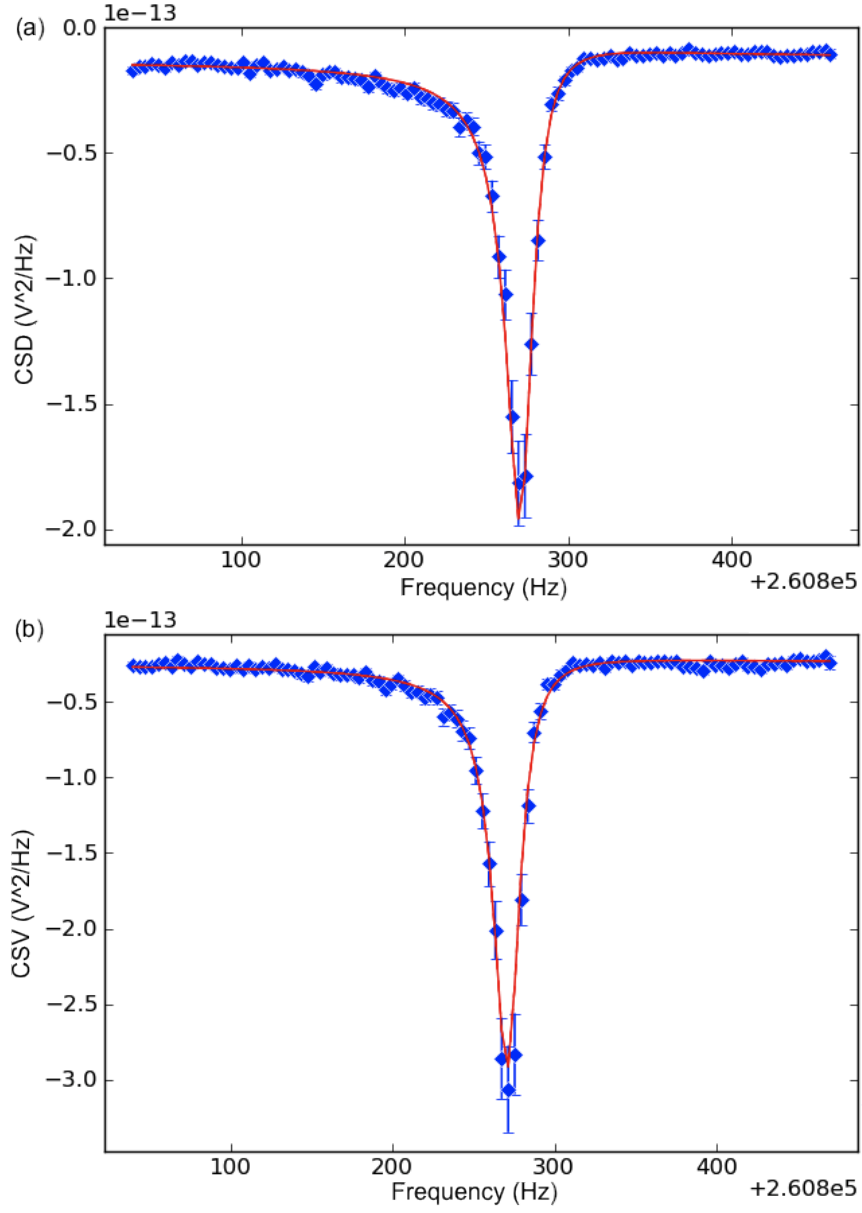


Figure 3.19: Fano fits of S_{23} (a) real and (b) imaginary parts, generated from the same dataset as Figure 3.17. The fit parameters: $f_c = 261.07$ Hz, $f_h = 9.30$ Hz, $b_{23,r} = -1.355 \times 10^{-14}$, $b_{23,i} = -2.535 \times 10^{-14}$, $s_{23,r} = -1.87 \times 10^{-13}$, $s_{23,i} = -2.75 \times 10^{-13}$, $a_2 = 4.77 \times 10^{-14}$, $a_3 = 5.06 \times 10^{-14}$.

Chapter 4

Laser Noise Characterization

As discussed in Section 2.2, to understand our ability to laser cool the membrane's motion, we need to characterize the classical noise of the input beams. The classical amplitude noise of a laser beam can be measured by shining it on a photodiode, while the phase noise is measured using the cavity as a phase discriminator and using the heterodyne signal.

4.1 Laser amplitude noise measurement

The laser amplitude noise is measured directly at a high power level. We then infer the noise at low powers used for cooling by scaling the noise with power P . In Figure 4.1, we plot the measured PSD of the signal beam photodiode signal. $P = 142 \mu\text{W}$ is incident on a PDA10CF photodiode. The photodiode gain is $G = 10^4 \text{ V/A}$, and the responsivity is $R = 0.72 \text{ A/W}$. The measured amplitude noise level is $2.9 \times 10^{-8} \text{ V}^2/\text{Hz}$. The shot noise level is $2PRG^2e = 3.2 \times 10^{-9} \text{ V}^2/\text{Hz}$. This implies the signal laser amplitude noise is 9.0 times above shot noise level at $142 \mu\text{W}$, $C_{\text{xx}} = 9.0/4 = 2.3$. At $1 \mu\text{W}$, $C_{\text{xx}} = 2.3/142 = 0.016$.

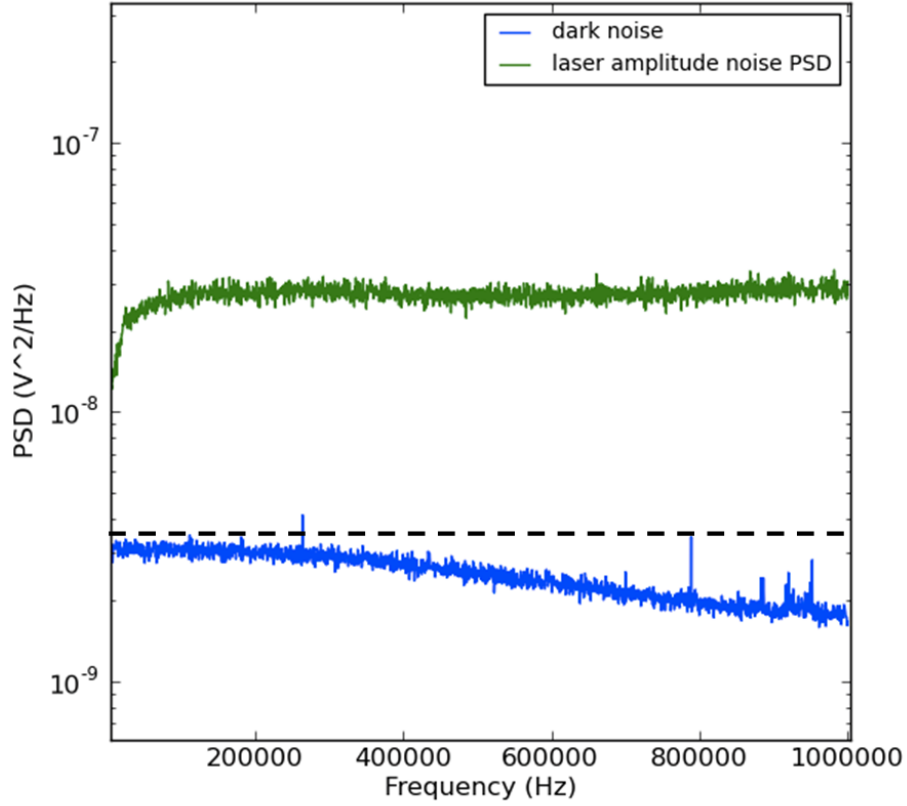


Figure 4.1: PSD of the signal laser amplitude noise. $142 \mu\text{W}$ from the signal beam is incident on a PDA10CF photodiode. The signal is amplified by an SRS 560 amplifier with 10^3 gain, and measured by a DAQ card. The blue curve is the dark noise of the detector. The green curve is the measured amplitude noise PSD. The noise level is $2.9 \times 10^{-8} \text{ V}^2/\text{Hz}$ at 261 kHz. The black dashed line is the expected shot noise level at $142 \mu\text{W}$.

The cooling laser amplitude noise is measured in the same way. Shown in Figure 4.2 is the PSD of the cooling beam photodiode signal. Incident power $P = 158 \mu\text{W}$. The photodiode and gain settings are the same as in the previous measurement. The measured amplitude noise level is $2.0 \times 10^{-8} \text{ V}^2/\text{Hz}$, the shot noise level is $3.65 \times 10^{-9} \text{ V}^2/\text{Hz}$. The cooling laser amplitude noise at $158 \mu\text{W}$ is 5.5 times the shot noise level, $C_{xx} = 1.4$. At $1 \mu\text{W}$, $C_{xx} = 0.0089$.

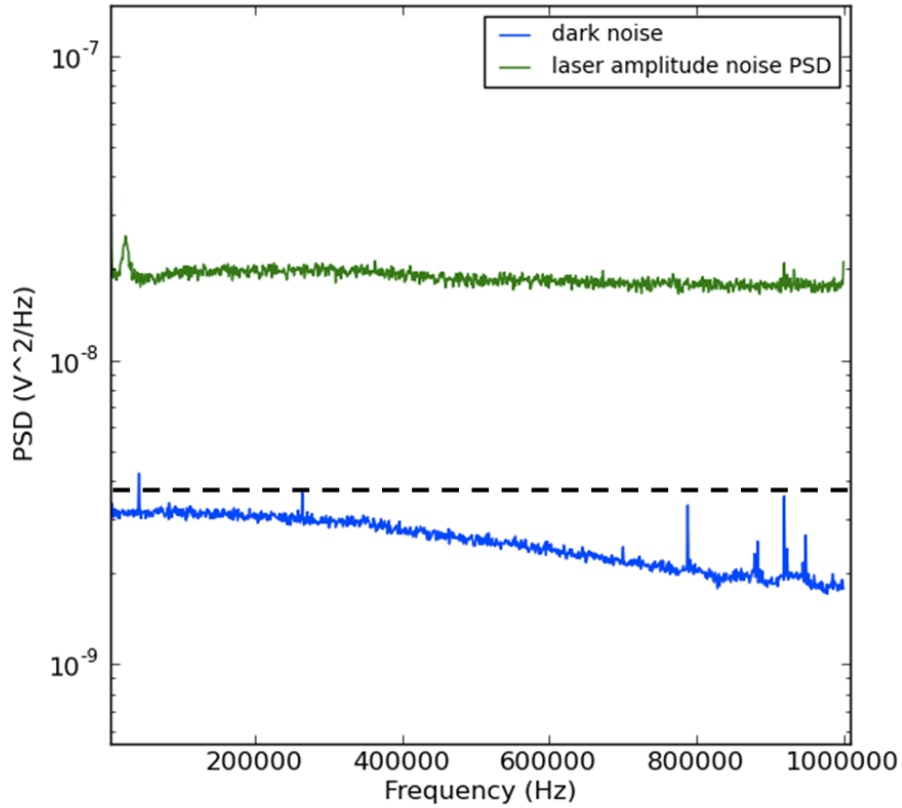


Figure 4.2: PSD of the cooling laser amplitude noise. $158 \mu\text{W}$ from the signal beam is incident on a PDA10CF photodiode, the signal is amplified by an SRS 560 amplifier with gain = 10^3 , and measured by a DAQ card. The blue curve is the dark noise of the detector. The green curve is the measured amplitude noise PSD. The noise level is $2.0 \times 10^{-8} \text{ V}^2/\text{Hz}$ at 261 kHz. The black dashed line is the expected shot noise level at $158 \mu\text{W}$.

4.2 Laser phase noise measurement

4.2.1 Measurement method

The phase noise of an optical field cannot be directly measured with a photodiode. But if we have another optical field as a reference, and beat the two fields using a heterodyne scheme, the fluctuation in the phase difference between the two fields is imprinted on the beat signal, and can be detected by a photodiode. If the reference (in other words, the LO) has negligible phase fluctuation at the frequency of interest, then the fluctuation in the phase difference we measured from the

heterodyne signal is the phase noise of the optical field. Obviously, this method fails if the phase fluctuation we want to measure is common to both optical fields. In this second case, we can use the optical cavity to create difference between the phase fluctuations in the two beams. Here I will show the details of this method.

In the heterodyne power spectra, we look at the background of the heterodyne power spectra at frequency ω , as generalized from Equations (2.70) and (2.85):

$$b_{\text{rr}}[\omega] = 1 + \sigma[(|\rho|^2 + |\kappa_{\text{L}}\chi_{\text{c,s}}[-\omega] - 1|^2)(C_{\text{xx}} + C_{\text{yy}}) - 2\text{Re}[\rho^*(\kappa_{\text{L}}\chi_{\text{c,s}}[-\omega] - 1)](C_{\text{xx}} + 2iC_{\text{xy}} - C_{\text{yy}})] \quad (4.1)$$

$$b_{\text{bb}}[\omega] = 1 + \sigma[(|\rho|^2 + |\kappa_{\text{L}}\chi_{\text{c,s}}[\omega] - 1|^2)(C_{\text{xx}} + C_{\text{yy}}) - 2\text{Re}[\rho^*(\kappa_{\text{L}}\chi_{\text{c,s}}[\omega] - 1)](C_{\text{xx}} + 2iC_{\text{xy}} - C_{\text{yy}})] \quad (4.2)$$

where the factor 1 is the heterodyne detection shot noise, and σ is the quantum efficiency of the photodiode. The various terms with the signal beam classical amplitude noise C_{xx} , phase noise C_{yy} , and their cross correlation C_{xy} contribute to the upper and lower sideband noise floors as a function of signal beam detuning Δ .

When there is no cavity involved, or equivalently the signal beam is far off the cavity resonance, $\Delta = \infty, \rho = 1$. Equations (2.70) and (2.85) simplify to

$$b_{\text{rr}} = b_{\text{bb}} = 1 + 4\sigma C_{\text{xx}} \quad (4.3)$$

The factor of 4 comes from the definitions of Equation (2.4), so that $C_{\text{xx}} = 0.25$ corresponds to a classical amplitude noise at the shot noise level. Phase noise does not contribute to the heterodyne PSDs, because the phase noise is common to both the signal beam and the LO beam, and there is no relative phase fluctuation between the two beating beams.

However, when the signal beam is close to the cavity resonance, we get the C_{yy} terms in the $b_{\text{rr}}, b_{\text{bb}}$ expressions in Equations (4.1) and (4.2). Here the cavity filters the signal beam, and its phase fluctuation is no longer the same as that of the LO beam. The beating between the part of the signal phase noise C_{yy} altered by cavity filtering, expressed by $\kappa_{\text{L}}\chi_{\text{c,s}}[\mp\omega]$ in $b_{\text{rr}}(b_{\text{bb}})$, and the LO carrier, is the signal we detect in the heterodyne power spectra.

To be more quantitative, we look at the coefficients of different noise sources' contributions to the lower sideband PSD background b_{rr} :

1. For phase noise common to both signal and LO beams, denoted as “Common C_{yy} ”, the coefficient is directly extracted from Equation (4.1) as

$$|\rho|^2 + |\kappa_L \chi_{c,s}[-\omega] - 1|^2 + 2\text{Re}[\rho^*(\kappa_L \chi_{c,s}[-\omega] - 1)] \quad (4.4)$$

Physically, $|\rho|^2$ is the beating between the reflected signal beam carrier and the noise in the promptly reflected LO beam. $|\kappa_L \chi_{c,s}[-\omega] - 1|^2$ is the beating between the promptly reflected LO beam carrier and the noise in the reflected signal beam. This noise in the reflected signal beam can be divided into two parts, the cavity filtered part $\kappa_L \chi_{c,s}[-\omega]$ and the promptly reflected part -1 . Finally, $2\text{Re}[\rho^*(\kappa_L \chi_{c,s}[-\omega] - 1)]$ is the interference between the two beating terms.

2. For phase noise only on the signal beam, denoted as “Signal C_{yy} ”, the only term is the beating between the promptly reflected LO beam carrier and the noise in the reflected signal beam. The coefficient is

$$|\kappa_L \chi_{c,s}[-\omega] - 1|^2 \quad (4.5)$$

3. For amplitude noise common to both signal and LO beams, denoted as “Common C_{xx} ”, the coefficient is directly derived from Equation (4.1) as

$$|\rho|^2 + |\kappa_L \chi_{c,s}[-\omega] - 1|^2 - 2\text{Re}[\rho^*(\kappa_L \chi_{c,s}[-\omega] - 1)] \quad (4.6)$$

4. For amplitude noise only on the signal beam, denoted as “Signal C_{xx} ”, the coefficient is the same as for the “Signal C_{yy} ”

$$|\kappa_L \chi_{c,s}[-\omega] - 1|^2 \quad (4.7)$$

5. For the cross noise term on both signal and LO beams, denoted as “Common C_{xy} ”, the coefficient is directly extracted from Equation (4.1) as

$$-4\text{Re}[i\rho^*(\kappa_L \chi_{c,s}[-\omega] - 1)] \quad (4.8)$$

The cross noise term only on the signal beam, “Signal C_{xy} ”, has no contribution to the spectrum.

Similar expressions can be derived for the upper sideband b_{bb} , by replacing $\kappa_L \chi_{c,s}[-\omega]$ with $\kappa_L \chi_{c,s}[\omega]$. We plot the coefficient of these different coefficients as a function of frequency $\omega/2\pi$ in Figure 4.3. Here we assume the signal beam is on resonance with the cavity.

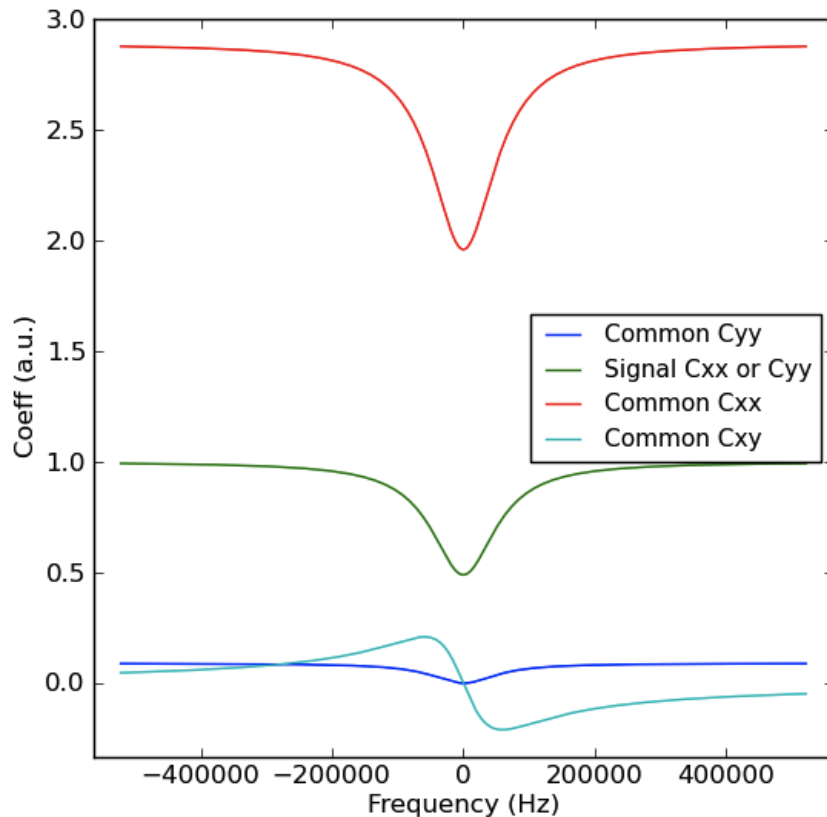


Figure 4.3: S_{rr} noise floor coefficients using experiment parameters $\kappa = 119$ kHz, $\kappa_L = 0.165\kappa$, $\Delta = 0$. At $\omega/2\pi = 261$ kHz, the coefficients for “Common C_{yy} ”, “Signal C_{xx} or C_{yy} ”, “Common C_{xx} ”, and “Common C_{xy} ” are 0.10, 0.97, 2.74, and -0.096 .

To measure the signal laser C_{yy} around 261 kHz, we use a calibrated reference. The method is listed as follows:

(1) We inject a phase modulation (PM) tone at 263 kHz into the EOM in the signal beam path. Since this 263 kHz PM only appears in the signal beam, we can see it directly in the beat signal of the two beams (into a photodiode) on an oscilloscope, and measure its magnitude.

(2) We measure the off resonance and on resonance sideband PSDs. The difference between the two PSD noise floors is due to the phase noise, as described by the “Common C_{yy} ” expression. The PM tone also shows up in both PSDs as a peak. We compare the area under the PM tone peak,

which corresponds to the total power in the PM tone, and scale it to the increased noise floor. This tells us the magnitude of the classical phase noise. Here the assumption is that the C_{yy} contribution is much larger than C_{xx} or C_{xy} and thus is the dominant term for the S_{rr} background change, and we can verify this assumption later.

(3) We calculate the phase shot noise level at the signal beam input power, compare it to the classical phase noise we inferred from step (2), and get the C_{yy} value.

4.2.2 Data analysis

4.2.2.1 Signal laser phase noise characterization

We measure the signal laser phase noise with $2.3 \mu\text{W}$ signal beam power and $333 \mu\text{W}$ LO power going down the ^3He fridge. There is a 15% power loss from the entrance of the fridge to the cavity. The actual input powers are $1.95 \mu\text{W}$ for the signal beam and $283 \mu\text{W}$ for the LO beam.

Injected PM tone To inject a PM tone, a 20 V_{pp} sinusoidal output at 263 kHz from an Agilent signal generator is sent to a coupler to be added with the 15 MHz RF signal sent to the signal beam EOM. The PM tone is measured by recording the reference photodiode signal on an oscilloscope. This time trace is demodulated at 80 MHz, and filtered to get rid of high frequency noise and $< 1 \text{ kHz}$ frequency drift. The fast Fourier transform (FFT) of the resulting normalized time trace plotted in mag-phase is shown in Figure 4.4(a). Its zoom-in for the 263 kHz peak is shown in Figure 4.4(b).

To illustrate the idea of this FFT measurement, we use the same classical picture described in Section 3.7.3. Consider the signal beam $\bar{a}_s e^{-i\omega_s t}$, with PM sidebands at $\pm\omega_{PM}$, and depth of modulation $\beta \ll 1$. The optical field can be written as

$$\begin{aligned} a_s &= \bar{a}_s e^{-i[\omega_s t - \beta \sin(\omega_{PM} t + \varphi_{PM})]} \simeq e^{-i\omega_s t} \bar{a}_s [1 + i \sin(\omega_{PM} t + \varphi_{PM})] \\ &= e^{-i\omega_s t} \bar{a}_s \left[1 + \frac{\beta}{2} e^{i(\omega_{PM} t + \varphi_{PM})} - \frac{\beta}{2} e^{-i(\omega_{PM} t + \varphi_{PM})} \right] \quad (4.9) \end{aligned}$$

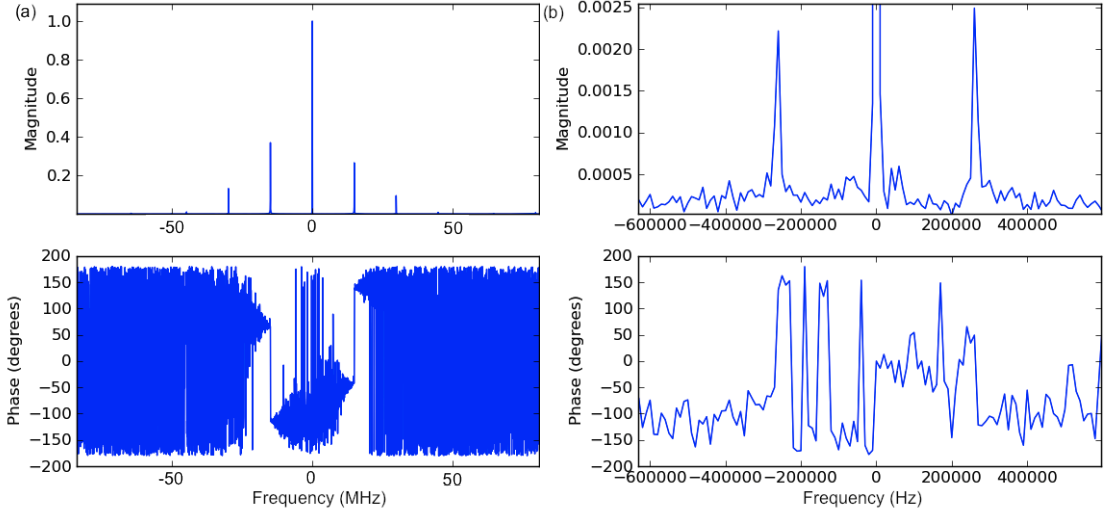


Figure 4.4: (a) FFT of reference photodiode oscilloscope time trace demodulated at 79.91 MHz. The Fourier transformed data is normalized, notice the center peak at 0 is 1. Big peaks show up at multiples of 15MHz . (b) Zoom in of the $\pm 260\text{kHz}$ peaks. The averaged height is 0.0023, the average phase is -90.7° . This confirms the injected noise is almost pure phase modulation, with magnitude 2.3 mrad.

When the signal beam beats with the LO beam $a_{\text{LO}}e^{-i(\omega_s - \omega_{\text{IF}})t}$, on the photodiode we get the signal

$$\begin{aligned}
 |a_s + a_{\text{LO}}|^2 &= ((a_s + a_{\text{LO}}e^{i\omega_{\text{IF}}t})(a_s + a_{\text{LO}}^*e^{-i\omega_{\text{IF}}t})) \\
 &\simeq |a_{\text{LO}}|^2 + a_{\text{LO}}e^{i\omega_{\text{IF}}t}\bar{a}_s[1 + \frac{\beta}{2}e^{i(\omega_{\text{PM}}t + \varphi_{\text{PM}})} - \frac{\beta}{2}e^{-i(\omega_{\text{PM}}t + \varphi_{\text{PM}})}] + c.c \quad (4.10)
 \end{aligned}$$

Demodulating this signal at $\omega_{\text{IF}} = 80\text{MHz}$, we get

$$Aa_{\text{LO}}\bar{a}_s[1 + \frac{\beta}{2}e^{i(\omega_{\text{PM}}t + \varphi_{\text{PM}})} + \frac{\beta}{2}e^{-i(\omega_{\text{PM}}t + \varphi_{\text{PM}} \pm \pi)}]$$

Taking normalized FFT of this signal, we get a center peak 1, and two sideband peaks at $\pm\omega_{\text{PM}}$. The magnitude of the peaks is $\frac{\beta}{2}$, the magnitude of the phase noise, in unit of radians. The average phase of the two sidebands is $(\omega_{\text{PM}}t + \varphi_{\text{PM}} - \omega_{\text{PM}}t - \varphi_{\text{PM}} \pm \pi)/2 = \pm\pi/2$.

The normalized FFT creates a carrier peak with magnitude 1.0. The peaks around $\pm 260\text{kHz}$ are averaged to 2.3×10^{-3} , with an averaged phase -90.7° . The measured data therefore confirms we are injecting a 2.3 mrad phase noise tone at $+260\text{kHz}$.

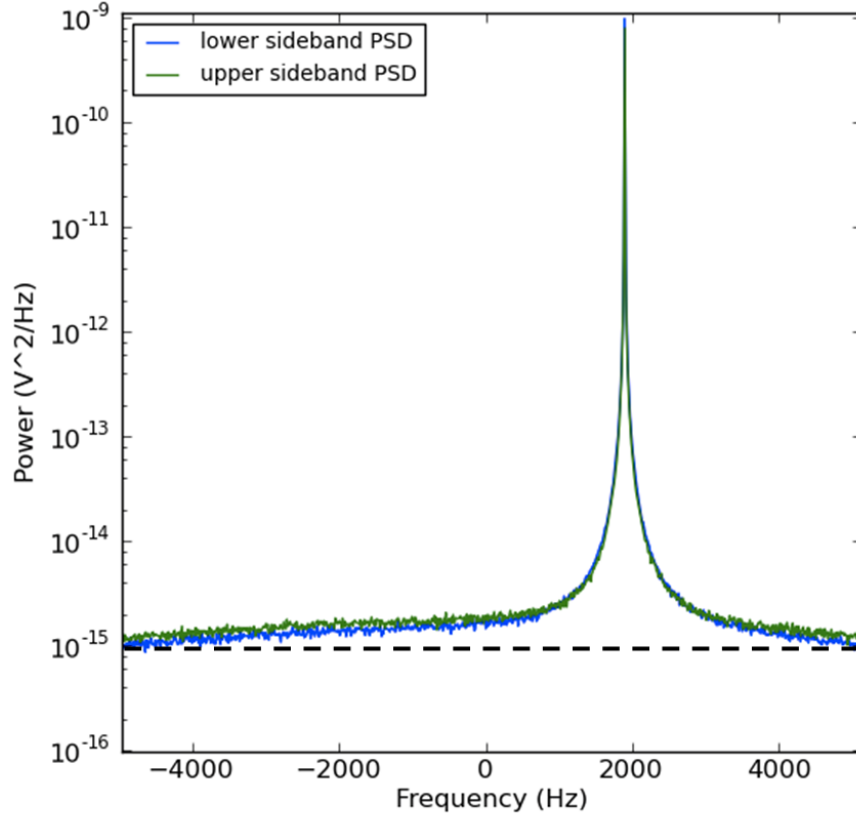


Figure 4.5: Signal laser off resonance heterodyne upper and lower sideband PSDs. The upper sideband PSD (green line) is reversed in frequency to compare with the lower sideband PSD (blue line). The noise floor is $1.8 \times 10^{-15} \text{ V}^2/\text{Hz}$. PM tone peak shows up at 2 kHz. The black dashed line is the inferred detection shot noise level.

Heterodyne PSDs When the signal beam is off resonance, S_{rr} and S_{bb} are plotted in Figure 4.5. The time traces taken are 1 s long, with HF2 settings: 48 dB filter, 7 kHz bandwidth, 28.8 kSample/s. In Figure 4.5, the original PSDs are coarsened by 10 times, the frequency step is 10 Hz. The PM tone peak shows up at 2 kHz. From equation (4.1), the off resonance PSD noise floor is determined by the detection shot noise and the classical amplitude noise. In reality, the noise floor is limited by both photodiode dark noise and heterodyne detection shot noise. The dark noise floor is $1.0 \times 10^{-15} \text{ V}^2/\text{Hz}$. The off resonance noise floor as shown in Figure 4.5 is $1.8 \times 10^{-15} \text{ V}^2/\text{Hz}$. This implies the shot noise level is about $0.8 \times 10^{-15} \text{ V}^2/\text{Hz}$.

S_{rr} and S_{bb} when the signal beam is locked near resonance are shown in Figure 4.6. Subtracting the off resonance noise floor, the average noise floor around the center is $S_{\text{noise floor}} = 1.3 \times 10^{-14} \text{ V}^2/\text{Hz}$, the integrated area for the PM tone is $A_{\text{PM}} = 8.6 \times 10^{-9} \text{ V}^2$. Since the PM

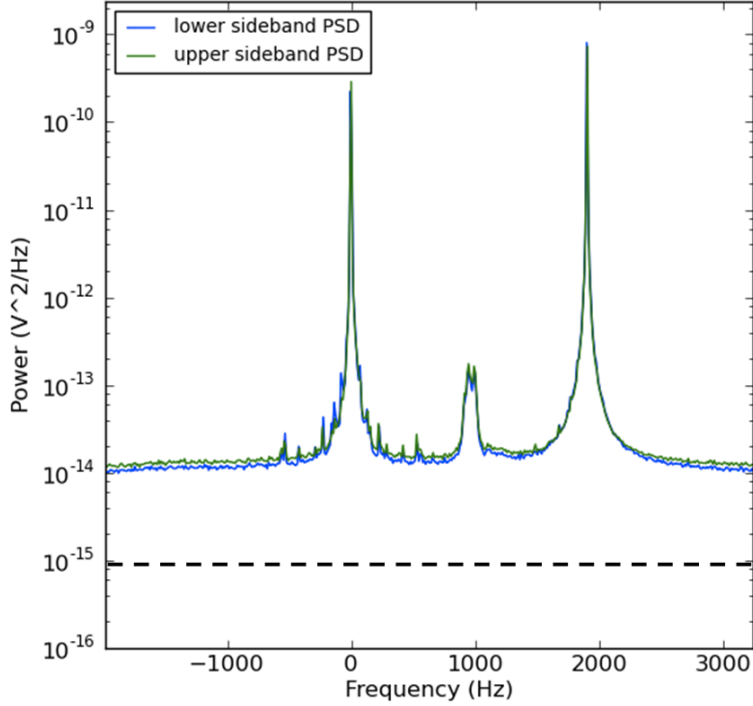


Figure 4.6: Signal laser on resonance heterodyne upper and lower sideband PSDs. The blue curve is the lower sideband PSD, and the green curve is the upper sideband PSD. The upper sideband PSD is reversed in frequency to compare with the lower sideband PSD. For the lower sideband, the noise floor is at $1.4 \times 10^{-14} \text{ V}^2/\text{Hz}$. The PM tone peak integrated area is $8.7 \times 10^{-9} \text{ V}^2$. For the upper sideband, the noise floor is at $1.6 \times 10^{-14} \text{ V}^2/\text{Hz}$. The PM tone peak integrated area is $8.5 \times 10^{-9} \text{ V}^2$. The peak around 0 Hz is the motional sideband, the peak around 1 kHz is due to signal laser phase noise. The black dashed line is the inferred detection shot noise level.

tone is only on the signal beam, whereas the phase noise floor is common to both beams, they contribute to the heterodyne PSDs with different coefficients as shown in Figure 4.3. Taking this into consideration, the phase noise floor is

$$S_{\phi\phi} = (2.3 \text{ mrad})^2 \times \frac{S_{\text{noise floor}}}{A_{\text{PM}}} \times \frac{0.97}{0.10} = 7.8 \times 10^{-11} \text{ rad}^2/\text{Hz}$$

At $1.95 \mu\text{W}$, the phase shot noise is $1/n = \hbar\omega/P = 9.57 \times 10^{-14} \text{ rad}^2/\text{Hz}$. This means the signal laser phase noise is 820 times above shot noise level in power at $1.95 \mu\text{W}$, or $C_{yy} = 204$ at $1.95 \mu\text{W}$. The frequency noise at $f = 261 \text{ kHz}$ can also be calculated as $S_{\dot{\phi}\dot{\phi}} = f^2 S_{\phi\phi} = 5.4 \text{ Hz}^2/\text{Hz}$.

Finally, the number we get is consistent with our assumption that C_{xx}, C_{xy} contributions are much smaller. As measured independently, we know $C_{xx} < 1$ at $1.95 \mu\text{W}$ and C_{xy} is limited by the

inequality for classical noise terms $C_{xx} \leq \sqrt{C_{xx}C_{yy}}$. The ratio between C_{yy} and C_{xx} , C_{xy} coefficients are 0.03 and 0.96 respectively. Taking these into consideration, C_{xx} , C_{xy} contributions are smaller than $1 \times 10^{-16} \text{ V}^2/\text{Hz}$ on the PSDs.

As a sanity check, we also calculate the heterodyne detection shot noise. The quantum efficiency of the PDA10CF photodiode used for detection is $\sigma_0 = 0.84$, counting in the extra 15% loss from the cavity to the photodiode, the total detection efficiency $\sigma = \sigma_0(1 - 15\%) = 0.71$. From Equations (4.1) and (4.2), the shot noise inferred from the C_{yy} value is

$$S_{\text{noise floor}}/(\sigma C_{yy} \times 0.1) = 8.8 \times 10^{-16} \text{ V}^2/\text{Hz}$$

consistent with the difference between the observed off resonance noise floor and the dark noise floor.

4.2.2.2 Cooling laser phase noise characterization

Similarly, we measure the cooling laser phase noise by sending its output to the signal HD and PDH setup. At the Helium fridge entrance, the cooling “signal beam” is $1.9 \mu\text{W}$ and the “LO beam” is $535 \mu\text{W}$. Counting the 15% power loss, the actual input powers are $1.62 \mu\text{W}$ for “signal beam” and $455 \mu\text{W}$ for “LO beam”.

The Agilent signal generator sends a 20 V_{pp} sinusoidal output at 263 kHz to the “signal beam” EOM. This creates the PM tone at 263 kHz . Its magnitude is measured with the reference photodiode, the FFT of the demodulated time trace is shown in Figure 4.7. The measured PM tone magnitude is 2.2 mrad .

The off resonance noise floor at the center is $2.3 \times 10^{-15} \text{ V}^2/\text{Hz}$, as shown in Figure 4.8. The detection dark noise is still $1.0 \times 10^{-15} \text{ V}^2/\text{Hz}$. The detection shot noise is therefore expected to be $1.3 \times 10^{-15} \text{ V}^2/\text{Hz}$. The near resonance power spectra are shown in Figure 4.9. The average PM tone integrated area $A_{\text{PM}} = 1.1 \times 10^{-8} \text{ V}^2$. After subtracting the off resonance noise floor, the

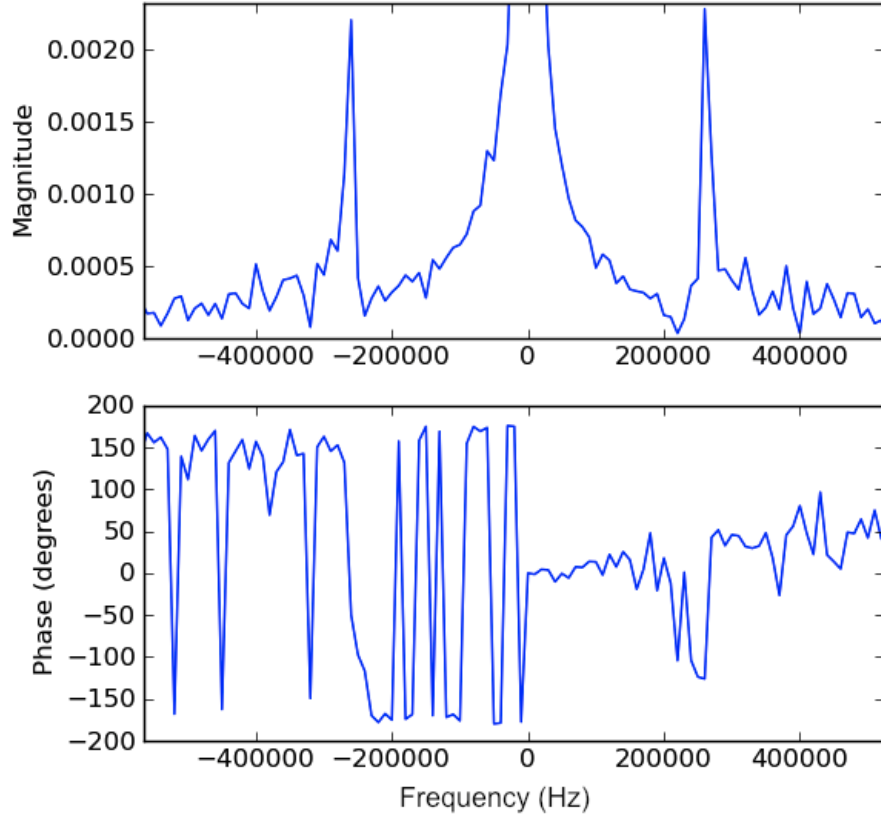


Figure 4.7: FFT of reference photodiode oscilloscope time trace demodulated at 79.91 MHz, zoomed in at the ± 260 kHz peaks. The averaged height is 0.0022, the averaged phase is -87.9° . This confirms the injected noise is almost pure phase modulation, with magnitude 2.2 mrad.

average noise floor at the center is $S_{\text{noise floor}} = 1.08 \times 10^{-14} \text{ V}^2/\text{Hz}$. The phase noise floor is

$$S_{\phi\phi} = (2.2 \text{ mrad})^2 \times \frac{S_{\text{noise floor}}}{A_{\text{PM}}} \times \frac{0.973}{0.10} = 4.5 \times 10^{-11} \text{ rad}^2/\text{Hz}$$

At $1.62 \mu\text{W}$, the phase shot noise is $1.15 \times 10^{-13} \text{ rad}^2/\text{Hz}$. Therefore the cooling laser phase noise at $1.62 \mu\text{W}$ is 460 times above shot noise level, or $C_{yy} = 98$ at $1.62 \mu\text{W}$. The cooling laser frequency noise at $f = 261 \text{ kHz}$ is $S_{\dot{\phi}\dot{\phi}} = f^2 S_{\phi\phi} = 3.1 \text{ Hz}^2/\text{Hz}$.

Notice the noise floor around 261 kHz is not flat, but varies over nearly an order of magnitude from -2 kHz to $+5 \text{ kHz}$. This is different from the assumption of flat classical noise used in the effective phonon number expression (2.42). However, for the measurements described in this thesis, the mechanical linewidths are relatively small ($\leq 200 \text{ Hz}$). Over such small frequency range, we can still treat the classical cooling laser noise as flat and use Equation (2.42). On the other hand,

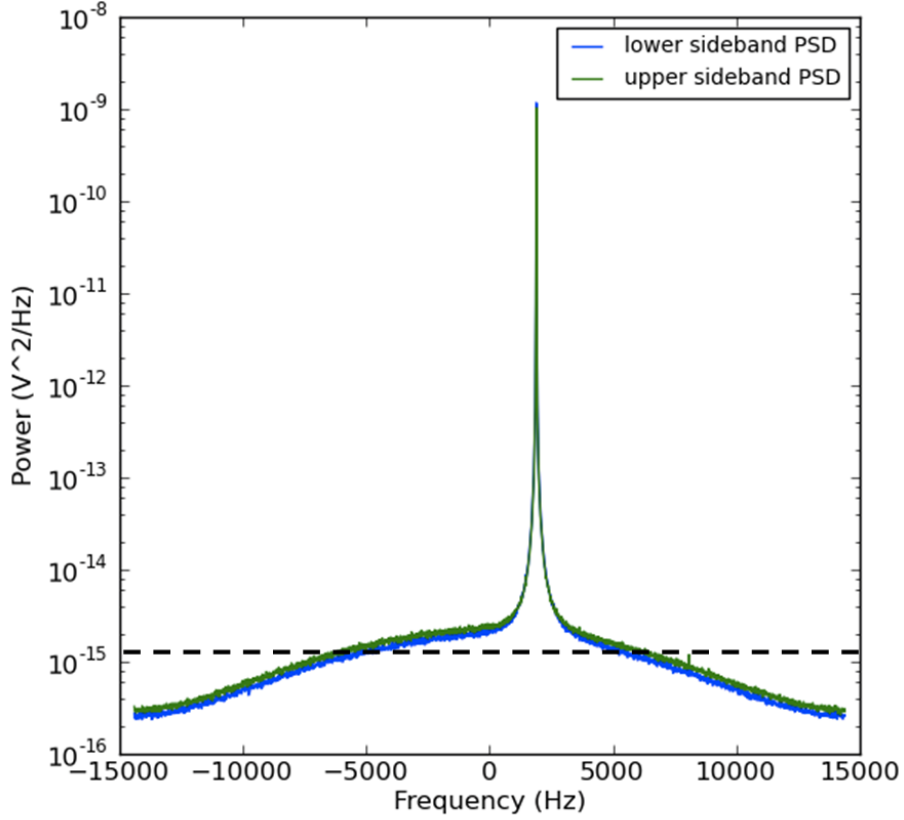


Figure 4.8: Cooling laser off resonance heterodyne upper and lower sideband PSDs. The blue curve is the lower sideband PSD, and the green curve is the upper sideband PSD. The upper sideband PSD is reversed in frequency to compare with the lower sideband PSD. The noise floor around 0 Hz is $2.3 \times 10^{-15} \text{ V}^2/\text{Hz}$. The noise floor roll-off is due to the 7 kHz low pass filters in the HF2. The black dashed line is the inferred detection shot noise level.

because the cooling laser noise does not alter the heterodyne spectra, the heterodyne detection theory described in Section 2.3 is not affected.

As a sanity check, we look at the inferred shot noise level. The measured C_{yy} implies the shot noise level is

$$S_{\text{noise floor}}/(\sigma C_{yy} \times 0.10) = 1.4 \times 10^{-15} \text{ V}^2/\text{Hz}$$

in agreement with the difference in measured off resonance PSD noise floor and dark noise floor. According to Equations (2.61) and (2.81), the dark noise is proportional to the LO beam power $p\bar{a}_{\text{in},s}^2$. In the previous section, the signal beam detection shot noise was inferred to be $8.8 \times 10^{-16} \text{ V}^2/\text{Hz}$. Scaled by the LO beam powers in the two measurements, the expected cooling detection shot noise

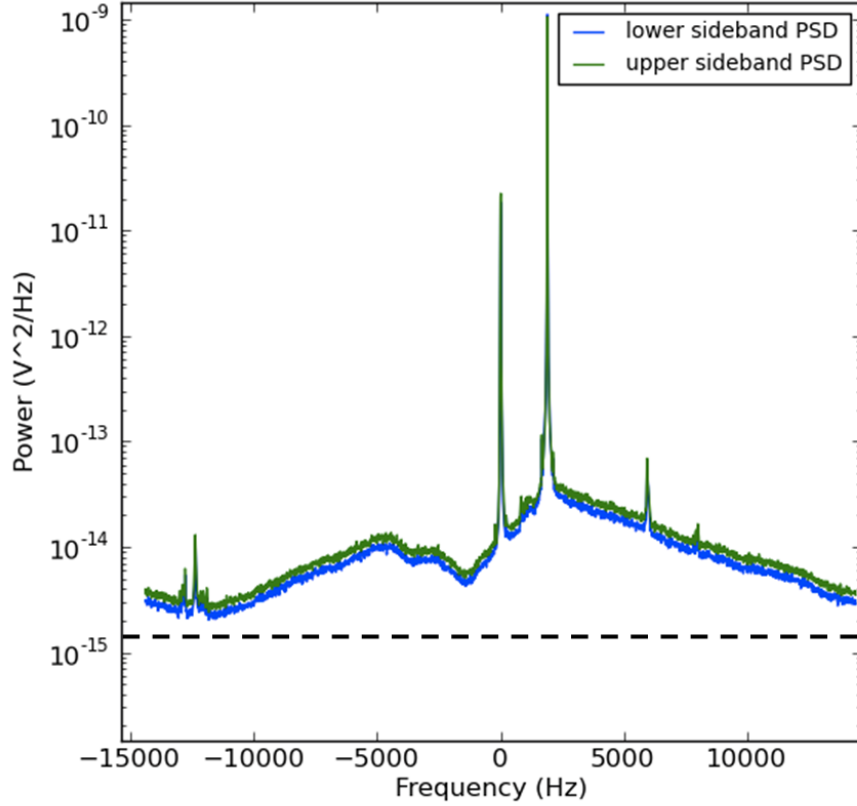


Figure 4.9: Cooling laser on resonance heterodyne upper and lower sideband PSDs. The blue curve is the lower sideband PSD, and the green curve is the upper sideband PSD. The upper sideband PSD is reversed in frequency to compare with the lower sideband PSD. For the lower sideband, the noise floor around 0 Hz at $1.3 \times 10^{-14} \text{ V}^2/\text{Hz}$. The PM tone peak integrated area is $1.1 \times 10^{-8} \text{ V}^2$. For the upper sideband, the noise floor at $1.2 \times 10^{-14} \text{ V}^2/\text{Hz}$. The PM tone peak integrated area is $1.07 \times 10^{-9} \text{ V}^2$. The peak around 0 kHz is the motional sideband. The overall roll-off at higher frequencies is due to the 7 kHz low pass filters in the HF2. The black dashed line is the inferred detection shot noise level.

level is

$$8.8 \times 10^{-16} \text{ V}^2/\text{Hz} \times \frac{535 \mu\text{W}}{333 \mu\text{W}} = 1.4 \times 10^{-15} \text{ V}^2/\text{Hz}$$

consistent with our measured value.

4.3 Filtered cooling laser phase noise characterization

As shown in the previous section, both lasers have excessive phase noise around the mechanical resonant frequency $\omega_m/2\pi = 261 \text{ kHz}$, limiting the minimum phonon number we can reach. As mentioned in Section 3.5, a filter cavity is built and can be inserted into the cooling beam path.

Here we show the filter cavity described indeed filters the cooling laser noise as predicted by theory. For the laser cooling data presented in this thesis, the filter cavity is not employed, but it will be a useful improvement for future experiments.

4.3.1 Theoretical predictions of filter cavity performance

The filter cavity linewidth is $\kappa_f/2\pi = 22$ kHz. According to Equation (2.140), we expect the classical noise at $\omega_m/2\pi = 261$ kHz to be filtered by a factor of $(\frac{2\omega_m}{\kappa_f})^2 = 563$ in a single pass. Because the filter cavity is not locked perfectly on resonance, we also need to consider the added transmitted amplitude noise caused by input phase noise. In reality, when locked to the experimental cavity, the filter cavity transmitted power average fluctuation is less than 5%, implying a detuning less than 2 kHz. Using Equation (2.141), the equivalent input amplitude noise caused by phase noise at $1 \mu\text{W}$ is less than

$$\frac{\Delta^2}{(\kappa_f/2)^2 + \omega^2} C_{yy,\text{in}} = \frac{(2 \text{ kHz})^2}{(11 \text{ kHz})^2 + (261 \text{ kHz})^2} \times 61 = 0.0036$$

small compared to $C_{xx,\text{in}} = 0.0089$. The equivalent input phase noise caused by amplitude noise is negligible. Therefore there is no need to worry about the added noise due to the cavity detuning.

4.3.2 Measurements of filter cavity performance

The filtered cooling beam phase noise is measured by dividing it into two beams. One passes through an EOM and serves as the “signal beam”. The other goes through an AOM and is shifted in frequency to produce the “LO beam”. The phase noise can then be measured using the same methods mentioned above. Since the phase noise is expected to be greatly reduced, we increase the “signal beam” power by 10 times, sending its output to the signal HD and PDH setup. At the Helium fridge entrance, the “signal beam” is $20.6 \mu\text{W}$ and the LO beam is $302 \mu\text{W}$. Counting the 15% power loss, the actual input powers are $17.5 \mu\text{W}$ for the signal beam and $257 \mu\text{W}$ for the LO beam.

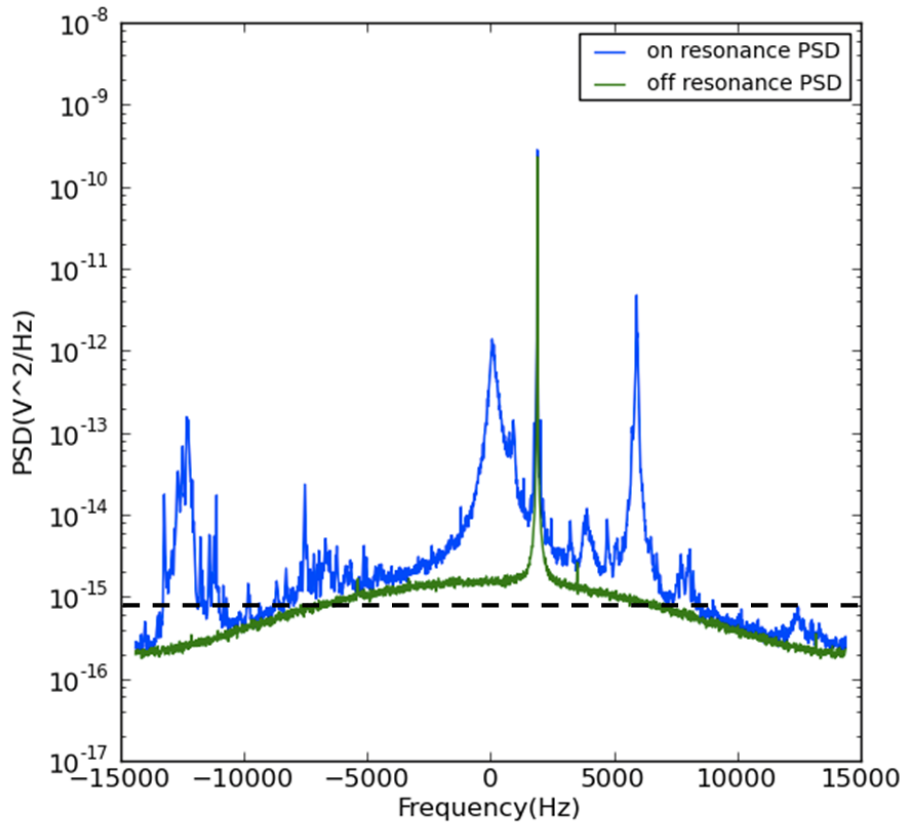


Figure 4.10: Heterodyne lower sideband PSD of filtered cooling laser. The green curve is the off resonance power spectrum. The blue curve is the on resonance power spectrum. The PM tone peak integrated area is $2.6 \times 10^{-9} \text{ V}^2$. Around 0 Hz , the noise floor change from off resonance to on resonance is about $1 \times 10^{-16} \text{ V}^2/\text{Hz}$. The broad peak around 0 kHz is the mechanical sideband. The other noise peaks are likely due to frequency fluctuations caused by an imperfect lock. The overall roll-off is due to the HF2 7 kHz low pass filters. The black dashed line is the inferred detection shot noise level.

A $0.2 \text{ V}_{\text{pp}}$ sinusoidal output at 263 kHz is sent to a Thorlabs EO-PM-NR-C2 EOM to create the PM tone. The measured PM tone magnitude is 0.45 mrad . The PM tone magnitude is different from those used in Section 4.2.2 because a different EOM is used here. The PSD of the lower sideband is plotted in Figure 4.10. The PM tone integrated area $A_{\text{PM}} = 2.6 \times 10^{-9} \text{ V}^2$. The off resonance noise floor is $1.7 \times 10^{-15} \text{ V}^2/\text{Hz}$. This implies a shot noise level of $0.7 \times 10^{-15} \text{ V}^2/\text{Hz}$. Because the phase noise is no longer significantly higher than the dark noise floor, it is difficult to extract a precise noise floor change near the motional peak around 0 Hz . But we could estimate the

noise floor change due to phase noise is about $S_{\text{noise floor}} = 1 \times 10^{-16} \text{ V}^2/\text{Hz}$. The phase noise level is then

$$S_{\phi\phi} = (0.45 \text{ mrad})^2 \times \frac{S_{\text{noise floor}}}{A_{\text{PM}}} \times \frac{0.973}{0.10} = 7 \times 10^{-14} \text{ rad}^2/\text{Hz}$$

At $17.5 \mu\text{W}$, the phase shot noise is $1.06 \times 10^{-14} \text{ rad}^2/\text{Hz}$. Therefore the cooling laser phase noise at $17.5 \mu\text{W}$ is about 7 times above shot noise level, or $C_{yy} = 1.8$ at $17.5 \mu\text{W}$. The cooling laser frequency noise at $f = 261 \text{ kHz}$ is $S_{\dot{\phi}\dot{\phi}} = f^2 S_{\phi\phi} = 0.005 \text{ Hz}^2/\text{Hz}$. Compared to the unfiltered cooling beam, the phase noise or frequency noise at 261 kHz is about 590 times smaller, in agreement with the theoretical prediction of 563 times reduction in Section 2.5.

The inferred shot noise level from C_{yy} is

$$S_{\text{noise floor}}/(\sigma C_{yy} \times 0.10) = 8 \times 10^{-16} \text{ V}^2/\text{Hz}$$

also in agreement with the measured value.

4.4 Summary

Finally, the classical noise levels of the signal laser, the unfiltered cooling laser, and the filtered cooling laser are summarized in Table 4.1.

The measured signal and cooling laser frequency noise at 261 kHz are $5.4 \text{ Hz}^2/\text{Hz}$ and $3.1 \text{ Hz}^2/\text{Hz}$ respectively. According to Equation (1.8), if we assume a white frequency noise spectrum, the inferred linewidths are 2.7 Hz and 1.6 Hz . This is much smaller than the laser linewidth $\Gamma_1/2\pi < 1 \text{ kHz}$ specified by the laser manufacturer. However, the measured results are consistent with the spec'd 1 kHz linewidth if the correlation bandwidth $\gamma_c/2\pi \simeq 12 \text{ kHz}$ in Equation (1.7).

	Phase noise	Frequency noise	C_{yy} at $1 \mu\text{W}$	C_{xx} at $1 \mu\text{W}$
Signal laser	$7.8 \times 10^{-11} \text{ rad}^2/\text{Hz}$	$5.4 \text{ Hz}^2/\text{Hz}$	105	0.016
Unfiltered cooling laser	$4.5 \times 10^{-11} \text{ rad}^2/\text{Hz}$	$3.1 \text{ Hz}^2/\text{Hz}$	61	0.0089
Filtered cooling laser	$7 \times 10^{-14} \text{ rad}^2/\text{Hz}$	$0.005 \text{ Hz}^2/\text{Hz}$	0.1	2×10^{-5}

Table 4.1: Summary of classical phase and amplitude noise at 261 kHz of the signal laser, unfiltered cooling laser, and filtered cooling laser.

Chapter 5

Preliminary laser cooling results and discussions

In this Chapter, I will first present optomechanical measurements when the cooling beam detuning is varied. Then I will look at laser cooling. A section is devoted to discuss how the measured laser phase noises limit the minimum phonon number achievable and change the heterodyne spectra. Finally, preliminary laser cooling results varying the cooling beam power and the signal beam detuning are presented.

5.1 Optomechanics as a function of cooling beam detuning

First we look at the frequency shift and linewidth change of the mechanical resonance when we vary the cooling beam detuning at a constant power. The signal beam is locked near the experimental cavity resonance. Its input power is $P_{\text{in},s} = 2.00 \mu\text{W}$, counting 15% loss from the fridge entrance to the cavity. The cooling beam is then brought close to resonance with a different cavity longitudinal mode, using the cooling beam lock described in Section 3.4. The cooling beam detuning is tuned by changing the RF drive frequency of an AOM in its beam path.

At a certain cooling beam detuning, we measure the sideband heterodyne PSDs. As described by Equations (3.29) and (3.30), we can fit the two PSDs simultaneously and extract the Fano peak center frequency f_c and halfwidth f_h . A pair of sideband PSDs from the dataset is shown in Figure

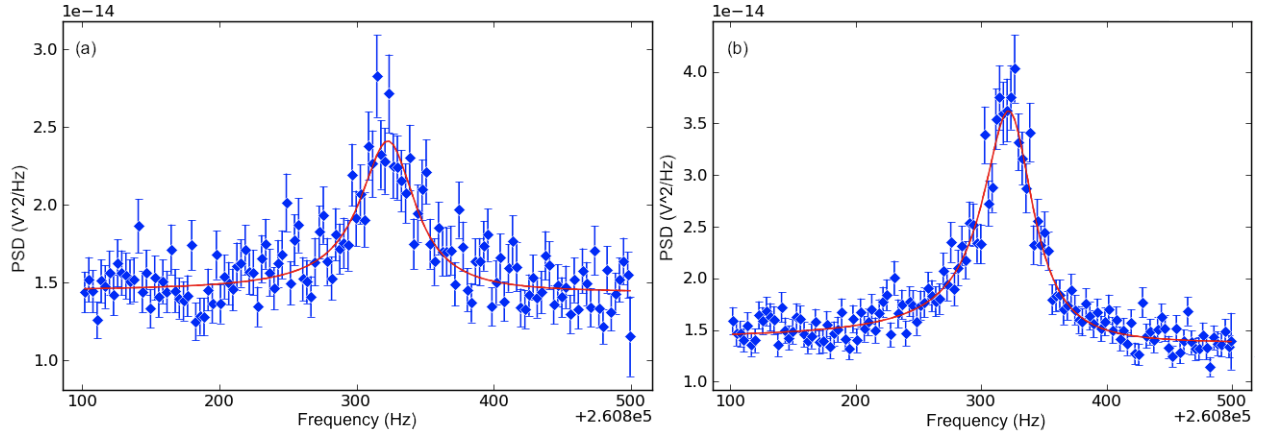


Figure 5.1: Fit of sideband heterodyne PSDs. (a) upper sideband, (b) lower sideband. The blue diamonds are data points, the red curves are the Fano peak fits using Equations (3.29) and (3.30). From the fits, we extract the center frequency $f_c = 261123.8$ Hz, peak halfwidth $f_h = 24.497$ Hz.

5.1.

Physically, f_c is the effective mechanical resonant frequency $\tilde{\omega}_m/2\pi$, f_h is related to the effective mechanical damping rate $\tilde{\gamma}_m$ by $f_h = \tilde{\gamma}_m/4\pi$. For the parameters in this experiment, change in f_h is mostly caused by the cooling beam optical damping $\gamma_{\text{opt,p}}$. We can compare the measured f_c and f_h with theory given by Equations (2.20)-(2.23). Plotted in Figure 5.1(a) and (b), Parameters used in the fit curves are: cavity coupling $A = 19.0$ rad/(m \times s), resonant frequency $\omega_m/2\pi = 261.153$ kHz, cavity decay rate $\kappa/2\pi = 119$ kHz, measured cooling power $P_{\text{in,p}} = 2.00$ μ W. The only fit parameters are: cavity coupling $\kappa_L/\kappa = 0.193$, corresponding to a reflection dip $R = 38\%$, consistent with our measured reflection dip $R \simeq 40\%$; intrinsic mechanical resonant frequency $\omega_m/2\pi = 261.153$ kHz; and offset in cooling beam detuning relative to an arbitrary setpoint $\Delta_0 = 52331.8$ kHz. In the linewidth fit, the contribution from the inherent mechanical linewidth γ_m and the signal beam induced $\delta\gamma_{m,s}$ are negligible.

5.2 Laser cooling limited by classical laser noise

Next we look at laser cooling with unfiltered lasers. As presented in Chapter 4, both lasers have excessive classical phase noise around $\omega_m/2\pi = 261$ kHz. Using the theory developed in Chapter 2, we can model how the classical noise limits our laser cooling capability and alters the heterodyne spectra.

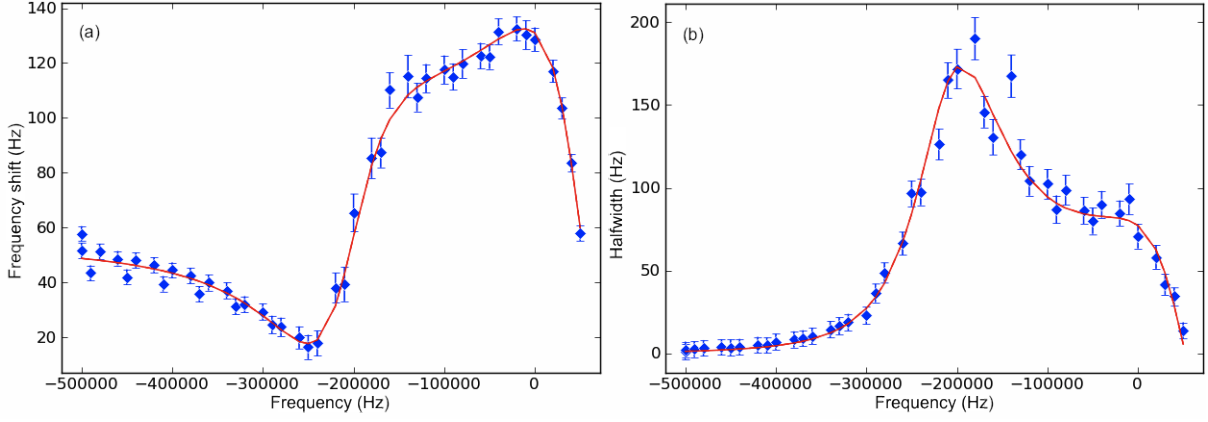


Figure 5.2: Fit of (a) Fano peak frequency shift and (b) Fano peak linewidth in the heterodyne sideband PSDs as a function of cooling beam detuning. The blue dots are data extracted from sideband heterodyne PSD fits. The red curves are the theory fits. Parameters used in the red curves are: cavity decay rate $\kappa/2\pi = 119$ kHz; cooling power $P_{\text{in,p}} = 2.35 \mu\text{W}$ before 15% power loss; cavity coupling $A = 19.0$ rad/(m \times s). The fit variables are: intrinsic mechanical resonant frequency $\omega_{\text{m}}/2\pi = 261.153$ kHz; cavity coupling $\kappa_{\text{L}}/\kappa = 0.193$; and an offset in the cooling beam detuning from an arbitrary setpoint $\Delta_0/2\pi = 52331.8$ kHz.

Using Equation (2.36), we plot n_{eff} as a function of cooling power in Figure 5.3, including the measured classical noise of both lasers. Here the signal beam input power is $P_{\text{in,s}} = 2 \mu\text{W}$. From Table 4.1, at $P_{\text{in,s}} = 1 \mu\text{W}$, the classical noise terms are $C_{\text{xx,s}} = 0.016$, $C_{\text{yy,s}} = 105$. The signal beam detuning is $\Delta_{\text{s}}/2\pi = -10$ kHz. The cooling laser classical noise terms are $C_{\text{xx,p}} = 0.0089$, $C_{\text{yy,p}} = 61$ at cooling input power $P_{\text{in,p}} = 1 \mu\text{W}$. The cooling detuning is $\Delta_{\text{p}}/2\pi = -260$ kHz for optimal cooling. The minimum phonon number we could achieve is $n_{\text{eff}} = 30$. Since the cooling beam detuning maximizes its classical noise contribution to the effective phonon number, as shown in Figure 2.2, the minimum phonon number is largely limited by the cooling phase noise.

Even though the signal beam classical noise has little influence on the laser cooling, it modifies the heterodyne spectra. As shown in Equations (2.81)-(2.82) and (2.86)-(2.87), in the heterodyne power spectra, the symmetric parts of the lower and upper sidebands s_{rr} and s_{bb} contain the effective phonon number. When there is no classical noise,

$$s_{\text{rr}} \propto |\chi_{\text{c,s}}[-\omega_{\text{m}}]|^2 (n_{\text{eff}} + 1)$$

$$s_{\text{bb}} \propto |\chi_{\text{c,s}}[\omega_{\text{m}}]|^2 n_{\text{eff}}$$

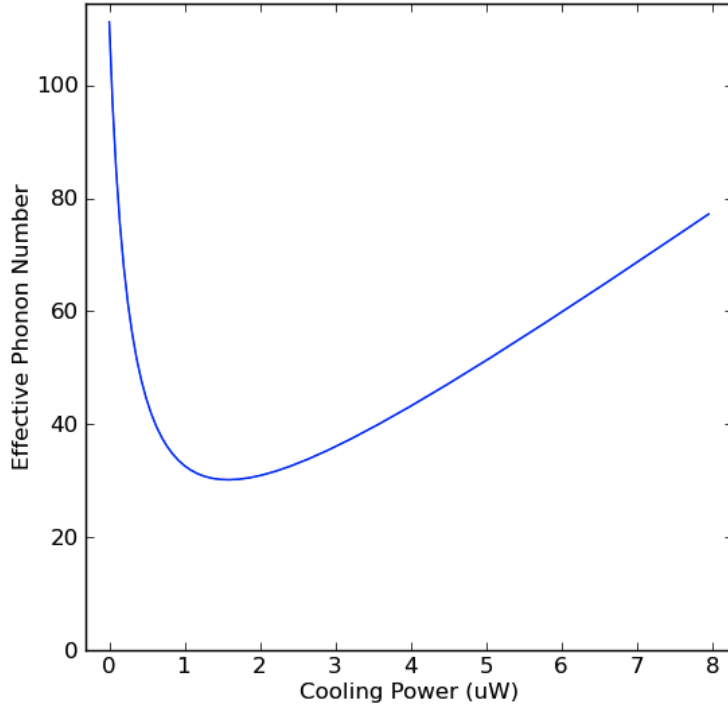


Figure 5.3: Theoretical plot of effective phonon number as a function of cooling beam input power, including all laser classical noise. The signal beam is $2 \mu\text{W}$ at -10 kHz detuning. The cooling beam is at -260 kHz detuning. The classical noise of the two lasers at $1 \mu\text{W}$ are: for the signal beam, $C_{xx,s} = 0.016$, $C_{yy,s} = 105$; for the cooling beam, $C_{xx,p} = 0.0089$, $C_{yy,p} = 61$. The lowest achievable phonon number is 30.

When there is classical noise, these terms change to

$$s_{rr} \propto |\chi_{c,s}[-\omega_m]|^2 (n_{\text{eff}} + 1) + \text{Re}(B_{\text{mod}}[\omega_m])$$

$$s_{bb} \propto |\chi_{c,s}[\omega_m]|^2 n_{\text{eff}} - \text{Re}(B_{\text{mod}}[-\omega_m])$$

We can define

$$n_{s,rr} \equiv \text{Re}(B_{\text{mod}}[\omega_m]) / |\chi_{c,s}[-\omega_m]|^2 \quad (5.1)$$

$$n_{s,bb} \equiv -\text{Re}(B_{\text{mod}}[-\omega_m]) / |\chi_{c,s}[\omega_m]|^2 \quad (5.2)$$

as the equivalent phonon numbers the signal beam classical noise added in the symmetric parts of the heterodyne power spectra. Similarly, we can define the equivalent phonon numbers the signal

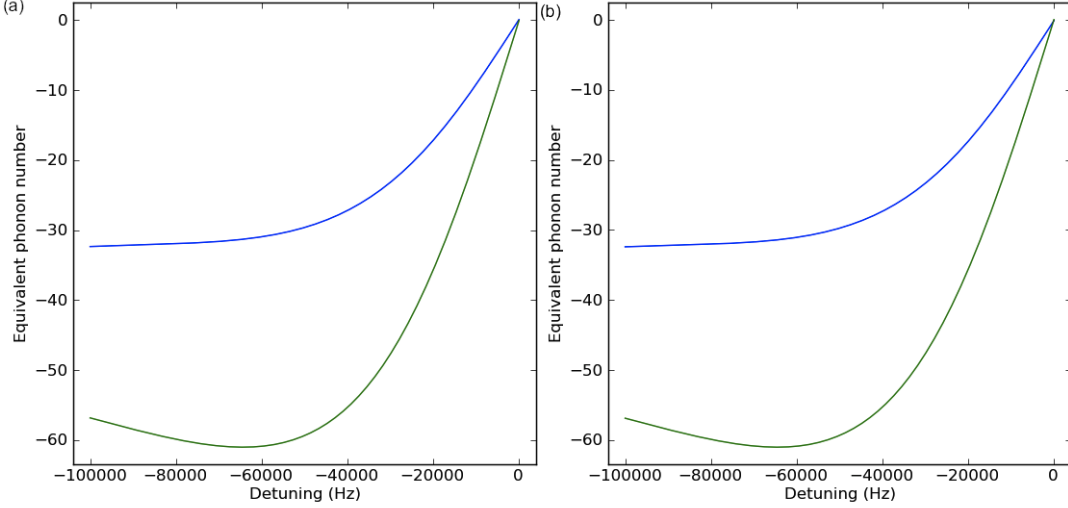


Figure 5.4: Theoretical plot of equivalent phonon numbers $n_{s,rr}$, $n_{s,bb}$, $n_{a,rr}$, and $n_{a,bb}$ created by signal laser classical noise in the (a) lower and (b) upper sideband heterodyne power spectra. The blue curves are for the symmetric terms, and the green curves are for the anti-symmetric terms. The parameters used in the plots are: signal beam input power is $2 \mu\text{W}$, $C_{xx,s} = 0.016$, $C_{yy,s} = 105$ at $1 \mu\text{W}$.

beam classical noise added in the anti-symmetric parts of the heterodyne power spectra,

$$n_{a,rr} \equiv \text{Im}(B_{\text{mod}}[\omega_m]) / |\chi_{c,s}[-\omega_m]|^2 \quad (5.3)$$

$$n_{a,bb} \equiv \text{Im}(B_{\text{mod}}[-\omega_m]) / |\chi_{c,s}[\omega_m]|^2 \quad (5.4)$$

Using the same parameters as in Figure 5.3, $P_{\text{in,p}} = 2 \mu\text{W}$, $C_{xx,s} = 0.016$, $C_{yy,s} = 105$ at $1 \mu\text{W}$, we plot $n_{s,rr}$, $n_{s,bb}$, $n_{a,rr}$, and $n_{a,bb}$ at different signal beam detunings in Figure 5.4. At reasonable $\Delta_s/2\pi \sim -10 \text{ kHz}$, these equivalent phonon numbers are $\sim 10^1$. When $\Delta_s = 0$, they are small because the phase noise contributions are zero and the amplitude noise terms are small. However, in reality it is difficult to maintain a constant very small Δ_s .

For small $n_{\text{eff}} < 1$, one way to verify the phonon number is to use the asymmetry of the heterodyne sideband PSDs. If there is no classical noise, the ratio of the lower to upper sideband heights is $\frac{s_{rr}}{s_{bb}} = \frac{|\chi_{c,s}[-\omega_m]|^2(n_{\text{eff}}+1)}{|\chi_{c,s}[\omega_m]|^2 n_{\text{eff}}} \gg 1$. However, when there is large classical noise, the large $n_{s,rr}$, $n_{s,bb}$ terms make it difficult to use this method. To observe $n_{\text{eff}} < 1$ accurately, we need to reduce the signal laser classical noise.

5.3 Laser cooling as a function of cooling beam power

Next we look at laser cooling when we increase the cooling beam power. The signal beam is locked to the experimental cavity at small detunings. The cooling beam is locked to the signal beam with a constant frequency offset. This offset is chosen so the cooling beam detuning is close to optimal ($\Delta_p/2\pi \sim -260$ kHz). The cooling power is then adjusted by changing the RF drive power to the AOM in the cooling beam path.

5.3.1 Classical noise measurement

In this measurement, we noticed the HF2 output contained extra white noise. When the HF2 output mixes with the 100 MHz signal to produce the RF drive for the signal beam AOM, the HF2 output noise creates additional amplitude noise on the signal beam. It also modifies the signal laser phase noise through the laser piezo feedback. So we need to remeasure the signal beam noise.

Using the methods detailed in Chapter 4, the classical noise terms of the signal laser are measured. The signal beam power is $1.95 \mu\text{W}$. The injected PM tones are the same as used in Section 4.2.2.1. The measured PM tone amplitude is 2.2 mrad. Shown in Figure 5.5 are the sideband heterodyne PSDs off resonance and near resonance. The PM peaks at 2 kHz in the PSDs have an average area of $A_{\text{PM}} = 6.3 \times 10^{-9} \text{V}^2$. The average noise floor after subtracting the dark noise is $2.5 \times 10^{-14} \text{V}^2/\text{Hz}$. This is substantially higher than the noise floor shown in Figure 4.5, due to additional amplitude noise in the signal beam. In Figure 5.6 we plot the on resonance sideband heterodyne PSDs. The average noise floor is $3.9 \times 10^{-14} \text{V}^2/\text{Hz}$. The difference between the two noise floors is $1.4 \times 10^{-14} \text{V}^2/\text{Hz}$. This is due to the signal beam phase noise common on both beams.

Using the coefficients listed in Figure 4.3, the phase noise level is

$$S_{\phi\phi} = (2.2 \text{ mrad})^2 \times \frac{1.4 \times 10^{-14} \text{V}^2/\text{Hz}}{A_{\text{PM}}} \times \frac{0.97}{0.10} = 1.1 \times 10^{-10} \text{ rad}^2/\text{Hz}$$

The shot noise level at $1.95 \mu\text{W}$ is $9.57 \times 10^{-14} \text{ rad}^2/\text{Hz}$. So the measured phase noise level corresponds to $C_{\text{vy}} = 280$ at $1.95 \mu\text{W}$.

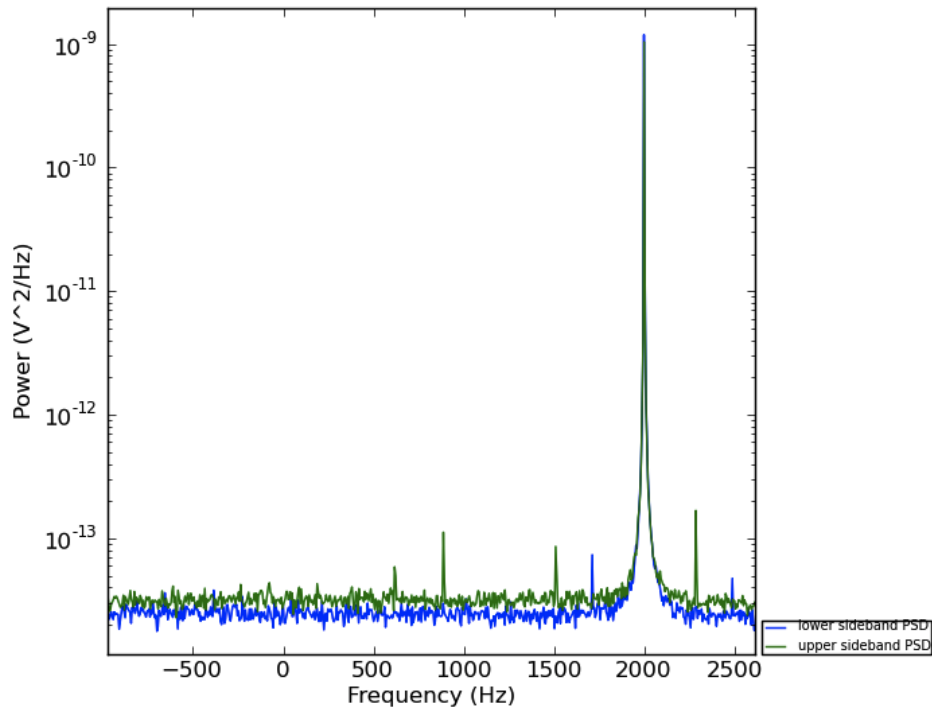


Figure 5.5: Off resonance upper and lower sideband heterodyne PSDs. The blue curve is for the lower sideband, the green curve is for the upper sideband. The upper sideband PSD is reversed in frequency to compare with the lower sideband PSD. The average noise floor is $2.7 \times 10^{-14} \text{ V}^2/\text{Hz}$.

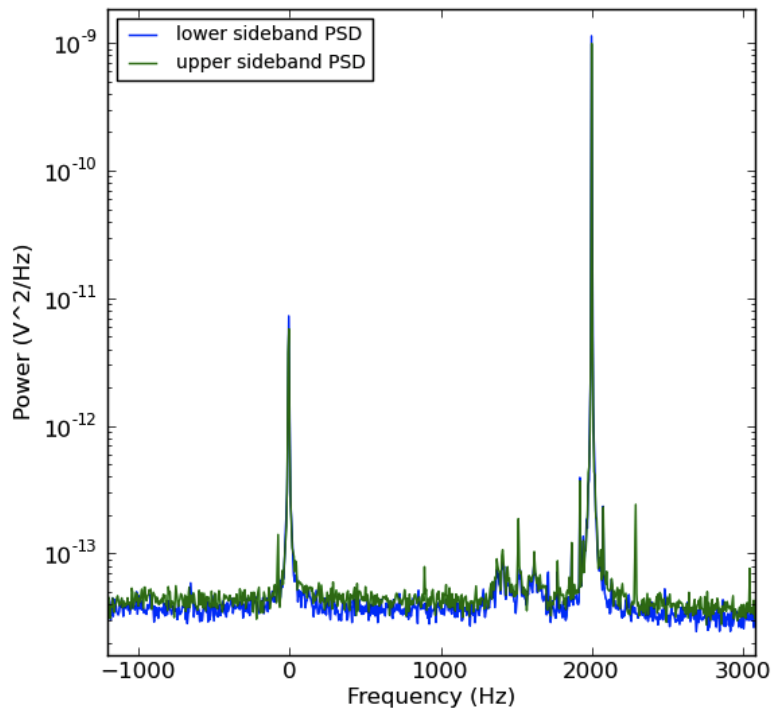


Figure 5.6: On resonance upper and lower sideband heterodyne PSDs. The blue curve is for the lower sideband, the green curve is for the upper sideband. The upper sideband PSD is reversed in frequency to compare with the lower sideband PSD. The average noise floor is $4.1 \times 10^{-14} \text{ V}^2/\text{Hz}$.

We can also calculate the additional amplitude noise in the signal beam. Since it is only on the signal beam, the coefficient off resonance is 1. We get the amplitude noise level

$$C_{xx}^{(1)} = C_{yy} \times \frac{2.5 \times 10^{-14} \text{ V}^2/\text{Hz}}{1.4 \times 10^{-14} \text{ V}^2/\text{Hz}} \times \frac{0.10}{1.0} = 49$$

at $1.95 \mu\text{W}$. The large $C_{xx}^{(1)}$ also means we could have a large C_{xy} limited by Cauchy's inequality. But such an assumption does not agree with our laser cooling data, as described in the next section.

5.3.2 Thermometry based on heterodyne PSDs

Using the measured heterodyne sideband PSDs, we can infer the effective phonon number. To do this, we first use the measured sideband background ratio to extract the signal beam detuning Δ_s . Then the ratio of the sideband Lorentzian peak heights is used to extract n_{eff} . The extracted Δ_s and n_{eff} are functions of the signal laser noise terms. As will be shown, using the measured signal laser noise values and $C_{xy} = 0$, the inferred n_{eff} match with theoretical predictions using the same parameters. The inferred Δ_s also agrees with the measured heterodyne carrier phase as described in Section 3.7.1. Finally, the detuning parameters used in these fits are also consistent with measured optical damping.

5.3.2.1 Extracting signal beam detuning from PSD background ratio

Since we do not have a direct measurement of Δ_s , we infer its value as follows. Modifying Equations (2.70) and (2.85) to include the extra signal beam amplitude noise $C_{xx}^{(1)}$ added by the HF2, at known signal beam power, the ratio between the sideband PSD backgrounds

$$\frac{b_{\text{bb}}}{b_{\text{rr}}} = \frac{1 + \sigma[A_1(\Delta_s)C_{xx} + A_2(\Delta_s)C_{xx}^{(1)} + A_3(\Delta_s)C_{yy} + A_4(\Delta_s)C_{xy}]}{1 + \sigma[A'_1(\Delta_s)C_{xx} + A'_2(\Delta_s)C_{xx}^{(1)} + A'_3(\Delta_s)C_{yy} + A'_4(\Delta_s)C_{xy}]} \quad (5.5)$$

is solely a function of signal beam detuning Δ_s . Here $A_1(\Delta_s) = |\rho|^2 + |\kappa_L \chi_{c,s}[\omega_m] - 1|^2 - 2\text{Re}[\rho^*(\kappa_L \chi_{c,s}[\omega_m] - 1)]$, $A_2(\Delta_s) = |\kappa_L \chi_{c,s}[\omega_m] - 1|^2$ etc. are the coefficients of classical noise terms as given by Equations (4.4)-(4.8).

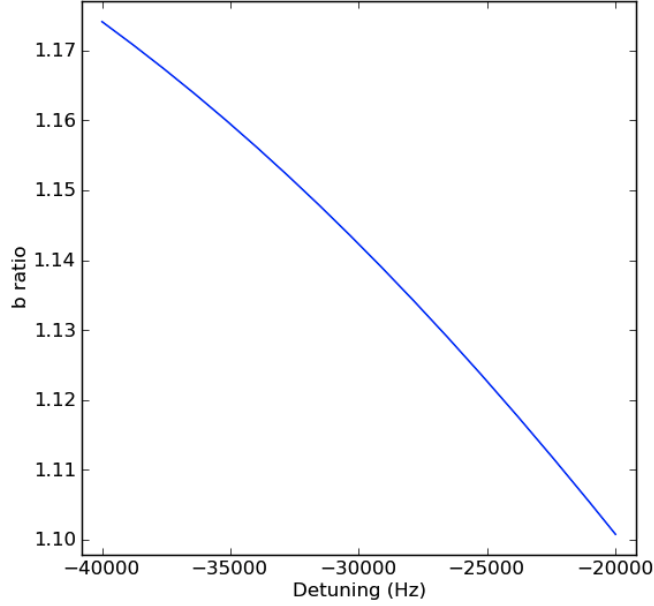


Figure 5.7: Theoretical plot of $\frac{b_{\text{bb}}}{b_{\text{rr}}}$ as a function of $\Delta_s/2\pi$. The signal beam classical noise terms used in this plot are $C_{\text{xx}} = 0.031$, $C_{\text{xx}}^{(1)} = 49$, $C_{\text{yy}} = 280$, and $C_{\text{xy}} = 0$ at $1.95 \mu\text{W}$.

From optical ringdown measurements we get $\kappa/2\pi = 119 \text{ kHz}$. From the reflection dip $R = 0.55$, we get $\kappa_L = 0.165\kappa$. In Figure 5.7, we plot the theoretical $\frac{b_{\text{bb}}}{b_{\text{rr}}}$ as a function of $\Delta_s/2\pi$. For the plot, we use the measured values of signal beam classical noise: $C_{\text{xx}} = 0.031$, $C_{\text{xx}}^{(1)} = 49$, and $C_{\text{yy}} = 280$ at $1.95 \mu\text{W}$. The signal beam power is $P_{\text{in,s}} = 2.04 \mu\text{W}$. The resulted curve can be approximately fit linearly

$$\frac{b_{\text{bb}}}{b_{\text{rr}}} = 1.030 - 3.674 \times 10^{-6} \Delta_s/2\pi \text{ (Hz)} \quad (5.6)$$

We infer Δ_s by comparing the measured $\frac{b_{\text{bb}}}{b_{\text{rr}}}$ to this theory curve. The result is plotted in Figure 5.8. The signal beam detuning has a roughly linear relation with the cooling power $P_{\text{in,p}}$:

$$\Delta_s/2\pi \text{ (Hz)} = -2424 \times P_{\text{in,p}}(\mu\text{W}) - 29962 \quad (5.7)$$

We will use this linear fit to generate the theory curves in Figure 5.8 and Figure 5.9.

Another way to infer Δ_s is by using the calibrated heterodyne carrier phase θ_{cal} , defined by Equation (3.16). From Equation (3.18), when $\Delta_s < \kappa/2$, θ_{cal} is approximately linear to Δ_s . In Figure 5.9, we plot the extracted $\frac{b_{\text{bb}}}{b_{\text{rr}}}$ against the average θ_{cal} at each cooling power setting. They

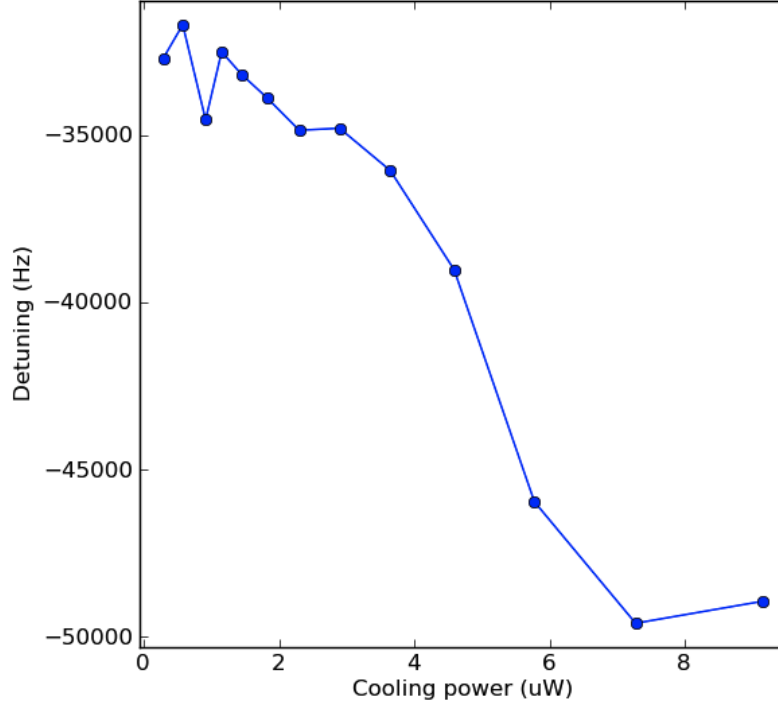


Figure 5.8: Inferred signal beam detuning $\Delta_s/2\pi$ as a function of cooling power $P_{\text{in,p}}$. At each $P_{\text{in,p}}$, $\Delta_s/2\pi$ value is inferred from the $\frac{b_{\text{bb}}}{b_{\text{rr}}}$ value extracted from the fitted heterodyne PSDs.

follow a linear relationship. θ_{cal} spans over 9° in the data, roughly from -115.3° to -106.4° . From Equation (3.18), this corresponds to about 20 kHz change in signal beam detuning. On the other hand, from Figure 5.7, $\frac{b_{\text{bb}}}{b_{\text{rr}}}$ spans over 0.065, corresponding to 18 kHz in signal beam detuning change. This agreement confirms the correctness of the $\frac{b_{\text{bb}}}{b_{\text{rr}}}$ method.

5.3.2.2 Extracting effective phonon number from PSD Lorentzian peak ratio

From Equations (2.81) and (2.86), the Lorentzian peak height ratio

$$\frac{s_{\text{bb}}}{s_{\text{rr}}} = \frac{\sigma\kappa_L|\alpha_s|^2\tilde{\gamma}_m[|\chi_{c,s}[\omega_m]|^2n_{\text{eff}} - \text{Re}(B_{\text{mod}}[-\omega_m])]}{\sigma\kappa_L|\alpha_s|^2\tilde{\gamma}_m[|\chi_{c,s}[-\omega_m]|^2(n_{\text{eff}} + 1) + \text{Re}(B_{\text{mod}}[\omega_m])]} = \frac{|\chi_{c,s}[\omega_m]|^2n_{\text{eff}} - \text{Re}(B_{\text{mod}}[-\omega_m])}{|\chi_{c,s}[-\omega_m]|^2(n_{\text{eff}} + 1) + \text{Re}(B_{\text{mod}}[\omega_m])} \quad (5.8)$$

From Equation (5.2) we can solve for the phonon number

$$n_{\text{eff}} = \frac{\text{Re}(B_{\text{mod}}[-\omega_m]) + \text{Re}(B_{\text{mod}}[\omega_m])\frac{s_{\text{bb}}}{s_{\text{rr}}} + |\chi_{c,s}[-\omega_m]|^2\frac{s_{\text{bb}}}{s_{\text{rr}}}}{|\chi_{c,s}[\omega_m]|^2 - |\chi_{c,s}[-\omega_m]|^2\frac{s_{\text{bb}}}{s_{\text{rr}}}} \quad (5.9)$$

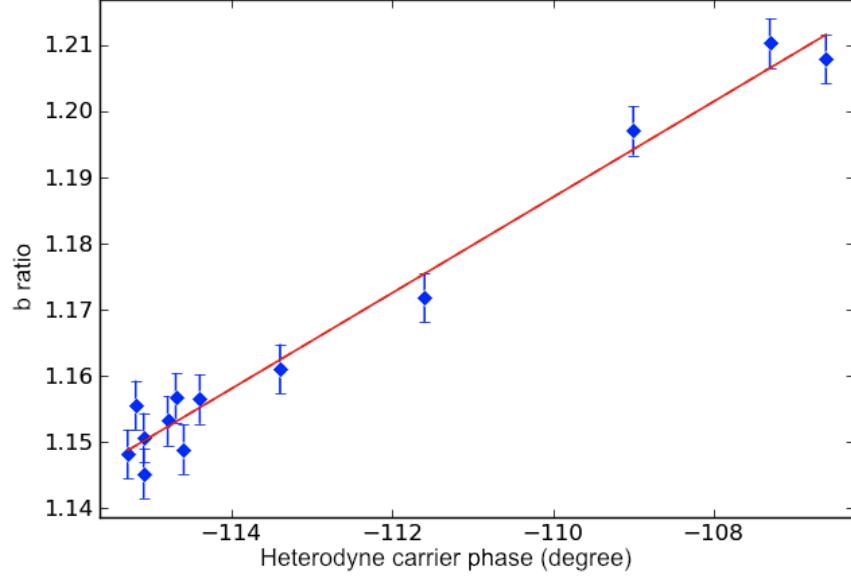


Figure 5.9: Measured background ratio $\frac{b_{bb}}{b_{rr}}$ vs measured calibrated heterodyne carrier phase θ_{cal} . The fit is $\frac{b_{bb}}{b_{rr}} = 1.98 + 0.0072\theta_{cal}(\text{°})$.

Once we know Δ_s from $\frac{b_{bb}}{b_{rr}}$, we can solve for n_{eff} from $\frac{s_{bb}}{s_{rr}}$. Again, in this measurement, to include the extra signal beam noise $C_{xx}^{(1)}$, the classical noise term $B_{mod}[\omega]$ is modified to

$$\begin{aligned}
B_{mod}[\omega] = & \kappa_L |\chi_{c,s}[-\omega]|^2 e^{-i\phi} [(C_{xx} + C_{xx}^{(1)} + iC_{xy})B_+[\omega] + (iC_{xy} - C_{yy})B_-[\omega]] \\
& - \chi_{c,s}^*[-\omega] e^{-i\phi} [(C_{xx}B_+[\omega] + iC_{xy}B_-[\omega])(1 + \rho) + (iC_{xy}B_+[\omega] - C_{yy}B_-[\omega])(1 - \rho) + C_{xx}^{(1)}B_+[\omega]]
\end{aligned} \tag{5.10}$$

From measured sideband PSDs, b_{rr} , b_{bb} , s_{rr} and s_{bb} are extracted. Using Equation (5.2), Δ_s is inferred from the measured $\frac{b_{bb}}{b_{rr}}$. We then calculate n_{eff} using Δ_s and the other measured parameters, and compare it to theory. In Figure 5.10, we plot the inferred n_{eff} as a function of cooling power $P_{in,p}$. This is compared to the theoretical n_{eff} vs $P_{in,p}$ curve calculated from Equation (2.37), including all the measured classical noise. The signal beam detuning is assumed to follow Equation (5.3). For comparison, a theory curve assuming no classical noise on the two lasers is also included in the plot. Parameters used in plotting Figure 5.10 are all measured independently, they are summarized in Table 5.1.

As a sanity check, we fit the optical damping data simultaneously. In Figure 5.11, we plot the

Parameter	Value	Measurement method
Detection efficiency σ	0.71	PDA10CF photodiode spec, 15% power loss
Signal beam power $P_{\text{in},s}$	$2.04 \mu\text{W}$.	Power meter direct measurement
Signal beam classical noise	$C_{xx,s} = 0.031, C_{xx,s}^{(1)} = 49, C_{yy,s} = 280$ at $1.95 \mu\text{W}$	Shown in Section 5.3.2.1
Cooling beam classical noise	$C_{xx,p} = 0.017, C_{yy,p} = 119$ at $1.95 \mu\text{W}$	Shown in Section 4.2.2.2
Cooling beam detuning	$\Delta_p/2\pi = \Delta_s/2\pi - 240 \text{ kHz}$	Set by cooling beam AOM
Membrane temperature	400 mK	Thermometer attached to the setup
Mechanical quality factor	$Q = 4.40 \times 10^6$	Mechanical ringdown
Cavity linewidth	$\kappa/2\pi = 119 \text{ kHz}$	Optical ringdown
Front mirror coupling	$\kappa_L = 0.165\kappa = 19.6 \text{ kHz} \times 2\pi$	Reflection dip $R = 0.55$
Optomechanical coupling	$A = 19.0 \text{ rad}/(\text{m} \times \text{s})$	Shown in Section 3.1.3

Table 5.1: Summary of parameters used in Figures 5.10 and 5.11 and measurement methods to independently verify them.

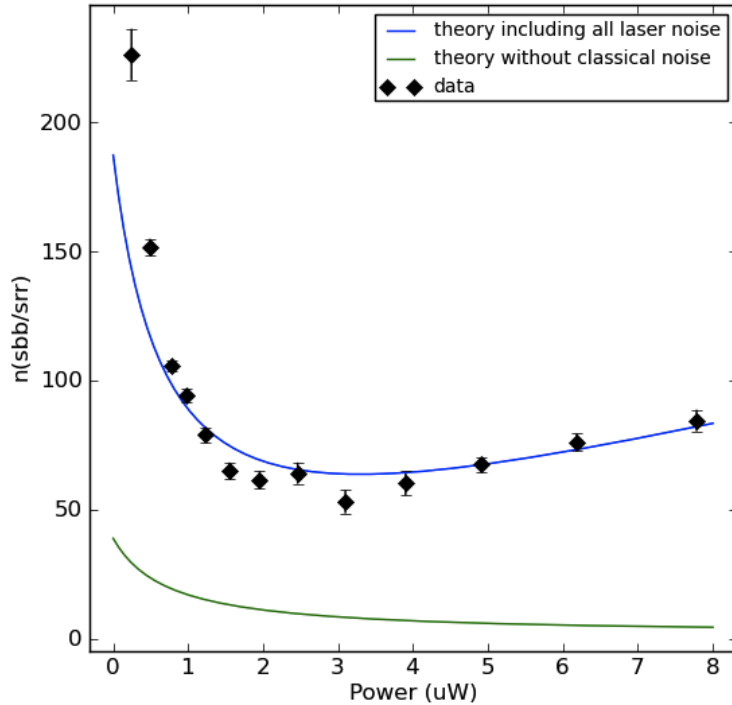


Figure 5.10: Plot of effective phonon number inferred from heterodyne PSDs as a function of cooling power. The black diamonds are n_{eff} inferred from measured $\frac{s_{\text{bb}}}{s_{\text{rr}}}$. The error bars only contain propagated uncertainties of s_{bb} and s_{rr} in the PSD Fano fits. The blue curve is the theory including all measured classical noise. The green curve is the theory without any classical noise. Parameters used for the plots are listed in Table 5.1.

Fano peak halfwidth f_h extracted from heterodyne PSDs. The data is compared to a theory curve containing both the cooling beam optical damping $\gamma_{\text{opt,p}}$ and the signal beam optical damping $\gamma_{\text{opt,s}}$. The theory curve is derived using the same set of parameters as the n_{eff} analysis.

In Figures 5.10 and 5.11, both the phonon number and the optical damping are consistent with theory over a large cooling power range, using independently measured laser classical noise and cavity parameters. This confirms that we were able to cool the membrane vibrational mode from 32,000 phonons down to about 65 phonons. Also notice the big difference between the phonon number inferred from the complete theory (the blue curve in Figure 5.10) and the number inferred naively from measured mechanical linewidths (the green curve in Figure 5.10). When the classical noise is large, we cannot use the mechanical linewidth to infer the phonon occupancy.

In both plots, at very low cooling power, the data deviate from theory predictions using Δ_s inferred from $\frac{b_{\text{bb}}}{b_{\text{rr}}}$ and θ_{cal} . Instead, they are consistent with smaller Δ_s . These data points correspond

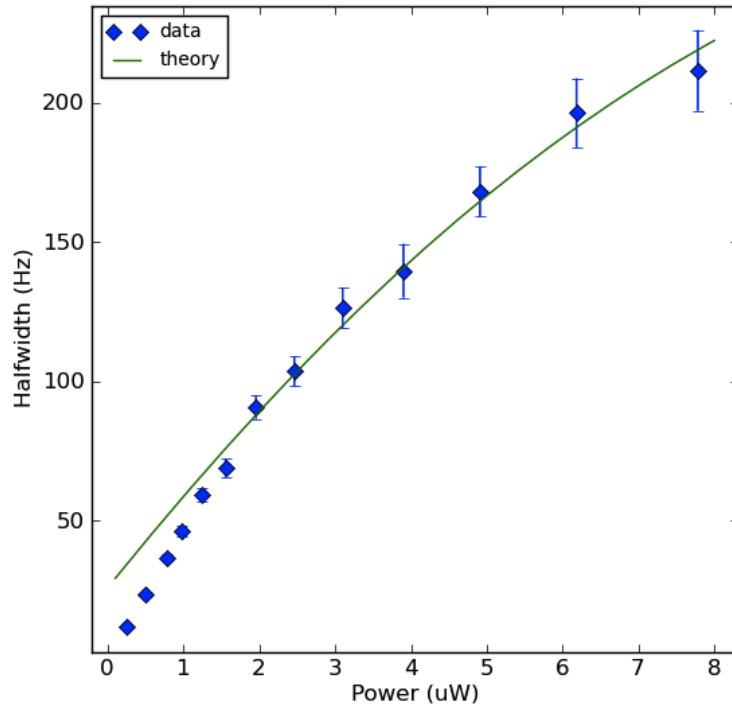


Figure 5.11: Plot of measured Fano peak halfwidth f_h as a function of cooling beam power. The blue dots are f_h extracted from heterodyne PSDs. The error bars only include uncertainties of f_h in the PSD Fano fits. The green curve is the theory including optical damping from both the signal beam and the cooling beam. Parameters used for the plot are the same as in Figure 5.10.

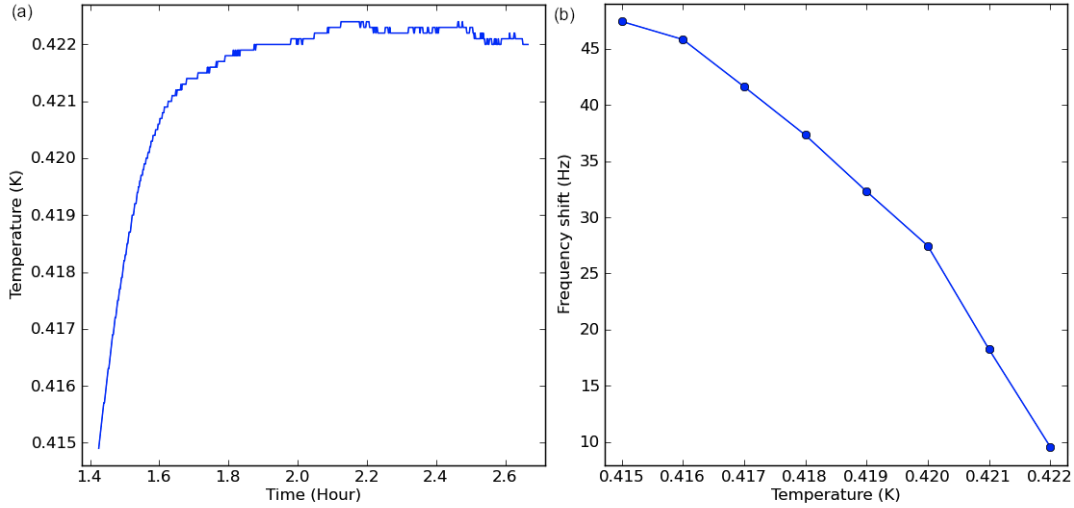


Figure 5.12: (a) Cavity temperature change when the signal beam is locked to the cavity and the LO beams is turned on. (b) Mechanical frequency shift as a function of cavity temperature. The cavity temperature is monitored by a sensor attached to the cavity. The mechanical frequency is extracted from sideband heterodyne PSDs. Both curves are measured with signal beam input $P_{\text{in},s} = 1.95 \mu\text{W}$, LO beam input $P_{\text{in},\text{LO}} = 298 \mu\text{W}$ and no cooling beam.

to the rise in cavity temperature at the beginning of the measurement. As shown in Figure 5.12(a), the cavity temperature rises when the strong LO beam is turned on, and saturates after about 20 minutes. A known effect of this temperature increase is the shift in mechanical resonant frequency, shown in Figure 5.12(b). Notice when the temperature changed by 0.07 K, the mechanical frequency shifted by over 30 Hz. For comparison, in Figure 5.13 we plot the measured mechanical resonant frequency of the fundamental mode of a lower stress Norcada $1 \text{ mm} \times 1 \text{ mm} \times 50 \text{ nm}$ Si_3N_4 membrane, as a function of fridge temperature. Even though this membrane has a lower stress and thus lower fundamental mode resonant frequency than the one used in our experiment, we expect their temperature dependences of resonant frequency to be similar. The frequency shift per unit temperature change in Figure 5.13 is much smaller than what we observed in Figure 5.12(b), hinting that the frequency shift in Figure 5.12(b) was caused not only by real temperature dependence of the membrane frequency, but also changing optomechanics. We therefore suspect the cavity temperature change shown in Figure 5.12(a) caused changes in cavity parameters, and led to the observed deviations.

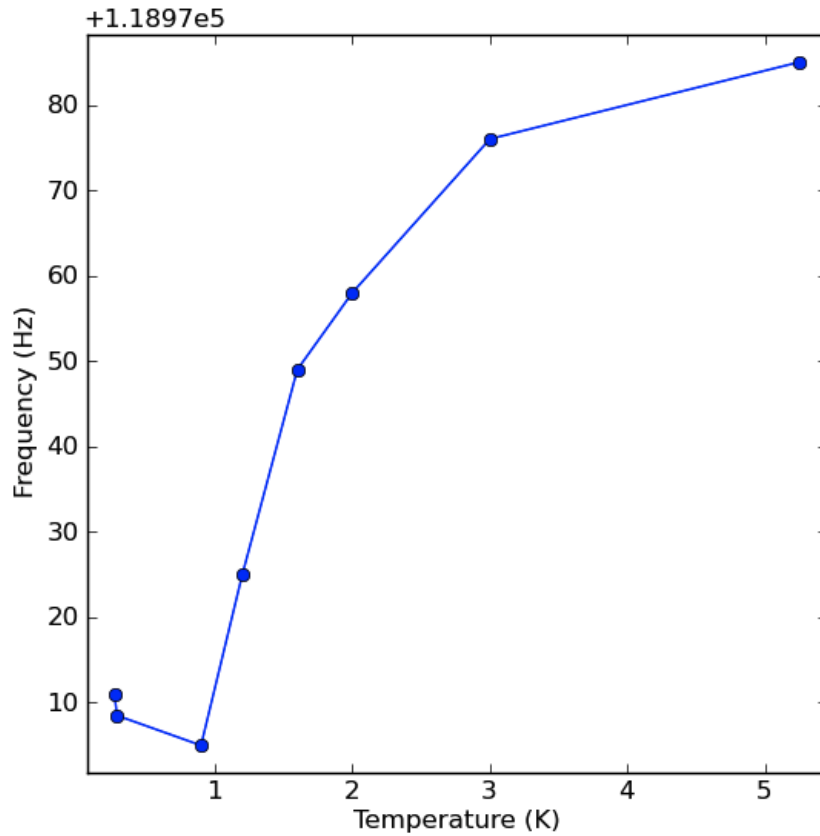


Figure 5.13: Measured mechanical frequency shift as a function of fridge temperature for a low stress $1\text{ mm} \times 1\text{ mm} \times 50\text{ nm}$ Si_3N_4 membrane. The fundamental vibrational mode's resonant frequency is around 118.98 kHz. The mechanical frequency is measured by a lock-in amplifier for mechanical ringdown measurements, the fridge temperature is measured by a thermometer near the membrane.

5.4 Laser cooling as a function of signal beam detuning

Finally, we look at laser cooling when we change the signal beam detuning Δ_s . The signal beam is locked to the experimental cavity, the detuning is adjusted by the input offset of its feedback PI controller. Its power is $P_{\text{in},s} = 1.95 \mu\text{W}$. The cooling beam is locked to the signal beam with a constant frequency offset $\Delta_p - \Delta_s \sim -230 \text{ kHz} \times 2\pi$.

First, we look at optomechanics. At each Δ_s , we take data at several cooling powers. The center frequency f_c of the sideband PSD Fano peaks changes linearly with cooling power $P_{\text{in},p}$. The slope of these linear relations $\frac{df_c}{dP_{\text{in},p}}$ can be extracted as a function of Δ_s . From Equation (2.22), we know the mechanical frequency shift is linear with the cooling power, and the slope $\frac{df_c}{dP_{\text{in},p}}$ as a function of cooling beam detuning is given by

$$\frac{df_c}{dP_{\text{in},p}} = \frac{\Delta |\chi_{\text{m},p}(\omega)|^2 |\chi_{\text{m},p}(-\omega)|^2 \frac{A^2}{2m\omega_m\omega_p} [(\kappa/2)^2 - \omega_m^2 + \Delta^2] \kappa_L}{\pi [(\frac{\kappa}{2})^2 + \Delta_p^2]} \quad (5.11)$$

Similar to Section 5.3.2.1, we get Δ_s from $\frac{b_{\text{bb}}}{b_{\text{rr}}}$ and θ_{cal} , using the signal laser noise measured in Section 4.2.2.1, and measured cavity parameters: $\kappa/2\pi = 119 \text{ kHz}$, $\kappa_L = 0.165\kappa$; coupling $A = 19.0 \text{ rad}/(\text{m} \times \text{s})$. The $\frac{df_c}{dP_{\text{in},p}}$ vs $\Delta_s/2\pi$ curve is fit with one variable: the fixed offset between the cooling beam and the signal beam. As shown in Figure 5.14, the best fit is produced when $\Delta_p - \Delta_s = -233 \text{ kHz} \times 2\pi$, consistent with our measured settings.

We then fit the phonon number n_{eff} as a function of Δ_s for a fixed cooling power $P_{\text{in},p} = 2.30 \mu\text{W}$, as shown in Figure 5.15. We use the cooling classical noise measured in Section 4.2.2.2. The mechanical $Q = 4.0 \times 10^6$ from ringdown measurements. In Figure 5.15, the error bars only include s_{rr} , s_{bb} uncertainties from the Fano fits of sideband PSDs. With the measurement parameters, n_{eff} is sensitive to small changes in $\frac{s_{\text{bb}}}{s_{\text{rr}}}$, and the uncertainties are large.

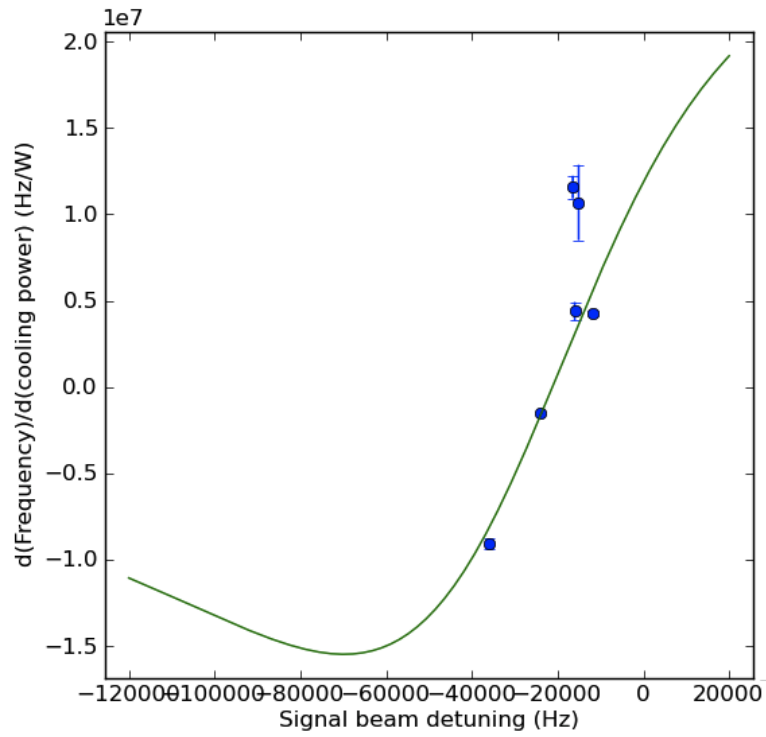


Figure 5.14: Plot of $\frac{df_c}{dP_{in,p}}$ as a function of signal beam detuning $\Delta_s/2\pi$. The signal beam detunings are inferred from $\frac{b_{bb}}{b_{rr}}$ and θ_{cal} using measured parameters.

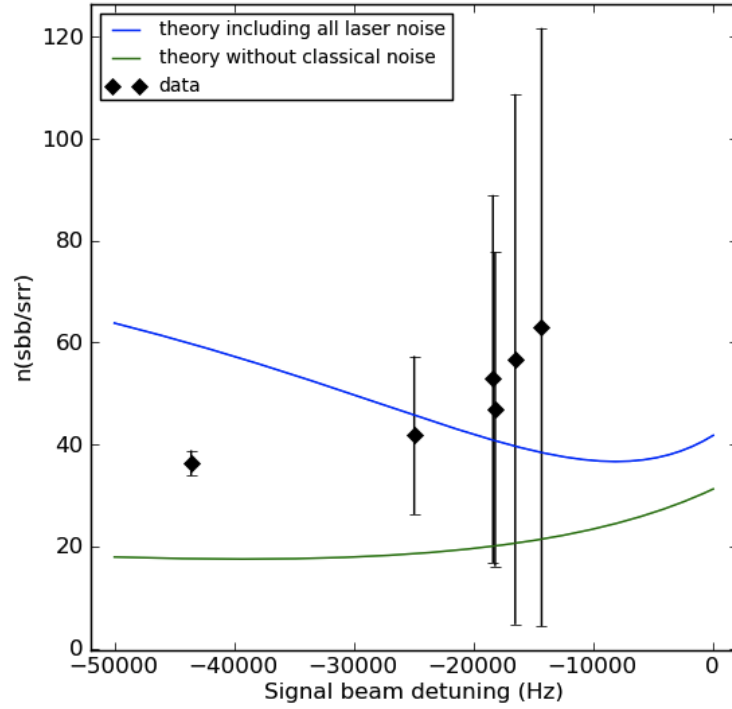


Figure 5.15: Plot of effective phonon number inferred from heterodyne PSDs as a function of signal beam detuning. The cooling power is fixed at $P_{\text{in,p}} = 2.30 \mu\text{W}$. The black dots are produced using measured parameters and $\Delta_p - \Delta_s = -233 \text{ kHz} \times 2\pi$. The error bars only contain propagated uncertainties of s_{rr} and s_{bb} in the PSD Fano fits. The blue curve is the theory including all measured classical noise. The green curve is the the theory without any classical noise.

Chapter 6

Future directions and conclusions

6.1 Future directions

In Chapter 5, we showed laser cooling results down to about 60 phonons. In order to further cool the membrane's motion to its ground state, we need to reduce the cooling laser noise. Using the filter cavity described in Section 3.5, we were able to lower the classical noise at 261 kHz by about 560 times, as demonstrated in Section 4.2.3. To further lower the classical noise, we can pass the cooling beam through the filter cavity twice. On the other hand, our ability to resolve the motional sidebands in heterodyne PSDs is also limited by the signal beam phase noise. The high classical phase noise floor makes it difficult to resolve small Fano peaks in the PSDs. There are also several phase noise peaks around the mechanical frequency, making it difficult to fit the mechanical Fano peaks in heterodyne PSDs. The dark noise floor of the heterodyne detection, limited by photodiode dark noise, is also going to make it more difficult to resolve small phonon number and to observe squeezed light. Finally, in the laser cooling measurements of Section 5.3, we do not have a direct measurement of the signal beam detuning. This increases the uncertainty in data analysis.

To solve these problems, three improvements are underway:

1. Use the signal laser only for locking to the experimental cavity, and use the double-pass filtered cooling beam to perform both cooling and detection.
2. Improve the photodiode signal to noise ratio around 80 MHz by using a different diode and

building a resonant circuit, this will lower the heterodyne dark noise floor.

3. Measure the laser detuning more accurately. This is done by putting an EOM in the detection beam (which is also the cooling beam in our new setup) path and creating a sweeping PM sideband on the cooling beam. The cavity response is then measured by demodulating the heterodyne signal at the sideband frequency. When the PM sideband is swept across the experimental cavity resonance, we get a Lorentzian peak centered at the cooling beam detuning $|\Delta_p|$ in the demodulated signal. The peak width is the experimental cavity linewidth κ . An additional feature of this sideband response is the Optomechanically Induced Transparency[33, 35, 58–60] phenomenon when the sideband detuning equals ω_m . Here the two-photon interaction of the cooling beam carrier and its sideband is on resonance with the mechanical oscillator, and creates a sharp hole-burning feature in the demodulated spectrum, providing information about the total mechanical damping.

The reduced laser noise and improved detection capability should enable us to observe ground state cooling and RPSN, and to carry out other interesting quantum experiments. In the next subsections, I will show the theory predictions of laser cooling and squeezing performance using the new setup.

6.1.1 Laser cooling with filtered lasers

In Figure 6.1, we plot the effective phonon number as a function of cooling power again. Here we include three cases: no filtering, filtering the cooling laser by passing it through the filter cavity once, and passing the cooling beam through the filter cavity twice. The signal beam is unfiltered in all three cases. In all three cases, the signal beam input power is $2 \mu\text{W}$, with -10 kHz detuning. The cooling beam detuning is $\Delta_p/2\pi = -260 \text{ kHz}$. As shown by the green curve, with single pass, we can reach close to ground state at about $50 \mu\text{W}$ cooling input power. With a cooling beam filtered twice, we can reach below 1 phonon at $40 \mu\text{W}$ and get to $n_{\text{eff}} < 0.1$ with 1 mW cooling power.

For the heterodyne spectra, the theory in Chapter 2 is still valid, the only difference is we need to replace those signal beam parameters with their corresponding cooling beam parameters. To see how much the cooling beam classical noise alters the heterodyne spectra in the new setup, in Figure 6.2 we plot the equivalent phonon numbers $n_{s,rr}$, $n_{s,bb}$, $n_{a,rr}$, and $n_{a,bb}$ in the sideband heterodyne

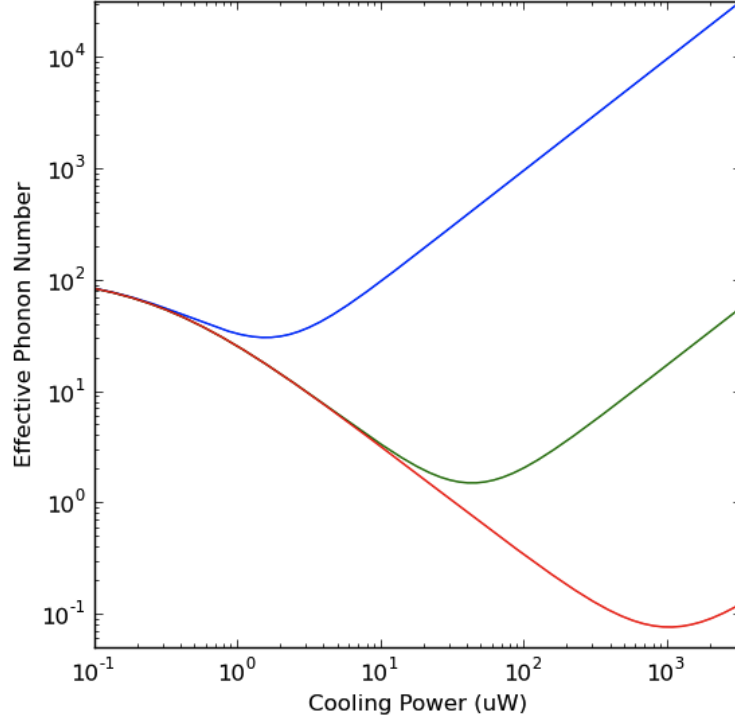


Figure 6.1: Theoretical plot of effective phonon number as a function of cooling beam input power. The blue curve includes all laser classical noise. The green curve has the cooling laser filtered by the filter cavity once. The red curve has the cooling laser filtered twice. In all three curves, the signal beam input power is $2 \mu\text{W}$, with -10 kHz detuning. The cooling beam detuning is $\Delta_p/2\pi = -260 \text{ kHz}$. The classical noise of the signal beam at $1 \mu\text{W}$ is $C_{xx,s} = 0.016$, $C_{yy,s} = 105$ for all three curves. The cooling beam classical noise terms at $1 \mu\text{W}$ are: for the blue curve, $C_{xx,p} = 0.0089$, $C_{yy,p} = 61$; for the green curve, $C_{xx,p} = 0.0089/563$, $C_{yy,p} = 61/563$; for the red curve, $C_{xx,p} = 0.0089/(563)^2$, $C_{yy,p} = 61/(563)^2$.

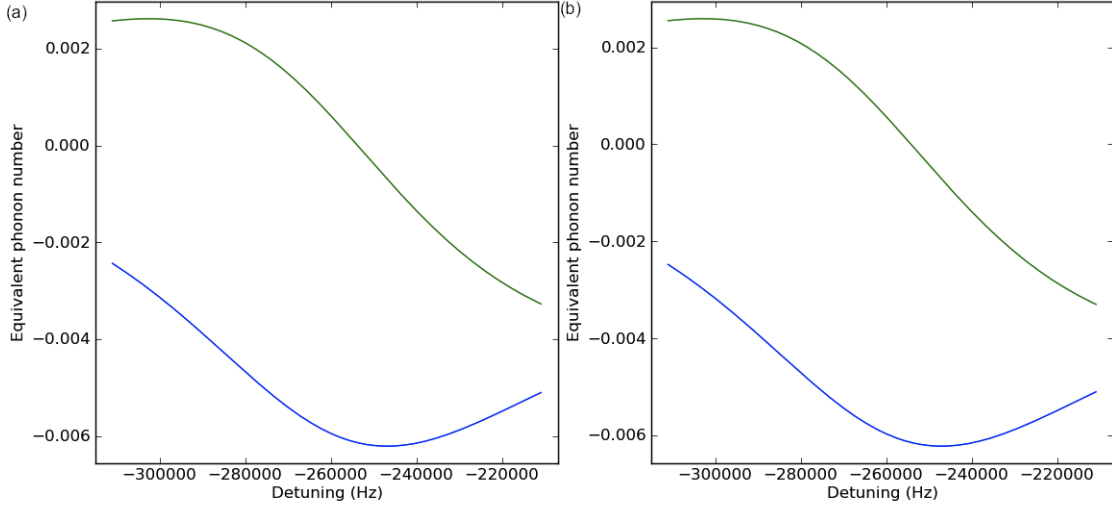


Figure 6.2: Theoretical plot of equivalent phonon numbers $n_{s,rr}$, $n_{a,rr}$, $n_{s,bb}$, and $n_{a,bb}$ created by signal laser classical noise in the (a) lower and (b) upper sideband heterodyne power spectra around $\Delta_p/2\pi = -260$ kHz. The blue curves are for the symmetric terms, and the green curves are for the anti-symmetric terms. The parameters used in the plots are: cooling beam power $P_{in,p} = 100 \mu\text{W}$; the filtered classical noise terms are $C_{xx,p} = 0.0089/(563)^2$, $C_{yy,p} = 61/(563)^2$ at $1 \mu\text{W}$.

PSDs defined by Equations (5.1)-(5.4) when the cooling beam detuning is around -260 kHz and the cooling beam power is $100 \mu\text{W}$. All these terms are much smaller than the expected n_{eff} at the corresponding settings as plotted in Figure 6.1. So we could directly use the asymmetry of sideband Lorentzian peaks to calculate $n_{\text{eff}} = \frac{|\chi_{c,s}[-\omega_m]|^2}{|\chi_{c,s}[\omega_m]|^2 \frac{s_{rr}}{s_{bb}} - |\chi_{c,s}[-\omega_m]|^2}$, simplified from Equation (5.9). Similarly, the classical noise terms in the cross correlation spectrum S_{rb} should also be negligible. In this case, the non-negligible anti-symmetric part in S_{rb} should be caused by RPSN.

6.1.2 Spectrum of squeezing

As discussed in Section 2.4, the squeezing in the reflected light can be inferred from the heterodyne spectra when $\omega \sim \omega_m$ by Equation (2.118):

$$S_\varphi^{\text{out}}[\omega] = \frac{1}{2}[b_{rr} + b_{bb} + 2\text{Re}(e^{2i(\varphi+\theta)}b_{rb}) + \frac{s_{rr} + s_{bb} + 2\text{Re}(e^{2i(\varphi+\theta)}s_{rb})}{(\tilde{\gamma}_m/2)^2 + (\omega - \tilde{\omega}_m)^2} + \frac{-a_{rr} + a_{bb} + 2\text{Re}(e^{2i(\varphi+\theta)}a_{rb})}{(\tilde{\gamma}_m/2)^2 + (\omega - \tilde{\omega}_m)^2}(\omega - \tilde{\omega}_m)]$$

The only difference is now the cooling beam is also used for detection, so all signal beam parameters in Equation (2.118) are replaced with those of the cooling beam.

In Figure 6.3, for a cooling beam with input power $P_{\text{in,p}} = 1 \text{ mW}$, at each cooling beam detuning Δ_{p} and frequency ω , we plot $\min(S_{\varphi}^{\text{out}}[\omega])$ when the quadrature phase φ is varied. The unfiltered signal beam power is $1 \mu\text{W}$, with detuning $\Delta_{\text{s}}/2\pi = -10 \text{ kHz}$. As seen in the previous subsection, its influence on the phonon number is negligible. We also assume detection efficiency $\sigma = 0.71$. This is calculated from the quantum efficiency of the PDA10CF photodiode used in the current setup, and the 15% power loss from the cavity to the photodiode. These numbers could improve with the new photodiode, and with improved optical alignment. According to Figure 6.3, we should be able to observe 5% squeezing with reasonable parameters.

As a sanity check, we compare Figure 6.3 to the analytical expressions of $\min(S_{\varphi}^{\text{out}}[\omega])$ in Section 2.4. Using the above listed parameters, when $\Delta_{\text{p}} = -\omega_{\text{m}}$, the effective phonon number is $n_{\text{eff}} = 0.066 \ll 1$. So we can use the analytical approximation of Equation (2.134). Putting in the numbers, we get for $\Delta_{\text{p}} = -\omega_{\text{m}}$ and $\omega \simeq \omega_{\text{m}}$,

$$\min(S_{\varphi}^{\text{out}}[\omega]) \simeq 1 + \frac{\sigma \kappa_{\text{L}} |\alpha_{\text{s}}|^2}{2\omega_{\text{m}}^2 \tilde{\gamma}_{\text{m}}} - \frac{2(\sqrt{2} - 1)\sigma \kappa_{\text{L}} |\alpha_{\text{s}}|^2}{\kappa \omega_{\text{m}} \tilde{\gamma}_{\text{m}}} = 0.992$$

in agreement with the results we get in Figure 6.3. On the other hand, when Δ_{p} approaches 0, n_{eff} gets larger, so the small n_{eff} assumption for the analytical approximation of Equation (2.132) no longer holds. Therefore we cannot use Equation (2.132) to compare with Figure 6.3.

6.2 Conclusion

In the past several decades, the application of radiation pressure to individual atoms and small particles have greatly improved human understanding and access to quantum mechanical effects. More recently, by applying radiation pressure to interact with the center-of-mass motion of various micromechanical devices, the field of optomechanics has been fast evolving. Since the first experiment to reach the quantum ground state in such devices[64], many groups have reached or are close to reaching the quantum ground state. There have also been a variety of experiments and

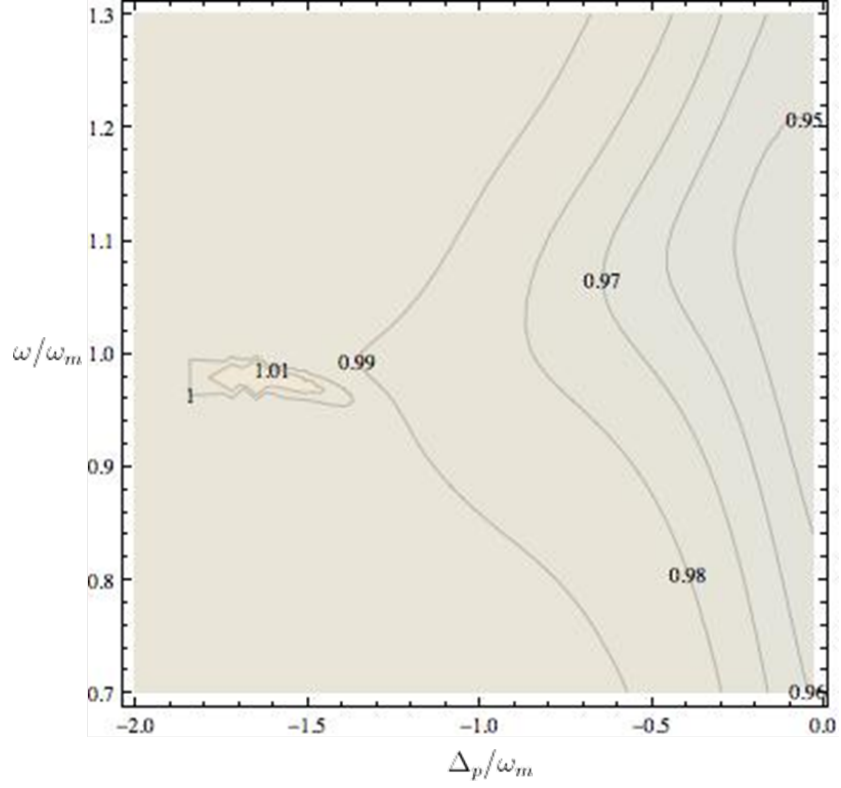


Figure 6.3: Theoretical plot of maximal output field squeezing $\min(S_\varphi^{out}[\omega])$ as a function of frequency ω and cooling beam detuning Δ_p . The cooling beam power is $P_{in,p} = 1$ mW, with double-pass filtered classical noise $C_{xx,p} = 0.0089/(563)^2$, $C_{yy,p} = 61/(563)^2$ at $1 \mu\text{W}$. The signal beam power $P_{in,s} = 1 \mu\text{W}$ with $C_{xx,s} = 0.016$, $C_{yy,s} = 105$. Its detuning is $\Delta_s/2\pi = -10$ kHz. The detection efficiency $\sigma = 0.71$.

theory proposals to explore other interesting quantum effects. Among the different optomechanical systems used, the system described in this thesis represents an effort to push the lower limit of the mechanical oscillator frequency. As shown in this thesis, a lower mechanical frequency means not only a higher thermal phonon number at the same temperature, but also the optomechanical system is more susceptible to classical noise from laser. Although the quantum ground state has not been reached in this first pass experiment, we have developed a clear understanding of how and to what extent classical laser noise limits optomechanical measurements.

To summarize, in Chapter 1 I discussed the basic idea of ground state cooling and observing RPSN. Different research groups' approaches in observing these quantum effects are reviewed and compared to our approach. Chapter 2 described the theory of laser cooling and heterodyne detection, with an emphasis on the complications created by classical laser noise. Chapter 3 described the experimental design and measurement methods. A good understanding of feedback theory and the feedforward method enabled the cooling laser lock and the filter cavity to work. Chapter 4 was devoted to describe our efforts in characterizing the classical laser noise, especially the classical phase noise. The measurements also confirmed our ability to filter the cooling laser noise with the filter cavity. Chapter 5 showed some preliminary results of optomechanics and laser cooling using unfiltered lasers. These results matched theory derived in Chapter 2, and showed laser cooling down to about 60 phonons. Finally, the detection methods developed and technical improvements we are working on now should enable us to achieve ground state cooling and observation of RPSN in the near future.

Appendix A

Membrane Mechanical Properties

A.1 Derivation of membrane vibrational mode frequency

The membrane we use is formed by depositing a square of silicon nitride (Si_3N_4) on a silicon substrate. The spacing difference between silicon nitride atoms and silicon atoms at the border of the membrane creates stress. This stress can be varied by changing the ratio of silicon vs nitrogen in the manufacturing process. The vibrational modes of such a highly stressed membrane can be modeled similar to drumheads. For a square membrane with side length a (XY plane) and thickness h (Z direction), if we neglect its longitudinal displacement, the total kinetic energy is

$$T = \frac{1}{2}\rho h \iint dx dy \left(\frac{\partial z}{\partial t}\right)^2 \quad (\text{A.1})$$

where ρ is the density of Si_3N_4 .

Since the membrane is taut, we can assume the pre-existing stress σ in the membrane is isotropic in the XY plane. Its contribution to the potential energy of the membrane is

$$V_1 = \sigma h \iint dx dy \left[\sqrt{1 + \left(\frac{\partial z}{\partial x}\right)^2 + \left(\frac{\partial z}{\partial y}\right)^2} - 1 \right] \quad (\text{A.2})$$

To first order, the total energy is

$$E = V_1 + T = \sigma h \iint dx dy \left[\frac{1}{2} \left(\frac{\partial z}{\partial x} \right)^2 + \frac{1}{2} \left(\frac{\partial z}{\partial y} \right)^2 \right] + \frac{\rho h}{2} \iint dx dy \left(\frac{\partial z}{\partial t} \right)^2 \quad (\text{A.3})$$

From the boundary conditions, we can decompose the membrane motion into orthogonal (m, n) modes ($m, n = 1, 2, 3, \dots$): displacement at any point (x, y) is $z(x, y) = A(t) \sin \frac{m\pi x}{a} \sin \frac{n\pi y}{a}$. Here $A(t)$ is the time varying vibration magnitude. The total energy for this mode is

$$E = V_1 + T = \frac{\sigma h \pi^2}{2} \frac{m^2 + n^2}{4 a^2} A^2 + \frac{\rho h a^2}{2} \frac{1}{4} \dot{A}^2 \quad (\text{A.4})$$

Taking derivative of Equation (A.4), we get the equation of motion for (m, n) mode:

$$\frac{1}{4} M \ddot{A} + \frac{1}{4} \sigma h (m^2 + n^2) \pi^2 A = 0 \quad (\text{A.5})$$

The effective mass for the vibrational modes of the membrane is $\frac{1}{4}$ of its mass $M = \rho h a^2$. The resonant frequency of the (m, n) mode is $\omega_{m,n}/2\pi = \sqrt{\frac{\sigma h}{M} (m^2 + n^2)}/2 = \frac{1}{2a} \sqrt{\frac{\sigma}{\rho} (m^2 + n^2)}$.

For the stoichiometric membrane we used in this experiment, the stress specified by Norcada is about 900 MPa, the measured $(1, 1)$ mode frequency is 261 kHz. Using the parameters: $a = 1.5$ mm, $h = 50$ nm, and $\rho = 3.44 \times 10^3$ kg/m³, we get the implied stress $\sigma = 940$ MPa, consistent with the spec. The effective mass of the membrane is $m_{\text{eff}} = \frac{1}{4} M = 9.68 \times 10^{-11}$ kg.

A.2 Derivation of membrane Duffing coefficient

The above described harmonic oscillator behavior agrees well with our observations at small external drive. If we increase the drive, the membrane deflection shows nonlinear behavior as a Duffing oscillator. To describe this effect, we need to include the additional potential energy term when the deflection is large[65].

The large deflection caused strain can be described by

$$\epsilon_x = \frac{1}{2}\left(\frac{\partial z}{\partial x}\right)^2, \epsilon_y = \frac{1}{2}\left(\frac{\partial z}{\partial y}\right)^2 \quad (\text{A.6})$$

Using generalized Hooke's Law for plane stress, we can express the stress tensor as

$$\begin{pmatrix} \sigma_x \\ \sigma_y \end{pmatrix} = \begin{pmatrix} 1 & \nu \\ \nu & 1 \end{pmatrix} \frac{Eh}{1-\nu^2} \begin{pmatrix} \epsilon_x \\ \epsilon_y \end{pmatrix} \quad (\text{A.7})$$

where E is the Young's modulus and ν is Poisson's ratio of Si_3N_4 .

The additional potential energy caused by the strain-displacement is

$$V_2 = \frac{1}{2} \iint (\sigma_x \epsilon_x + \sigma_y \epsilon_y) dx dy = \frac{1}{8} \frac{Eh}{1-\nu^2} \iint \left[\left(\frac{\partial z}{\partial x}\right)^2 + \left(\frac{\partial z}{\partial y}\right)^2 \right] dx dy \quad (\text{A.8})$$

And the total energy of the (m, n) mode becomes

$$E = V + T = \frac{\sigma h \pi^2 m^2 + n^2}{2} \frac{A^2}{4} + \frac{\rho h a^2}{2} \frac{\dot{A}^2}{4} + \frac{1}{8} \frac{Eh}{1-\nu^2} \left[\frac{9}{64} (m^4 + n^4) + \frac{m^2 n^2}{32} \right] \frac{\pi^4}{a^2} A^4 \quad (\text{A.9})$$

The equation of motion now becomes

$$\frac{1}{4} M \ddot{A} + \frac{1}{4} \sigma h (m^2 + n^2) \pi^2 A + \frac{1}{2} \frac{Eh}{1-\nu^2} \left[\frac{9}{64} (m^4 + n^4) + \frac{m^2 n^2}{32} \right] \frac{\pi^4}{a^2} A^3 = 0 \quad (\text{A.10})$$

The A^3 term is the Duffing term that explains the nonlinear behavior we see at large deflections. Here we neglected the A^3 term from the expansion of the pre-existing stress. For Si_3N_4 , the strain-displacement term is 3 orders of magnitude bigger than the third order term caused by σ .

For a Duffing oscillator described by

$$\ddot{x} + \frac{\omega_0}{Q} \dot{x} + \omega_0^2 x + \beta x^3 = 0 \quad (\text{A.11})$$

The nonlinearity could be characterized by its critical amplitude $a_c = \left(\frac{4}{3}\right)^{3/4} \frac{\omega_0}{\sqrt{Q\beta}}$. In the membrane

characterization paper [46], we measured $a_c = 3.1$ nm for a $1\text{ mm} \times 1\text{ mm} \times 50\text{ nm}$ low stress membrane. The fundamental mechanical mode frequency is $\omega_0/2\pi = 133.8$ kHz, with $Q = 1.1 \times 10^6$. Using commonly cited numbers $E = 390$ GPa, $\nu = 0.24$, we can calculate the critical amplitude for the (1, 1) mode

$$a_c = \left(\frac{4}{3}\right)^{3/4} \frac{\omega_0}{\sqrt{Q \frac{Eh}{1-\nu^2} \frac{5}{8} \frac{\pi^4}{a^2 M}}} = 10.3\text{ nm}$$

about a factor of 3 larger than the measured value. This difference could be due to uncertainties in the critical amplitude measurement and difference in actual Young's modulus from the number cited here.

Appendix B

Laser Technical Notes

Most of the laser cooling and detection measurements mentioned in this thesis are conducted using Innolight's Prometheus Nd : YAG cw laser at a wavelength of 1064nm. The Prometheus laser is popular in quantum optics research because of its low amplitude and phase noise, and because of its ease of use. However, degradations of the laser's performance will occur when the laser diode wears out, or when certain settings are not optimized. Based on the experience we gained in the past few years, here I summarize the steps to properly change the laser diode and re-optimize the laser settings.

B.1 Basics of Nd:YAG laser

B.1.1 Nd:YAG laser

Solid state lasers[66] use crystals (or glass) doped with elements that have incomplete inner shell electron states. Optical transitions that occur between these inner states are shielded from external crystal lattice perturbations by the outer shell, so sharp fluorescent lines can be achieved.

In Nd : YAG lasers, the host material $Y_3Al_5O_{12}$ (YAG) is very hard, isotropic, with good optical quality, and has a high thermal conductivity, making it ideal for lasers. The Nd atom has vacant $4f$ orbits: $4f^4 5s^2 5p^6 6s^2$. The trivalent ion Nd^{3+} that forms inside the host crystal loses its $6s$ shell and one electron in $4f$. The hyperfine structure manifolds $^{2s+1}L_J$ used for laser transitions are

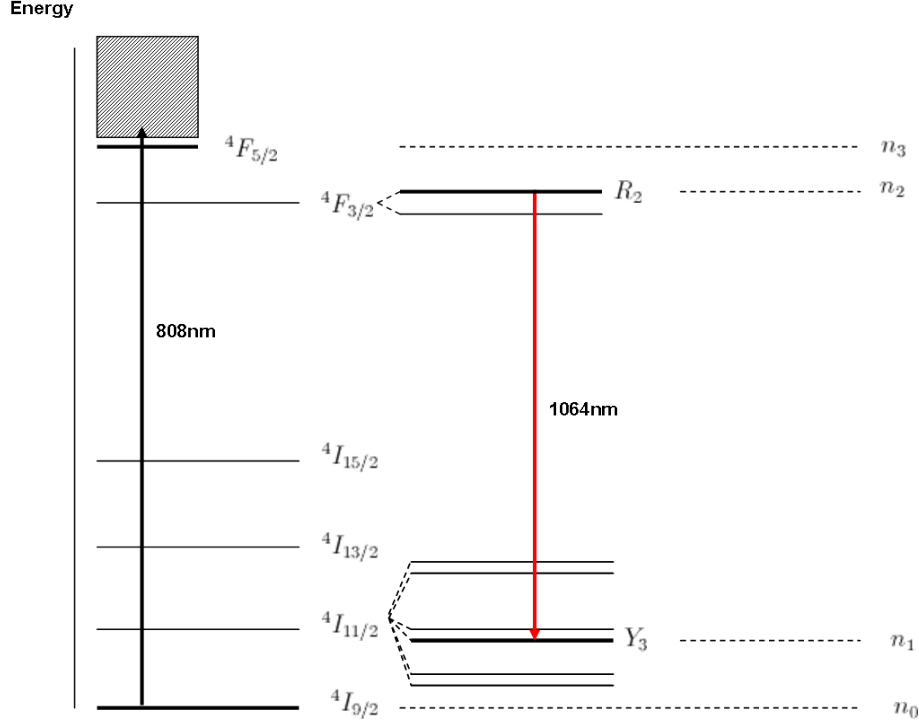


Figure B.1: Energy levels of Nd^{3+} used to form the 1064 nm four-level system

obtained by different combinations of orbital angular momentum L (depending on the orientation of the three 4f electrons left) and spin angular momentum $s = 3/2$. The manifolds are further split into $2J + 1$ sublevels by the crystal field. In particular, the 1064nm laser transition occurs between the R_2 sublevel of ${}^4F_{3/2}$ and the Y_3 sublevel of ${}^4I_{11/2}$ states, as shown in Figure B.1.

Once the laser transition occurs, the ion population is quickly transferred to the ground state ${}^4I_{9/2}$. The ions then get pumped up to the pumping band starting with the ${}^4F_{5/2}$ manifold. Ions pumped into the pumping bands then quickly relax to the upper laser transition level. By pumping strongly at 808 nm for the transition from the ground state to the pumping bands, population inversion between the laser levels is created, as in any typical four-level system.

One well-known fact about the Nd : YAG laser is the phenomenon of relaxation oscillation. It creates sinusoidal oscillations in the output of the cw laser. To model this, we denote the electron population of the four energy levels as n_0, n_1, n_2 and n_3 . Since relaxation from the pumping bands to the upper laser level is very fast, $n_3 \approx 0$. The rate equations of the two laser levels are then:

$$\frac{dn_2}{dt} = R_p n_0 - (n_2 - n_1)\sigma\phi c - \left(\frac{n_2}{\tau_{21}} + \frac{n_2}{\tau_{20}}\right) \quad (\text{B.1})$$

$$\frac{dn_1}{dt} = (n_2 - n_1)\sigma\phi c + \left(\frac{n_2}{\tau_{21}} - \frac{n_1}{\tau_{10}}\right) \quad (\text{B.2})$$

where R_p is the pumping rate, σ the stimulated emission cross section, ϕ the photon density, c the speed of light in the medium, and the various τ_{ij} terms are the radiationless relaxation rates between different levels. Because relaxation from the lower laser level to the ground state is also very fast, we can write $\tau_{10} \simeq 0$. Then $n_1 = 0$ and we get:

$$\frac{dn_2}{dt} = R_p n_0 - n_2 \sigma \phi c - \left(\frac{n_2}{\tau_{21}} + \frac{n_2}{\tau_{20}}\right) \quad (\text{B.3})$$

Within the laser resonator, we also have the rate equation of photon density:

$$\frac{d\phi}{dt} = n_2 \sigma \phi c - \frac{\phi}{\tau_c} + S \quad (\text{B.4})$$

where the first term denotes an increase in the photon density by stimulated emission, the second term denotes cavity losses, and τ_c is the cavity decay rate. The third term S is the small rate of spontaneous emission added to the laser emission (usually negligible except for explaining how the laser emission started).

Relaxation oscillation occurs as a perturbation around the stable solution of the above two equations. We could write the fluctuations as $n_2 = n_{2s} + \Delta n_2$, $\phi = \phi_s + \Delta\phi$. The linearized equations then simplify Equations (B.3) and (B.4), to give to the first order

$$\frac{d^2\Delta\phi}{dt^2} + \sigma\phi c \frac{d\phi}{dt} + (\sigma c)^2 \phi n_2 \Delta\phi = 0 \quad (\text{B.5})$$

The e^{st} form solution of this equation gives, after transient spikes caused by initial conditions,

$$\Delta\phi = \exp\left(-\frac{\sigma\phi c}{2}t\right) \sin[\sigma c \sqrt{\phi n_2} t] = 0 \quad (\text{B.6})$$

One conclusion from Equation (B.6) is that the frequency of the relaxation oscillation is proportional to n_2 , or the square root of the intracavity power I . Therefore the higher the output power from

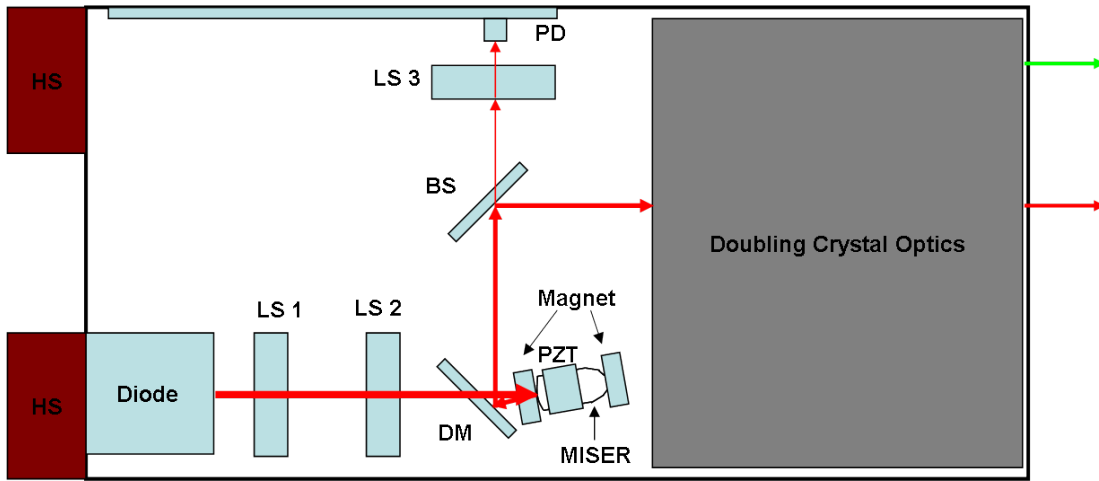


Figure B.2: Schematic of the Prometheus laser optical setup. The pump diode output at 808 nm goes through two lenses (LS1 and LS2) and a dichroic mirror (DM), into the MISER. The 1064 nm output of the MISER then goes to a beam sampler (BS) where a small part of it goes to a lens (LS3) and onto a photodiode (PD), which is used for the noise eater to feedback to the pump diode current. The rest of the beam goes through doubling crystal optics, where a small portion of the 1064 nm beam is used to generate 532 nm output. The pump diode is connected to a heat sink (HS). The MISER has two magnets on its sides, and a piezoelectric transducer (PZT) on its top.

the laser, the higher the oscillation frequency. This is consistent with what we see when we change the pumping diode current, thus changing the output power of the laser.

The decay time constant $\tau_d = 2/\sigma\phi c$ is inversely proportional to the stimulated emission rate, thus it is proportional to the lifetime of the upper laser level. This makes physical sense because if the lifetime of upper state is long, any fluctuation in the electron population will create a fluctuation in the photon density before it dies out, this photon density fluctuation will then cause more fluctuation in the electron population in return, thus creating the relaxation oscillation. This also explains why the relaxation oscillation is mostly observed in solid state lasers, which have relatively long upper laser level lifetimes.

B.1.2 Inside the Prometheus laser

The Prometheus laser is a typical Nd : YAG laser setup, including a pumping diode, a lasing material and an optical resonator (which in this case are combined in a laser crystal called the MISER), a noise eater for feeding back on the pumping diode, and a doubling crystal setup for producing the 532 nm output. A schematic of the setup is shown in Figure B.2.

The diode used in our laser is Coherent s-81-2700c-200-H/L, with an output centered at 808 nm. The noise in the diode output contributes to the laser output intensity fluctuation at low frequencies. As discussed in the last section, when the pumping diode degrades, fluctuations in its output power will cause relaxation oscillations. The lowered laser output will also cause the laser noise eater to malfunction, this will be discussed later.

The centerpiece of the laser is a MISER, or monolithic isolated single-mode end-pumped ring. It is a Nd : YAG crystal which also forms a nonplanar ring optical cavity. The front surface of the crystal has a partially reflective dielectric mirror coating which serves as the output coupler mirror of the cavity. The light bounces around the internal surfaces due to total internal reflection.

Besides the obvious advantage of being mechanically stable, the MISER also easily provides a single frequency output. The small size of the crystal (usually on mm scale) makes the axial mechanical modes sufficiently far apart. The design of the MISER also makes the beam a unidirectional traveling wave. This prevents creating standing wave in the gain medium, where population inversion could be saturated at antinodes, and untapped inversions at nodes will contribute to other modes. Such distortion of the gain shape, known as spatial hole burning[67], makes it difficult to achieve single frequency output.

The MISER eliminates standing wave by working as an optical isolator. The MISER crystal is nonplanar, this acts as a half waveplate that rotates the light polarization everytime it touches a surface. A magnet is attached to the crystal (as will be mentioned later, special attention is needed when using tools around the MISER because of the magnet) to create the Faraday effect. Finally, the front surface coating has a reflectivity that is polarization dependent, and acts like a polarizer. It favors one beam direction over the other, and avoids forming a standing wave.

The frequency of the laser output can be tuned by varying the crystal temperature, which changes the ring cavity length. For Nd : YAG crystal at 1064 nm, the thermal tuning coefficient is $-3 \text{ GHz}/^\circ\text{C}$. Changing the pumping power also changes the crystal temperature, and thereby changes the output frequency. Another way to tune the frequency is to apply stress on the MISER by a piezoelectric transducer (PZT). The PZT creates stress-induced birefringence in the crystal refractive index, and changes the cavity shape. The Prometheus laser PZT has a frequency tuning

range of ± 200 MHz, with a bandwidth up to 200 kHz, making it convenient for fast feedback.

Theoretically, the fundamental limit of the laser linewidth is the Schawlow-Townes equation[68] when only quantum noise is considered. For a finesse $F = 100$ cavity at 1 mW output, this limit is $\Delta\nu_L = 1$ Hz. As seen in the previous paragraph, significant additional frequency noise can be added by temperature fluctuations, pumping power fluctuations, and mechanical vibrations. The Prometheus laser has a typical linewidth of less than 1 kHz. Again, suppressing the pumping power fluctuation helps to reduce the laser frequency noise.

As shown in Figure B.2, the output from the MISER goes to a beam sampler, where a small part of the beam is picked off by a noise eater. The noise eater feeds back on the pumping diode current to suppress its fluctuations. In the Prometheus laser, this eliminates the relaxation oscillation and lowers the laser intensity noise.

B.2 Instructions for replacing laser diode

B.2.1 Replacing the laser diode

A sign that the laser diode is degrading is a decrease in output laser power at the nominal current. Notice at high powers (> 100 mW), the power measurement should be carried out using a power attenuator (e.g. Coherent 1000:1 Attenuator), or a combination of several beamsplitters, before the power meter.

The replacement laser diode part number is Coherent s-81-2700c-200-H/L. A thin graphite or indium sheet is also needed to provide good thermal contact between the laser diode and the heat sink. To replace the diode, the procedure is as follows:

1. Turn off the laser, disconnect the power cable and the GPIB cable from the back of the laser. Move the laser from the optical breadboard to somewhere easy to access (we will need to access several screws on the bottom of the laser later). The laser position on the breadboard can be reproduced accurately by locking down several posts on the sides of the laser before moving it out.
2. Remove the laser cover by unscrewing the IR beam shutter (two M2 screws). Then remove

four black M2 screws on each side of the cover. Lift up the cover, watch out for the mirror mounts to the rear of the laser.

3. Disconnect the noise eater black wires from the toroid. Disconnect the LED white wires from the PCB on the bottom next to the diode. Disconnect the three MISER cables at the connector. Cut off the cable tie and disconnect the MISER piezo cable that is tied to the three MISER cables.

4. Unscrew the M3 screw of the stabilization rod on the side. Remove the five M4 screws on the rear bottom of the laser (two on each side, and one in the center), and remove the heat sink with the laser diode attached to it.

5. Wear gloves. Unscrew the laser diode from the heat sink and gently remove the graphite sheet on the back. Disconnect the diode wires from its connector.

6. Attach the graphite sheet (remember to ask for a new graphite sheet when you order the diode replacement from Innolight) to the new diode and rub it gently so you get good contact between the diode and the heat sink. Reconnect the laser diode wires and cut off the short circuit pin.

7. Attach the diode to the heat sink and put the heat sink back onto the laser. Reconnect all the wires. Put a new cable tie to bundle the MISER cables. Reconnect all cables to the laser controller.

B.2.2 Laser output optimization

Now we can put the laser back onto the optical breadboard and start optimizing its output.

1. Turn the laser on, set the diode current at 0.2 A. Set the diode temperature at 25 °C. Use an IR viewer (not an IR card!) to look at the spot where the diode output hits in the MISER, make sure it is centered on the front surface of the MISER. You can check this by adjusting the two lenses between the diode and the MISER in the X and Y directions. To be able to adjust the X, Y set screws on the lenses, you need to loosen the lock screw on the lens holders. As you move the Y set screws of the lenses, you can easily identify when the spot hits the edge of the MISER crystal, then recenter it. When using an Allen wrench to access the set screws, pay attention to the magnet on the MISER as it can attract the wrench and damage the crystal.

2. Once you are sure the beam is quite well centered, increase the diode current all the way to 2.2 A. You should be able to see some output from the MISER by now, open the IR beam shutter and measure the IR output. Again, be careful with the high power output.

3. Now you can adjust the X and Y set screws of the two lenses iteratively to maximize the IR output. Although it is mentioned in Innolight's instruction sheet that you also can try to adjust the Z positions of the lenses, we think it is usually unnecessary. Besides, loosening the screws for the lens mounts may cause mechanical perturbations to all the optics inside the laser.

4. As you might notice, at low diode currents above the lasing threshold, you can see two beams in the laser output, and the main output looks clipped on an IR card. Do not worry. As you increase the diode current to 2.1 A, the other beam will become dimmer and the main beam will become more circular. At low pumping power, the MISER allows significant lasing of a second mode, but as we approach the nominal conditions, that stray beam becomes negligible.

5. Once the laser output power is maximized by the lens adjustments, change the laser diode temperature to maximize the output power. The temperature range to look for the power maximum is 18 °C to 35 °C. If more than one power maximum appears in this range, use the lower one.

6. Now turn down the diode current a bit and reoptimize the temperature to put the laser output power at the level suggested on the laser datasheet. We need the laser output power to be the same as before to get the noise eater to work properly. Write down the optimal diode current level for future reference. Lock down the laser diode temperature setting on the laser controller.

7. Lower the diode current, tighten the lock screws on the two lens mounts. Turn the diode current back to the optimal value, and make sure the laser output stays the same.

8. You can verify the laser output mode with a scanning Fabry-Perot cavity to check if it is single mode.

9. During the adjustment, there is never the need to adjust the lens after the MISER, or anything in the doubling crystal beam path. Because it is difficult to get the mode shape right once you change it, such adjustments are not recommended. If you are absolutely sure the doubling crystal alignment has changed and it is difficult to recover the optimal IR output, you can always take the doubling crystal black box out, this will not affect the IR output.

B.2.3 Noise eater adjustment

The output from the MISER goes to a beam sampler, where a small part of the beam is directed to the noise eater. Input to the noise eater is produced at a photodiode, which requires an optimal power. Three potentiometers on the noise eater PCB adjust the gains of the feedback loop. The potentiometers look like copper screw heads. They are three amplifiers that largely do the same thing, although the one closest to the photodiode has the largest effect in changing the gain. It is recommended that the potentiometers be left at their factory settings, since bad settings can make the laser output unstable. Instead, we can adjust the power landing on the photodiode.

There are two LEDs on the noise eater to show if the power into the photodiode is within its working range. The green LED is on when there is too little power, the red LED is on when there is too much power. The noise eater monitor (pin 12) on the back of the laser controller tells us how much power is on the photodiode. In Innolight's instruction sheet, it is suggested that the noise eater monitor be set between 2.6 – 3.6 V. However, we found 4.0 V optimal for a laser we have. To change the amount of light onto the photodiode, adjust the Z position of the lens in front of the noise eater photodiode and recenter the beam in the X and Y directions.

The way to verify if the noise eater is working properly is to measure the laser output amplitude noise on a photodiode when the noise eater is on and off. As mentioned earlier, the classical amplitude noise of the IR output at 15mW should be at the shot noise level.

B.3 Changing the laser controller potentiometer

One problem we have seen over the years is that the potentiometer knobs on the laser controller front panel can have bad connections. When you turn the laser diode current knob, if you see the current display fluctuating up and down, it is most likely due to the potentiometer connection problem. The potentiometer part number is Bourns 3540S-1-103L, follow Innolight's instruction sheet to replace it.

Bibliography

- [1] Børkje, K. Unpublished notes on heterodyne thermometry (2011).
- [2] Nichols, E. F. & Hull, G. F. A preliminary communication on the pressure of heat and light radiation. *Physical Review* **13**, 307 (1901).
- [3] Levedew, P. Untersuchungen über die druckkräfte des lichtes. *Ann. der Physik* **6**, 433 (1901).
- [4] Ashkin, A. Applications of laser radiation pressure. *Science* **210**, 1081 (1980).
- [5] Ashkin, A., Dziedzic, J. M., Bjorkholm, J. E. & Chu, S. Observation of a single-beam gradient force optical trap for dielectric particles. *Optics Letters* **11**, 288 (1986).
- [6] Hansch, T. W. & Schawlow, A. L. Cooling of gases by laser radiation. *Optics Communications* **13**, 68 (1975).
- [7] Wineland, D. J., Drullinger, R. E. & Walls, F. L. Radiation-pressure cooling of bound resonant absorbers. *Physical Review Letters* **40**, 1639 (1978).
- [8] Chu, S., Hollberg, L., Bjorkholm, J. E., Cable, A. & Ashkin, A. 3-dimensional viscous confinement and cooling of atoms by resonance radiation pressure,. *Physical Review Letters* **55**, 48 (1985).
- [9] Stenholm, S. The semiclassical theory of laser cooling. *Review of Modern Physics* **58**, 699 (1986).
- [10] Anderson, M. H., Ensher, J. R., Matthews, M. R., Wieman, C. E. & Cornell, E. A. Observation of bose-einstein condensation in a dilute atomic vapor. *Science* **269**, 198 (1995).

- [11] Metzger, C. H. & Karrai, K. Cavity cooling of a microlever. *Nature* **432**, 1002 (2004).
- [12] Kleckner, D. & Bouwmeester, D. Sub-kelvin optical cooling of a micromechanical resonator. *Nature* **444**, 75 (2006).
- [13] Gigan, S. *et al.* Self-cooling of a micromirror by radiation pressure. *Nature* **444**, 67 (2006).
- [14] Arcizet, O., Cohadon, P.-F., Briant, T., Pinard, M. & Heidmann, A. Radiation-pressure cooling and optomechanical instability of a micro-mirror. *Nature* **444**, 71 (2006).
- [15] Naik, A. *et al.* Cooling a nanomechanical resonator with quantum back-action. *Nature* **443**, 193 (2006).
- [16] Schliesser, A., Del’Haye, P., Nooshi, N., Vahala, K. J. & Kippenberg, T. J. Radiation pressure cooling of a micromechanical oscillator using dynamical backaction. *Physical Review Letters* **97**, 243905 (2006).
- [17] Corbitt, T. *et al.* An all-optical trap for a gram-scale mirror. *Physical Review Letters* **98**, 150802 (2007).
- [18] Thompson, J. D. *et al.* Strong dispersive coupling of a high-finesse cavity to a micromechanical membrane. *Nature* **452**, 900 (2008).
- [19] Mancini, S. & Tombesi, P. Quantum noise reduction by radiation pressure. *Physical Review A* **49**, 4055 (1994).
- [20] S. Bourzeix, E. G., A. Heidmann *et al.* Quantum-noise reduction using a cavity with a movable mirror. *Physical Review A* **49**, 1337 (1994).
- [21] Mari, A. & Eisert, J. Gently modulating optomechanical systems. *Physical Review Letters* **103**, 213603 (2009).
- [22] Vitali, D. *et al.* Optomechanical entanglement between a movable mirror and a cavity field. *Physical Review Letters* **98**, 030405 (2007).

- [23] Braginsky, V. B. & Manukin, A. B. Ponderomotive effects of electromagnetic radiation. *Sov. Phys. Sov. Phys. JETP-USSR* **25**, 653 (1967).
- [24] Braginsky, V. B., Manukin, A. B. & Tikhonov, M. Y. Investigation of dissipative ponderomotive effects of investigation of dissipative ponderomotive effects of of electromagnetic radiation. *Sov. Phys. Sov. Phys. JETP-USSR* **31**, 829 (1970).
- [25] Clerk, A. A., Devoret, M. H., Girvin, S. M., Marquardt, F. & Schoelkopf, R. J. Introduction to quantum noise, measurement and amplification. *Review of Modern Physics* **82**, 1155 (2010).
- [26] Marquardt, F., Chen, J. P., Clerk, A. A. & Girvin, S. M. Quantum theory of cavity-assisted sideband cooling of mechanical motion. *Physical Review Letter* **99**, 093902 (2007).
- [27] Gröblacher, S. *et al.* Demonstration of an ultracold micro- optomechanical oscillator in a cryogenic cavity. *Nature Physics* **5**, 485 (2009).
- [28] Knight, J. C., Cheung, G., Jacques, F. & Birks, T. A. Phase-matched excitation of whispering-gallery-mode resonances by a fiber taper. *Optics Letters* **22**, 1129 (1997).
- [29] Vernooy, D. W., Ilchenko, V. S., Mabuchi, H., Streed, E. W. & Kimble, H. J. High-q measurements of fused-silica microspheres in the near infrared. *Optics Letters* **23**, 247 (1998).
- [30] Armani, D. K., Kippenberg, T. J., Spillane, S. M. & Vahala, K. J. Ultra-high-q toroid microcavity ultra-high-q toroid microcavity on a chip. *Nature* **421**, 925 (2003).
- [31] Schliesser, A., Arcizet, O., Rivière, R., Anetsberger, G. & Kippenberg, T. J. Resolved-sideband cooling and position measurement of a micromechanical oscillator close to the heisenberg uncertainty limit. *Nature Physics* **5**, 509 (2009).
- [32] Rivière, R. *et al.* Optomechanical sideband cooling of a micromechanical oscillator close to the quantum ground state. *PHYSICAL REVIEW A* **83**, 063835 (2011).
- [33] Verhagen, E., Deléglise, S., Weis, S., Schliesser, A. & Kippenberg, T. J. Quantum-coherent coupling of a mechanical oscillator to an optical cavity mode. *ArXiv* 1107.3761v1 (2011).

- [34] Park, Y.-S. & Wang, H. Resolved-sideband and cryogenic cooling of an optomechanical resonator. *Nature Physics* **5**, 489 (2009).
- [35] Chan, J. *et al.* Laser cooling of a nanomechanical oscillator into its quantum ground state. *ArXiv* 1106.3614v1 (2011).
- [36] Rocheleau, T. *et al.* Preparation and detection of a mechanical resonator near the ground state of motion. *Nature* **463**, 72 (2009).
- [37] Teufel, J. D. *et al.* Sideband cooling of micromechanical motion to the quantum ground state. *Nature* **475**, 359 (2011).
- [38] Caves, C. M. Quantum-mechanical noise in an interferometer. *Physical Review D* **23**, 1693 (1981).
- [39] Kimble, H. J., Levin, Y., Matsko, A. B., Thorne, K. S. & Vyatchanin, S. P. Conversion of conventional gravitational-wave interferometers into quantum nondemolition interferometers by modifying their input and/or output optics. *Physical Review D* **65**, 022002 (2001).
- [40] Mow-Lowry, C. M., Sheard, B. S., Gray, M. B. & McClelland, D. E. Experimental demonstration of a classical analog to quantum noise cancellation for use in gravitational wave detection. *Physical Review Letters* **92**, 161102 (2004).
- [41] Jacobs, K., Tombesi, P., Collett, M. J. & Walls, D. F. Quantum-nondemolition measurement of photon number using radiation pressure. *Physical Review A* **49**, 1961 (1994).
- [42] Heidmann, A., Hadjar, Y. & Pinard, M. Quantum nondemolition measurement by optomechanical coupling. *Applied Physics B: Lasers and Optics* **64**, 173 (1997).
- [43] Verlot, P., Tavernarakis, A., Briant, T., Cohadon, P.-F. & Heidmann, A. Scheme to probe optomechanical correlations between two optical beams down to the quantum level. *Physical Review Letters* **102**, 103601 (2009).
- [44] Børkje, K. *et al.* Observability of radiation pressure shot noise in optomechanical systems. *Physical Review A* **83**, 013818 (2010).

- [45] Zwickl, B. M. *Progress Toward Observation of Radiation Pressure Shot Noise*. Ph.D. thesis, Yale University (2011).
- [46] Zwickl, B. M. *et al.* High quality mechanical and optical properties of commercial silicon high quality mechanical and optical properties of commercial silicon high quality mechanical and optical properties of commercial silicon nitride membranes. *Applied Physics Letter* **92**, 103125 (2008).
- [47] Jayich, A. M. *et al.* Dispersive optomechanics: a membrane inside a cavity. *New Journal of Physics* **10**, 095008 (2008).
- [48] Sankey, J. C., Yang, C., Zwickl, B. M., Jayich, A. M. & Harris, J. G. E. Strong and tunable nonlinear optomechanical coupling in a low-loss system. *Nature Physics* **6**, 707 (2010).
- [49] Elliott, D. S., Roy, R. & Smith, S. J. Extracavity laser band-shape and bandwidth modificatio. *Physical Review A* **26**, 12 (1981).
- [50] Rabl, P., Genes, C., Hammerer, K. & Aspelmeyer, M. Phase-noise induced limitations on cooling and coherent evolution in optomechanical systems. *Physical Review A* **80**, 063819 (2009).
- [51] Diósi, L. Laser linewidth hazard in optomechanical cooling. *Physical Review A* **78**, 021801 (2008).
- [52] Clerk, A. A., Devoret, M. H., Girvin, S. M., Marquardt, F. & Schoelkopf, R. J. Introduction to quantum noise, measurement and amplification: Online appendices. *Review of Modern Physics* **82**, 1155 (2010).
- [53] Collett, M. J. & Gardiner, C. W. Squeezing of intracavity and traveling-wave light fields produced in parametric amplification. *Physical Review A* **30**, 1386 (1984).
- [54] Giovannetti, V. & Vitali, D. Phase-noise measurement in a cavity with a movable mirror undergoing quantum brownian motion. *Physical Review A* **63**, 023812 (2001).

- [55] Genes, C., Vitali, D., Tombesi, P., Gigan, S. & Aspelmeyer, M. Ground-state cooling of a micromechanical oscillator: Comparing cold damping and cavity-assisted cooling schemes. *Physical Review A* **77**, 033804 (2008).
- [56] Carmichael, H. J. Spectrum of squeezing and photocurrent shot noise: a normally ordered treatment. *Journal of Optical Society America B* **4**, 1588 (1987).
- [57] Nunnenkamp, A., Børkje, K., Harris, J. G. E. & Girvin, S. M. Cooling and squeezing via quadratic optomechanical coupling. *Physical Review A* **2**, 021806 (2010).
- [58] Weis, S. *et al.* Optomechanically induced transparency. *Science* **330**, 1520 (2010).
- [59] Agarwal, G. S. & Huang, S. Electromagnetically induced transparency in mechanical effects of light. *Physical Review A* **81**, 041803 (2010).
- [60] Teufel, J. D. *et al.* Circuit cavity electromechanics in the strong-coupling regime. *Nature* **471**, 204 (2011).
- [61] Black, E. D. An introduction to pound–drever–hall laser frequency stabilization. *American Journal of Physics* **69**, 79 (2001).
- [62] Schuenemann, U., Engler, H., Grimm, R., Weidemüller, M. & Zielonkowskic, M. Simple scheme for tunable frequency offset locking of two lasers. *Review of Scientific Instruments* **70**, 242 (1999).
- [63] J.L.Hall, M.S.Taubman & J.Ye. Laser stabilization. *OSA Handbook* **v14** (2001).
- [64] O’Connell, A. D. *et al.* Quantum ground state and single-phonon control of a mechanical resonator. *Nature* **464**, 697 (2010).
- [65] Szilard, R. *Theory and Analysis of Plates: Classical and Numerical Methods* (Prentice Hall, 1974).
- [66] Koechner, W. *Solid-State Laser Engineering*, vol. 1 of *SPRINGER SERIES IN OPTICAL SCIENCES* (Springer, 2006).

- [67] Kimura, T., Otsuka, K. & Saruwatari, M. Spatial hole-burning effects in a Nd³⁺ : YAG laser. *IEEE Journal of Quantum Electronics* **7**, 225 (1971).
- [68] Schawlow, A. L. & Townes, C. H. Infrared and optical masers. *Physical Review* **112**, 1940 (1958).